Quasi-long-range order and topological defects in graphene on rhenium studied by scanning tunneling microscopy

Alexandre Artaud

To cite this version:

Alexandre Artaud. Quasi-long-range order and topological defects in graphene on rhenium studied by scanning tunneling microscopy. Condensed Matter [cond-mat]. Université Grenoble Alpes, 2017. English. NNT : 2017GREAY009 . tel-01628213

HAL Id: tel-01628213
https://theses.hal.science/tel-01628213v1

Submitted on 3 Nov 2017

Communauté
UNIVERSITÉ Grenoble Alpes

THÈSE

Pour obtenir le grade de

DOCTEUR DE LA COMMUNAUTE UNIVERSITE GRENOBLE ALPES

Spécialité : **Physique de la matière condensée et du rayonnement**

Arrêté ministériel : 7 août 2006

Présentée par

Alexandre ARTAUD

Thèse dirigée par **Claude CHAPELIER** et
codirigée par **Johann CORAUX**

préparée au sein du **Laboratoire de Transport Electronique Quantique et Supraconductivité, de l'Institut Nanosciences et Cryogénie – CEA Grenoble**
et du **Département Electronique quantique, surfaces et spintronique, de l'Institut Néel – CNRS**
dans **l'École Doctorale de Physique de Grenoble**

Quasi-ordre à longue distance et défauts topologiques dans le graphène sur rhénium étudié par microscopie à effet tunnel

Thèse soutenue publiquement le **28 Février 2017**,
devant le jury composé de :

Prof. Richard BERNDT
Professeur à la Christian-Albrechts-Universität zu Kiel, Examinateur
Dr. Mark Oliver GOERBIG
Directeur de recherche au Laboratoire de Physique des Solides d'Orsay, Rapporteur
Prof. José Ángel MARTIN-GAGO
Professeur à l'Instituto de Ciencia de Materiales de Madrid, Rapporteur
Dr. Claudine NOGUERA
Directrice de recherche à l'Institut des Nanosciences de Paris, Examinatrice
Dr. Marek POTEMSKI
Directeur de recherche au Laboratoire National des Champs Magnétiques Intenses de Grenoble, Président

Communauté
UNIVERSITÉ Grenoble Alpes

THESIS

To obtain the degree of

DOCTOR OF THE COMMUNAUTE UNIVERSITE GRENOBLE ALPES

Specialty: **Condensed matter and radiation physics**

Ministerial order: 7 August 2006

Presented by

Alexandre ARTAUD

Thesis supervised by **Claude CHAPELIER** and
Co-supervised by **Johann CORAUX**

prepared in **Laboratoire de Transport Electronique Quantique et Supraconductivité, de l'Institut Nanosciences et Cryogénie – CEA Grenoble**
and **Département Electronique quantique, surfaces et spintronique, de l'Institut Néel – CNRS**
in **École Doctorale de Physique de Grenoble**

Quasi-long-range order and topological defects in graphene on rhenium studied by scanning tunneling microscopy

Publicly defended thesis on the **28th of February 2017**,
In front of the jury composed of:

Prof. Richard BERNDT
Professor at the Christian-Albrechts-Universität zu Kiel, Examiner
Dr. Mark Oliver GOERBIG
Senior research fellow at the Laboratoire de Physique des Solides d'Orsay, Reviewer
Prof. José Ángel MARTIN-GAGO
Professor at the Instituto de Ciencia de Materiales de Madrid, Reviewer
Dr. Claudine NOGUERA
Senior research fellow at the Institut des Nanosciences de Paris, Examiner
Dr. Marek POTEMSKI
Senior research fellow at the Laboratoire National des Champs Magnétiques Intenses de Grenoble, President

Remerciements

Personne n'est dupe, et chacun sait que la section des remerciements est la partie la plus lue de tout manuscrit de thèse. C'est d'autant plus ironique que c'est le seul passage écrit sans correction ni caféine. Or, celles et ceux qui me connaissent savent à leurs dépens que je suis moins avare en mauvaises blagues qu'en remerciements émus. Aussi, j'espère que chacun saura apprécier la sincérité fugace mais authentique de ces quelques lignes. Et si d'aventure quelque lecteur venait à me croire toujours tendre et mielleux, je me tiens à disposition pour corriger de visu cette erreur d'appréciation.

J'ai eu la chance de préparer ma thèse dans deux laboratoires. D'une part, au Laboratoire de Transport Électronique Quantique et Supraconductivité (LaTEQS) du CEA Grenoble, au sein du Service de Physique Statistique Magnétisme et Supraconductivité (SPSMS). Et d'autre part, dans l'équipe Systèmes Hybrides de basse dimensionnalité (Hybrid), au sein du département Electronique QUantique Surfaces et spinTronique (QUEST) de l'Institut Néel (CNRS). En premier lieu, je voudrais donc remercier Jean-Pascal Brison, Marc Sanquer, Etienne Bustarret, et Laurence Magaud, directeurs et directrice respectifs du SPSMS, du LaTEQS, de l'Institut Néel et du département QUEST. Grâce à eux, j'ai pu bénéficier d'exceptionnelles conditions de travail, tant sur les plans humain que matériel. Je remercie également celles qui ont rendu cette thèse possible par leur assistance toujours appréciée, et parfois providentielle : Marielle Perrier, Sabine Gadal et Florence Pois.

Par ailleurs, je tiens à remercier chaleureusement mes directeurs de thèse Claude et Johann. D'abord scientifiquement, nos échanges m'ont beaucoup apporté pour développer davantage d'esprit critique et de capacité d'analyse. J'aimerais dire que cela tient essentiellement à votre patience, mais je ne voudrais pas qu'on la méprenne pour celle du professeur qui ré-explique encore et encore à un élève. Au contraire, votre patience a été celle de respecter mon avis, et de m'amener à le nuancer par petites touches. Il ne faudrait pas non plus sous-évaluer le rôle central qu'a joué l'humour dans nos conversations, et qui a garanti l'ambiance de nos "points thèse". Je vous suis reconnaissant pour tout cela, et cette ambiance de travail va me manquer.

Je dois aussi beaucoup à votre accompagnement et à votre bienveillance, qui ont été pour moi de réels moteurs pendant la thèse, me poussant à avancer et à tenir bon dans les moments difficiles. J'ai ainsi été sensible à vos conseils avisés, qui ont toujours su me faire relativiser mes doutes. Plus encore, je me sens honoré de la confiance que vous m'avez accordée, et j'aimerais que vous sachiez combien elle m'a aidé à persévérer et à m'épanouir. En somme, vous êtes tous les deux d'excellents encadrants, dans deux styles différents et complémentaires, et je n'aurais pas pu rêver mieux pour me guider pendant ces années.

Je souhaite te remercier plus particulièrement, Claude. Pendant ces trop courtes années de thèse, tu as été remarquablement à mon écoute, et tu m'as toujours accordé beaucoup de temps. Je ne crois pas être le premier à le souligner dans des remerciements, car d'autres avant moi ont déjà loué ta disponibilité et ta sincérité. Et pour cause, même débordé par ce que tu as à faire en parallèle, tu n'hésites pas à tout mettre de côté pour t'intéresser aux problèmes de tes étudiants, et comme eux, j'y ai été sensible. J'aimerais aussi te remercier pour l'exemple que tu offres de dépassement perpétuel de soi-même, à toujours t'aventurer hors de ta zone de confort avec une curiosité renouvelée et l'envie d'apprendre. Enfin, et c'est sûrement le trait de ta personnalité qui suscite le plus mon admiration, je voudrais saluer ton intégrité et ton indépendance d'esprit. Que ce soit en recherche ou au quotidien, tu n'es pas parmi ceux qui acceptent l'incohérence et l'injustice, mais de ceux qui font porter la voix de leur désaccord. Ce courage ne te vaut pas que des amitiés, mais ce faisant, je pense que tu portes haut les valeurs de la recherche fondamentale.

J'aimerais aussi t'exprimer une reconnaissance plus personnelle, Johann. Je te remercie en effet pour toutes les fois où tes petits conseils en passant m'ont débloqué. Cette déconcertante capacité à avoir raison en dépit de tout contre-argumentaire a parfois pu me rendre chèvre, mais à ce jeu-là, tu as toujours eu l'élégance d'avoir le triomphe modeste. Tu figures aussi pour moi un modèle d'équilibre et de sens des réalités – ce qui est rare dans notre milieu –, et j'ai souvent été impressionné par ton sang-froid (presque autant que par l'éclectisme de tes goûts musicaux). Au-delà de cela, et c'est ta force, tu mets ces qualités au service de tes étudiants, quitte à les bousculer un peu. Ce n'est pas un rôle facile, mais tu l'endosses avec tact et brio, et je t'en suis profondément reconnaissant.

Je souhaite aussi remercier Mark Oliver Goerbig et José Ángel Martin-Gago pour avoir relu mon manuscrit de thèse, ainsi que Richard Berndt, Claudine Noguera et Marek Potemski pour avoir accepté de faire partie de mon jury de thèse. Je leur adresse ma gratitude pour l'intérêt qu'ils ont porté à mon travail, pour le temps qu'ils ont consacré à la lecture du manuscrit, et pour les questions stimulantes qu'ils ont posées lors de la soutenance. Ils ont ainsi contribué à en faire un moment unique.

J'adresse aussi des remerciements sincères à nos collaborateurs. D'abord, je remercie Laurence pour sa bonne humeur et sa persévérance, en dépit de toutes les difficultés qu'on a pu lui imposer. Sans son importante implication, il aurait été impossible d'aller aussi loin. Je remercie aussi nos collègues du SIMAP, Bruno Gilles et ses étudiants Kitti Ratter et Benjamin Delsol, pour avoir fourni les couches minces de rhénium, ainsi que pour l'éclairage de leurs avis sur nos résultats. Je suis également reconnaissant à Florent Calvo et Daniel Förster pour leurs contributions au projet, mais aussi pour les intéressantes questions qu'ont soulevées nos échanges.

Je voudrais aussi exprimer ma reconnaissance envers toutes celles et tous ceux qui m'ont accompagné pendant cette thèse. Votre présence à mes côtés a rendu mon séjour à Grenoble inoubliable, et exprimer la gratitude que je ressens est un exercice périlleux, tant je chéris les nombreux souvenirs des moments passés ensemble. Je pense d'abord à mes compagnons de manip, avec qui nous avons traversé pannes et montages fastidieux, mais aussi quelques moments de grâce. Merci à Sergio pour m'avoir pris sous son aile à mes débuts, à Shashank pour nos discussions enrichissantes (parfois enflammées !) sur toutes sortes de sujets, et à Simone pour son style authentique et inégalable. D'immenses remerciements vont aussi à Valérie et Philippe pour la complicité et l'aide qu'ils m'ont apportées pendant trois ans. J'aimerais aussi remercier Eduard pour son humour décapant, Toai pour tous ces bons moments passés en conférence, et Loïc pour avoir supporté mes plus mauvaises blagues avec une endurance et un panache démontrant ses grandes qualités de STM-iste. Je remercie aussi celles qui ont assuré la continuité du projet de recherche dans lequel s'inscrit cette thèse : Charlène, Amina et Estelle, qui m'ont accompagné de leur bonne humeur et de leurs conseils, et avec qui j'ai eu un grand plaisir à travailler. Je souhaite d'ailleurs du bonheur et du succès à Estelle, la future championne du rhénium !

Ayant eu le plaisir de bénéficier de deux laboratoires, l'un au CEA et l'autre au CNRS, j'aimerais aussi remercier les équipes qui m'y ont accueilli. Merci aux chercheurs du LaTEQS : Christophe, François pour nos discussions impromptues à la MC2, Louis, Marc, Max, Silvano, Vincent pour nos conversations interminables mais toujours passionnantes, et Xavier et son ironie délicieuse et caustique. Je salue aussi les chercheurs du laboratoire-frère IMAPEC : Alexandre pour son franc-parler, Dai, Daniel, Georg, et Jean-Pascal pour sa bienveillance. Je remercie de plus les ingénieurs du C1 parmi lesquels Frédéric, Iulian, Jean-Luc (le nostradamus des chutes à vélo) et Pierre.

Au sein du SPSMS, j'ai aussi eu la chance de connaître de (trop ?) nombreuses vagues de thésards qui ont apporté leur lots de rires et d'échanges à la vie de laboratoire. Je remercie en particulier les "anciens" que constituent Andreas, Benoit, Boris, Caroline, Charlène, Driss, Mathieu T. pour leur bonne humeur et leur entrain. Merci aussi à Jean-Eudes, Paul, Toai, et à mes camarades de promotion Adrien, Andrea, Bei-Lun, Gaël, Juan Carlos, Patrick et Salha. Je salue plus particulièrement mes trois comparses Alexander – qui a porté haut l'honneur des Pipotages –, Joseph et Lars, pour leur humour et leurs rires (surtout celui de Lars). Je souhaite également une heureuse poursuite aux prochaines générations, parmi lesquelles Anaïs, Loïc, Florian, Heorhii, Mathieu qui s'tasse, Pacôme, Anthony, Estelle, Romain A. et Thomas. Je remercie aussi les quelques post-docs qui ont émaillé mon parcours au CEA de leur expérience, de leur conseil et de leur gentillesse. Je pense bien sûr à Eduard, au tribun Felipe, au sage Dibyendu, au fort sympathique Romain M., à ces messieurs Alessandro et Dharam, au stochastique Roman, et aux doctes théoriciens Tania et Kostya.

De la même manière, j'aimerais exprimer la gratitude que j'ai pour mes collègues du CNRS. Je remercie donc en particulier les chercheurs de l'équipe Hybrid, Julien, Laëtita, Laurence, Nedjma et Vincent, pour l'énergie et l'inventivité qu'ils déploient dans l'encadrement des étudiants et dans la vie de l'équipe. Mes amitiés vont aux thésards qui m'y ont chaleureusement accueilli, Amina, Cornelia, Dipankar, Farida, Hadi, Fabien, Vitto, Yani, ainsi qu'à ceux qui nous ont rejoints : Pauline, Goutham, Ana, Estelle, Roberto et Van-Dung. Je remercie également les post-docs que j'ai eu le plaisir de rencontrer : John, Sergio, Mira, Duc, Riadh, Simone, Sudipta et Debora. J'ai passé de très bons moments avec vous tous, que ce soit lors des conversations qui ont animé nos repas, des cafés pris sur le pouce et se prolongeant en longues discussions, ou des si fameuses réunions d'équipe.

J'ai bien entendu eu beaucoup de plaisir à interagir avec d'autres personnes hors des équipes auxquelles j'étais rattaché. A cet égard, j'aimerais remercier Pierre Mallet, Jean-Yves Veuillen et Nicolas Roch avec qui j'ai eu plaisir d'échanger sur un mode plus ou moins scientifique selon les circonstances. Des mercis reviennent naturellement aussi à quelques figures sympathiques qui ont animé ma vie au laboratoire, dont Adib, André, Benjamin, Clément, Hanno, Hugo, Joachim, Johanna, Katrin, Kevin, Logi, Nicolas, Oleg, Quentin, Sayanti, Valérie R et bien d'autres. Qu'aurait été ma thèse sans la présence réconfortante de mes co-bureaux Martin, Quanbo, Michal, Jorge, et encore d'autres, avec qui nous avons traversé les affres de l'été grenoblois ? Peu de choses, sans aucun doute. Et parmi eux, je tiens à remercier plus particulièrement Alexis pour les précieux moments que nous avons partagés dans ce bureau, qu'ils fussent d'échanges d'avis esthétiques, de débats scientifiques, ou d'humour de douteuse teneur à l'approche du week-end. Mon séjour à Grenoble n'aurait jamais été le même sans les vacances, excursions, dîners et autres fêtes qui l'ont ponctué, et qui constituent pour moi de formidables souvenirs. Certains – parfois déjà cités ci-dessus – y ont beaucoup contribué, et même si les mots manquent, j'aimerais leur exprimer ma plus sincère gratitude. Merci à Chloé, Elie, Emilie, Gilles, Gogo, Karim, Ketty, Laure, Olivier, Marine, Yann, Sylvain et Valoche.

Parmi certains collègues cités plus haut, certains m'ont aussi accompagné dans mon parcours d'enseignant. J'aimerais en particulier saluer la bienveillance avec laquelle Alexandre, Nedjma et Vincent m'ont fait profiter de leur expérience de maître de conférence. J'aimerais aussi adresser mon admiration à Alain Drillat pour le dévouement et la passion qu'il met dans son travail, et ma sincère reconnaissance à Elise Ghibaudo pour sa gentillesse et pour le temps et l'attention qu'elle m'a consacrés. Mon expérience d'enseignement n'aurait jamais pu être aussi enrichissante sans vous.

J'adresse aussi des remerciements un peu spéciaux à la fine équipe de Ma Thèse en 180 secondes. Merci à Marine et Emilie pour m'avoir toujours accompagné avec vos conseils et vos sourires, à Julien et Xavier pour m'avoir précieusement épaulé, ainsi qu'à Denis, Jean-Loup, Johanne, Kevin, Tania, Jean-Louis, Jonathan et Loïc avec qui j'ai découvert des lieux et rencontré des personnes au-delà de ce que je pouvais imaginer.

Au cours de ces dernières années, j'ai eu la joie de faire du théâtre grâce à l'entremise inespérée de Dipankar auprès de Laëtitia. Laëtitia, je ne saurais jamais assez te remercier pour m'avoir introduit à la troupe, où j'ai pu m'épanouir hors du labo pendant deux ans et demi. J'ai une reconnaissance particulière pour Christine et pour Bruno, qui ont encadré nos troupes chacun avec leur style. Et je salue affectueusement celles et ceux avec qui on s'est amusé sur les planches : Alizé, Benoit, Emilie, Eve, Fabienne, Jeff, Laurent, Marie-Christine, Pierre, Alix, Clémence, Danielle, Francine, et les couples David et Sabrina, et Nathalie et Julien.

Je voudrais également dire merci aux amis qui m'ont soutenu pendant la thèse, à distance, en vacances, ou sur les pistes de ski, et ce même si je les soupçonne de n'avoir jamais vraiment compris ce que je faisais. Je pense ainsi à Sév – mon rival de toujours –, à Pierre même s'il n'a pas de cerveau, et à Charlotte, ma petite préférée. Je remercie aussi Anna et Ghyom pour leur grande hospitalité, et tous les bons moments passés chez eux. Ma gratitude va également aux londoniens qui ont su garantir des séjours outre-manche toujours revigorants : Thomas pour son rare sens de l'écoute, Zaz pour le réconfort qu'elle apporte quand ça ne va pas, Paul pour ses plans de vacances si enthousiasmants qu'ils permettent d'endurer n'importe quelle charge de travail, Mélina pour sa fraicheur authentique et bienveillante, et Simon, le petit nouveau que j'ai eu le plaisir de découvrir à Londres. Je profite d'ailleurs de ces lignes pour remercier et féliciter les jeunes mariés Hala et Dani, à qui je souhaite le bonheur de dire beaucoup de choses... Merci aussi à Julien, qui a eu la noblesse d'âme de partager avec moi le statut d'éternel étudiant, à Aurore pour sa douceur légendaire, à Rattena qui sait autant que moi apprécier cette douceur, à Raphaëlle K qui conserve le nom le plus stylé du monde, ainsi qu'à Etienne pour les petits week-ends où il a su démontrer qu'il sait bien recevoir. Il faut aussi que je remercie Guillemette, mais c'est bien parce que je m'en sens obligé.

Je salue aussi le club des 5, et remercie ainsi Charles, Clément, Dany, Olivier et Pierre pour avoir comblé avec du rire quelques moments de flottement. Mes remerciements vont aussi à Violaine, à qui je souhaite beaucoup d'épanouissement dans la poursuite de sa thèse, à François pour sa présence toujours amicale auprès de moi, ainsi qu'à Matthieu, le dernier baroudeur de notre siècle qui sait encore me faire rêver. Un salut admiratif va également à Dimitri, qui du jeune étudiant que j'ai connu a su évoluer en un modèle d'indépendance et de liberté.

Enfin, j'aimerais remercier ma famille, qui a toujours été un soutien indéfectible. Au-delà de la gratitude, je suis touché que vous respectiez qui je suis et les décisions que je prends, quand bien même ce n'est pas toujours facile à suivre. Ce que j'ai accompli de meilleur, c'est en grande partie grâce à vous, et je vous en suis sincèrement reconnaissant.

Résumé

La découverte du graphène en 2004 constitue une double avancée en physique de la matière condensée. D'une part, ses propriétés électroniques sont celles d'un gaz de fermions de Dirac sans masse. D'autre part, sa structure fournit le tout premier exemple d'un matériau ordonné à deux dimensions.

Cette seconde caractéristique est étudiée dans cette thèse par microscopie à effet tunnel (STM), dans le cas du graphène synthétisé en ultra-haut vide sur la face (0001) du rhénium. A deux dimensions, l'ordre cristallin est en effet impossible, et il est prédit qu'un quasi-ordre à longue distance s'y substitue, où la phase du paramètre d'ordre fluctue. Le substrat de rhénium intervient alors comme une influence extérieure qui peut restaurer l'ordre cristallin, en forçant la structure du graphène à épouser une relation d'épitaxie avec le rhénium.

L'étude proposée de la structure du graphène démontre qu'elle est en fait tributaire de contraintes cinétiques héritées de sa croissance. Plusieurs nanostructures caractéristiques ont ainsi été identifiées à l'échelle atomique, permettant de remonter au mécanisme de croissance. Deux chemins réactionnels y entrent ainsi en compétition. Le premier aboutit à une famille d'agrégats de carbone métastables, de structures bien définies, en épitaxie sur le rhénium. Le second mène à la croissance d'îlots de graphène qui s'étendent sur quelques nanomètres. La coalescence de ces îlots et l'incorporation des agrégats en leur sein conduit à des défauts structurels dont la structure atomique est détaillée pour la première fois. Cette étude exhaustive révèle la diversité des chemins réactionnels lors de la croissance de graphène sur rhénium, qui sont autant de compromis entre cinétique et thermodynamique.

Au terme de cette croissance, le graphène obtenu n'est pas uniforme, mais comme constitué de domaines s'étendant sur des distances de l'ordre de 10 nm. Chaque domaine présente une relation d'épitaxie entre le graphène et le rhénium qui lui est propre, où le graphène s'avère à la fois tourné et cisaillé par rapport à son substrat, comme le montre une méthode d'analyse d'images STM développée à cet effet. L'élaboration d'une classification universelle de ces relations d'épitaxie montre leur grande diversité. Deux interprétations se confrontent alors. Les parois entre domaines de graphène peuvent en effet être interprétées comme des défauts topologiques dans l'ordre cristallin imposé au graphène par le substrat de rhénium. Alternativement, ce sont des modes de fluctuations dont la dynamique est gelée par l'interaction avec le substrat. Ces résultats remettent donc en question la notion d'ordre cristallin imposé par son substrat à un matériau bidimensionnel. Ils montrent qu'au lieu de forcer une relation d'épitaxie particulière, l'interaction du graphène avec son substrat donne lieu à une phase dite chaotique.

Abstract

The discovery of graphene in 2004 is a two-fold breakthrough in condensed matter physics. On the one hand, its electronic properties are that of a massless Dirac fermion gas. On the other hand, its structure is the very first example of an ordered material in two dimensions.

This second characteristics is studied in this thesis by scanning tunneling microscopy (STM), in the case of graphene grown in ultra-high vacuum on the (0001) surface of rhenium. In two dimensions, crystalline order is indeed impossible, and it is predicted to be replaced by a quasi-long-range order, for which the phase of the order parameter fluctuates. The rhenium substrate then acts as an outside influence that can restore crystalline order, as it forces graphene's structure to adopt an epitaxial relation with rhenium.

The study of graphene's structure proposed here proves it actually originates from kinetic constraints inherited from its growth. Many typical nanostructures have indeed been identified at the atomic scale, giving access to the growth mechanism. Two reaction pathways compete. The first one gives rise to a family of metastable carbon clusters with well-defined structures in epitaxy on rhenium. The second one leads to growing graphene islands of a few nanometers in size. The coalescence of these islands and the incorporation of the carbon clusters ends up forming structural defects whose atomic structure is detailed for the first time. This exhaustive study reveals reaction pathways in the growth of graphene on rhenium are diverse, and constitute compromises between kinetics and thermodynamics.

At the end of that growth, the obtained graphene is not uniform, but somehow made of roughly 10 nm-large domains. Each domain displays a specific epitaxial relation with rhenium, in which graphene is both twisted and sheared with respect to rhenium, as revealed a STM image analysis method developed for this purpose. Elaborating a universal classification of such epitaxial relations shows they are very diverse. Two interpretations of this morphology are possible. The graphene domain walls can indeed be interpreted as topological defects in the crystalline order set in graphene by the rhenium substrate. Otherwise, they are fluctuation modes whose dynamics is frozen by the interaction with the substrate. These results put into question the notion of crystalline order set by a substrate to a two-dimensional material. They show that instead of forcing a specific epitaxial relationship, the graphene-substrate interaction gives rise to a so-called chaotic phase.

Contents

Introduction

Graphene is a two-dimensional material composed of carbon atoms arranged in a honeycomb lattice. Its discovery in 2004 has triggered scientific interest for two main reasons. Firstly, its electronic properties are those of a semi-metallic electron gas with a tunable electron density, thus giving rise to features as unique as the anomalous Quantum Hall effect. Additionally, due to a simple but particular band structure, electrons in graphene are analogous to massless relativistic particles.

Secondly, graphene is the first experimentally observed truly two-dimensional material. Changing the dimensionality of a system has critical consequences on its properties. Graphene is then the first experimental testbed of the possible changes due to two-dimensionality. For example, it was known long before the first studies on graphene that in two dimensions, systems with finite-range interactions do not break any continuous symmetry. This is especially true for translational invariance, which means that the long-range order that exists in three-dimensional crystals is impossible in graphene. Instead, it is predicted to display quasi-long-range order.

This two-fold gallery of uncommon traits motivates the present thesis. Indeed, even if graphene intrinsically hosts such peculiar properties, they are inevitably altered by its environment. At the very minimum, graphene has to lie partially on a substrate. Depending on how intimate the graphene-substrate contact is, the electronic behaviour may change critically. Besides, when supported by a crystal, conformation of graphene to the long-range order of the substrate is also expectable. Then, to what extent the properties of graphene are modified by the interaction with a crystalline substrate? In this thesis, this question will be answered in the case of the (0001) surface of rhenium.

The apparent simplicity of the electronic band structure of graphene is rich in unusual properties. The concepts of pseudo-spin and chirality derive from it, and give a far-reaching understanding of the behaviour electrons in graphene. In the first chapter, they will be introduced, and a specific attention will be given to the analogy made between graphene and quantum relativity. But are these notions and analogy suitable to understand the impact of a substrate on graphene? It will be shown that by relying on them, effects due to the interaction with its environment can be understood based on relatively crude models.

Growing graphene on various crystalline substrates has brought considerable insight on the structure of supported graphene. In particular, graphene is known to be rigid, so when supported, it tends to maintain its structure rather than adopt that of the substrate. Supported graphene then leads to the superposition of two unmatched lattices that gives rise to a moiré superlattice. Do the models introduced in the first chapter help to understand the electronic properties of graphene moiré superlattices? This question will be addressed in the light of current literature. It will actually appear that many electronic features relate to structural aspects. This connection brings naturally to the other question of the second chapter: what are the structural phases of supported graphene? With this focus, supported graphene can be understood as either commensurate or incommensurate, or equivalently as displaying long-range or quasi-long-range order. These notions and their implications will be explained to anticipate experimental results. In particular, topological defects will be introduced as a possible signature of commensurate phases.

An introduction to the experimental and numerical tools used here will be given in the third chapter. It will explain the basic concepts of scanning tunneling microscopy (STM), of reflection high energy electron diffraction (RHEED), and of the two numerical methods employed.

Two experimental works will then be presented. The first one is a STM study of moiré superlattices observed in different supported graphene systems. For each, can graphene be assumed to be commensurate as it is usually done? The consequences of this assumption will be tested in the fourth chapter. To that end, an original analysis of STM images based on commensurability will be presented. When used on graphene on Re(0001) (and on other metals as well, like Ir(111)), it will show graphene is subjected to a non-trivial strain distribution. Besides, the very large number of similar commensurate structures accessible to graphene moiré superlattices will put into question the usual commensurability hypothesis.

The second study will go further, and interpret the STM results as the signature neither of a commensurate, nor of an incommensurate phase, but of a chaotic one. From what does this chaotic state originate? An answer will be given to this final question in the fifth chapter. A discussion will indeed be provided on why the commensurate and incommensurate phases fail to account for experimental data. The reason for such a failure will be detailed in an exhaustive study of graphene growth on Re(0001).

CHAPTER 1

Electronic properties of graphene

Since its first experimental identification in its pristine form in 2004 [152], graphene has focused scientific and public attention both as a new kind of material with various potential applications [46], and as a candidate system to explore exotic electronic phases [151]. In this Chapter, this second aspect will be presented for both pristine and supported graphene. In particular, the influence of a substrate on the electronic properties of graphene will be considered following two elementary models.

1.1 Dirac-Weyl excitations in pristine graphene

Graphene has raised theoretical interest long before its experimental identification [210], and its electrons have been predicted to mimic massless relativistic particles [180], so they would be called Dirac-Weyl excitations in a particle physics context.

In this section, the crystal structure and electronic bands of graphene are going to be introduced, in order to clarify this link to particle physics. This will require to remind elementary concepts of relativistic quantum mechanics, which find a condensed matter equivalent in graphene. The experimental signatures and theoretical limitations of this analogy will also be briefly discussed.

1.1.1 Crystallographic structure of graphene

Graphene is a two-dimensional crystal made of carbon atoms arranged in a honeycomb lattice. As such, it has a triangular Bravais lattice with two atoms per unit cell, labelled A and B on Fig. 1.1a. Every A atom has three B atoms as first neighbours and vice versa, so graphene has a bipartite lattice. As a convention, an A atom is placed on the origin, and the unit vectors $(\mathbf{a_1}, \mathbf{a_2})$ express according to the basis vectors as:

$$\mathbf{a_1} = \frac{a_{gr}}{2}\mathbf{e_x} - \frac{a_{gr}\sqrt{3}}{2}\mathbf{e_y} \text{ and } \mathbf{a_2} = \frac{a_{gr}}{2}\mathbf{e_x} + \frac{a_{gr}\sqrt{3}}{2}\mathbf{e_y} \tag{1.1}$$

with $a_{gr} = 2.46$ Å the graphene unit distance, related to the interatomic distance $a = 1.42$ Å through $a_{gr} = a\sqrt{3}$. This situation can also be considered as two identical triangular lattices A and B with one atom per unit cell, shifted with respect to each other, called the A and B sub-lattices of graphene. Owing to its three-fold symmetry, there are three possible vectors to express the shift between the two sub-lattices:

$$\mathbf{d_1} = \frac{a_{gr}}{2}\mathbf{e_x} + \frac{a_{gr}\sqrt{3}}{6}\mathbf{e_y} \text{ , } \mathbf{d_2} = -\frac{a_{gr}}{2}\mathbf{e_x} + \frac{a_{gr}\sqrt{3}}{6}\mathbf{e_y} \text{ and } \mathbf{d_3} = -\frac{a_{gr}\sqrt{3}}{3}\mathbf{e_y} \tag{1.2}$$

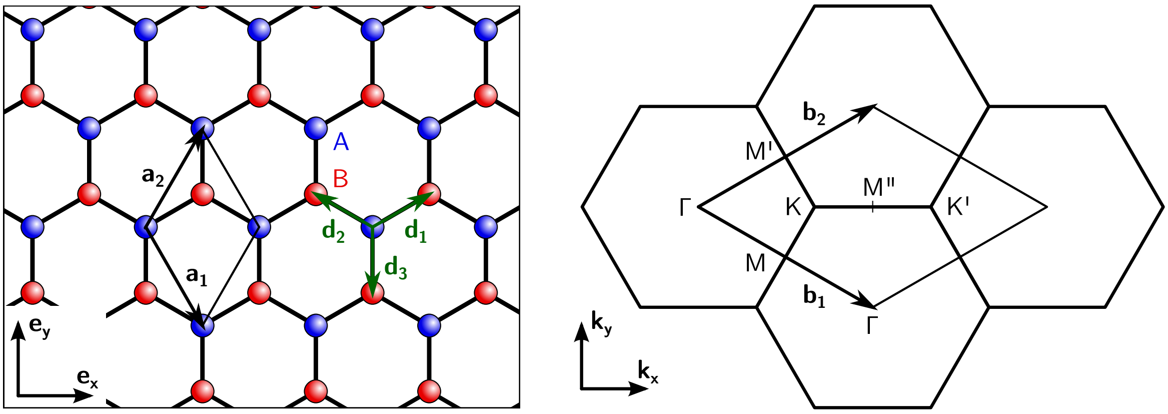

Figure 1.1: **Graphene's direct and reciprocal lattices. Left**: the honeycomb lattice of graphene has a periodicity of unit cell $(\mathbf{a_1}, \mathbf{a_2})$, which contains two atoms labelled A and B. A and B atoms are coloured respectively in red and blue, making the decomposition of the honeycomb lattice into two triangular sub-lattices visible. **Right**: the periodicity of the reciprocal lattice of graphene is given by $(\mathbf{b_1}, \mathbf{b_2})$, which defines a hexagonal first Brillouin zone with two inequivalent corners K and K'.

The reciprocal lattice of graphene can be expressed with its unit vectors $(\mathbf{b_1}, \mathbf{b_2})$ using $\mathbf{a_i} \cdot \mathbf{b_j} = 2\pi\delta_{ij}$ (δ_{ij} is the Kronecker delta), which gives:

$$\mathbf{b_1} = \frac{2\pi}{a_{gr}}\mathbf{k_x} - \frac{2\pi\sqrt{3}}{3a_{gr}}\mathbf{k_y} \text{ and } \mathbf{b_2} = \frac{2\pi}{a_{gr}}\mathbf{k_x} + \frac{2\pi\sqrt{3}}{3a_{gr}}\mathbf{k_y} \tag{1.3}$$

This definition gives rise to a hexagonal first Brillouin zone, comprising a few high symmetry points: Γ, M, K, M', K' and M'' as represented on Fig. 1.1b. Among them, the two corners K and K' play a critical role in the electronic properties of graphene.

1.1.2 Band structure of graphene

As a two-dimensional crystal, the electronic properties of graphene can be properly described using electronic bands $E(\mathbf{k})$ defined over the periodic two-dimensional reciprocal space represented on Fig. 1.1b. Their dispersion was first calculated in 1947 by Philip R. Wallace [210], using a tight-binding model to determine the band structure of graphite. More recent and exhaustive studies have been published since then [6, 22, 59, 171], and have served as an inspiration for the following. The tight-binding model provides a simple and yet rich picture of graphene's band structure. Before employing it, this model is going to be briefly presented, and its validity discussed.

The tight-binding model relies on two main hypotheses. As its name suggests, the tight-binding model is a model where the electrons are strongly bound to the individual atoms of a solid. The first hypothesis thus consists in building the electronic bands of this solid, based on the discrete levels of its constituting individual atoms. Consistently,

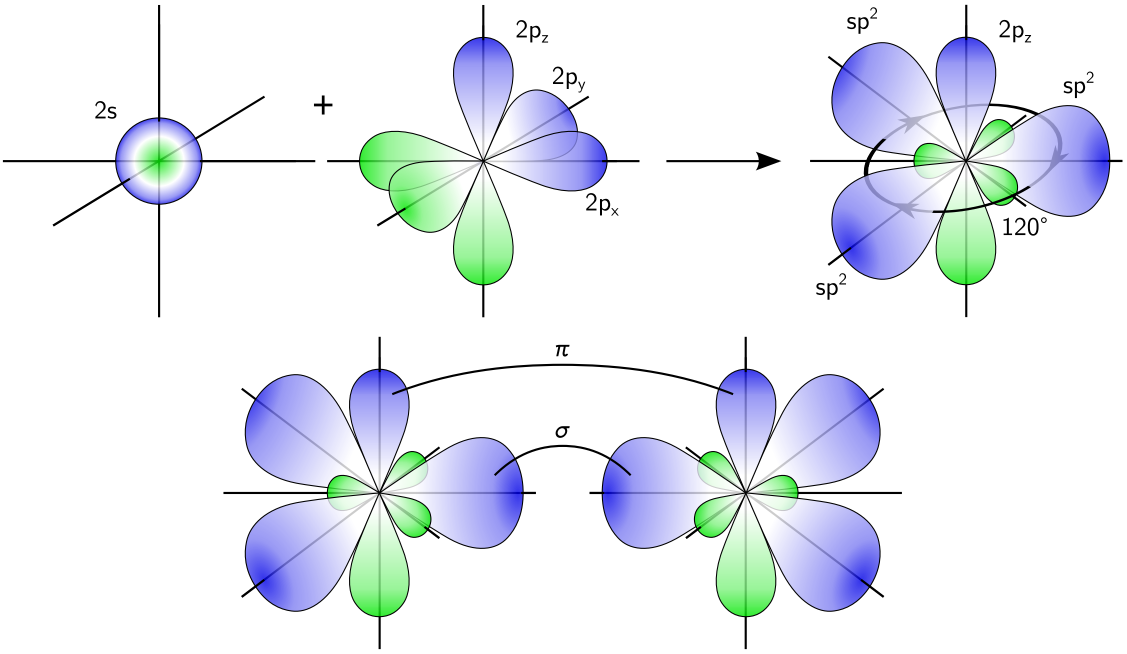

Figure 1.2: **sp^2 hybridization of carbon. Top:** to get an in-plane three-fold symmetry, the $2s$, $2p_x$ and $2p_y$ atomic orbitals recombine intro three sp^2 orbitals, while the out of plane $2p_z$ orbital remains unchanged. **Bottom:** for two adjacent carbon atoms, the large overlap of sp^2 orbitals forms σ bonds, while the smaller overlap of $2p_z$ orbitals leads to a delocalized π bond.

the associated electronic wave functions are assumed to be linear combinations of the atomic orbitals. This means electrons localized on atomic orbitals are still considered as a relevant basis for electrons in a solid. This process relies on two basic assumptions.

The first one consists in considering (usually a few) atomic levels close enough in energy to each other. The second one is to assume the corresponding atomic orbitals of two neighbouring atoms have only a small overlap. These minimal assumptions mean that each atom can host electrons in these atomic orbitals – they play a role of possible sites for the electrons.

As for the chemical bonds sustaining the crystal, they correspond to electrons that are shared by neighbouring atoms. Therefore, they are modelled by the dynamic exchange of electrons in between neighbouring sites. In other words, the electrons of the solid are delocalized over the considered orbitals of all its atoms. Nevertheless, as the overlap between neighbouring sites is small, this delocalization is weak. As a result, the second hypothesis of the tight-binding model is to authorize exchange of electrons only between neighbouring sites.

One may wonder why a model where electrons are tightly bound to atoms is relevant for graphene, where electrons are delocalized as in a two-dimensional electron gas. Indeed, the tight-binding model was originally used to calculate the electronic band dispersion associated with weakly overlapping orbitals of the core electrons in metals.

Their conduction band results on the other hand of highly hybridized orbitals. For graphene, the valence and conduction bands are going to be shown to actually arise from the out-of-plane $2p_z$ orbitals, which have a smaller overlap than the in-plane orbitals, thus making a tight-binding approach appropriate.

To use this model in the case of graphene, one has to first consider the atomic orbitals of its individual atoms, which are carbon atoms. When considered isolated, carbon has the electronic configuration $(1s)^2(2s)^2(2p)^2$. Since the $1s$ electrons are core electrons, they can be assumed to play no role in the electronic properties, contrary to the $2s$ and $2p$ valence electrons. They are about to be used to build a relevant basis of atomic orbitals for electrons in graphene.

As it has been presented in the previous section, each carbon atom of graphene is in a configuration with three-fold in-plane symmetry. Due to this local environment, the relevant atomic orbitals cannot be the usual $2s$, $2p_x$, $2p_y$ and $2p_z$, which do not satisfy this symmetry constraint: they need to undergo a sp^2 hybridization. This means that in order to account for the three-fold in-plane symmetry, the $2s$, $2p_x$ and $2p_y$ atomic orbitals linearly recombine into 3 sp^2 in-plane orbitals, while the $2p_z$ orbital remains unchanged. The electronic configuration of carbon can then be rewritten as $(1s)^2(sp^2)^3(2p_z)^1$. In the framework of the tight-binding model, this operation is a mere change of basis, but this new basis is more appropriate, as it is compatible with the symmetry of the crystallographic structure.

The honeycomb structure leads to a large overlap of the sp^2 orbitals of the neighbouring atoms, giving rise to 3 strong in-plane localized σ bonds for each carbon atom. These σ bonds are responsible for the skeleton of the honeycomb lattice. As for the remaining electron, the smaller overlap of the neighbouring $2p_z$ orbitals creates a π state delocalized over the whole lattice. This π band explains the electronic properties of graphene.

From these considerations, one then needs to take only this last electron into account in the tight-binding model. In this case, each carbon atom corresponds to one site (its $2p_z$ orbital), and it contributes for one to the total number of electrons in the crystal. As a consequence, the electronic wave function ψ will be written as a linear combination of the $2p_z$ orbitals ϕ of each carbon atom.

It is necessary to distinguish between the A and B sub-lattices, because both hold a triangular translational invariance, as seen in the previous section. This translational invariance enables to define the crystal wave vector $\mathbf{k}$ as a good quantum number, and to use the Bloch theorem for each sub-lattice:

$$\begin{aligned} \psi_{\mathbf{k}}(\mathbf{r}) &= a(\mathbf{k})\,\psi_{\mathbf{k}}^{A}(\mathbf{r}) + b(\mathbf{k})\,\psi_{\mathbf{k}}^{B}(\mathbf{r}) \\ &= \frac{1}{\sqrt{N}}\sum_{j} e^{i\mathbf{k}\cdot\mathbf{r_j}}\left(a(\mathbf{k})\,\phi(\mathbf{r}-\mathbf{r_j}) + b(\mathbf{k})\,\phi(\mathbf{r}-\mathbf{r_j}-\mathbf{d})\right) \end{aligned} \tag{1.4}$$

where $\psi_{\mathbf{k}}^{A}$ and $\psi_{\mathbf{k}}^{B}$ are Bloch waves associated to sub-lattices A and B, and $\phi(\mathbf{r}) = \langle \mathbf{r}|\phi\rangle$ is the $2p_z$ orbital in the $\mathbf{r}$ representation. The sum on j runs over the N unit cells of the honeycomb lattice. The positions of the A and B atoms are given respectively by the vectors $\mathbf{r_j}$ and $\mathbf{r_j}+\mathbf{d}$, where $\mathbf{d}$ is any of the vectors introduced in Equation (1.2). As a result, Equation (1.4) is a decomposition of the electronic wave function onto the two Bloch waves, each of them centred on the atoms of a given sub-lattice, with weights given by the complex coefficients $a(\mathbf{k})$ and $b(\mathbf{k})$.

Since this decomposition on sub-lattice Bloch waves holds the essence of both the relevant electronic properties of individual carbon atoms and the translational invariance, $\left(\psi_{\mathbf{k}}^{A}, \psi_{\mathbf{k}}^{B}\right)$ is going to be used a basis for the electronic wave function[1] as:

$$\psi_{\mathbf{k}} = \begin{pmatrix} a(\mathbf{k}) \\ b(\mathbf{k}) \end{pmatrix} \tag{1.5}$$

Nonetheless, it should be noted that it is not an orthonormal basis. Indeed, although $\psi_{\mathbf{k}}^{A*}\psi_{\mathbf{k}}^{A} = \psi_{\mathbf{k}}^{B*}\psi_{\mathbf{k}}^{B} = 1$ due to normalization, $\psi_{\mathbf{k}}^{A*}\psi_{\mathbf{k}}^{B} = S_{AB} \neq 0$. Using a wave function of this form, it is possible to calculate the band dispersion of graphene close to the Fermi level by solving the time-independent Schrödinger equation $H\psi_{\mathbf{k}} = E_{\mathbf{k}}\psi_{\mathbf{k}}$. By multiplying it by $\psi_{\mathbf{k}}^{\dagger}$, one gets $\psi_{\mathbf{k}}^{\dagger}H\psi_{\mathbf{k}} = E_{\mathbf{k}}\psi_{\mathbf{k}}^{\dagger}\psi_{\mathbf{k}}$, which can be written in a 2×2 matrix form:

$$\psi_{\mathbf{k}}^{\dagger} \begin{pmatrix} \mathcal{H}_{AA} & \mathcal{H}_{AB} \\ \mathcal{H}_{BA} & \mathcal{H}_{BB} \end{pmatrix} \psi_{\mathbf{k}} = E_{\mathbf{k}}\psi_{\mathbf{k}}^{\dagger} \begin{pmatrix} 1 & S_{AB} \\ S_{BA} & 1 \end{pmatrix} \psi_{\mathbf{k}} \tag{1.6}$$

At this point, a few assumptions can be made to simplify the problem. Since the two sub-lattices are identical, $\mathcal{H}_{AA} = \mathcal{H}_{BB}$, and this value is set to 0 as it will only result in an additional on-site energy term that shifts the bands rigidly without changing the position of the Fermi level. Moreover, since a small overlap between the adjacent $2p_z$ orbitals has been assumed, so $S_{AB} = S_{BA} \simeq 0$. Besides, one needs to determine $\mathcal{H}_{AB}$, which corresponds to the electron hopping term from one Bloch wave to the other. For simplicity, only nearest-neighbour hopping will be taken into account, so the electron can hop from A sub-lattice to B sub-lattice via either of $\mathbf{d_1}$, $\mathbf{d_2}$ or $\mathbf{d_3}$ vectors represented on Figure 1.1 (left).[2] Therefore, the tight-binding hamiltonian writes as:

$$H = -t\sum_{\langle i,j\rangle} \left|\phi_i^B\right\rangle \left\langle\phi_j^A\right| + h.c. \tag{1.7}$$

with t the hopping amplitude ($\sim$ 2.7 eV), and where the sum runs over nearest-neighbour atoms. Using Equations (1.4) and (1.7), $\mathcal{H}_{AB}$ can be calculated as:

$$\mathcal{H}_{AB} = -t\left(1 + e^{-i\mathbf{k}\cdot\mathbf{a_1}} + e^{-i\mathbf{k}\cdot\mathbf{a_2}}\right) = \underline{t}(\mathbf{k}) \text{ and } \mathcal{H}_{BA} = \underline{t}^{*}(\mathbf{k})$$

---

[1] This time in an arbitrary representation of the Hilbert space, and not necessarily the $\mathbf{r}$ representation as above.

[2] For further reading, the effects of the overlap correction $S_{AB} = S_{BA} \neq 0$ and of the next-nearest-neighbour hopping have been treated in other works [59, 171].

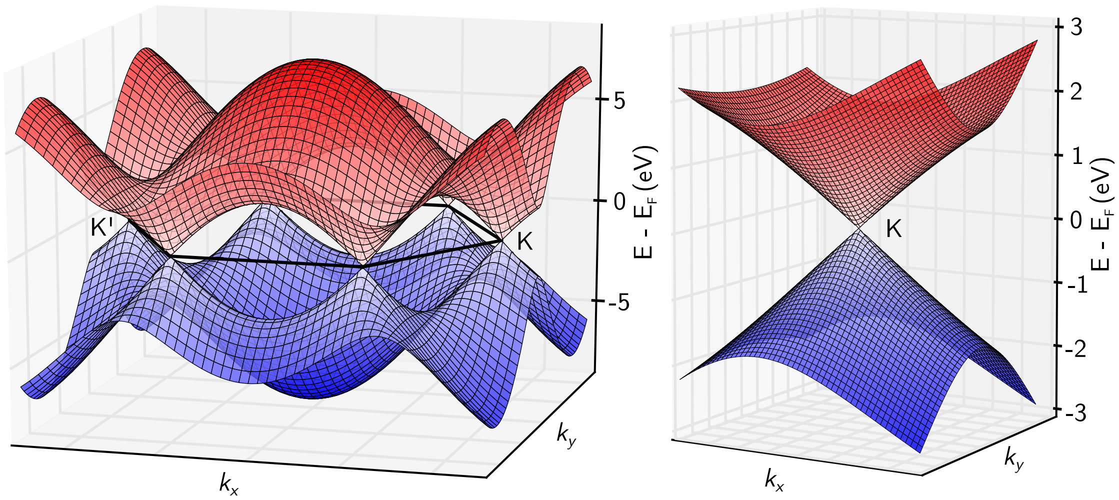

Figure 1.3: **Graphene's band structure close to Fermi energy. Left:** π (blue) and π^* (red) bands obtained with the nearest-neighbour tight-binding approach. The black hexagon indicates the first Brillouin zone. **Right:** a zoom shows the conical dispersion of the electronic bands around one of the first Brillouin zone corner.

Under these assumptions, the Schrödinger equation in the sub-lattice basis simplifies drastically, and its solutions are given by the secular determinant:

$$\det \begin{pmatrix} -E_{\mathbf{k}} & \underline{t}\left(\mathbf{k}\right) \\ \underline{t}^*\left(\mathbf{k}\right) & -E_{\mathbf{k}} \end{pmatrix} = 0 \tag{1.8}$$

which yields:

$$E_{\mathbf{k}} = \pm t \sqrt{3 + 2\cos\left(a_{gr}k_x\right) + 4\cos\left(\frac{a_{gr}k_x}{2}\right)\cos\left(\frac{a_{gr}k_y\sqrt{3}}{2}\right)} \tag{1.9}$$

Positive (resp. negative) energy solutions correspond to electrons in the conduction band (resp. holes in the valence band), as represented on Figure 1.3a. Noticeably, at the Fermi level, only two states are available, respectively at K and K'. This vanishing density of states at the Fermi level makes graphene a semi-metal. Additionally, around these points, the valence and conduction bands have a conical shape, translating a linear dependence in k, as emphasized on Figure 1.3b. A Taylor expansion of Equation (1.9) around K and K' can be performed to express this dependence. The crystal wave vector can then be written $\mathbf{k} = \xi\mathbf{K} + \mathbf{q}$, with $\xi = \pm$ and $\mathbf{K} = \left(\frac{4\pi}{3a_{gr}}, 0\right)$, in order to get the expression:

$$E_{\mathbf{q}} = \pm\frac{a_{gr}t\sqrt{3}}{2}\left|\mathbf{q}\right| = \pm\hbar v_F\left|\mathbf{q}\right| \tag{1.10}$$

which is independent of ξ. One can then extract $v_F = \frac{a_{gr}\sqrt{3}t}{2\hbar} \sim 10^6$ m.s^{-1}. This linear dependence is at odds with the parabolic bands usually encountered in semiconductors, where an inertial effective mass m^* is defined in the form $E = E_0 + \frac{\hbar^2 \mathbf{k}^2}{2m^*}$. Using this effective mass picture, electrons in semiconductors are modelled as independent free electrons with a renormalized mass. No such effective mass can be defined in graphene, so this analogy breaks[3]. Instead, Equation (1.10) can rather be compared to the relativistic energy-momentum relation $E^2 = m^2c^4 + p^2c^2$ with rest mass $m = 0$. From this point of view, electrons in graphene resemble massless relativistic fermions with an effective light speed v_F. In particle physics, such particles are called massless Dirac fermions, and the analogy between them and electrons in graphene can be pushed further using a low-energy hamiltonian of graphene. Before presenting it, the Dirac equation in particle physics is going to be shortly reminded, so as to make the analogy clearer.

1.1.3 Massless Dirac fermions in particle physics

In 1926, Erwin Schrödinger introduced his famous equation that describes the time evolution of a quantum state. Although successful to account for the discrete energy spectrum of the electron of an hydrogen atom and its $\frac{1}{n^2}$ dependence, it did not satisfy the requirements of special relativity. Indeed, the Schrödinger equation is not a relativistic wave equation, so its solutions do not satisfy the relativistic energy-momentum relation:

$$E^2 = m^2c^4 + p^2c^2 \tag{1.11}$$

where E is the energy of a particle, m its rest mass, p its momentum, and c the celerity of light.

This motivated physicists to provide a relativistic generalization of the Schrödinger equation. One such is known as the Klein-Gordon equation, which applies to spinless bosons such as the pi-meson or the Higgs boson. Another one was formulated by Paul Dirac in 1928, and applies to spin-$\frac{1}{2}$ particles, like electrons. This so-called Dirac equation proved to have deeper consequences on the structure of matter, as it predicted the existence of antimatter.[4] The Dirac equation states in its covariant form as:

$$\left(i\hbar c\gamma^\mu \partial_\mu - mc^2\right)\psi = 0 \tag{1.12}$$

where ψ is the wave function for the electron of rest mass m, defined over a 4-dimensional spacetime with coordinates $x^\mu = (ct, \mathbf{r})$. Accordingly, ∂_μ is the 4-gradient $(\frac{\partial_t}{c}, \partial_{\mathbf{r}})$. $\hbar$ and c are respectively the reduced Planck constant and the speed of light. γ^μ is a set of 4 "well-chosen dimensionless coefficients" called Dirac matrices, which are constrained due to the relation (1.11) to the anticommutation rule $\{\gamma^\mu, \gamma^\nu\} = 2\eta^{\mu\nu}$, where $\eta^{\mu\nu}$ is the Minkowski metric tensor ($\eta^{00} = -\eta^{ii} = 1$ and $\eta^{ij} = 0$ if $i \neq j$, with $i = x, y, z$).

To solve this equation, it is then necessary to identify a set of γ^μ matrices satisfying such an algebra. It is emphasized that many possible representations can be chosen.

---

[3] Other effective masses can still be defined, like the cyclotron mass.

[4] In its standard (or Dirac) representation, the negative energy solutions of the Dirac equation for an electron correspond to the positive energy solutions of the later-discovered positron.

For ultrarelativistic particles, it is relevant to write the Dirac equation in the so-called chiral representation. This form will prove useful to compare the Dirac equation with the low energy hamiltonian of graphene later on. In this representation, the γ^μ are 4×4 matrices, which can be expressed as tensor products between Pauli matrices that will be noted σ_i and τ_i to distinguish between them. Pauli matrices were originally introduced to describe the spin of the electron as:

$$\sigma_x = \begin{pmatrix} 0 & 1 \\ 1 & 0 \end{pmatrix}, \ \sigma_y = \begin{pmatrix} 0 & -i \\ i & 0 \end{pmatrix} \text{ and } \sigma_z = \begin{pmatrix} 1 & 0 \\ 0 & -1 \end{pmatrix} \tag{1.13}$$

The γ^μ then state as:

$$\gamma^0 = \sigma_0 \tau_x = \begin{pmatrix} 0 & \sigma_0 \\ \sigma_0 & 0 \end{pmatrix} \text{ and } \gamma^i = i\sigma_i \tau_y = \begin{pmatrix} 0 & \sigma_i \\ -\sigma_i & 0 \end{pmatrix} \tag{1.14}$$

where σ_0 is the 2×2 identity matrix. In this representation, the Dirac equation (1.12) can be decomposed onto the so-called chiral (or Weyl) basis (ψ_-, ψ_+) associated to the τ_i matrices. This notation refers to the chirality (or "handedness") of the electron, which is either "left-handed" $(-)$ or "right-handed" $(+)$. This notion is going to get clearer in the coming lines. The decomposition leads to the following system:

$$\begin{cases} (i\hbar\ \sigma_0 \partial_t + i\hbar c\ \boldsymbol{\sigma} \cdot \partial_{\mathbf{r}})\, \psi_+ = mc^2\ \sigma_0\ \psi_- \\ (i\hbar\ \sigma_0 \partial_t - i\hbar c\ \boldsymbol{\sigma} \cdot \partial_{\mathbf{r}})\, \psi_- = mc^2\ \sigma_0\ \psi_+ \end{cases} \tag{1.15}$$

In this form, the mass term clearly appears as a coupling factor between the two-component chiral (or Weyl) spinors ψ_- and ψ_+ of the basis. For massless particles ($m = 0$), the two equations decouple, so the electronic wave function ψ can be decomposed into two independent chiral components ψ_- and ψ_+, whose chiralities are respectively $\lambda = -$ and $\lambda = +$.[5] These chiral components are described by the Weyl equation, which expresses as:

$$(\sigma_0 \partial_t + \lambda\ c\ \boldsymbol{\sigma} \cdot \partial_{\mathbf{r}})\, \psi_\lambda = 0 \tag{1.16}$$

It can be solved directly, and its solution takes the form of a plane wave $\psi = \chi\ e^{\frac{i}{\hbar}(\mathbf{p}\cdot\mathbf{r} - Et)}$, where χ is 2-component Weyl spinor. From Equation (1.11), massless particles have $E = pc$, so injecting the plane wave solution in Equation (1.16) leads to:

$$\frac{\boldsymbol{\sigma} \cdot \mathbf{p}}{p} \psi_\lambda = \lambda \psi_\lambda \tag{1.17}$$

---

[5] To this extent, the chiral representation actually proves relevant when defining the chirality operator $\gamma^5 = i\gamma^0\gamma^1\gamma^2\gamma^3$ which is then block-diagonal $\gamma^5 = -\sigma_0\tau_z = \left(\begin{smallmatrix} -\sigma_0 & 0 \\ 0 & \sigma_0 \end{smallmatrix}\right)$. In other words, this representation defines naturally the chiral basis (ψ_-, ψ_+), with ψ_- and ψ_+ eigenvectors of γ^5 with eigenvalues $\lambda = -$ and $\lambda = +$. The residual mass term in (1.15) then translates the fact that γ^5 does not commute with the Dirac hamiltonian, and therefore is not a symmetry unless the particle is massless.

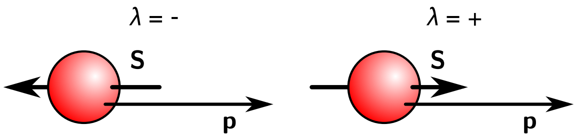

Figure 1.4: **Chirality for massless Dirac fermions.** The chirality of massless Dirac fermions coincide with their helicity. A left-handed ($\lambda = -$) particle has its spin $\mathbf{S}$ anti-aligned with its momentum $\mathbf{p}$ (left), while a right-handed ($\lambda = +$) particle has its spin $\mathbf{S}$ aligned with its momentum $\mathbf{p}$ (right).

which means the right-handed and left-handed states are eigenfunctions of the $\frac{\boldsymbol{\sigma}\cdot\mathbf{p}}{p}$ operator with opposite eigenvalues. This operator is the helicity operator, and its eigenvalues indicate whether the particle's spin $\mathbf{S}$ is aligned ($\lambda = +$) or anti-aligned ($\lambda = -$) with its momentum $\mathbf{p}$. This situation is schematically represented on Figure 1.4.

This last equation calls for two comments. First, the $\boldsymbol{\sigma}$ operator introduced in equation (1.14) only aimed at providing a suitable algebraic structure to the γ^μ matrices. In the chiral representation of a spin-$\frac{1}{2}$ massless fermion, it comes to coincide with its spin operator.

Secondly, in the case of spin-$\frac{1}{2}$ massless fermions, there is also a coincidence of chirality and helicity, which provides a convenient picture of spin-momentum alignment or anti-alignment for $+$ or $-$ chiralities. This picture will prove useful in the next part, when it comes to the low energy hamiltonian of graphene.

In summary, the Dirac equation provides a quantum mechanical framework for relativistic particles. In its chiral representation for massless spin-$\frac{1}{2}$ fermions, Pauli matrices σ_i and τ_i – originally used to account for algebraic reasons – correspond to the spin and chirality degrees of freedom. Furthermore, due to their zero mass, this kind of particle decomposes into two independent Weyl particles with opposite chiralities. In that sense, a massless Dirac fermion is the direct sum of two Weyl fermions.

Although this seems rather unconnected to the condensed matter context of graphene physics, it appears that from the electronic bands of graphene and its bi-partite lattice emerge similar properties.

1.1.4 Low-energy effective hamiltonian of graphene

Equation (1.10) shows a linear dispersion relation for electrons in graphene, which is reminiscent of the relativistic energy-momentum relation of massless fermions $E = pc$. As this relation emerges naturally from the Dirac equation, one can seek Dirac fermion properties in graphene electrons by linearising their hamiltonian at the Fermi level. First, the nearest-neighbour hamiltonian of Equation (1.7) can be simply rewritten in a

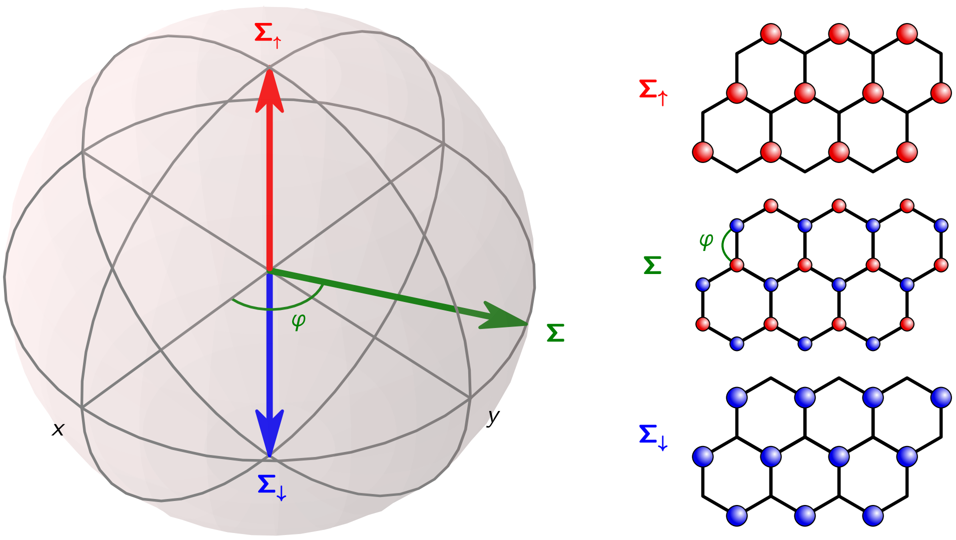

Figure 1.5: **Pseudo-spin of electrons in graphene. Left:** the pseudo-spin of graphene electrons is represented as a vector $\mathbf{\Sigma}$ on the Bloch sphere, in analogy with the usual $\frac{1}{2}$ spin of electrons. **Right:** wave functions corresponding to typical pseudo-spin directions are represented on top of the honeycomb lattice of graphene: $\mathbf{\Sigma}_\uparrow$ (resp. $\mathbf{\Sigma}_\downarrow$) for electrons delocalized only on the A (resp. B) sub-lattice, and an in-plane $\mathbf{\Sigma}$ for electrons with equal weights on both sub-lattices.

second quantization formalism as:

$$H = t \sum_{\langle i,j \rangle} c_B^\dagger \left(\mathbf{r_i} + \mathbf{d}\right) c_A \left(\mathbf{r_j}\right) + c_A^\dagger \left(\mathbf{r_j}\right) c_B \left(\mathbf{r_i} + \mathbf{d}\right) \tag{1.18}$$

with $c_n \left(\mathbf{r_i} + \mathbf{d_n}\right)$ (resp. $c_n^\dagger \left(\mathbf{r_i} + \mathbf{d_n}\right)$) annihilation (resp. creation) operator for an electron on the i^{th} site of the n sub-lattice ($\mathbf{d_A} = 0$ and $\mathbf{d_n} = \mathbf{d}$). Using Bloch electrons as in Equation (1.4) is equivalent to performing a Fourier transform[6], and leads to:

$$H = \sum_{\mathbf{k} \in BZ} \begin{pmatrix} c_A^\dagger (\mathbf{k}) \, c_B^\dagger (\mathbf{k}) \end{pmatrix} \begin{pmatrix} 0 & \underline{t} (\mathbf{k}) \\ \underline{t}^* (\mathbf{k}) & 0 \end{pmatrix} \begin{pmatrix} c_A (\mathbf{k}) \\ c_B (\mathbf{k}) \end{pmatrix} \tag{1.19}$$

where $c_n (\mathbf{k})$ (resp. $c_n^\dagger (\mathbf{k})$) stands for the annihilation (resp. creation) operator for a Bloch electron associated with the n sub-lattice ($n = A, B$). For each $\mathbf{k}$, one can use the hamiltonian density:

$$\mathcal{H}_\mathbf{k} = \begin{pmatrix} c_A^\dagger (\mathbf{k}) \, c_B^\dagger (\mathbf{k}) \end{pmatrix} \begin{pmatrix} 0 & \underline{t} (\mathbf{k}) \\ \underline{t}^* (\mathbf{k}) & 0 \end{pmatrix} \begin{pmatrix} c_A (\mathbf{k}) \\ c_B (\mathbf{k}) \end{pmatrix} \tag{1.20}$$

---

[6] It is performed as: $c_n (\mathbf{k}) = \frac{1}{\sqrt{N}} \sum_j e^{i\mathbf{k}\cdot\mathbf{r_j}} c \left(\mathbf{r_j} + \mathbf{d_n}\right)$, $n = A, B$, with N the total number of sites in the lattice, and $c \left(\mathbf{r_j} + \mathbf{d_n}\right)$ annihilation operator for an electron on the j^{th} site of the n sub-lattice.

Secondly, similarly to what has been done for Equation (1.10), this hamiltonian can be linearised around the K and K' points. Rewriting the crystal wave vector as $\mathbf{k} = \xi\mathbf{K} + \mathbf{q}$, with $\xi = \pm$, one gets the expression:

$$\mathcal{H}_{\mathbf{q}} = \hbar v_F \left(c^{\dagger}_{A,\xi\mathbf{K}}\left(\mathbf{q}\right) c^{\dagger}_{B,\xi\mathbf{K}}\left(\mathbf{q}\right) \right) \underbrace{\begin{pmatrix} 0 & \xi q_x - i q_y \\ \xi q_x + i q_y & 0 \end{pmatrix}}_{= \xi q_x \sigma_x + q_y \sigma_y} \begin{pmatrix} c_{A,\xi\mathbf{K}}\left(\mathbf{q}\right) \\ c_{B,\xi\mathbf{K}}\left(\mathbf{q}\right) \end{pmatrix} \tag{1.21}$$

where Pauli matrices σ_i are here again conveniently introduced. In this case, they refer to the decomposition of the wave function on the two Bloch waves associated to the A and B sub-lattices, and not to the spin degree of freedom of the electron.[7] As such, they represent a sub-lattice isospin, but in an analogy to the Dirac equation, this isospin is also called the pseudo-spin of electrons in graphene. Based on this analogy, the pseudo-spin vector $\boldsymbol{\sigma} = (\sigma_x, \sigma_y, \sigma_z)$ is defined. In the same way the electronic spin is represented by a vector on the Bloch sphere, the electronic pseudo-spin in graphene can be represented by a vector, whose direction depends on the relative weights and phases of the A and B components of the wave function. For clarity, this vector will be noted $\mathbf{\Sigma}$ to distinguish it from the Pauli vector operator $\boldsymbol{\sigma}$. The pseudo-spin up $\mathbf{\Sigma}_{\uparrow} = \left(\begin{smallmatrix}1\\0\end{smallmatrix}\right)$ and pseudo-spin down $\mathbf{\Sigma}_{\downarrow} = \left(\begin{smallmatrix}0\\1\end{smallmatrix}\right)$ states then correspond to electronic states delocalized exclusively either on sub-lattice A or on sub-lattice B. In Equation (1.21), there are only σ_x and σ_y terms, so the z component of $\mathbf{\Sigma}$ has to be zero, which means the pseudo-spin of electrons in pristine graphene lies in the plane, with its direction given by an azimuth angle $\varphi_{\mathbf{q}}$. In other words, the wave function of these electrons has equal weights on both sub-lattices, although these two components have a phase difference $\varphi_{\mathbf{q}}$. This is pictured on Figure 1.5.

To determine the physical meaning of this phase, one can first see in the hamiltonian form in Equation (1.21) that there is a coupling between the quasi-momentum $\mathbf{q}$ and the pseudo-spin, given by $\xi\sigma_x q_x + \sigma_y q_y$. This is close to the helicity operator $\frac{\boldsymbol{\sigma}\cdot\mathbf{p}}{p}$ introduced in the case of massless Dirac fermions in Equation (1.17), but slightly different. The first difference is the absence of a z term, which limits the analogy to two dimensions. Secondly, the additional ξ factor makes the coupling between $\boldsymbol{\sigma}$ and $\mathbf{q}$ valley-dependent. Indeed, the isospin ξ has been introduced as $\mathbf{k} = \xi\mathbf{K} + \mathbf{q}$, and should not be mistaken with the pseudo-spin. ξ is the valley isospin: it equals $+$ for the K valley, and $-$ for the K' valley of graphene.[8] The role it plays in Equation (1.21) reminds that of chirality λ in the Dirac-Weyl equation (1.16), but one should not be confused, as it acts only on the q_x, and not on the q_y components.

In order to apprehend the notion of chirality in graphene, one can use the bi-spinor

---

[7] Still, electrons in graphene carry a $\frac{1}{2}$ spin, for which a spin vector $\mathbf{s} = (s_x, s_y, s_z)$ can be defined. Yet, due to the weak intrinsic spin-orbit coupling in graphene, in the absence of a magnetic field, the electronic bands of graphene are spin-degenerate.

[8] The pseudo-spin $\boldsymbol{\sigma}$ is a sub-lattice isospin, whereas ξ is the valley isospin. This means $\boldsymbol{\sigma}$ acts on the A-B sub-lattices, while ξ acts on the K-K' valleys. These are independent degrees of freedom, and there is no one-to-one correspondence between the two.

representation $c^\dagger_\alpha(\mathbf{q}) = \left(c^\dagger_{A,+\mathbf{K}}(\mathbf{q})\, c^\dagger_{B,+\mathbf{K}}(\mathbf{q})\, c^\dagger_{B,-\mathbf{K}}(\mathbf{q})\, c^\dagger_{A,-\mathbf{K}}(\mathbf{q})\right)$ and rewrite the above hamiltonian density as:

$$\mathcal{H}_\mathbf{q} = \hbar v_F \sum_{\alpha,\beta=1}^{4} c^\dagger_\alpha(\mathbf{q}) \underbrace{\left[(q_x\sigma_x + q_y\sigma_y)\,\tau_z\right]_{\alpha,\beta}}_{=\left[(\boldsymbol{\sigma}\cdot\mathbf{q})\,\tau_z\right]_{\alpha,\beta}} c_\beta(\mathbf{q}) \tag{1.22}$$

which has a form similar to the Dirac-Weyl equation for massless particles (1.16) where the 4×4 matrix is here again decomposed into Pauli matrices tensor products. In the Dirac-Weyl equation, $\boldsymbol{\sigma}$ refers to the Pauli vector for spin-$\frac{1}{2}$ fermions, and $\boldsymbol{\tau}$ corresponds to the Pauli vector for their chirality degree of freedom, with eigenvalues $\lambda = \pm$. For electrons in graphene, $\boldsymbol{\sigma}$ is the Pauli vector for pseudo-spin, related to the decomposition of the wave function on A and B sub-lattices. As for $\boldsymbol{\tau}$, it appears in Equation (1.22) as an effective Pauli vector for chirality, due to the specific choice of representation given by $c_\alpha(\mathbf{q})$.

This choice is based on both pseudo-spin and valley isospin, and decomposes electronic wave functions as $((A,+\mathbf{K}),(B,+\mathbf{K}),(B,-\mathbf{K}),(A,-\mathbf{K}))$. Two things can be noticed in this decomposition. First, the two valleys K and K' are treated separately, so Equation (1.22) is equivalent to Equation (1.21) used for both valleys. Secondly, the decomposition on the A and B sub-lattices is inverted depending on the valley, so the K' valley is the same as its K counterpart, with A and B sub-lattices swapped. This inversion is indeed necessary to introduce the τ_z matrix and perform an analogy with chirality in particle physics. In particle physics, chirality λ has indeed been shown to be equivalent to helicity, that is to say to the projection of the particle's spin $\boldsymbol{\sigma}$ onto its momentum $\mathbf{p}$, as detailed in Equation (1.17). Similarly, for graphene, chirality λ corresponds to the projection of the electron's pseudo-spin $\boldsymbol{\Sigma}$ onto its quasi-momentum $\hbar\mathbf{q}$. In other words, the wave function of a right-handed (resp. left-handed) electron is an eigenfunction of $\boldsymbol{\sigma}\cdot\mathbf{q}$ with $\lambda = +$ (resp. $\lambda = -$). As a consequence, if one considers an excitation in the conduction band ($E_\mathbf{q} = +\hbar v_F\,|\mathbf{q}|$), the effective Dirac-Weyl hamiltonian (1.22) imposes it is right-handed around the K point ($\xi = +$), and left-handed around the K' point ($\xi = -$). For the same reasons, hole excitations in the valence band ($E_\mathbf{q} = -\hbar v_F\,|\mathbf{q}|$) are right-handed around the K' point ($\xi = -$), and left-handed around the K point ($\xi = +$). This means that the two valleys are decoupled, with corresponding degenerate wave functions written as:

$$\psi_K(\mathbf{q}) = \begin{pmatrix} 1 \\ \pm e^{-i\varphi_\mathbf{q}} \\ 0 \\ 0 \end{pmatrix} \frac{e^{i\mathbf{q}\cdot\mathbf{r}}}{\sqrt{2}} \text{ and } \psi_{K'}(\mathbf{q}) = \begin{pmatrix} 0 \\ 0 \\ \mp e^{i\varphi_\mathbf{q}} \\ 1 \end{pmatrix} \frac{e^{i\mathbf{q}\cdot\mathbf{r}}}{\sqrt{2}} \tag{1.23}$$

with $\varphi_\mathbf{q} = \arctan\left(\frac{q_y}{q_x}\right)$ the angle between $\mathbf{q}$ and $\mathbf{k_x}$. This expression then links literally the phase difference between the A and B components, *i.e.* the pseudo-spin, to the orientation of the wave vector $\mathbf{q}$. The additional ± indicates whether the wave function corresponds to an electron or a hole state. Consistently, the π shift it creates reverses the direction of the pseudo-spin.

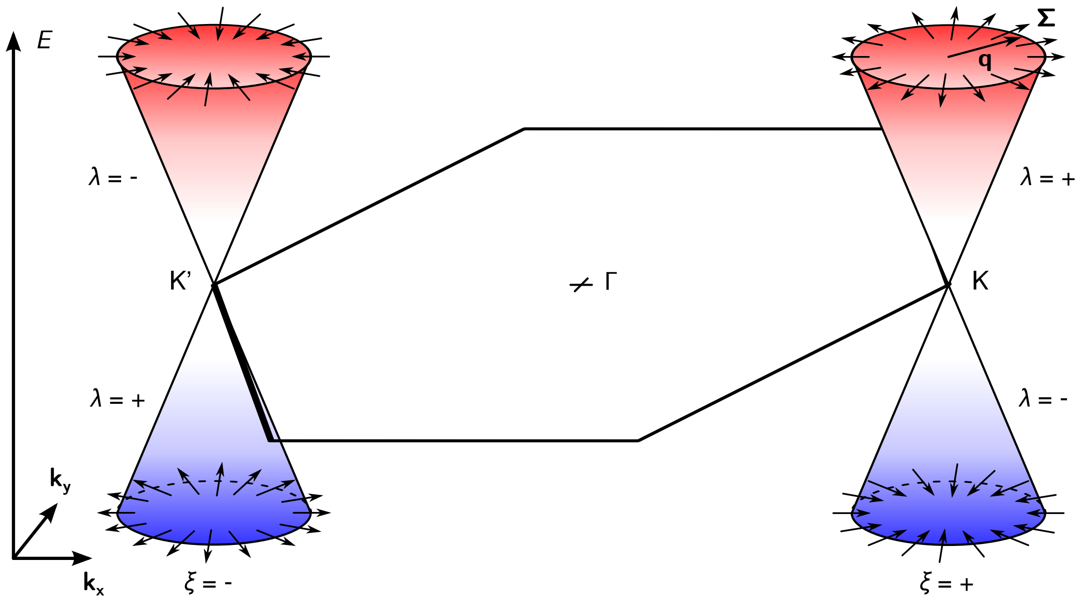

Figure 1.6: **Chirality of electrons in graphene.** Linearised π (blue) and π^* (red) bands have a conical shape and are centred at the K and K' points of the first Brillouin zone (black hexagon). On both bands, the pseudo-spin $\mathbf{\Sigma}$ is represented, and its alignment (resp. anti-alignment) with the wave vector $\mathbf{q}$ indicates the chirality $\lambda = +$ (resp. $\lambda = -$).

A straightforward picture for the chirality of Dirac electrons in graphene can be built, using the representation of pseudo-spin $\mathbf{\Sigma}$ introduced on Figure 1.5 and the spin-momentum alignment picture of massless Dirac fermions presented on Figure 1.4. In this picture, right-handed chirality $\lambda = +$ corresponds to a pseudo-spin $\mathbf{\Sigma}$ aligned with the wave vector $\mathbf{q}$, and left-handed chirality $\lambda = -$ corresponds to $\mathbf{\Sigma}$ anti-aligned with $\mathbf{q}$. When considering an entire band taken around either K or K' point, all the pseudo-spins point either outwards ($\lambda = +$) or inwards ($\lambda = -$). This picture is sketched on Figure 1.6.

When considering this global picture, it appears that the emergence of chirality in graphene is equivalent to locking the electron's wave vector $\mathbf{q}$ to its pseudo-spin $\mathbf{\Sigma}$ over a whole band. Consequently, in the absence of pseudo-spin flip events and considering no intervalley scattering, an electron of wave vector $\mathbf{q}$ cannot be backscattered to an electronic state of wave vector $-\mathbf{q}$, as this breaks chirality conservation. This phenomenon – known as chiral tunneling – has been predicted in 2006 [91] and experimentally observed in 2009 [224], and is a hallmark of chiral properties of electrons in graphene. This is analogous to the absence of backscattering in the surface state of a topological insulator. Indeed, in this class of systems, due to strong spin-orbit coupling, the electron's wave vector is locked to its spin. Therefore, as long as time-reversal symmetry is preserved, backscattering is forbidden. This requires the absence of magnetic field, and of spin-flip scatterers like magnetic impurities. In both cases, a symmetry prevents backscattering, and is therefore responsible for an improved electronic mobility. Yet, this mechanism is far less efficient in graphene, as many perturbations and defects can break chirality conservation.[9]

Although the analogy between electrons in graphene and Dirac physics provides a good picture for graphene's exotic electronic properties, it is important to keep two limitations in mind. To start with, despite the fact the Dirac equation is used for ultrarelativistic particles, electrons in graphene are not relativistic. Indeed, due to their high speed, ultrarelativistic particles induce time-retardation delays in the interactions, as formally established in the Liénard-Wiechert potentials. In graphene however, the speed of electrons is given by the Fermi velocity $v_F \sim 10^6$ m.s$^{-1} \ll c$, so the interactions can be considered instantaneous. Moreover, due to its light atoms, intrinsic spin-orbit coupling in graphene is very weak, so this relativistic effect has essentially no impact on the electrons. In short, electrons in graphene are effectively described by a Dirac-Weyl equation, but one should not forget this comes from a linearised Schrödinger equation, and that all relativistic effects are negligible.

Secondly, in Dirac-Weyl equation, both spin and chirality are intrinsic properties that arise from fundamental symmetries, and they are defined over the whole Minkowski spacetime. In graphene however, pseudo-spin and chirality exist locally in k-space, assuming low energy excitations around K and K' points. Additionally, they are defined provided that A and B sub-lattices are well-defined. Most structural defects in the honeycomb lattice of graphene locally mix the two sub-lattices, so pseudo-spin is then ill-defined. Besides, chirality is a relevant tool only if K and K' valleys are treated separately. In other words, all chiral properties of electrons in graphene last as long as intervalley scattering is weak compared to intravalley scattering. For these reasons, observing massless Dirac fermions requires graphene samples with high crystalline quality.

1.2 Graphene-based massive Dirac fermions

So far, graphene has been considered as pristine, so its intrinsic electronic properties have been detailed. Nevertheless, in most experimental works, it relies on a support, which alters these properties. In the coming section, two effects a substrate can have on graphene's electronic properties are going to be considered separately. First, the different sites the surface of a substrate offers usually lift the A and B sub-lattices equivalence, leading to a so-called Semenoff insulator. Secondly, when interacting with a surface or with atomic adsorbates, graphene can have its chemical bonds distorted periodically, as it undergoes a Kekulé distortion.

---

[9] On the contrary, local defects which do not break time-reversal symmetry do not affect the surface states of topological insulators.

1.2.1 Semenoff insulator

In the model for pristine graphene, both A and B sub-lattices have been assumed identical, which enabled to consider the on-site energies of an electron on each sub-lattice $\mathcal{H}_{AA}$ and $\mathcal{H}_{BB}$ equal, and they have been set to 0. In a more general approach, one can consider these two energies – hereafter called ϵ_A and ϵ_B – are different. This is true if the carbon atoms of each sub-lattice of graphene are surrounded by different local environment, as for graphene supported on Ni(111). Another example is given by hexagonal boron nitride (h-BN), which has the same crystallographic structure as graphene, but with B as A atoms, and N as B atoms. In such a situation, electrons have a tendency to localize rather on one sub-lattice than the other. This translates in an additional hamiltonian term to Equation (1.18):

$$H_S = \sum_i \epsilon_A c_A^\dagger\left(\mathbf{r_i}\right) c_A\left(\mathbf{r_i}\right) + \epsilon_B c_B^\dagger\left(\mathbf{r_i}+\mathbf{d}\right) c_B\left(\mathbf{r_i}+\mathbf{d}\right) \tag{1.24}$$

Since there is a staggered on-site potential on this graphene, only the difference between these two energies has an influence on the band structure. Introducing $\mu = \frac{\epsilon_A - \epsilon_B}{2}$ as a chemical potential difference, this can be rewritten as an additional hamiltonian density term. Equation (1.20) then becomes:

$$\mathcal{H}_\mathbf{k} = \left(c_A^\dagger\left(\mathbf{k}\right) c_B^\dagger\left(\mathbf{k}\right)\right) \begin{pmatrix} \mu & \underline{t}\left(\mathbf{k}\right) \\ \underline{t}^*\left(\mathbf{k}\right) & -\mu \end{pmatrix} \begin{pmatrix} c_A\left(\mathbf{k}\right) \\ c_B\left(\mathbf{k}\right) \end{pmatrix} \tag{1.25}$$

From this, one can extract the energy dispersion of electrons, which can be linearised as:

$$E_\mathbf{q} = \pm\sqrt{\hbar^2 v_F^2 \mathbf{q}^2 + \mu^2} = \pm\sqrt{\left(\hbar q\right)^2 v_F^2 + m_S^2 v_F^4} \tag{1.26}$$

Compared to the linearised dispersion of semi-metallic graphene (1.10), it is clear a gap μ has opened at the K and K' points of the band structure, so this system is an insulator. Such a staggered on-site potential on A and B atoms of graphene was first theoretically investigated in 1984 by Gordon Semenoff [180]. For this reason, this system is sometimes referred to as the Semenoff insulator, and $m_S = \frac{\mu}{v_F^2}$ is introduced as the Semenoff mass, in an analogy to the rest mass in the relativistic energy-momentum relation (1.11). However, this mass is slightly different from that of massive Dirac fermions as seen in Equation (1.15). Indeed, when using the bi-spinor representation introduced earlier, the hamiltonian density becomes:

$$\mathcal{H}_\mathbf{q} = \hbar v_F \sum_{\alpha,\beta=1}^{4} c_\alpha^\dagger\left(\mathbf{q}\right) \left[\left(q_x\sigma_x + q_y\sigma_y + \frac{v_F}{\hbar} m_S \sigma_z\right)\tau_z\right]_{\alpha,\beta} c_\beta\left(\mathbf{q}\right) \tag{1.27}$$

so the Semenoff mass term has a $\sigma_z\tau_z$ form, whereas the rest mass term of a Dirac particle in the chiral representation states as $\sigma_0\tau_x$. In both cases, the Pauli matrices commutation rules show these terms do not commute with the hamiltonian, but not the same Pauli matrices are at stake. In the context of particle physics, the mass has been

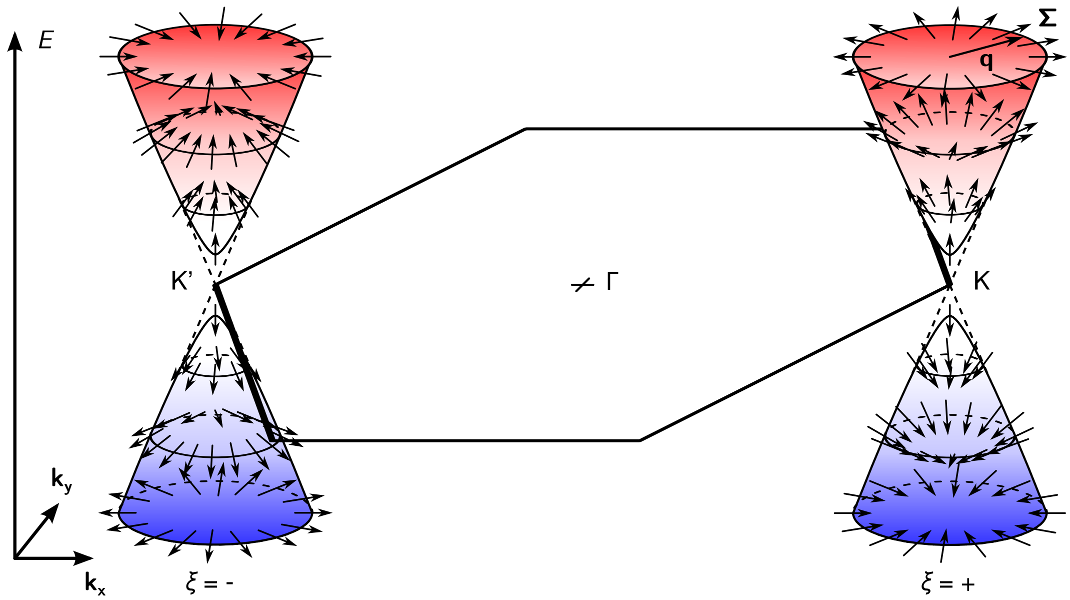

Figure 1.7: **Pseudo-spin texture of the Semenoff insulator.** Linearised π (blue) and π^* (red) bands are centred at the K and K' points of the first Brillouin zone (black hexagon). On both bands, the pseudo-spin $\mathbf{\Sigma}$ is represented, with a tilt θ with respect to the horizontal plane.

shown to appear as a coupling term between the two chiralities, as expressed by the τ_x matrix. As a consequence, chirality is not a good quantum number for massive Dirac fermions. In contrast, the Semenoff mass term in Equation (1.27) opens a gap because of its σ_z matrix. This means the Semenoff term opens a gap only because of its action on the sub-lattice degree of freedom. Its τ_z matrix leaves the valley a good quantum number.

Still, the Semenoff mass makes the sub-lattices different, therefore influencing the pseudo-spin $\mathbf{\Sigma}$ of electrons. As their chirality λ is equivalent to $\frac{\mathbf{\Sigma}\cdot\mathbf{q}}{q}$, this mass may break chirality conservation. To understand this, the influence of the Semenoff mass on pseudo-spin is going to be detailed, before getting back to chirality.

One can get back to the definition of the pseudo-spin, which is pointing up for electrons exclusively on the A sub-lattice, and down for electrons exclusively on the B sub-lattice. In graphene, identical sub-lattices means the pseudo-spin lies in-plane, with a polar angle $\theta_{\mathbf{q}} = \frac{\pi}{2}$ with respect to the vertical direction. In the Semenoff insulator, electrons would rather stay on one of the two sub-lattices, so their pseudo-spin is tilted out of plane, with an angle $\theta_{\mathbf{q}} \neq \frac{\pi}{2}$. The larger this tilting, the more electrons delocalize on one sub-lattice rather than both. This tilting thus results from the competition for an electron between staying on-site and hopping to the other sub-lattice, whose characteristic energies are respectively $m_S v_F^2$ and $\hbar\,|\mathbf{q}|\,v_F$. Consistently, this ratio also corresponds to the ratio of the out-of-plane and in-plane components of $\mathbf{\Sigma}$ in Equation (1.27), so $\theta_{\mathbf{q}} = \frac{\pi}{2} - \arctan\left(\frac{m_S v_F}{\hbar|\mathbf{q}|}\right)$.

This tilting has a direct influence on chirality, because $\frac{\mathbf{\Sigma}\cdot\mathbf{q}}{q}$ is then not equal to ±, but varies continuously between -1 and $+1$. Indeed, in the hamiltonian (1.27), the Semenoff mass corresponds to an additional z component to $\mathbf{\Sigma}$. However, $\mathbf{q}$ is constrained in the $x-y$ plane, so it can neither align nor anti-align with $\mathbf{\Sigma}$. Consequently, chirality is not a good quantum number anymore.

Two comments can be made about the schematic view of the pseudo-spin texture illustrated on Figure 1.7. First, pseudo-spin tilting affects mostly the electrons close to the K and K' points. Far from the K and K' points, the conical dispersion of electrons in graphene is recovered, as well as the planar orientation of their pseudo-spin. Only the states at the K and K' points have a pseudo-spin exactly vertical, and depending on whether the A or B sub-lattice has been made more stable, the pseudo-spin up or down state lies in the valence band. Secondly, it appears that despite the tilting, the pseudo-spin still points outwards or inwards on entire bands, as it was the case for graphene. This is not a signature of different chiralities anymore, but the pseudo-spin texture will serve as a characterization tool for the other hamiltonians in this section.

Beside the formal introduction of a staggered on-site potential on each sub-lattice, one may wonder about the practical situations where a Semenoff gap opens in graphene. As mentioned earlier, the presence of a substrate beneath graphene provides the required modification. Another example is the coupling of the electrons to the out-of-plane optical (ZO) phonon mode with B_{2g} symmetry at Γ point. Indeed, this vibrational mode corresponds to the out-of-plane movement of all C atoms, with the two sub-lattices oscillating in phase opposition, as illustrated on Fig. 1.8 (left). This mode therefore breaks the sub-lattice equivalence, but one may wonder if the electrons indeed couple to it.

In pristine graphene, due to symmetry arguments, in-plane phonons couple linearly to electrons, whereas out-of-plane phonons couple only quadratically [123]. This implies a negligible electron-phonon coupling for the ZO phonon. However, in presence of a substrate, the horizontal plane symmetry σ_h is broken, which lifts this symmetry constraint and makes a substantial electron-ZO phonon coupling possible. In this case, the associated contribution to the electronic hamiltonian has a σ_z form [118] identical to the Semenoff term. Still, these symmetry arguments do not deliver a quantitative estimate of the electron-phonon coupling.

Determining how much electrons couple to the ZO phonon can be achieved by observing a Kohn anomaly in the ZO phonon dispersion, as it is a direct signature of electron-phonon coupling. Indeed, when a phonon of wave vector $\mathbf{q}$ connects two electronic states of the Fermi surface, a Kohn anomaly can occur [99]. It can be understood with the following picture: because the phonon connects two electronic states, the vibration of the atoms is screened by the conduction electrons, which dampens the oscillation and reduces the phonon frequency. As a result, a Kohn anomaly gives rise to a dip in the phonon dispersion curve. In the case of graphene, there are only two electronic states at K and K' points. Only phonons with $\mathbf{q} = 0$ and $\mathbf{q} = \mathbf{\Gamma K}$ can then display a Kohn anomaly. In the case of the ZO phonon, the presence of a substrate is paramount. In-

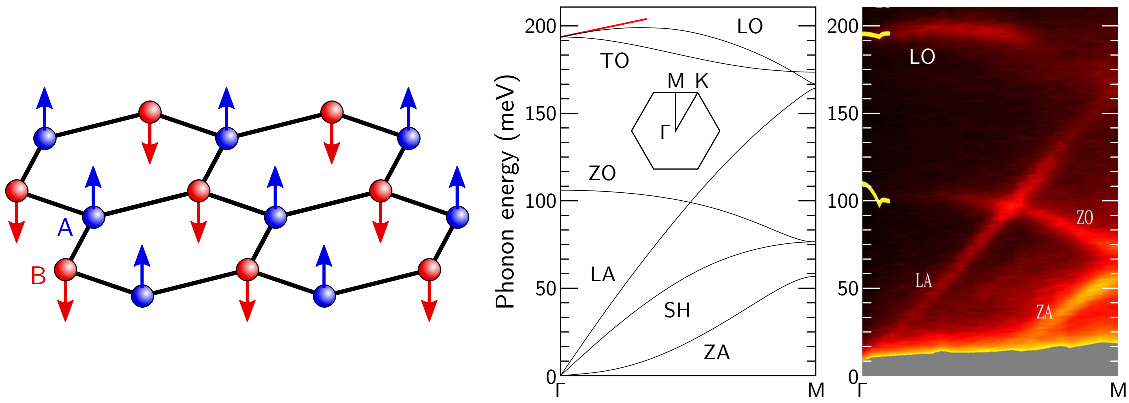

Figure 1.8: **ZO phonon of graphene. Left:** Sketch of the atomic displacements of the ZO phonon. The movements of the A (blue arrows) and B (red arrows) atoms are in phase opposition. **Middle:** Phonon dispersion in pristine graphene along the ΓM direction. A Kohn anomaly results in a dip in the LO phonon dispersion at Γ. Adapted from [204]. **Right:** HREELS intensity plot for phonon dispersion of graphene on Pt(111). The LO, LA, ZO, and ZA branches are clearly identified, contrary to the TO and SH branches whose intensities are reduced by a selection rule. Yellow lines close to Γ indicate fits to the LO and ZO dispersions, where Kohn anomalies arise at about $q \sim 0.13$ Å^{-1}. Adapted from [167].

deed, DFT calculations performed for pristine graphene and shown on Fig. 1.8 (center) reveal no Kohn anomaly in the ZO branch. Nonetheless, for graphene lying on a Pt(111) surface, a Kohn anomaly has been measured by High Resolution Electron Energy Loss Spectroscopy (HREELS) [167], as illustrated on Fig. 1.8 (right). Due to the slight p-doping induced by the substrate, it lies 0.13 Å^{-1} away from the Γ point. The presence of the substrate therefore enables a large electron-phonon coupling, which means the ZO phonon plays a role in the opening of a Semenoff gap in supported graphene.

In this first example, a band gap has opened at the Fermi energy due to the difference in sub-lattices introduced by the Semenoff mass term. In essence, this term actually breaks the inversion symmetry of graphene. Given the representation chosen here, inversion operation is given by $\sigma_z \tau_x$, which commutes with the graphene hamiltonian, but not with the Semenoff mass term.[10] This can be comprehended in real space, as the inversion operation swaps the sub-lattices A and B, which are identical for graphene,

---

[10] Under inversion operation, the two sub-lattices A and B are swapped, as well as the two corners of the first Brillouin zone K and K'. Due to the choice of representation $c^\dagger_\alpha(\mathbf{q}) = \left(c^\dagger_{A,+\mathbf{K}}(\mathbf{q})\, c^\dagger_{B,+\mathbf{K}}(\mathbf{q})\, c^\dagger_{B,-\mathbf{K}}(\mathbf{q})\, c^\dagger_{A,-\mathbf{K}}(\mathbf{q})\right)$, swapping both A and B, and K and K' is achieved by the single operator τ_x. However, an additional σ_z proves necessary. Indeed, the linearisation of $c^\dagger_n(\mathbf{k})$ ($n = A, B$) yields an additional phase factor, which differs depending on A/B and K/K'. To compensate them, a $-$ sign has to be added to one of the sub-lattice components when swapping valleys. Those additional phase factors will be detailed in a more simple 1D case later on.

but different for the Semenoff insulator. This inversion symmetry breaking has been attributed to the opening of a band gap in various graphene systems, like graphene on SiC [231] or aligned on h-BN [80, 216]. Additionally, the analogy between the Semenoff insulator and the Dirac equation also shows the electronic excitations are not chiral anymore, as the pseudo-spin tilts upwards and downwards within the Brillouin zone. In the case of the Kekulé insulator, a different symmetry is broken, leading to a gap opening with a completely different nature.

1.2.2 Kekulé insulator

In 1865, the German chemist August Kekulé suggested the long-sought structure of the benzene molecule was a six-membered carbon ring with alternating single and double bonds. Since double bonds are shorter than single bonds, this structure is not strictly hexagonal but a bit distorted, as illustrated on Figure 1.9. This suggestion then leads to two possible symmetric structures for benzene.

In the light of the tight-binding model exposed earlier, it is now clear the six electrons involved in the double bonds are actually delocalized within a π orbital all over the benzene ring. Benzene is thus an aromatic molecule and has a hexagonal shape. Still, molecular distortions along double bonds can happen via the Jahn-Teller effect, for instance in the case of antiaromatic molecules.

Nevertheless, one can still imagine a situation where the constituting hexagons of a graphene sheet would undergo a similar distortion in a permanent way, which is called the Kekulé distortion, schematically represented on Figure 1.9. In this distortion, carbon atoms regroup by pairs, where a double bond is drawn, while single bonds elongate: this is a dimerization process. The elastic energy required to distort graphene's structure in such a way is prohibitive at first sight. In order to understand what would be its driving force, a simplified one-dimensional (1D) system where a similar dimerization occurs can first be considered: polyacetylene.

Undistorted polyacetylene

Polyacetylene is a polymer chain with repeating unit $(C_2H_2)_n$, made of carbon atoms with alternative single and double bonds. As such, it resembles graphene and benzene, and the dimerization of its atoms leads to a distortion referred to as the Peierls distortion. To explain its cause, the band structure of undistorted polyacetylene is first going to be calculated in a tight-binding scheme similar to that used for graphene. The calculations and discussions provided here are inspired from the SSH model[11] [187, 188].

For simplicity, polyacetylene can be considered as a 1D chain of carbon atoms indexed by the integer n. Like graphene, these carbon atoms have sp^2 hybridization, so for each atom, only one electron in a $2p_z$ orbital contributes to electron transport. Besides, only nearest-neighbour hopping is going to be considered in between these orbitals. Due to translational invariance along the chain, Bloch's theorem can be used. Here, the

---

[11] This model is called after the name of its authors: Wu-Pei Su, John Robert Schrieffer and Alan J. Heeger. It provides a simple but rich understanding for the conductive properties of polymers.

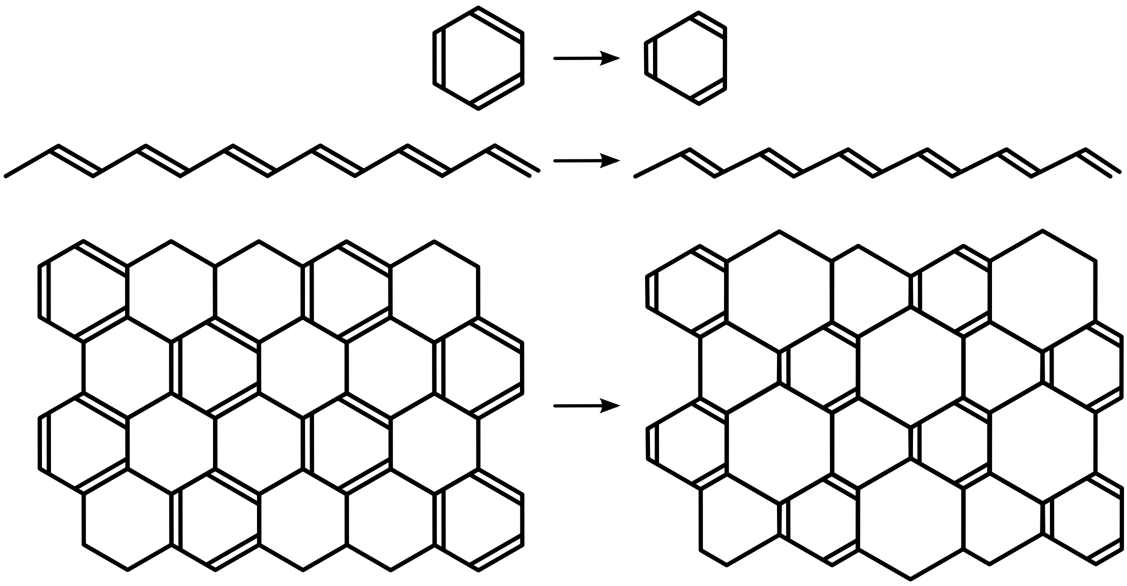

Figure 1.9: **Kekulé distortion in graphene. Top:** as in the original picture of Kekulé, a hexagonal benzene ring can be distorted due to its alternated simple and double bonds. **Middle:** in polyacetylene, the shortening of double bonds corresponds to a Peierls distortion. **Bottom:** a similar distortion on the honeycomb lattice of graphene is called a Kekulé distortion.

invariance is considered to occur every two atoms, labelled A and B, with a lattice constant $a \sim 2.42$ Å (the C-C distance is ~ 1.40 Å).[12] As a result, the electronic states ψ of the chain will be linear combinations of atomic orbitals ϕ_n, and two Bloch waves corresponding to either A or B atoms are used, as was done for graphene in Equation (1.4). In a second quantization approach, the wave function is then given by:

$$\begin{aligned} c\left(k\right) &= a\left(k\right) c_A\left(k\right) + b\left(k\right) c_B\left(k\right) \\ &= \frac{1}{\sqrt{N}} \left(a\left(k\right) \sum_{n \text{ even}} e^{ikna} c_n + b\left(k\right) \sum_{n \text{ odd}} e^{ikna} c_n \right) \end{aligned} \tag{1.28}$$

As for the hamiltonian, similar to graphene, only the hopping terms influence the energy dispersion, and here only nearest-neighbour hopping is considered:

$$H = -t \sum_n c^\dagger_{n+1} c_n + c^\dagger_n c_{n+1} \tag{1.29}$$

---

[12] Indeed, according to the structure of polyacetylene represented on Figure 1.10, the invariance does occur every two atoms. Yet, the tight-binding model assumed here neglects the difference between these two atoms, so $\frac{a}{2}$ would be a more relevant lattice constant. In any case, this choice is conventional, so it does not influence the electronic dispersion. Still, as the Peierls distortion will need a two atom unit cell, a conventional a lattice constant is set here too.

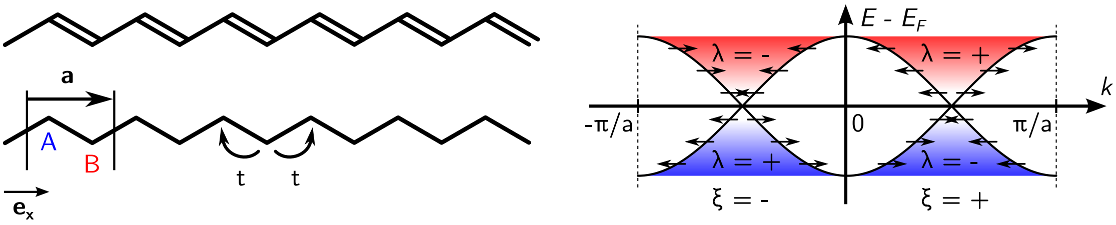

Figure 1.10: **Undistorted polyacetylene.** **Left:** An undistorted polyacetylene chain hosts two atoms A and B per unit cell with a uniform hopping texture t. **Right:** this gives rise to a semi-metallic band structure with two Dirac cones located at $k = \pm K = \pm\frac{\pi}{2a}$. Dotted lines indicate the Brillouin zone edges. A valley isospin $\xi = \pm$ can be defined decomposing $k = \xi K + q$. The pseudo-spin $\mathbf{\Sigma}$ is represented on both bands, pointing towards either $+x$ or $-x$. For each state, the alignment (resp. anti-alignment) of $\mathbf{\Sigma}$ with $\mathbf{q}$ corresponds to a $\lambda = +$ (resp. $\lambda = -$) chirality.

with hopping parameter $t \sim 2.5$ eV. Using the Bloch waves introduced above, this hamiltonian can be rewritten in k space using a decomposition of the wave function on the A and B atoms. The following hamiltonian density is obtained:

$$\mathcal{H}_k = \begin{pmatrix} c_A^\dagger(k) & c_B^\dagger(k) \end{pmatrix} \underbrace{\begin{pmatrix} 0 & -2t\,\cos(ka) \\ -2t\,\cos(ka) & 0 \end{pmatrix}}_{= -2t\,\cos(ka)\,\sigma_x} \begin{pmatrix} c_A(k) \\ c_B(k) \end{pmatrix} \tag{1.30}$$

This holds the electron energy dispersion as:

$$E_k = \pm 2t\,|\cos(ka)| \tag{1.31}$$

Without any surprise, this result is very similar to that found for graphene in Equation (1.9), as around the Fermi energy, the band structure comes down to a linear dependence around $k = \pm\frac{\pi}{2a}$. This is all the more apparent that the bands are crossing at these points, mimicking the Dirac cones of graphene in 1D. $k = \frac{\pi}{2a}$ and $k = -\frac{\pi}{2a}$ then play the role of the inequivalent K and K' points of graphene, and the electron wave vector k can be rewritten $k = \xi K + q$, with $\xi = \pm$ the valley isospin.

Besides, the hamiltonian density is such that the Pauli matrix σ_x is introduced conveniently. Once again, this defines a pseudo-spin Σ associated to the wave function's relative weights on the A or B atoms. Since only σ_x is present, the eigenstates have their pseudo-spin constrained along the x axis, so only two pseudo-spin orientations are possible. For both, the weights on atoms A and B are equal. However, when Σ points to $+x$, the components are in-phase ($\Sigma = \frac{1}{\sqrt{2}}\left(\begin{smallmatrix}1\\1\end{smallmatrix}\right)$), whereas when Σ points to $-x$, the components are out of phase ($\Sigma = \frac{1}{\sqrt{2}}\left(\begin{smallmatrix}1\\-1\end{smallmatrix}\right)$).

To make the analogy with graphene complete, one can linearise the hamiltonian in Equation (1.34) using the $c_\alpha^\dagger(q) = \left(c_{A,K}^\dagger(q), c_{B,K}^\dagger(q), c_{B,-K}^\dagger(q), c_{A,-K}^\dagger(q)\right)$ representation analogous to that used before, and get:

$$H = \hbar v_F \sum_q \sum_{\alpha,\beta=1}^{4} c_\alpha^\dagger(q) \underbrace{\left[q\ \sigma_x \tau_z\right]_{\alpha,\beta}}_{=\left[(\boldsymbol{\sigma}\cdot\mathbf{q})\,\tau_z\right]_{\alpha,\beta}} c_\beta(q) \tag{1.32}$$

where $v_F = \frac{2at}{\hbar} \sim 10^6$ m.s^{-1}. This is exactly the same hamiltonian as the one written for graphene in Equation (1.22) but in 1D.

If this model applied successfully to polyacetylene, the conclusions drawn previously for graphene would apply to polyacetylene. It appears not to be a realistic model, as Peierls distortion modifies this picture. Kekulé distortion induces a similar modification to graphene. Exposing the origin and consequences of Peierls distortion will then provide some insight on Kekulé distortion in graphene.

Peierls distortion in polyacetylene

As explained in the introduction of this section, under certain circumstances, it proves more stable for delocalized electrons in a π system to localize on double bonds, which then shorten, inducing a distortion of the atomic structure. This is especially true for polyacetylene, which is known to undergo a Peierls distortion, making half of its bonds shorter and the other half longer.

In the crude tight-binding model presented above, this distortion can be taken into account with a texture of hopping parameters. In other words, electrons have a higher probability to hop from site to site for a short bond than for a long bond. Two hopping parameters t_1 and t_2 can then be introduced for short and long bonds respectively, as on Figure 1.11. For simplicity, the displacement u of each atom will be assumed small, so $t_1 = t + gu$ and $t_2 = t - gu$, with $g \sim 4.1$ eV.Å^{-1} the electron-phonon coupling constant [188]. With this hypothesis, an additional term goes in the hamiltonian (1.29), which expresses as:

$$H = -t \sum_n \left(1 + \frac{gu}{t}(-1)^n\right) \left(c_{n+1}^\dagger c_n + c_n^\dagger c_{n+1}\right) \tag{1.33}$$

With this formulation, the modulation of bond lengths is translated in the hamiltonian, so translational invariance truly occurs once every two atoms, with a period a. As before, one can use the Bloch basis introduced by Equation (1.28) to rewrite the hamiltonian density in k space:

$$\mathcal{H}_k = -2t \left(c_A^\dagger(k)\ c_B^\dagger(k)\right) \left(\cos(ka)\,\sigma_x + \frac{gu}{t}\sin(ka)\,\sigma_y\right) \begin{pmatrix} c_A(k) \\ c_B(k) \end{pmatrix} \tag{1.34}$$

The hopping texture adds a σ_y component, which has a critical impact on the electronic energy dispersion:

$$E_k = \sqrt{4t^2\cos^2(ka) + g^2u^2\sin^2(ka)} \tag{1.35}$$

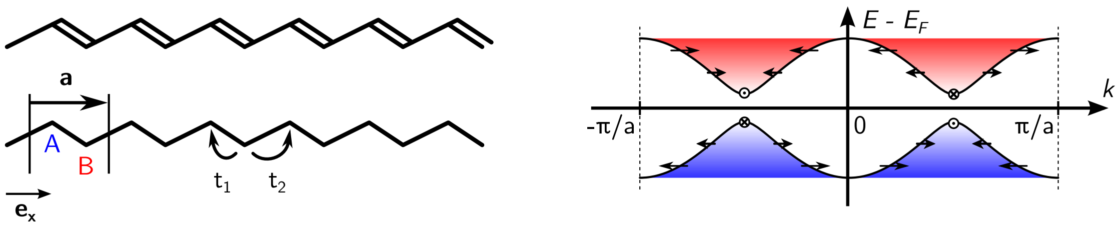

Figure 1.11: **Peierls distortion in polyacetylene. Left:** one every two bonds of polyacetylene gets shorter, while the other gets longer, so two hopping parameters t_1 and t_2 are needed. **Right:** as a consequence, a gap opens at the Dirac cones of polyacetylene.

As represented on Figure 1.11, a band gap gu opens at the Dirac cones ($k = \pm\frac{\pi}{2a}$). If one sets the displacement u to zero, the gap closes, and the Dirac cones are recovered, consistently with Equation (1.31). This shows that the two bands that are merely crossing for undistorted polyacetylene hybridize due to the Peierls distortion. In other words, at a given k, the two states of the valence and conduction bands from the original undistorted chain recombine to give rise to the new states of the distorted chain.

To go one step further, the hamiltonian can be linearised using $k = \xi K + q$, and rewritten in the representation $c_\alpha^\dagger(q) = \left(c_{A,K}^\dagger(q), c_{B,K}^\dagger(q), c_{B,-K}^\dagger(q), c_{A,-K}^\dagger(q)\right)$ as:

$$H = \hbar v_F \sum_q \sum_{\alpha,\beta=1}^{4} c_\alpha^\dagger(q) \left[\left(q\sigma_x - \frac{2gu}{\hbar v_F}\sigma_y\right)\tau_z\right]_{\alpha,\beta} c_\beta(q) \tag{1.36}$$

This raises the question of the pseudo-spin texture in the first Brillouin zone. The above hamiltonian shows that the pseudo-spin takes an additional y component. As a result, its orientation is modulated depending on q, as pictured on Figure 1.11. Contrary to the Semenoff σ_z term, which tilts the pseudo-spin out of plane, the Peierls distortion σ_y term rotates the pseudo-spin in-plane. This means that the states of the undistorted chains – which have pseudo-spins pointing towards $\pm x$ – hybridize in a way that rotates their pseudo-spins towards the y direction, altering only the phase difference between their A and B components. In other words, the Semenoff mass term influences the weights of the wave function on the A and B components while preserving their relative phases, whereas the Peierls term tunes the phase difference between the two components while leaving their relative weights equal.[13]

Now considering fundamental symmetries, the gap opening is actually due to the distortion imposing a doubled unit cell. It reduces translational invariance, and opens the band gap. This is clearly different from the Semenoff insulator, for which inversion

---

[13] Although giving a simple picture of the situation, it should be emphasized this image is entirely dependent on the chosen representation. Indeed, contrary to graphene, polyacetylene is 1D, so only two Pauli matrices are needed: σ_x for the dispersion term, and σ_y for the Peierls term. A unitary transformation of the $\left(c_A^\dagger(k), c_B^\dagger(k)\right)$ basis could change these matrices into σ_x and σ_z. This means that in 1D, there is actually no difference between the Peierls and Semenoff masses. The discussion detailed here serves merely as a preparation for graphene, whose higher dimensionality makes the Semenoff and Kekulé masses distinct.

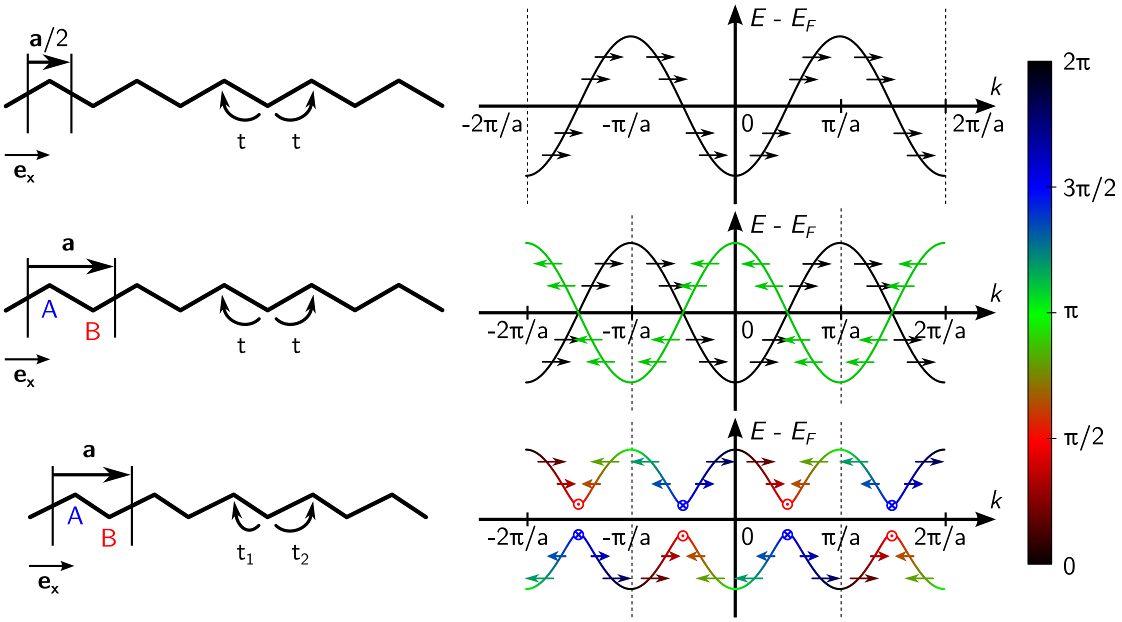

Figure 1.12: **Peierls distortion in a band folding approach.** An undistorted polyacetylene chain is described with either 1 (top left) or 2 (middle left) atoms per unit cell. The deduced band structure then contains either 1 band with $\frac{4\pi}{a}$ periodicity (top right), or 2 bands with $\frac{2\pi}{a}$ periodicity (middle right). The two descriptions are equivalent by folding the single band on itself. When the chain is distorted (bottom), gaps open at $k = \pm\frac{\pi}{2a}$, where the bands of the undistorted chain intersect.

symmetry is broken. In the approach derived here, the symmetry breaking is hardly apparent for two reasons. First, the same lattice constant was considered for both undistorted and distorted polyacetylene. Secondly, the above hamiltonian shows a band hybridization where phase differences are tuned, but does not explain clearly its origin. These two issues are going to be addressed in the following, using the so-called band folding model.

Band folding model

In the previous section, the electronic structure of undistorted polyacetylene close to the Fermi energy has been calculated using two atoms per unit cell. This is artificial, as the translational invariance in this model occurs every atom. When considering one atom per unit cell, the use of A and B Bloch waves makes no longer sense, and there is a single Bloch wave given by:

$$c(k) = \frac{1}{\sqrt{N}} \sum_n e^{ikna} c_n \tag{1.37}$$

This enables a simple diagonal expression of the hamiltonian (1.29), as:

$$H = -2t\sum_{k} \cos\left(ka\right) c^{\dagger}(k)c(k) \tag{1.38}$$

This means this Bloch wave already provides the relevant states of the system. Their energy dispersion is deduced from this as:

$$E_k = -2t\ \cos(ka) \tag{1.39}$$

This is close to but different from the expression of Equation (1.31). This time, indeed, there is a single electronic band, and as the lattice constant is $\frac{a}{2}$, the first Brillouin zone extends from $-\frac{2\pi}{a}$ to $\frac{2\pi}{a}$, as represented on the top panel of Figure 1.12. This situation will then be termed the single band picture, in opposition to the previously studied two-band picture.

When comparing the undistorted and distorted polyacetylene chain, pseudo-spin proved to be a useful tool to characterize the electronic states. Here, there is no A and B atom, so no pseudo-spin. Still, considering that Equation (1.37) can be interpreted as $c\left(k\right) = c_A\left(k\right) + c_B\left(k\right)$. This means the two components would always be in phase, so the pseudo-spin would be $\Sigma = \frac{1}{\sqrt{2}}\left(\begin{smallmatrix}1\\1\end{smallmatrix}\right)$ over the whole band, as pictured by the right-pointing black arrows on the band structure of the top panel of Figure 1.12.

With this in mind, one can now get back to the band structure derived in the previous section for the undistorted polyacetylene chain, which is illustrated on the middle panel of Figure 1.12. Because the unit cell in direct space is artificially twice larger and contains two atoms, in reciprocal space, the first Brillouin zone is twice smaller and contains two bands. As a result, this smaller Brillouin zone is referred to as a reduced Brillouin zone. As can be expected, in both pictures, the number of electronic states is the same.

Besides, when comparing the top and middle panels, the orientation of the pseudo-spin arrows gives the impression that to go from one band structure to the other, one needs to fold the left and right ends ($|k| > \frac{\pi}{a}$) of the band structure onto its central part ($|k| < \frac{\pi}{a}$). Although this impression is the reason behind the name of the "band folding model", it is in fact not accurate. Indeed, the band portions are actually rigidly shifted in k: the left end ($k < -\frac{\pi}{a}$) is shifted by $+\frac{\pi}{a}$, while the right end ($k > \frac{\pi}{a}$) is shifted by $-\frac{\pi}{a}$. When doing this, the original black bands of the top panel do superimpose with the additional green band on the middle panel, but their pseudo-spins do not match. To understand this pseudo-spin flip, one can apply a $+\frac{\pi}{a}$ shift in k space to an electronic state delocalized either on the A or B atoms:

$$\begin{cases} c_A\left(k \pm \dfrac{\pi}{a}\right) = \dfrac{1}{\sqrt{N}} \displaystyle\sum_{n \text{ even}} e^{ikna}\left(-1\right)^n c_n = c_A\left(k\right) \\ c_B\left(k \pm \dfrac{\pi}{a}\right) = \dfrac{1}{\sqrt{N}} \displaystyle\sum_{n \text{ odd}} e^{ikna}\left(-1\right)^n c_n = -c_B\left(k\right) \end{cases}$$

This shows a shift in k yields different additional phase factors depending on the sub-lattice. In terms of pseudo-spin, this means such a shift turns $\Sigma = \frac{1}{\sqrt{2}}\left(\begin{smallmatrix}1\\1\end{smallmatrix}\right)$ into $\Sigma = \frac{1}{\sqrt{2}}\left(\begin{smallmatrix}1\\-1\end{smallmatrix}\right)$, thus flipping its direction.

This property can be used to re-interpret the hamiltonian expression in Equation (1.36). Indeed, applying a $+\frac{\pi}{a}$ shift in k space brings a state from one valley to the other, so using the above expressions, one can for instance rewrite $c^{\dagger}_{A,K}c_{B,K} = -c^{\dagger}_{A,K}c_{B,-K}$. The hamiltonian density can thus be rewritten as:

$$H = \hbar v_F \sum_{q} \sum_{\alpha,\beta=1}^{4} c^{\dagger}_{\alpha}(q) \left[q\sigma_x\tau_z - \frac{2gu}{\hbar v_F}\sigma_0\tau_x \right]_{\alpha,\beta} c_{\beta}(q) \tag{1.40}$$

In this formulation, the Peierls term couples both valleys (τ_x) with no distinction between the two sub-lattices (σ_0). The distortion then results in an intervalley coupling term, so the gap opening is revealed as the hybridization of the two Dirac cones.

So far, the band folding model has just shown the two faces of the same coin, but this preliminary step now proves useful to interpret the consequences of the Peierls distortion. Indeed, in the two-band picture, the gap opening has been interpreted as the hybridization of states from the valence and conduction bands with opposite pseudo-spins occurring at each value of k. In the single band picture, for each value of k, there is only one state. The hybridization actually takes place between states separated by $q = \frac{\pi}{a}$ from each other. This is a direct consequence of the reduced translational invariance implied by the distortion: it induces nesting vectors $q = \pm\frac{\pi}{a}$ that couple electronic states by pairs all over the first Brillouin zone. The closer in energy these states are, the stronger their resulting hybridization. As a result, the most striking consequence of this distortion is the gap opening at the Dirac cones. A related consequence is the acquired phase difference between their two sub-lattice components described earlier.

The interpretation of the reduced translational invariance described here is actually the same as the nearly free electron model in metals. In the nearly free electron models, a quadratic energy dispersion of free electrons $\frac{\hbar^2 k^2}{2m}$ is assumed, and the influence of the periodic crystal potential is weak enough to be considered as a perturbation. Since it imposes a reduced translational invariance, this potential defines the first Brillouin zone and the quadratic band of free electrons folds into it. This is the same effect as the distortion considered here: states with originally different k wave vectors but equal energies superimpose due to the band folding and hybridize, resulting in band gap openings.

Using this simple model, one can get an intuitive idea for the effect of reduced translational invariance. The large direct space periodicity indeed induces nesting vectors $\mathbf{q}$ between electronic states, which can be visualized conveniently with folded bands in a reduced Brillouin zone. In the case of polyacetylene, doubling the lattice constant happens to make electrons scatter in between the two states located exactly at the Fermi energy. Their hybridization leads to a gap opening, which makes the chain insulating. As a consequence, the electrons at the Fermi level for the undistorted chain move to lower energy states when it is distorted. This energy saving actually drives the distortion: the elastic energy spent to distort the bonds is overcome by the electronic energy gained by opening a gap at the Fermi energy.[14]

With this underlying mechanism in mind, it is no surprise that not any kind of distortion occurs. It has to obey two main constraints: the band folding it generates has to lower the total electronic energy by opening gaps at the Fermi energy, and its mechanical cost has to be smaller than this lowering of electronic energy. In this case, the system can be considered as undergoing a phase transition between a undistorted metallic phase, and a distorted insulating phase. The generated gap Δ would be the order parameter of such a phase transition. This formalism will prove useful in the case of graphene, where the Kekulé distortion is not necessarily favourable.

Kekulé distortion in graphene

Similar to the Peierls distortion in polyacetylene, the Kekulé distortion of graphene introduced on Figure 1.9 can be included in a tight-binding model resorting to a hopping texture. This texture reduces translational invariance as indicated by the supercell $(\mathbf{a_{Kek_1}}, \mathbf{a_{Kek_2}})$ on Figure 1.13. Following the original description of the benzene molecule formulated by August Kekulé, the Kekulé distortion in graphene provides a supercell whose unit vectors are $\sqrt{3}$ times larger than that of graphene, and rotated by 30° with respect to them. In Wood's notation, this triple supercell then corresponds to a $\left(\sqrt{3} \times \sqrt{3}\right)$ R30°. When going to reciprocal space, the unit wave vectors $(\mathbf{k_{Kek_1}}, \mathbf{k_{Kek_2}})$ associated to this supercell then have to be $\sqrt{3}$ shorter than those of graphene and rotated by 30° with respect to them. The resulting reduced Brillouin zone is thus three times smaller and is also rotated by 30° with respect to the graphene Brillouin zone, as pictured in the lower left panel of Figure 1.13.

Here too, the effect of the reduced translational invariance on the band structure of graphene can be interpreted in two equivalent ways. Using the graphene first Brillouin zone, reduced translational invariance gives rise to nesting vectors $\mathbf{q}$ in the band structure, which correspond to linear combinations of $\mathbf{k_{Kek_1}}$ and $\mathbf{k_{Kek_2}}$. Furthermore, the supercell geometry is such that $\mathbf{k_{Kek_1}}$ and $\mathbf{k_{Kek_2}}$ actually connect the K and K' points of the graphene first Brillouin zone, where the Dirac cones originally lie. As a consequence, reduced translational invariance allows nesting vectors that hybridize electronic states from the two valleys of graphene, as illustrated on the top right panel of Figure 1.13. This situation is alike the Peierls distortion in polyacetylene, and therefore results in gap openings at the K and K' points.

This situation is also well explained in a band folding picture. With this model, the band structure of graphene is folded into the reduced Brillouin zone, as schematically presented on the bottom right panel of Figure 1.13. There, the reduced Brillouin zone lies as a smaller hexagon at the center of the larger hexagonal first Brillouin zone of graphene. Six portions of the graphene first Brillouin zone coloured in red, blue and

---

[14] The same behaviour is at stake in the Jahn-Teller effect for molecules: partially filled and degenerate molecular orbitals get their degeneracy lifted under the effect of a distortion, but more energy is saved on the electronic side than spent on the mechanical side.

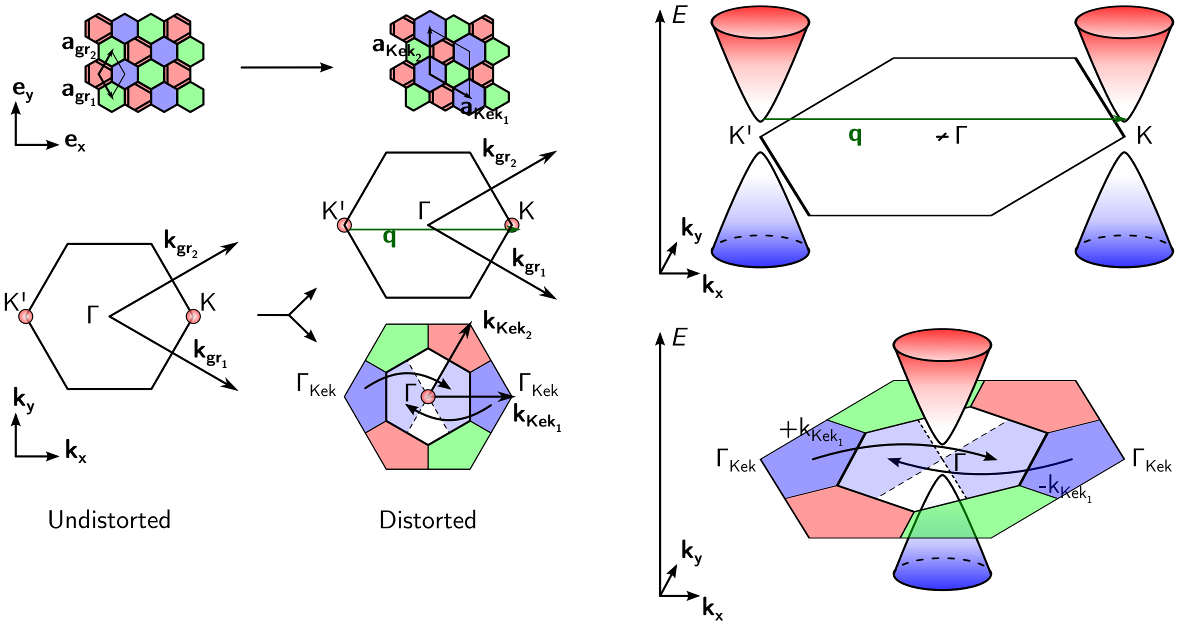

Figure 1.13: **Gap opening due to a Kekulé distortion. Top left:** in direct space, a Kekulé distortion reduces translational invariance, as three different types of hexagon (red, green, blue) can be found in a tripled unit cell ($\mathbf{a}_{\mathbf{Kek_1}}, \mathbf{a}_{\mathbf{Kek_2}}$). **Bottom left:** in reciprocal space, two equivalent scenarios explain the gap opening at two Dirac cones (red circles) originally located at K and K'. **Top right:** on the one hand, in the graphene Brillouin zone, reduced translational invariance allows nesting vectors $\mathbf{q}$ to couple different states in the band structure, and in particular the states around the K and K' points, which hybridize and open a gap. **Bottom right:** on the other hand, using a band folding picture in the reduced Brillouin zone, the cones originally at K and K' are both shifted to Γ, and their superimposition implies they hybridize with each other, opening a gap.

green lie outside the reduced Brillouin zone. Band folding is achieved by shifting them rigidly into it using $\pm\mathbf{k}_{\mathbf{Kek_1}}$, $\pm\mathbf{k}_{\mathbf{Kek_2}}$ or their combinations. In the process, the Dirac cones located at each corner of the graphene Brillouin zone get all shifted to the Γ point of the reduced Brillouin zone. Hence, the two Dirac cones superimpose, and the distortion induces their hybridization, resulting in a band gap opening.

No matter with which picture this situation is interpreted, a gap opens owing to the hybridization of electronic states from both Dirac cones, which means there is some cross-talking between the two valleys of graphene. This can be introduced in the graphene hamiltonian density in the form of a coupling term [78] similar to the one introduced in Equation (1.40) as:

$$\mathcal{H}_{\mathbf{q}} = \sum_{\alpha,\beta=1}^{4} c_{\alpha}^{\dagger}(\mathbf{q}) \left[(\hbar v_F \mathbf{q}\cdot\boldsymbol{\sigma}\ \tau_z + \boldsymbol{\Delta}\cdot\sigma_0\boldsymbol{\tau})\right]_{\alpha,\beta} c_{\beta}(\mathbf{q}) \tag{1.41}$$

where $\boldsymbol{\Delta}$ is here a 2-component vector that indicates how strong the intervalley coupling is. Its form is $\sigma_0 \boldsymbol{\tau}$ with $\boldsymbol{\tau} = (\tau_x, \tau_y)$, which shows it couples the K and K' valleys (τ_x and τ_y), and makes no distinction between the A and B sub-lattices (σ_0). The energy dispersion can be extracted from this as:

$$E_{\mathbf{q}} = \pm\sqrt{\hbar^2 v_F^2 \mathbf{q}^2 + |\boldsymbol{\Delta}|^2} \tag{1.42}$$

so a gap of width $\Delta = |\boldsymbol{\Delta}|$ opens at both Dirac cones. As introduced earlier, $\boldsymbol{\Delta}$ appears as the order parameter of the distortion, when considered as a phase transition. Similar to the Semenoff mass, Δ can be expressed with a Kekulé mass term as $m_{Kek} v_F^2$. The difference with the Semenoff mass lies in the eigenfunctions. In the Semenoff insulator, the relative weights on sub-lattices A and B were different. Here, the valleys are mixed, so the wave functions from Equation (1.23) become:

$$\psi_1(\mathbf{q}) = \begin{pmatrix} 1 \\ \pm e^{-i\varphi_{\mathbf{q}}} \frac{\hbar v_F q}{\sqrt{\hbar^2 v_F^2 \mathbf{q}^2 + \Delta^2}} \\ \pm \frac{\Delta}{\sqrt{\hbar^2 v_F^2 \mathbf{q}^2 + \Delta^2}} \\ 0 \end{pmatrix} \frac{e^{i\mathbf{q}\cdot\mathbf{r}}}{\sqrt{2}} \text{ and } \psi_2(\mathbf{q}) = \begin{pmatrix} 0 \\ \pm \frac{\Delta}{\sqrt{\hbar^2 v_F^2 \mathbf{q}^2 + \Delta^2}} \\ \mp e^{i\varphi_{\mathbf{q}}} \frac{\hbar v_F q}{\sqrt{\hbar^2 v_F^2 \mathbf{q}^2 + \Delta^2}} \\ 1 \end{pmatrix} \frac{e^{i\mathbf{q}\cdot\mathbf{r}}}{\sqrt{2}} \tag{1.43}$$

with $q = \|\mathbf{q}\|$. When Δ is set to zero, the eigenstates of pristine graphene (1.23) are recovered, as ψ_1 and ψ_2 identify respectively to ψ_K and $\psi_{K'}$. Besides, the larger the value of Δ, the more the states originally around K get a contribution around K', and vice-versa. Moreover, one can easily check that the relative weights on the A and B sub-lattices are equal. Due to the contributions on both valleys however, expressing the phase difference between the two sub-lattice components is equivocal, so defining the pseudo-spin is impossible.

In summary, the Kekulé distortion acts as a phase transition from a semi-metallic to an insulating state, by coupling the states from both valleys. Similar to the Peierls distortion, this can be interpreted in two equivalent ways: either with nesting vectors in the graphene first Brillouin zone, or with folded bands in a reduced Brillouin zone. Once again, it is important to distinguish the Kekulé mass from the Semenoff mass. On the one hand, the Kekulé distortion influences the valley degree of freedom by reducing translational invariance, but maintains equal electronic weights on each sub-lattice. On the other hand, the Semenoff term alters the sub-lattice equivalence by breaking inversion symmetry, but preserves the valley quantum number.

Experimentally, both effects can be observed simultaneously, which brings a discussion on how one can observe a Kekulé distortion, and what effects might have an identical signature. To date, few experimental works could clearly identify a Kekulé distortion in graphene. Theoretical studies predict it can only be observed close to its mechanical failure in ideal conditions [82,112,130], unlikely to be tested experimentally. Nonetheless, this challenge has been circumvented by studying artificial graphene with STM, which enabled to measure a Kekulé-induced band gap [61]. Finally, since a Kekulé

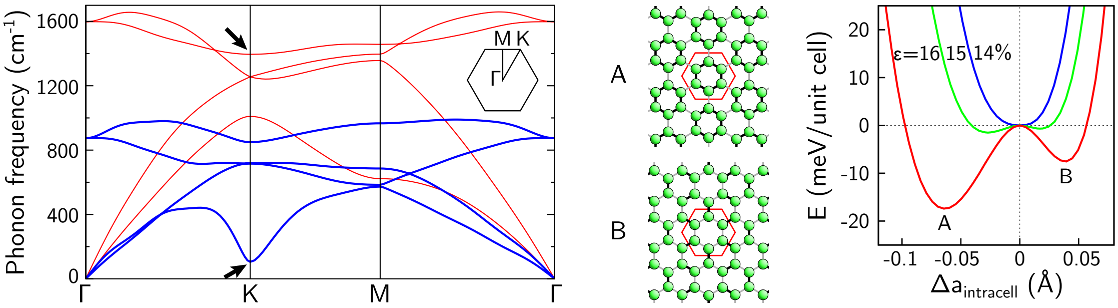

Figure 1.14: **Biaxial strain-induced Kekulé distortion in graphene. Left::** in-plane phonon dispersion of graphene with 0% (red) and 20.5% (blue) biaxial strain. The A_1' phonon at K point is emphasized by a black arrow, with its frequency approaching 0 cm^{-1} at high strain. Adapted from [130]. **Middle:** two possible Kekulé distortions indexed A (inward) and B (outward) can occur, both with a tripled unit cell depicted in red, but with either positive or negative relative intracell atomic distance $\Delta a_{\text{intracell}}$. **Right:** energy profile calculated as a function of $\Delta a_{\text{intracell}}$ with 14, 15, and 16% of biaxial strain. Below 15% strain, the minimum at 0 indicates undistorted graphene is the stable configuration, whereas above 15% strain, the two minima A and B become more favourable. Adapted from [112].

distortion couples electrons from opposite valleys, one has to consider other mechanisms that couple the K and K' valleys. For instance, electronic scattering events induced by phonons [165, 178] or adatoms [24, 25, 65] have physical origins different from a Kekulé distortion, but hold similar signatures. These different approaches are now going to be briefly discussed.

As detailed before, the Peierls distortion is favourable in polyacetylene, and thus occurs at ambient conditions. On the contrary, a Kekulé distortion at ambient conditions is not favourable in graphene. Indeed, in the Peierls instability picture, a transition from the undistorted to the distorted structure requires the lowering of the electronic energy to outweigh the elastic energy cost of the distortion. In polyacetylene, as the electronic density of states is flat, the Peierls gap opening contributes to a significant energy gain. On the contrary, graphene has a linear density of states around the Fermi level, so a Kekulé distortion provides a marginal electronic energy gain. For the transition to occur, it is predicted graphene has to be biaxially strained up to either $\sim 16\%$ [112] or $\sim 21\%$ [82, 130]. Indeed, biaxial strain softens the phonons of graphene, as shown on Figure 1.14. As a result, above a critical strain value, the frequency of a given phonon can become imaginary: it is called a soft mode. A soft mode is then an atomic displacement with no energy cost, which triggers a displacive phase transition. In graphene, this transition is a Kekulé transition, whose soft mode is the transverse optical (TO) phonon with A_1' symmetry at the K point, as illustrated on Figure 1.14 (left). Moreover, when considering the energy landscape along the distortion coordinate on Figure 1.14 (right), the minimum shifts continuously from zero to a finite value, which is the hallmark of a

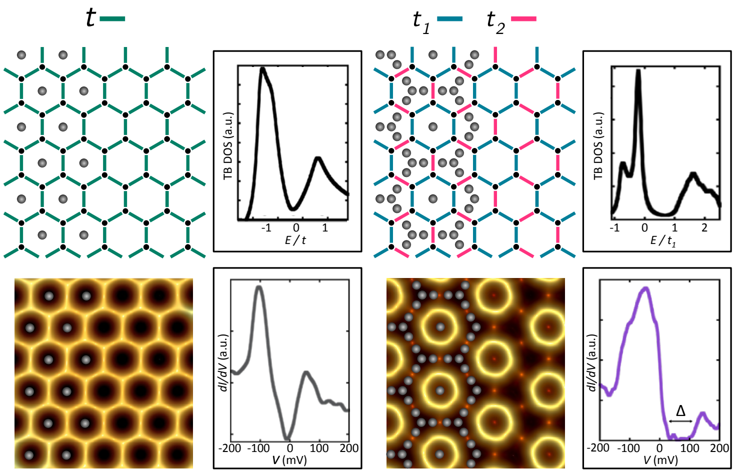

Figure 1.15: **Kekulé distortion in artificial graphene. Top left:** the honeycomb structure of graphene with a uniform hopping texture (t) gives rise to a linear electronic density of states. **Bottom left:** They are effectively reproduced by arranging CO molecules in a triangular pattern on a Cu(111) surface. On the corresponding STM image, high electronic density regions appear as bright, while CO molecules appear as dark spots, schematically represented as gray balls. The associated STS spectrum reveals the linear dependence of the density of states. **Top right:** when a Kekulé hopping texture ($t_1 > t_2$) is added to graphene, a band gap opens at the Fermi level. **Bottom right:** by regrouping CO molecules in the appropriate pattern, the Kekulé ordering is observed on the corresponding STM image, and a band gap Δ appears in the STS spectrum. Adapted from [61]

second-order transition.

However, although these theoretical works provide a route to the Kekulé distortion, there are two obstacles. First, in a real graphene sample, high biaxial strain may result in a mechanical failure below 16%, stemming from any kind of structural defect. This experiment would then require very high crystalline quality samples. Secondly, assuming a perfect graphene sheet, the strain-induced Kekulé distortion takes place as a preliminary step to the mechanical breaking of graphene in a tiny window of parameter [112, 130], making it potentially challenging to observe.

Investigating artificial graphene then appears as an alternative route, which has achieved success [61]. By arranging CO molecules on a Cu(111) surface, one can indeed artificially confine the electrons on a honeycomb lattice similar to graphene. More precisely, the negative potential of CO molecules act as repellents for the electrons of the Cu(111) surface state, which can be assumed to be two-dimensional electron gas. By achieving atomically precise positioning with an STM tip, the authors could realize and probe many exotic electronic phases, including Kekulé-distorted graphene, as illustrated on Figure 1.15. In particular, the $\left(\sqrt{3} \times \sqrt{3}\right)$ R30° modulation of electronic density is clearly visible on the constant-current STM image, and the associated band gap is observed in the STS spectrum.

Beside this work, there is little evidence of a Kekulé distortion in graphene. Other studies have provided examples of an apparent Kekulé order that should not be confused with the distortion itself. The theoretical proposal consists in depositing a low concentration of adatoms on pristine graphene, so they adopt adsorption sites following a Kekulé-like $\left(\sqrt{3}\times\sqrt{3}\right)$ R30° order [24, 25]. As the concentration is low, the ordering of the adatoms can easily go unnoticed, that is why it has been nicknamed the hidden Kekulé order.

Although this ordering has a symmetry similar to the Kekulé distortion, it has a distinct origin. Indeed, the Kekulé insulator is a graphene sheet that is globally distorted, which induces a hopping texture that reduces translational invariance, leading to the opening of a band gap. Depositing an adatom on graphene is different. Indeed, it does not reduce, but breaks translational invariance completely. In other words, while the Kekulé distortion could be handled with a few appropriate nesting vectors $\mathbf{q}$, broken translational invariance authorizes every possible $\mathbf{q}$ in the first Brillouin zone[15]. This means an incoming electron with wave vector $\mathbf{k}$ can be scattered to any state of same energy with wave vector $\mathbf{k}+\mathbf{q}$. For pristine graphene, only two states at K and K' happen to be available at the Fermi energy. As a result, in terms of Brillouin zone vectors, only $\mathbf{q}=0$ and $\mathbf{q}=\mathbf{\Gamma K}$ are possible. A local defect such as an adatom then causes a standing wave pattern of electronic density to form around it, whose periodicity is given by the possible $\mathbf{q}$ vectors. This standing wave pattern is called Friedel oscillations. Since $\mathbf{q}=0$ already corresponds to the modulation imposed by the graphene lattice, only $\mathbf{q}=\mathbf{\Gamma K}$ adds a new $\left(\sqrt{3}\times\sqrt{3}\right)$ R30° electronic modulation, identical to the Kekulé distortion periodicity, and visible in STM imaging of local defects [125, 177]. This electronic modulation surrounding the adatom promotes specific adsorption sites for other adatoms, even at a few nm of distance, so below a critical temperature, arranging of the adatoms following this so-called hidden Kekulé order occurs.

Once again, it should be emphasized this process has little to do with a Kekulé distortion. The Kekulé distortion corresponds to a phase transition of graphene towards an insulating phase with $\left(\sqrt{3}\times\sqrt{3}\right)$ R30° unit cell. On the contrary, here, adatoms arrange themselves along a $\left(\sqrt{3}\times\sqrt{3}\right)$ R30° pattern due to the electron density oscillations they create. This pattern of adatoms may in turn slightly distort the chemical bonds of graphene, but this distortion is not thermodynamically driven over the whole crystal like in the Peierls mechanism.

With this caveat clarified, it is worth noting this effect has been experimentally observed by STM [65]. In that study, graphene has been epitaxially grown on Cu(111) with a particular process resulting in a (1 × 1) relationship at the graphene-Cu interface. As for the deposited adatoms, they actually correspond to copper vacancies below the graphene sheet, therefore called "ghost adatoms". They appear as bright features on

---

[15] For broken translational invariance, the band folding picture would require to fold the complete band structure onto the Γ point, which simply means energy bands no longer exist.

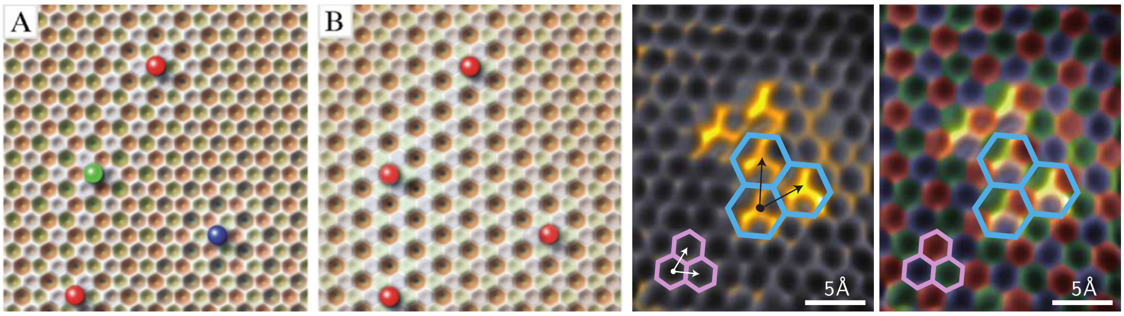

Figure 1.16: **Kekulé-like ordering of adsorbates on graphene.** Electronic potential landscape in graphene. (left) Each adatom creates a $\left(\sqrt{3}\times\sqrt{3}\right)$ R30° modulation around itself, which leads randomly placed adatoms (A) to occupy equivalent sites of a Kekulé order(B). Adapted from [24]. Such ordering is experimentally observed on STM images of substrate vacancies – appearing as bright features – below graphene grown Cu(111) (right). Adapted from [65]. On both panels, a red-green-blue tiling is overlaid to emphasize the Kekulé-like ordering.

STM images, and their position can be identified with atomic resolution. As illustrated on Figure 1.16, these vacancies tend to order along the Kekulé-like $\left(\sqrt{3}\times\sqrt{3}\right)$ R30° pattern.

In the previous situation, an apparent Kekulé order can be observed because of adatom-induced intervalley scattering. A similar result can be obtained when relying on phonon-induced intervalley scattering. To couple the K and K' points of the band structure, a phonon at the K point is then necessary. Besides, this phonon needs to display a sufficiently large electron-phonon coupling constant in order to provide an efficient scattering channel. In graphene, both conditions are fulfilled by the TO phonon with A_1' symmetry at K point.[16] Its coupling to graphene electrons is first going to be justified in the context of Kohn anomaly, and then its influences on the electronic bands will be discussed.

In the Born-Oppenheimer approximation, electrons and phonons are considered separately, assuming their time constants differ significantly. In other words, the atoms vibrate in a quasi-static manner, so they are slow enough for the electronic properties to evolve at equilibrium. When this approximation is not valid, electrons and phonons interact, and in the case considered here, this manifests itself in two ways.

On the one hand, as explained earlier, electrons influence the phonon properties through a Kohn anomaly [99]. In graphene, only phonons with $\mathbf{q} = 0$ and $\mathbf{q} = \mathbf{\Gamma K}$ can display a Kohn anomaly, which is indeed the case of the LO phonon at Γ and of the TO phonon at K [165], as visible on Figure 1.17 (left).[17] The observation of this anomaly

---

[16] Without any surprise, the very same phonon has been introduced earlier as the soft mode involved in the biaxial strain-induced Kekulé transition. Indeed, the requirements to trigger a Kekulé transition are the same: a phonon at K so as to couple the two valleys, and a large electron-phonon coupling.

[17] In Raman spectroscopy, the TO phonon gives rise to both so-called D and $2D$ peaks. The dip

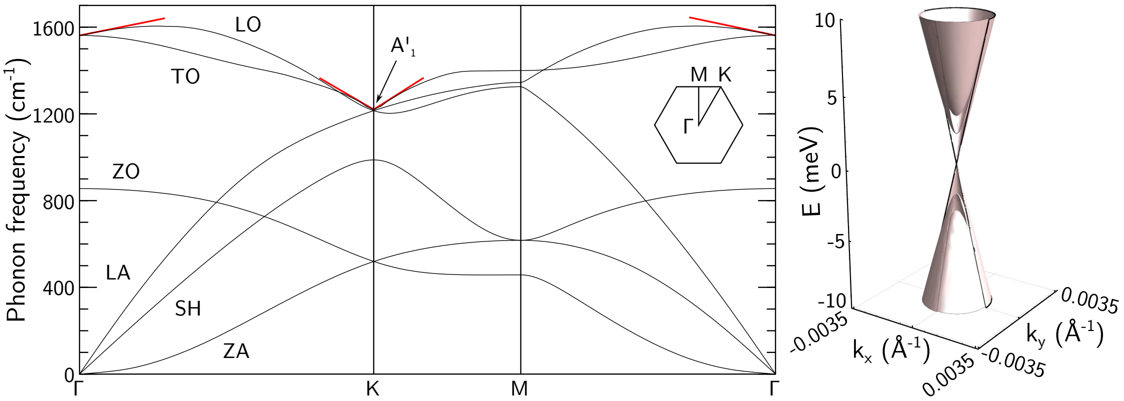

Figure 1.17: **Electron-phonon interaction in graphene. Left:** Phonon dispersion in graphene. A Kohn anomaly gives rise to a dip in the dispersion of the LO phonon at Γ and TO phonon at K, as emphasized with red lines. Adapted from [204]. **Right:** in return, the intervalley scattering promoted by the TO phonon at K induces a small band gap (< 10 meV) in the band structure of graphene. Adapted from [89].

is the direct proof of a non-negligible electron-phonon coupling for these phonons. As a side note, although electron-phonon coupling lowers the energy of the phonon, it is not sufficient to make it a soft mode as earlier considered.

On the other hand, the TO phonon at K point provides a scattering channel for electrons between K and K' points. In order to account for it, a model with both the electrons and phonons has to be formulated. This has stimulated theoretical work, which has predicted the opening of a dynamical band gap at K and K' points of < 10 meV, either in a tight-binding approach [178], or with a Fröhlich type hamiltonian [89], as pictured on Figure 1.17 (right).

As a conclusion, pristine graphene provides a remarkable system, whose conical bands at Fermi energy give rise to electronic excitations to some extent analogous to Dirac-Weyl particles. When graphene is supported by a substrate, the pictures provided by the Semenoff and Kekulé insulators justify a gap opening at the Fermi energy, either due to inversion symmetry or translational symmetry breaking. Two issues naturally arise from those considerations. First, one may wonder whether such simple pictures grasp the properties of supported graphene samples observed in experiments. Second, symmetry breaking and phase transitions appear as key-concepts with far-reaching consequences on supported graphene systems. Determining these consequences is the second issue at stake in this thesis.

---

induced by the Kohn anomaly is responsible for their high dispersion versus laser wavelength. Combined with their resonant Raman activation process [204], this dispersion has made the D and $2D$ peaks in carbon-based materials a 20-year old puzzle in Raman spectra.

Chapter 2

Moiré superlattices and topological defects in graphene

In the previous Chapter, the influence of a substrate on the electronic properties of graphene has been taken into account with model systems, where this influence translates as an additional term in the hamiltonian. These models have now to be compared with more realistic situations. In particular, the structure of graphene on a periodic substrate is known to give rise to a moiré superlattice, whose structural features will be discussed first.

Next, the impact of the substrate on the electronic properties is going to be discussed, and the concept of Semenoff and Kekulé insulators will prove useful under certain hypotheses. In particular, these insulators can display topological defects, which dominate their electronic properties, and which relate to topological defects in their atomic structure.

This link will then raise the issue of the possible structural phases for supported graphene, which will be presented in the framework of the Frenkel-Kontorova model. Describing these phases and their dynamics will require to introduce a few concepts about phase transitions and symmetry breaking. Finally, a few systems where these tools may apply will be briefly reviewed.

2.1 Structure of graphene moiré superlattices

When supported by a substrate, graphene has a crystallographic structure that generally does not match exactly that of its substrate.[1] The superposition of the two lattices then leads to a long wavelength beating phenomenon called a moiré superlattice. From a structural point of view, a moiré superlattice has two distinctive features: a large unit cell with typical periodicity from $\sim$ 1 to $\sim$ 15 nm (so-called superperiodicity), and within this unit cell, a varying local stacking of graphene onto its substrate.

As a starting point, the moiré superperiodicity and its origin can be considered through two simple situations:

- On the one hand, graphene and its substrate have their atomic rows aligned, but do not share the same lattice parameter $a_{gr} \neq a_s$. The moiré superperiodicity is then defined by the integer number i of graphene cells that match the integer number m of substrate cells. In this case, graphene is to some extent strained to match

---

[1] Exact matching is very rare, and earlier mentioned graphene on Ni(111) is one of the very few examples.

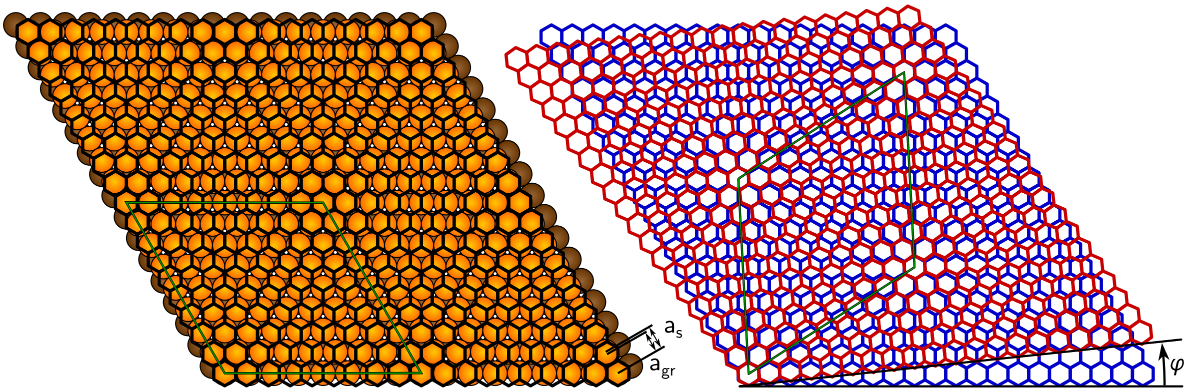

Figure 2.1: **Graphene moiré superlattice.** A moiré is a beating phenomenon emerging from the superposition of two mismatched lattices, and giving rise to a large superperiodicity (green rhombi). **Left:** the mismatch can be due to different lattice parameters for graphene (a_{gr}) and its substrate (a_s), as often attributed to graphene on a metal. **Right:** it can also be related to a twist angle φ, which is typical of twisted graphene bilayers.

its substrate with commensurate $ia_{gr} = ma_s$. This situation is usually assigned to the most commonly observed phases of graphene on metallic surfaces, such as Ir(111) [31], Ru(0001) [129], Rh(111) [214] or Re(0001) [193], and is sketched on Fig. 2.1 (left).

- On the other hand, graphene has the same lattice parameter as its substrate, but is twisted with respect to it by an angle φ. This second situation is typical of graphene bilayers, either stacked artificially, or formed naturally at the surface of highly oriented pyrolytic graphite (HOPG) or SiC(000$\bar{1}$) (C-face SiC). It is represented on Fig. 2.1 (right).

Although these simple situations help to distinguish two possible origins of a moiré superlattice in graphene, they are actually neither exclusive, nor exhaustive. Both twisted and strained graphene has indeed been observed for instance on Ru(0001) [12] and Ir(111) [10]. In the latter case, an additional shear strain contribution could also be evidenced, thereby showing the two pictures of Fig. 2.1 are not exhaustive. A systematic analysis method able to quantify all these different contributions will be presented in Chapter 4.

Beside a moiré superperiodicity, graphene has periodically varying stacking configurations with its substrate within the moiré unit cell [5, 47, 173, 191, 217], as detailed on Fig. 2.2. This stacking configuration determines how much graphene tends to bind to its substrate.

For graphene on a metal, out-of-plane bonds are favoured for sites on top of a metal atom (later on referred to as "top"), where the overlap between the π orbital of graphene and the d orbital of the underlying metal atom is maximum. On the contrary, carbon

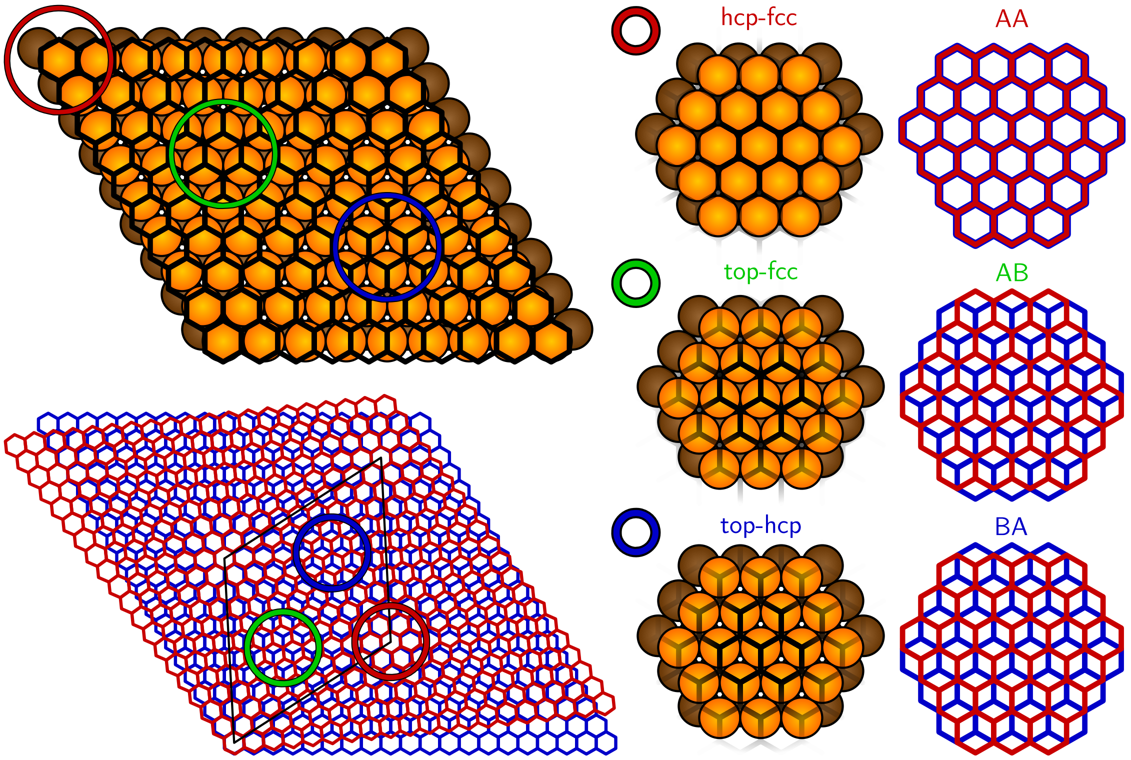

Figure 2.2: **Varying stacking within a moiré unit cell. Left:** Coloured circles emphasize different typical stacking configurations of graphene on its substrate. **Middle:** for graphene on a metal, they correspond to hcp-fcc (red), top-fcc (green) and top-hcp (blue) stackings. **Right:** Respectively, for a twisted graphene bilayer, they correspond to AA (red), AB (green) and BA (blue) stackings.

atoms are more decoupled from their substrate on hollow sites, as no metal atoms lies underneath them. Two inequivalent hollow sites exist, depending on the presence (hcp) or absence (fcc) of a metal atom from the second topmost layer below it. As a result, when graphene lies on a metallic substrate, its atoms adopt successively hcp-fcc, top-fcc and top-hcp local stackings, as drawn on Fig. 2.2. Similarly, for graphene lying on a honeycomb substrate such as another layer of graphene or hexagonal boron nitride (h-BN), one can define AA, AB and BA local stackings, also drawn on Fig. 2.2.

Beyond this exclusively structural description, the chemical and electronic properties of graphene can be dramatically affected by the moiré superlattice, and as a result modify its structure in return. Two extreme regimes can be considered depending on the coupling between graphene and its substrate:

- Some substrates show only a weak interaction dominated by van der Waals (vdW) forces, such as graphene on h-BN [36] or multilayer graphene on the C-face of SiC [70]. In this case, the graphene-substrate distance is of the order of 3.4 Å

[68,70], very close to the value 3.3539 Å in HOPG [97], and graphene's electronic properties are mostly preserved [68,155].

- Other surfaces interact more strongly with graphene, and are prone to exchange electrons with it, establishing partially covalent bonds. Graphene-substrate bonding then implies both vdW forces (physisorption) and partial covalent bonds (chemisorption), and is modulated along the moiré superperiodicity [13, 18, 55, 185, 193]. Graphene is thus nanorippled with short graphene-substrate distances where the tendency to covalent bonding is more prominent. Nanorippling amplitudes varying from 0.03 (on Pt(111) [196]) to 1.6 Å (on Re(0001) [193]) have been reported depending on the strength of the graphene-substrate coupling [191]. For all those metals, the moiré modulation of graphene's electronic properties goes along with a modulation of its chemical reactivity, inducing preferential sites for adsorption or functionalization. This renders possible to use moiré superlattices as a template for self-organized arrays of metallic clusters [37, 147] or molecules [220,230].

As a first comment, one should be aware of the simplification performed here. Indeed, instead of two extreme categories, there is rather a continuum of graphene systems with a varying degree of graphene-substrate interaction, and each with specific properties.

Secondly, with these concepts in mind, one may wonder how the electronic and chemical properties relate to the structure of the graphene-substrate system. There is no simple one-to-one correspondence between the weak and strong coupling systems presented above, and the two structural situations for moiré superlattices detailed earlier. There is rather a complex interplay between structural and electronic/chemical properties. The intrinsic properties of the substrate such as its band structure and its electronic surface state favour a specific stacking for graphene. And at the same time, the local lattice mismatch, twist angle and distance between graphene and its substrate influence its tendency for physisorption or chemisorption. These mutually influencing factors result in competing phases in the course of graphene growth, whose understanding requires to consider graphene and its substrate as a single system. Density functional theory (DFT) calculations then appear as an appropriate tool, but the large moiré unit cells make them demanding in terms of computing time. Another approach consists in defining empirical interatomic potentials that match typical results obtained by DFT, and to use them in more complex situations. Both these methods will be reviewed in Chapter 3, and used in the case of graphene on Re(0001) in Chapters 4 and 5.

2.2 Electronic properties of graphene moiré superlattices

In the current section, a more simple approach is going to be examined to discuss how moiré superlattices impact graphene's electronic properties. To start with, the electronic coupling between graphene and its substrate will be presented, so as to justify the simple

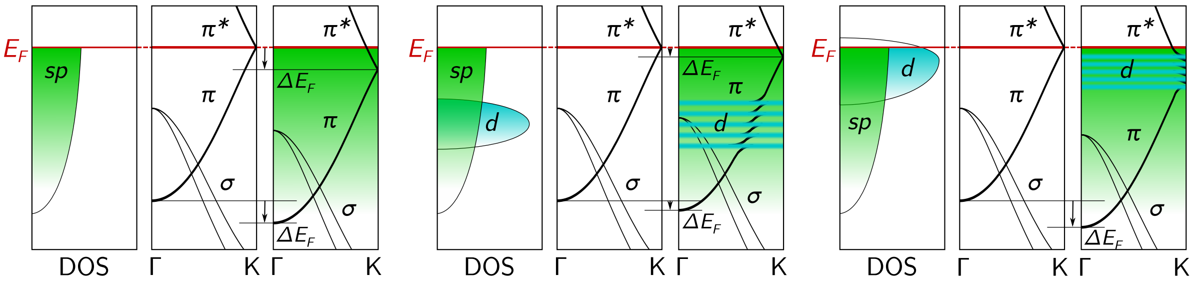

Figure 2.3: **Hybridization gap opening.** Band structure schemes illustrating the electronic effect of the chemical bonds between graphene and its substrate. **Left:** for graphene on a *sp*-metal like Al(111), there is only a Fermi level shift ΔE_F, visible because of both the Dirac point and the π band bottom positions. **Middle:** when lying on a weakly interacting *d*-metal such as Au(111), hybridization gaps open at the intersection of *d*-bands with graphene π band, well below the Dirac cone. The Dirac cone is then preserved, and the Fermi level shift ΔE_F is generally small. **Right:** for graphene on a strongly interacting *d*-metal like Re(0001), hybridization gaps open at the Dirac cone and a large Fermi level shift ΔE_F is observed. Adapted from [206].

classification of either weak or strong coupling substrates. For weak coupling substrates, all the effects of the substrate have energy scales much smaller than the typical energy scale of electrons in graphene, i.e. the hopping amplitude $t \sim 2.7$ eV defined earlier. For instance, electron transfer from/to the substrate will be considered small, so the Fermi level in graphene lies close to the Dirac cones, whose curvature can also be neglected. More generally, the substrate will act as a perturbation, which can be analysed in terms of the Semenoff and Kekulé masses presented earlier.

In that context, the two structural features presented above are going to be reviewed successively:

- The moiré superperiodicity, which is going to be treated with a band folding model, similarly to the Kekulé distortion,
- The varying local stacking within the moiré unit cell, which results in a spatially modulated Semenoff mass.

In this second situation, topological defects host important signatures in the electronic properties. To get a better grasp of the mathematical objects at stake, solitons in polyacetylene will be briefly discussed.

2.2.1 Hybridization gaps and charge transfer

Hybridization gaps

As a starting point, the chemical bonds formed between graphene and its substrate directly alter graphene's electronic properties. This is revealed by the hybridization gaps that open where their respective electronic bands intersect. Besides, the energy

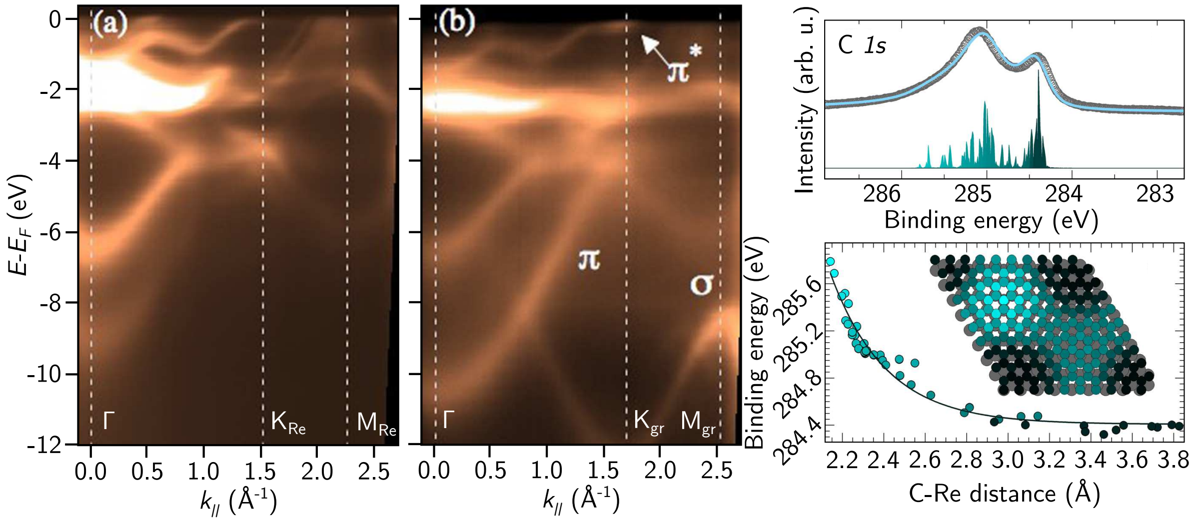

Figure 2.4: **Band structure of graphene on Re(0001).** **Left** ARPES data of a Re(0001) single crystal. Re $5d$ bands extend mainly from $E - E_F = 0$ to -2.5 eV. **Middle:** When graphene is grown on Re(0001), they hybridize to the π band of graphene, disrupting the linear dispersion of its Dirac cone at the K point. The bottom of the π band at Γ lies at $E - E_F = -10.6$ eV, which is 2.9 eV below its value for pristine graphene. Adapted from [158]. **Right:** XPS spectrum of carbon $1s$ core-level of graphene on Re(0001) (top), revealing two main contributions actually originating from the continuum of carbon atoms with varying C-Re distance (bottom). Adapted from [142].

at which these hybridization gaps open determines how strong graphene couples to its substrate. If they open close to the Fermi level, graphene is strongly bound to its substrate and its Dirac cones are disrupted. Alternatively, when the hybridization gaps have a higher binding energy, graphene-substrate coupling is weak, and the Dirac cones are marginally altered. This is illustrated in the case of graphene on a d-metal on Fig. 2.3, and offers more generally a convenient classification for supported graphene systems.

In real space, this electronic coupling corresponds to the chemical bonds, that is to the overlap of graphene's π and π^* orbitals with the substrate electronic states. For graphene on a metal, such overlap gives rise to hybridized bonding and anti-bonding states with partially π and d characters. For bilayer graphene or graphene on h-BN, this overlap is smaller and occurs in between π orbitals, so it is referred to as π-stacking.

In this respect, Re(0001), Au(111), and h-BN as substrates for graphene are going to be presented as illustrations of different coupling regimes.

Graphene on Re(0001)

First, Re(0001) is a $5d$-metal whose electronic configuration is $[\mathrm{Xe}](4f)^{14}(6s)^2(5d)^5$. Due to this half-filled $5d$ shell, $5d$ bands lie in its band structure at energies ranging from $E - E_F = 0$ to -2.5 eV, as presented on Fig. 2.4 (left). They can then be expected to open hybridization gaps with graphene at the Fermi level. Instead of a Dirac cone, angle-resolved photoemission spectroscopy (ARPES) indeed shows that graphene displays a parabolic π band with maximum at $E - E_F = -3.9$ eV [158], as displayed on Fig. 2.4 (middle). Additionally, the position of the bottom of the π band of graphene at the Γ point is $E - E_F = -10.6$ eV indicating the Fermi level is 2.9 eV above what would be the Dirac point in the absence of the Re $5d$ bands. This means graphene on Re(0001) is heavily n-doped.[2]

This strong $\pi - d$ hybridization and charge transfer are consistent with DFT calculations, which predict graphene is corrugated by 1.6 Åat the moiré scale, with hcp-fcc regions with large graphene-Re distance ($\sim$ 3.9 Å) and top-hollow regions with short graphene-Re distance ($\sim$ 2.3 Å) [142,193]. In the latter, $\pi - d$ hybridization is maximum, due to the large overlap of graphene and Re orbitals. These DFT results are justified by STM measurements, which indeed observe a large corrugation at the moiré scale, with marked electronic effects at the atomic scale, which are reported in [193], and will also be detailed in Chapter 4. Furthermore, the varying C-Re chemical interaction results in a dispersive signature in X-ray photoemission spectroscopy (XPS) [142,143]. As plotted on Fig. 2.4, carbon atoms close to the Re surface have their $1s$ core level shifted to 285.6 eV, while those further apart have a $1s$ core level around 284.4 eV [142], close to the value of 284.5 eV obtained for HOPG.

In short, both electronic and structural features indicate Re(0001) is a substrate that binds strongly to graphene, disrupting its electronic properties, as illustrated on the right panel of Fig. 2.3. As such, one could even say it is the epitome of strong graphene-substrate interaction, but other metals display similar features, such as Ru(0001) [189] or Rh(111) [207].

Graphene on Au(111)

Now turning to weakly interacting metallic substrates, many examples have been reported such as Ir(111) [166], Pt(111) [222], Cu(111) [212], Al(111) [208], Ag(111) [98] or Au(111) [218]. The weakest known interaction with graphene is achieved by Au(111), which can be considered as the opposite of Re(0001). Indeed, its electronic configuration is $[\mathrm{Xe}](4f)^{14}(6s)^1(5d)^{10}$, so contrary to Re, it has a filled $5d$ shell. Consistently, ARPES data reveal its $5d$ electronic bands lie at binding energies between 3 and 6.5 eV, as visible on Fig. 2.5 (left). As a consequence, hybridization gaps open in the band structure of graphene well below its Dirac cone, as measured by ARPES [127,128,183], an example

---

[2] Intercalation of a Ag monolayer proves to effectively decouple graphene from Re(0001), as Ag has d bands extending from $E - E_F \sim -4$ to -7 eV. Graphene's Dirac cone is then restored, but with the Fermi level 0.4 eV above the Dirac point, and with a $\sim$ 0.45 eV band gap. Consistently, DFT calculations estimate a graphene-Ag distance close to 3.5 Å [158].

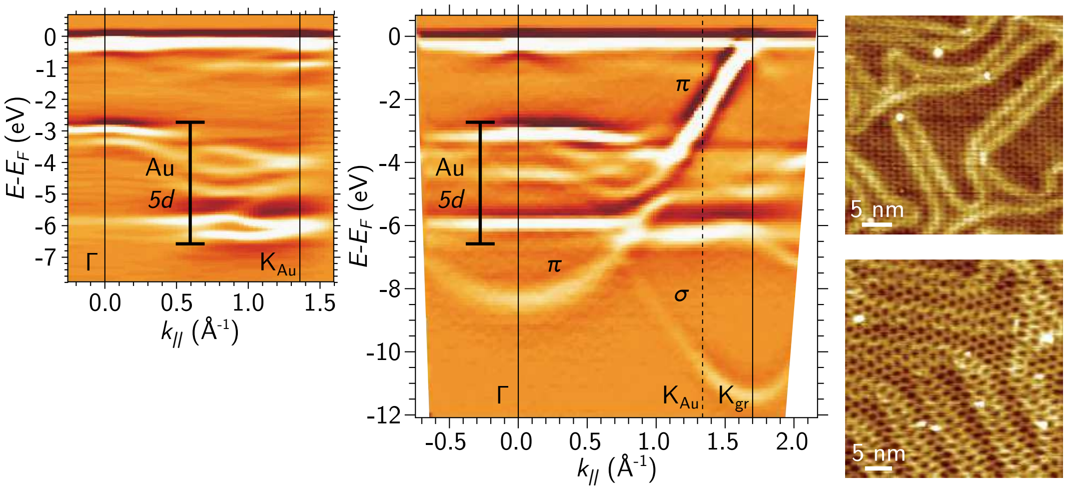

Figure 2.5: **Band structure of graphene on Au(111). Left and middle** ARPES data of a Au(111) overlayer on a Ni(111)/W(110) thin film and of a Au-intercalated graphene over Ni(111)/W(110) thin film, displayed with identical scales for comparison. Hybridization gaps open at the intersection of the $5d$ bands of Au with the π band of graphene at energies around $E - E_F$ from -6.5 to -3.5 eV, while the Dirac cone at K is visible with marginal doping. Adapted from [183]. **Right:** STM topographs of graphene grown by PVD on Au(111), revealing the coexistence of the Au(111) herringbone reconstruction with moiré superlattices. The angles between graphene $[11\bar{2}0]$ and Au$[1\bar{1}0]$ directions is respectively 11° (top) and 0° (bottom). Adapted from [150].

of which is displayed on Fig. 2.5 (middle). The high binding energies at which $\pi - d$ hybridization occurs are reminiscent of the middle situation pictured on Fig. 2.3.

When considering the charge transfer between graphene and its Au(111) substrate, different values have been reported depending on sample preparation. In this regard, graphene can be prepared on Au(111) by three main methods:

- By intercalation of evaporated Au atoms under graphene grown beforehand on a strongly interacting metal, such as Ni(111) [127, 183, 202] or Ru(0001) [44]. Graphene on Au(111) then inherits the alignment of graphene with Ni(111) or Ru(0001), giving rise to the so-called $R0$ phase. All reported samples of this sort display a small p-doping of 0.1 eV [44, 202].
- By intercalation of evaporated Au atoms under graphene prepared on Si-face SiC [56, 128]. In that case however, the resulting graphene is rotated by 30° with respect to Au(111), in a so-called $R30$ phase [56]. Besides, the charge transfer with graphene depends critically on the amount of intercalated Au, varying from strong n-doping of -0.85 eV for sub-monolayer Au, to slight p-doping of 0.1 eV for a complete monolayer.[3]

---

[3] DFT calculations attribute this behaviour to a significant variation of in-plane strain in graphene upon intercalation of Au [29]. Nevertheless, this scenario needs to be clarified, as it does not discuss the

- By evaporation of atomic carbon directly on a Au(111) single crystal (physical vapour deposition, PVD) [150, 218]. This method forms mainly the $R0$ phase, alongside with a non-negligible fraction of $R30$ phase [218]. Other rotated phases have also been locally identified by STM [150], as exemplified on Fig. 2.5 (right). It is worth noting the simultaneous observation of moiré superlattices emerging from the superposition of graphene onto its Au(111) substrate, with the herringbone reconstruction of Au(111). It translates the very weak influence that graphene has on the surface structure of Au(111), giving a higher bound to the graphene-metal interaction energy of 13 meV/C atom. As for the charge transfer, ARPES data reveal a p-doping level of 0.1 eV, consistent with samples prepared with other techniques.

As a side note, graphene cannot be grown by conventional chemical vapour deposition (CVD) on Au(111), due to its limited chemical reactivity. Still, a modified CVD growth using ionized fragments of ethylene has been developed to form graphene on Au(111), leading to various coexisting orientations [132].

In all cases, the high binding energy of hybridization gaps and the weak charge transfer from graphene to Au(111) translate a remarkably good decoupling of graphene's Dirac cones from the influence of its substrate.

Graphene on h-BN

Finally, h-BN can be considered as a reference for even weaker coupling. Its electronic band structure is that of a Semenoff insulator, which means it is identical to graphene's, except for a large band gap at the Fermi level, and for a Brillouin zone rescaling due to their 1.8 % lattice parameter difference. Consequently, one can expect graphene and h-BN bands to almost superimpose, except in the large band gap of h-BN, where graphene should have a pristine-like isolated Dirac cone.

Probing the band structure of graphene on h-BN experimentally with ARPES requires large area samples, which rules out heterostructures prepared by transfer techniques [36]. Therefore, graphene has to be grown on h-BN prepared beforehand on thin films [197] or single crystals such as Cu(111) [176]. In both cases, d bands arising from the metallic substrate are visible, but the Au(111) and Cu(111) substrates used have a filled d-shell, and h-BN acts as a buffer layer, leading to a very weak $\pi - d$ hybridization. As a consequence, the conical dispersion of the π band of graphene is observed with no band gap, as shown on Fig. 2.6. In the first presented work [197], intercalation of a Au(111) monolayer between h-BN and its Ni(111) substrate achieves very good electronic decoupling, so the Dirac point of graphene is found at the Fermi level within experimental uncertainty. For graphene prepared on h-BN/Cu(111) [176], a Fermi level

---

non-uniform morphology of partially intercalated graphene on SiC revealed by STM studies [145, 169], nor the critical impact of the graphene-Au distance on the charge transfer [179]. Finally, STM analysis of graphene on Au(111) moiré superlattices identify very weak strain in graphene [150], questioning the relevance of these calculations. Without any structural detail on the morphology of the graphene-Au interface of these strongly n-doped graphene samples, finding a convincing explanation for this behaviour might remain speculative.

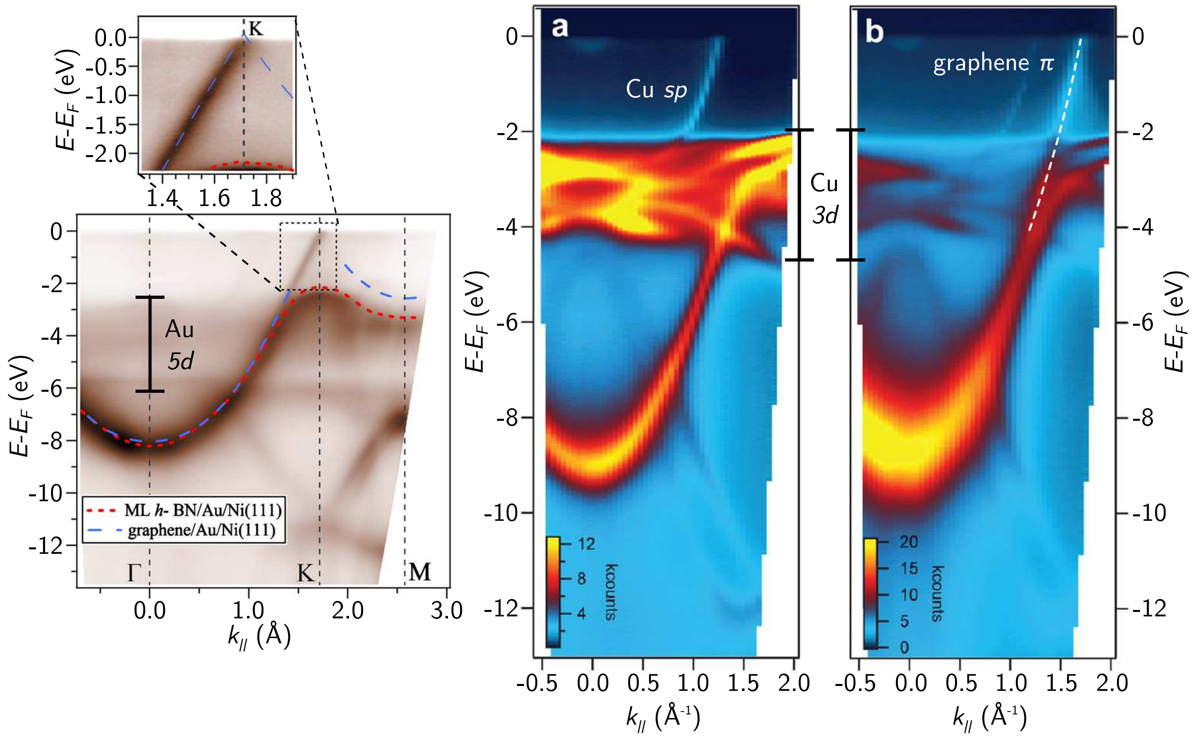

Figure 2.6: **Band structure of graphene on h-BN. Left:** ARPES data of a graphene/h-BN/Au(111)/Ni(111)/W(110) thin film taken along the ΓK and KM directions. The π band of h-BN is identified by a red dashed line, and the inset reveals the linear dispersion of the graphene π band, with undetectable doping or band gap. Adapted from [197]. **Middle and right:** ARPES data of h-BN/Cu(111) and graphene/h-BN/Cu(111) single crystal taken along the ΓK direction. The linear π band of graphene is identified (white dashed line) with its Dirac point 0.25 eV below the Fermi level. Adapted from [176].

shift $\Delta E_F = -0.25$ eV is observed, indicating a slight n-doping of graphene, lower than the $\Delta E_F = -0.38$ eV measured for graphene on Cu(111) [62].

In summary, these results show a weak graphene-h-BN hybridization, consistent with the large 3.3 Ådistance measured by high-resolution transmission electron microscopy (HRTEM) [68].

These three examples provide insight on how much the electronic bands of the substrate can alter the electronic properties of graphene. In the particular case of graphene on Re(0001), none of the Dirac properties of graphene can be expected unless it is intercalated with another weakly interacting material.[4] For this reason, strongly interacting substrates such as Re(0001) on which graphene is chemisorbed will be momentarily set

---

[4] The study of the intercalation of Au under graphene on Re(0001) has been performed in the course of this Ph.D., but will not presented.

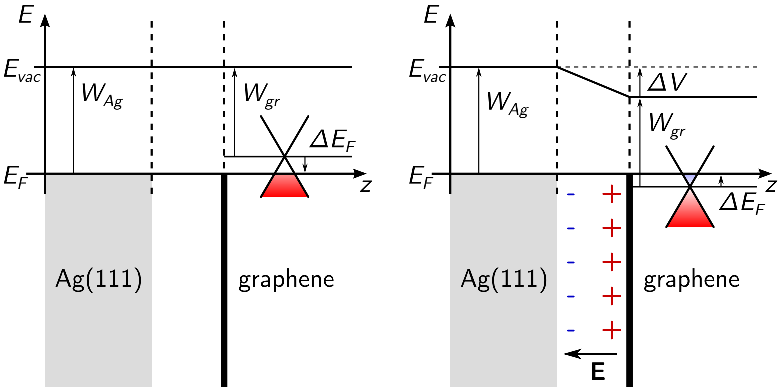

Figure 2.7: **Phenomenological capacitor model.** In the limit of weak graphene-substrate coupling, the charge transfer is accounted for by an effective plane capacitor. A voltage difference is generated by the different work functions of graphene W_{gr} and its metallic substrate W_{m}. **Left:** for graphene on Ag(111), this effect should lower the Fermi level in graphene and p-dope it. **Right:** additionally, both the charge density difference in graphene and the metal and their chemical interaction create an electric dipole field $\mathbf{E}$ at the interface. This field lowers the vacuum level E_{vac} with a voltage drop ΔV, favouring electron transfer to graphene. For graphene on Ag(111), this contribution outweighs the work function difference, so graphene is actually n-doped. Adapted from [57].

aside in the following.

Charge transfer in the capacitor model

In this limit, graphene is physisorbed on its substrate, which influences its Dirac cone only through charge transfer. This charge transfer can be deduced using a phenomenological capacitor model, where graphene and its substrate act as two plane electrodes [57, 94]. The voltage difference between them sets the position of the Fermi level E_{F} in graphene, which indicates the charge transfer.

Two terms contribute to the voltage difference between graphene and its metallic substrate. The first one is intuitive, and corresponds to the work function difference between graphene W_{gr} and the metal W_{m}. The work function is the energy required to extract an electron from the surface of a material and bring it to a vacuum state at rest. If $W_{\text{m}} > W_{\text{gr}}$, one would indeed expect electrons to rather populate the metal, where it is more difficult to extract them. As a result, the electronic states of graphene are depleted, and the Fermi level in graphene is lowered down to the point where it matches the Fermi level in the metal. In other words, the work function mismatch between graphene and the metal is corrected by rigidly shifting the bands of graphene so as to make them match. This situation is schematically presented on Fig. 2.7 (left).

This naive interpretation actually neglects the second term in the voltage difference: the voltage drop ΔV at the interface due to charge reordering. Indeed, in the intuitive

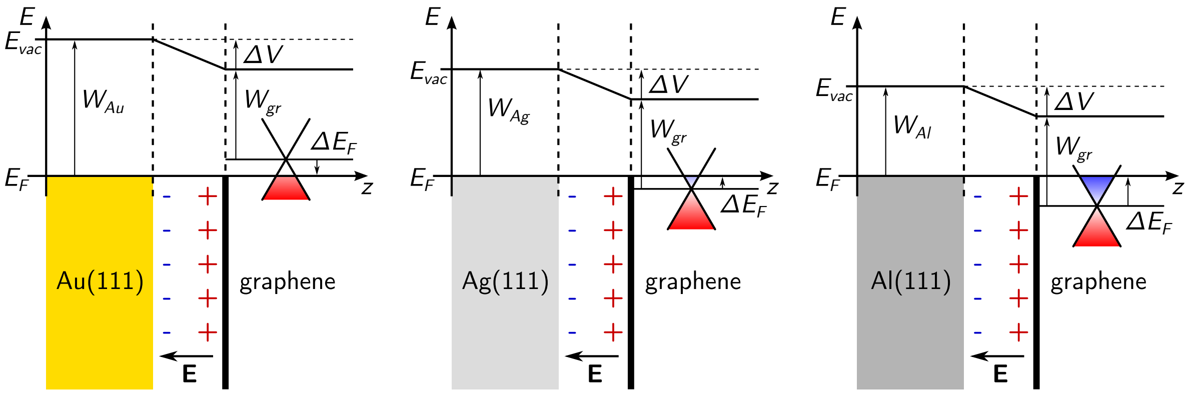

Figure 2.8: **Competition between work function difference and interface electric dipole.** Depending on the metallic substrate work function W_m and on the induced voltage drop ΔV, graphene is either n or p-doped. **Left:** for Au(111), the large work function W_Au compensates the electric dipole field at the graphene-metal interface, so graphene is p-doped. **Middle:** for Ag(111), this electric field outweighs the work function $W_\mathrm{Ag} > W_\mathrm{gr}$, leading to n-doping of graphene. **Right:** for Al(111), both the work function difference $W_\mathrm{Al} - W_\mathrm{gr}$ and the interface electric dipole induce electron transfer towards graphene. Adapted from [57].

picture described above, the Fermi level in graphene is merely adjusted to make work functions match. This implies that covering a metal with graphene does not change its work function at all. However, two major effects contradict this, and are encoded in $\Delta V = \Delta_\mathrm{tr} + \Delta_\mathrm{c}$.

On the one hand, due to the charge transfer driven by the work function difference, graphene and its substrate carry different charge densities. This creates a capacitive coupling between graphene and its metallic substrate. Like in a capacitor, graphene and its substrate are then two charged electrodes creating an electric dipole field which renormalizes the work functions. This effect is taken into account by the Δ_tr term in ΔV.

On the other hand, beyond purely electrostatic effects, graphene and its substrate also interact chemically, through the overlap of π and d orbitals. This adds a chemical contribution to the interface electric dipole field, included in the Δ_c term.[5] For a graphene-metal distance of 3.3 Å, typical of weakly interacting metals, $\Delta_\mathrm{c} \sim 0.9$ eV, therefore lowering the vacuum level of graphene, and favouring electron transfer towards graphene.

Taking both the work function difference and the interface electric dipole field into account, charge transfer at the interface can be deduced, as depicted on Fig. 2.7 (right) for graphene on Ag(111). In that case, $W_\mathrm{Ag} = 4.92$ eV $> W_\mathrm{gr} = 4.48$ eV, which

---

[5] In [57, 94], Δ_tr is truly modelled by an effective capacitor, whose charge corresponds to the charge transferred from/to graphene. Yet, Δ_c is fitted with DFT calculations to a phenomenological function that vanishes exponentially at large graphene-metal distance. Remarkably, this function weakly depends on the considered metal, making the model versatile.

means it is easier to extract electrons from graphene, so p-doping of graphene is naively expectable. Nevertheless, due to the interface electric dipole field, graphene is actually n-doped.

This competition gives rise to three possible situations illustrated on Fig. 2.8:

- $W_{\mathrm{m}} > W_{\mathrm{gr}} + \Delta V$: the work function of the metal is so large that it compensates for the electric field at the interface, leading to p-doped graphene. This corresponds to graphene on Au(111).
- $W_{\mathrm{gr}} < W_{\mathrm{m}} < W_{\mathrm{gr}} + \Delta V$: the work function of the metal is larger than that of graphene, but is outweighed when the interface electric field is accounted for, leading to n-doped graphene. This corresponds to graphene on Ag(111).
- $W_{\mathrm{m}} < W_{\mathrm{gr}} < W_{\mathrm{gr}} + \Delta V$: the work function difference already favours n-doping of graphene, and is further favoured by the interface dipole field. This corresponds to graphene on Al(111).

As a final comment, it should be reminded this model is valid for physisorbed graphene. That means the band structure of graphene is conical with a negligible band gap. Strongly interacting substrates that open hybridization gaps at the Dirac cones should thus not be considered.

Beyond hybridizations gaps and charge transfer, a substrate also modifies graphene due to the moiré superperiodicity and the varying local stacking it adopts with graphene, as detailed earlier. In the following sections, the influence of these features around the Dirac cone is going to be considered. There too, the implications will not apply to strongly interacting substrates.

2.2.2 Superlattice-induced secondary Dirac cones

As shown earlier, a moiré superlattice has a superperiodicity comprising a large number of graphene unit cells. In reciprocal space, this corresponds to wave vectors $(\mathbf{k_{m_1}}, \mathbf{k_{m_2}})$ smaller than those of graphene, and defining the reduced Brillouin zone. In the context of superlattices, this reduced Brillouin zone is also called "mini-Brillouin zone". When studying graphene, the mini-Brillouin is often conventionally defined such that its center Γ_m matches the original Dirac cone lying at K [154].

The slightest imaginable influence of the superlattice consists in a smooth periodic superpotential, which reduces the translational invariance of graphene but preserves chirality.[6] As a consequence, in the reduced zone scheme, graphene's band structure is folded back into the mini-Brillouin zone defined by $(\mathbf{k_{m_1}}, \mathbf{k_{m_2}})$. When displaying it in

---

[6] In the framework of the low-energy effective hamiltonian of graphene, it expresses as an additional $V(\mathbf{r})\,\sigma_0\tau_0$ superpotential term. This means it acts the same way on both sub-lattices and on both valleys, with the reduced translational invariance encoded in the periodicity of the $V(\mathbf{r})$ function. Hence, it trivially commutes with the hamiltonian, so it reduces translational invariance while preserving chirality as a good quantum number. On the contrary, the Kekulé term considered before also breaks chirality by explicitly connecting the K and K' valleys.

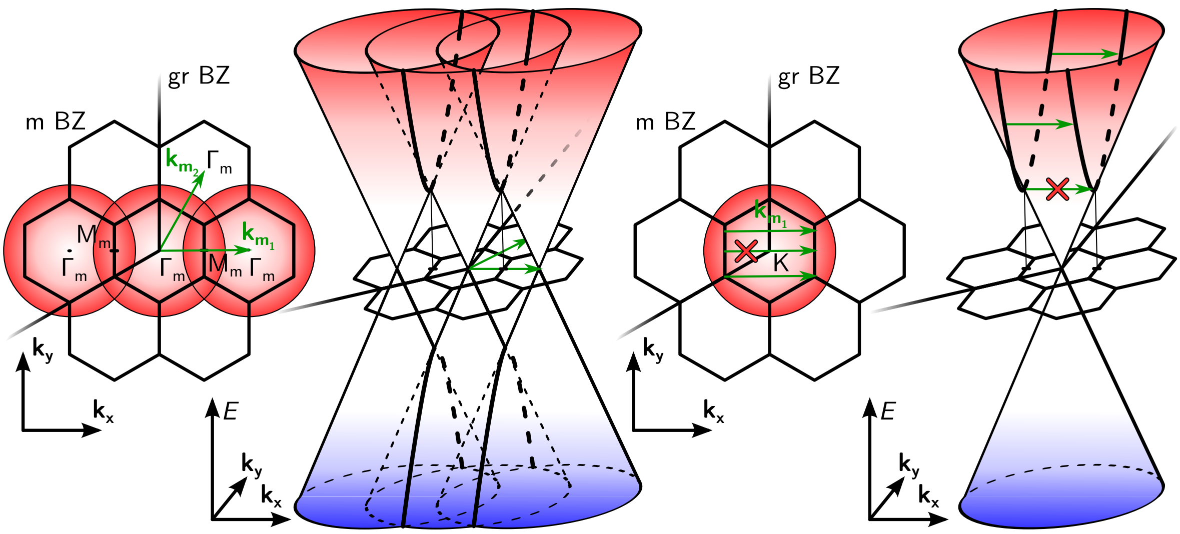

Figure 2.9: **Superlattice-induced secondary Dirac cones in graphene.** In both schemes, the band structure is plotted both in a 2D view from above, and in a 3D view. **Left:** in the repeated zone scheme, the original graphene Dirac cone is replicated in adjacent mini-Brillouin zones at the Γ_m points. A band gap opens at the intersection between the original and the replica Dirac cones (thick black lines), except for states with opposite chiralities, i.e. at M_m and M'_m points. **Right:** in the extended zone scheme, nesting vectors associated to the moiré superperiodicity hybridize states from the Dirac cone, except in between M_m and M'_m points.

the repeated zone scheme, new so-called replica Dirac cones lie at $\pm\mathbf{k_m}$ from the original Dirac cone. Equivalently, the $\mathbf{k_m}$ wave vectors of the superpotential can be interpreted as nesting vectors within the band structure of graphene displayed in the extended zone scheme. Both situations are schematically represented on Fig. 2.9.

As an analogy to the Kekulé distortion, the reduced translational invariance should also open a band gap all along the mini-Brillouin zone edge. In the repeated zone scheme, the Dirac cone indeed intersects its replicas along this edge. Likewise, nesting vectors in the extended zone scheme connect the corresponding electronic states to each other.

However, the preserved chirality of electrons forbids electronic states with opposite wave vectors $\mathbf{q}$ and $-\mathbf{q}$ to hybridize to each other. In other words, states lying at opposite sides of the Dirac cone cannot hybridize to each other. When considering which points of the Dirac cones are connected by the superpotential, it appears only the M_m points of the mini-Brillouin zone are concerned, as sketched on Fig. 2.9. In other words, at the M_m points, no band gap opens, and the electronic bands locally have a conical shape. New so-called secondary Dirac cones are said to be generated at these points [159, 160].[7] It is also worth noting that contrary to the replica Dirac cones, the

---

[7] The appearance of new Dirac cones at the M_m points may appear counter-intuitive. Indeed, the M points of hexagonal systems are time-reversal invariant momenta (TRIM), where no Dirac cone can be

secondary Dirac cones lie at energies $\frac{1}{2}\hbar v_F \left|\mathbf{k_m}\right|$ above and below the Dirac energy.

In short, like the Kekulé distortion, a moiré superpotential breaks translational invariance, which can be accounted for in a band folding model or with nesting vectors. However, the simple model presented here neglects many aspects of a moiré superlattice, so chirality is preserved. Specific points of the graphene band structure are thus protected from a gap opening, giving rise to secondary Dirac cones. Many additional features could be added, some of which open a gap at these new Dirac cones, or move them to K_m points [211]. Among those features, graphene's stacking onto its substrate is now going to be introduced.

2.2.3 Mini-gaps due to inversion symmetry breaking

The second structural feature of a moiré superlattice is the varying local stacking of graphene onto its substrate. While the moiré superlattice acts as a long wavelength superpotential acting smoothly over a large number of carbon atoms, the local stacking has an influence at the atomic scale, within the graphene unit cell. This length scale difference will now be shown to hold different signatures in the electronic properties.

Electrons in graphene are sensitive to the substrate electronic potential, which is directly related to the substrate atomic structure. Therefore, one has to consider the detailed stacking configuration. In the previous section, typical adsorption sites for honeycomb (A and B) and triangular (top, hcp and fcc) substrates have been introduced, and the latter is going to be considered here as an example.

The difference between top, hcp and fcc sites is crucial. On a top site, the overlap between the π orbital of graphene and the d orbital of the underlying metal atom is maximal, while it is less for hcp or fcc sites. Hence, the top sites are where the $\pi - d$ hybridization takes place. For weakly interacting substrates at stake here, $\pi - d$ hybridization does not affect the Dirac cone. Still, from the perspective of the capacitor model, the larger overlap between π and d orbitals means a local electric dipole of higher magnitude, so a larger charge transfer. The charge transfer is thus higher on a top site than on a hollow hcp or fcc site. As a result, the stacking of graphene results in a modulation of the chemical potential of each carbon atom depending on its adsorption site.

Any given stacking of graphene on a triangular substrate breaks inversion symmetry like in a Semenoff insulator. As an example, when graphene lies on a metallic substrate with a top-hcp stacking, the atoms of the A sub-lattice are on a top site, while those of the B sub-lattice adopt a hcp hollow site. The staggered electron transfer on each sub-lattice alters their respective chemical potential as in a Semenoff insulator. Consequently, a gap opens at the Dirac energy and chirality is no longer a good quantum

---

expected [58]. Nevertheless, the M_m points at stake here are those of the conventional mini-Brillouin zone, so they do not need to be TRIM. Moreover, depending on the superpotential term $V(\mathbf{r})$, the position of the secondary Dirac cones is predicted at the M_m or K_m points [211].

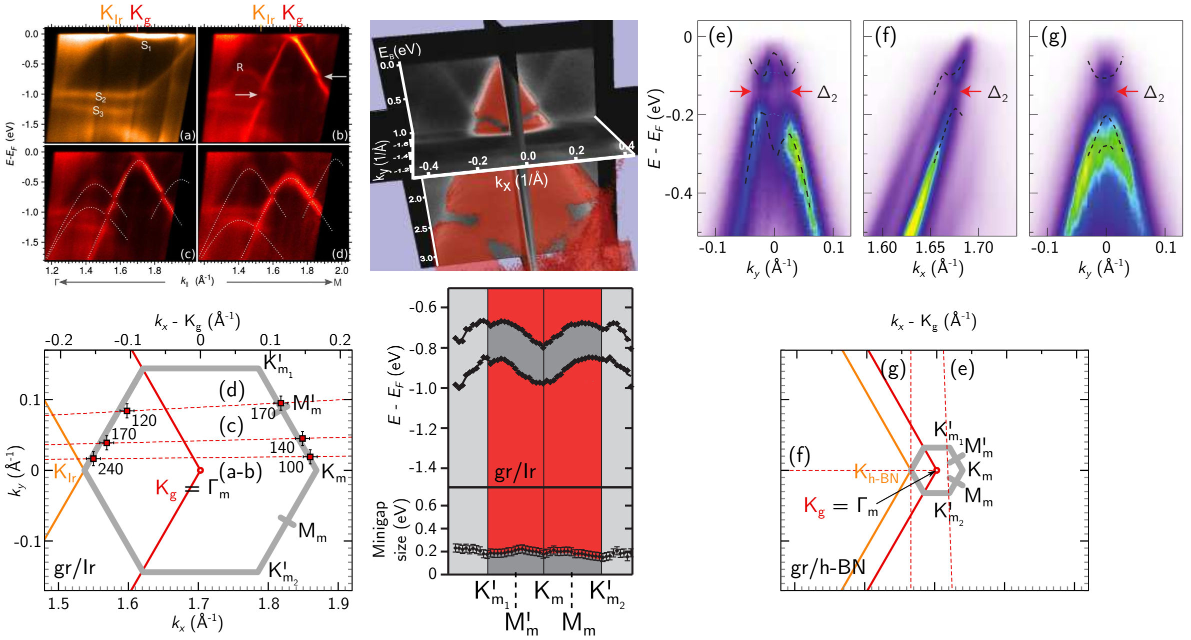

Figure 2.10: **ARPES-measured mini-gaps at the secondary Dirac cones in graphene. Left:** ARPES data of clean Ir(111) (a) and gr/Ir (b,c,d) along different azimuths defined on the lower panel. K points of Ir and graphene are marked as K_{Ir} and K_g, respectively. S1 – S3 are Ir surface states, while R is a replica Dirac cone. Horizontal arrows denote the mini-gap. The dashed lines are tight-binding-approximation-calculated bands for Dirac cones. Adapted from [166]. **Middle:** Tomographic view of the gr/Ir band structure around K. The lower panel shows the mini-gap dispersion and size along the mini-Brillouin zone edge. Adapted from [184]. **Right:** ARPES data of gr/h-BN through the secondary Dirac cones along different directions indicated on the lower panel. Black dashed lines indicate the fitted band dispersion. Horizontal arrows denote the mini-gaps. Adapted from [216].

number.

As a consequence, so-called mini-gaps also open at the secondary Dirac cones. This is consistent with ARPES data taken on graphene supported by weakly-interacting substrates, such as Ir(111) [104, 166, 184, 198] or h-BN [216], as shown on Fig. 2.10. In both cases, a band gap opens along the edge of the mini-Brillouin zone, with no secondary Dirac cone.

In the case of a moiré superlattice, the local stacking varies continuously over the moiré unit cell. This means the inversion symmetry breaking imposed by the substrate is modulated at the moiré scale, or equivalently that the Semenoff mass follows the moiré superperiodicity. One can then model how graphene's local stacking impacts its electronic properties with a spatially-dependent Semenoff mass field. This Semenoff mass field is periodic in the case of a moiré superlattice, but can have a more complex

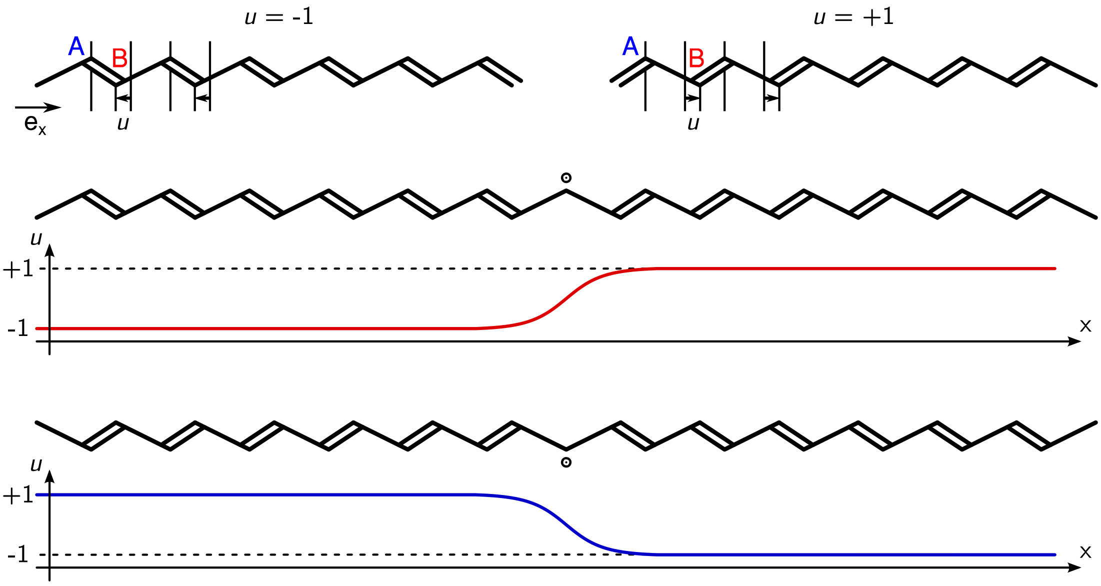

Figure 2.11: **Soliton in Peierls-distorted polyacetylene. Top:** polyacetylene can be dimerized in two equivalent ways, associated with their uniform displacement fields $u = \pm 1$, which constitute degenerate stable vacua. **Middle and bottom:** two soliton solutions called kink and antikink are also possible, and connect respectively the boundary conditions $u(-\infty) = -1$ and $u(+\infty) = +1$ (middle), and $u(-\infty) = +1$ and $u(+\infty) = -1$ (bottom).

dependence. In particular, while areas with non-zero Semenoff mass hold an insulating behaviour, places where it changes sign need to be metallic [22, 181]. Such places actually correspond to topological defects called solitons. The concepts of soliton and topological defect will also prove necessary to understand some structural aspects of supported graphene. They will be introduced formally in the next section, but in order to apprehend them, a simple analogous system already introduced before is now going to be reviewed: Peierls-distorted polyacetylene.

2.2.4 Solitons in polyacetylene

It has been discussed earlier that a trade-off between the electronic and elastic energies favours a spontaneous bond distortion in polyacetylene. This distortion consists in a dimerization: one bond out of two shortens while the other one stretches. However, there are two equivalent ways of performing this dimerization, as sketched on Fig. 2.11. From this picture, a continuous displacement field u can be defined considering the position of the B atoms with respect to their A counterparts. With this definition, the two degenerate distortions correspond to uniform displacement fields labelled $u = -1$ and $u = 1$. Since these fields are uniform, from the point of field theory, they can be interpreted as empty of any source term, and called stable vacua.

Beside these two degenerate vacua, two soliton solutions are also possible, when considering appropriate boundary conditions. By setting $u\,(-\infty) = -1$ and $u\,(+\infty) = +1$, a kink in the displacement field has to be added somewhere for these conditions to be matched. The associated solution is therefore simply called a kink. Similarly, an antikink results from the boundary conditions $u\,(-\infty) = +1$ and $u\,(+\infty) = -1$. The kink and antikink fields are shown on Fig. 2.11.

Three important comments have to be made about these additional solutions. First, to address their nature, one has to consider that contrary to the vacua fields, the kink and antikink fields both contain a singular source term.[8] It is visible either as a smooth jump in u, or as an unpaired electron on Fig. 2.11. It is quite intuitive such a singularity has an energetic cost. Still, the boundary conditions force its existence: this property is the hallmark of a soliton.

Secondly, when considering its properties, it is worth noting the unpaired electron associated with a soliton and the spin it carries can easily be moved along the chain. Since polyacetylene is insulating, the solitons are responsible for its charge and spin transport properties. Additionally, they are topological defects in the displacement field: they cannot be removed by a continuous transformation of the field. A way to visualize a continuous transformation is to consider the displacement field u. It consists in distorting the $u\,(x)$ curve without cutting it. No matter how it is distorted, the final $u\,(x)$ curve is always equivalent to the step-like kink on Fig. 2.11. In short, the properties of the solitons persist no matter what their detailed geometrical configuration is. This behaviour is related to topology, so the solitons of polyacetylene are also called topological defects.[9]

Thirdly, the topological solitons of polyacetylene have been predicted to carry a fractional charge $1/2$ [74]. They indeed correspond to stable excitations of a system with a broken symmetry [83] – here by the dimerization.

As a final comment, the topological solitons described here constitute the charge carriers in polyacetylene. When pristine, it is insulating because of the Peierls distortion. But doping polyacetylene leads to soliton formation, so its conductivity increases dramatically, as was measured in 1977 by Alan J. Heeger, Hideki Shirakawa, Alan G. MacDiarmid and co-authors [28]. The underlying mechanism was explained theoretically short after by the already mentioned SSH model [187, 188]. The outcome of this work is the Nobel prize in chemistry awarded to Heeger, Shirakawa, MacDiarmid in 2000 for opening the field of conductive polymers [74]. From a physicist point of view, their work provides a simple system whose properties are well accounted for by topology.

In summary, when supported by a substrate, graphene acquires additional structural features related to a moiré superlattice. For substrates such as Re(0001), these features come along a strong hybridization that disrupts its electronic properties. Other materials only give rise to a marginal charge transfer, so effects related to the moiré superlattice are

---

[8] This formulation in terms of fields containing source terms is usual in classical electrodynamics, where charges indeed act as singular source terms in the electromagnetic field.

[9] As a counter-example, a kink-antikink pair is not a topological defect, because when they are brought together, the kink and antikink annihilate each other and the displacement field is equivalent to a vacuum field.

observed, such as band folding and mini-gap openings. In particular, a moiré superlattice can be interpreted as periodically modulated Semenoff mass field. In analogy to the kink and antikink in polyacetylene, this interpretation raises a fundamental question: does supported graphene host topological solitons?

To formulate this question, the electronic properties of supported graphene have been understood based on its structural features: superperiodicity and local stackings. To elaborate an answer, it is then logical to address the issue of topology in the structural phases of supported graphene.

2.3 Structural phases of supported graphene

The topological solitons of polyacetylene bridge two degenerate vacua solutions of the Peierls distortion. They constitute a simple and illustrative example because two degenerate vacua is the smallest possible number of vacua to have solitons. Similarly, in order to determine the possible topological defects in supported graphene, it is necessary to enumerate its degenerate vacua. This may appear a complicated task, as graphene moiré superlattices have been showed to display an extensive variety of phases. With the motivation of simplifying this problem, the Frank and van der Merwe model and its application to supported graphene will be presented here.

2.3.1 Frank and van der Merwe model

Yakov Frenkel and Tatyana Kontorova are Soviet physicists who formulated a 1D model that accounts for dislocations in crystals, published in 1938 [51], and best-known as the Frenkel-Kontorova model. In 1949, this model has been extended by Frederick Charles Frank and Jan van der Merwe with an emphasis on crystal growth and epitaxy [49,50]. It provides a simple picture where the concepts introduced earlier of moiré superlattices and solitons find a natural framework. More recent reviews have since then reformulated this model [3], benefiting from discussions on the nature of the involved phase transitions. In the following, the Frank and van der Merwe model is going to be presented. Its solutions in the continuum approximation will be derived, in order to present the possible commensurate and incommensurate ground states. The commensurate-incommensurate transition will be addressed in particular.

Although supported graphene is a 2D problem, the more simple 1D picture as formulated by Frank and van der Merwe is going to be addressed for simplicity. As schematically drawn on Fig. 2.12, graphene then simplifies to a chain of atoms indexed by their position x_n and held together by harmonic springs, with spring constant μ. This harmonic chain imposes an interatomic distance a, and displacement from this value costs an elastic energy T. As for the substrate, it is considered infinitely rigid, and acts on the chain as a periodic potential energy landscape of amplitude $\frac{1}{2}V$, whose minima correspond to the stable adsorption configurations of the substrate. For simplicity, a

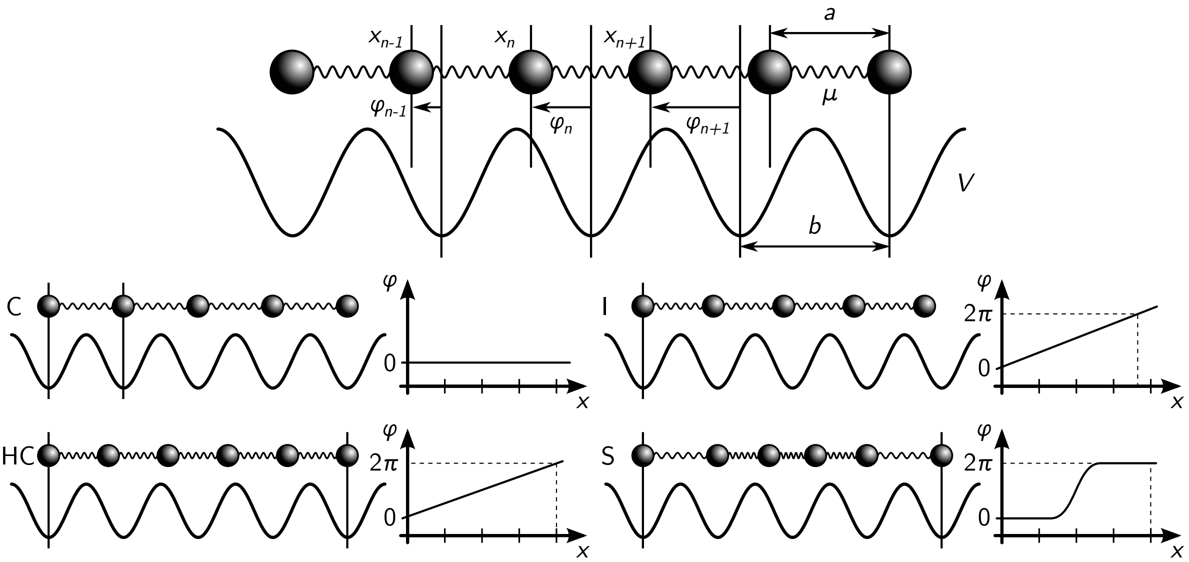

Figure 2.12: **Frank and van der Merwe model. Top:** the structure of an overlayer on a lattice-mismatched substrate is modelled by a 1D chain of atoms on a sinusoidal potential. The interatomic distance results from a competition between the harmonic springs (a) and the substrate potential (b). **Bottom:** this model gives rise to many possible phases, characterized by phase profiles in the continuum approximation: a strictly commensurate (C) phase where each potential minimum hosts a single atom ($a = b$), assuring translational invariance at every atom; a high order commensurate (HC) phase where translational invariance occurs every few atoms; an incommensurate (I) phase, where the lattice mismatch is such that no translational invariance ever occurs. In the soliton incommensurate phase (S), an average $^a/_b$ ratio can be made equal to the latter I phase.

harmonic potential will be considered.[10] The interatomic distance b imposed by the potential landscape is thus that of the substrate, and displacement from this value costs a potential energy U. Identifying the stable phase requires to find the positions x_i minimizing the total energy of the system:

$$H = T + U = \frac{\mu}{2}\sum_n (x_{n+1} - x_n - a)^2 + \frac{V}{2}\sum_n \left(1 - \cos\left(2\pi\frac{x_n}{b}\right)\right) \tag{2.1}$$

This model obviously features a competition between elastic and potential energies, each promoting a different lattice constant. One naturally expects the emergence of different phases depending on the lattice mismatch and ratio between elastic and potential energy. For a soft chain on a sharp potential, the potential energy term forces a lattice constant $a = b$, corresponding to a strictly commensurate (C) phase. If the chain is more rigid or the lattice mismatch larger, the commensurate matching occurs with a

---

[10] It can be considered as the first-order harmonic of the potential Fourier series.

larger unit cell such that $Ma = Nb$, with N and M two integers. The ratio $^{a}/_{b}$ then corresponds to a rational number $^{N}/_{M} \in \mathbb{Q}$, and this is called a high order commensurate (HC) phase. On the contrary, for very rigid interatomic bonds on a shallow substrate potential, the elastic energy term imposes a lattice constant a with no influence of the substrate. This situation shall be called an incommensurate (I) phase, as the ratio $^{a}/_{b}$ can take any value in $\mathbb{R}$. This latter phase may be considered as academic or naive. It is academic, because any real number can be considered rational with infinitely small error, so the slightest influence of a substrate could lock the chain to a sufficiently high order commensurate phase. On the other hand, it is naive, since one can imagine the ratio $^{a}/_{b}$ to be irrational only on average. The chain would then be composed of areas locked to a strictly commensurate relation to the substrate, and of other areas locally strained to relieve the elastic energy build-up. This last situation will be shown to be a soliton solution to the Frank and van der Merwe model, and will therefore be called soliton incommensurate (S). Those four phases are schematically drawn on Fig. 2.12 (bottom).

The simple model at stake holds some of them. This can be revealed by first rewriting the hamiltonian to make it dimensionless, introducing the so-called geometrical phase φ_n as $x_n = nb + \frac{b}{2\pi}\varphi_n$:

$$H = \frac{V}{2}\sum_n l^2\left(\varphi_{n+1} - \varphi_n - \delta\right)^2 + \left(1 - \cos\varphi_n\right) \tag{2.2}$$

where $\delta = 2\pi\frac{a-b}{b}$ is the mismatch between graphene and its substrate in units of phase, and $l = \frac{1}{2\pi}\sqrt{\frac{\mu b^2}{V}}$. For now, l corresponds to the ratio between elastic and potential energy, but it will prove to have additional significance. As for the geometrical phase φ_n, it translates as a phase the position of the carbon atom relative to the unit cell of substrate, as indicated on Fig. 2.12 (top). For the harmonic potential used here, the stable adsorption site corresponds to $\varphi_n = 0$, while the unstable site is $\varphi_n = \pi$. Minimization of the hamiltonian requires the condition $\frac{\partial H}{\partial \varphi_n} = 0$, which results in:

$$\varphi_{n+1} - 2\varphi_n + \varphi_{n-1} = \frac{1}{4l^2}\sin\varphi_n \tag{2.3}$$

Solutions of this equation can be built iteratively given a choice for φ_1 and l ($\varphi_0 = 0$ as a phase reference). Among them, the most obvious is given by setting $\varphi_1 = 0$, which results in a uniform vacuum solution $\varphi_n = 0$, where all atoms adopt the stable site of the substrate. This corresponds to the strictly commensurate (C) phase. In the context of epitaxy, a layer growing on its substrate with such strictly commensurate relation is called pseudomorphic.

2.3.2 Continuum limit: the Sine-Gordon equation

Finding analytical solutions of Equation (2.3) is very challenging in the discrete case, but it can be achieved easily in the continuum limit. Although convenient, the contin-

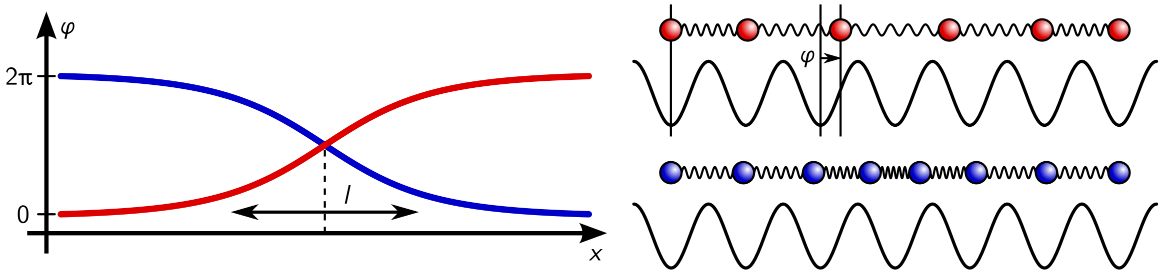

Figure 2.13: **Continuum kink and antikink solutions.** **Left:** the Sine-Gordon equation has a kink (red) and an antikink (blue) solutions. **Right:** they correspond to misfit dislocations, respectively adding or removing an atom to the chain.

uum limit is an approximation, which assumes the local variation of φ_n is slow enough to interpolate it with a continuous function $\varphi(x)$, with x an dimensionless space coordinate.[11] The above difference equation then becomes a differential equation, which is the time-independent version of the Sine-Gordon equation:

$$\frac{\mathrm{d}^2\varphi}{\mathrm{d}x^2} = \frac{1}{4l^2} \sin \varphi \tag{2.4}$$

Integration of the above equation yields:

$$\left(\frac{\mathrm{d}\varphi}{\mathrm{d}x}\right)^2 = \varepsilon^2 + \frac{1}{2l^2} (1 - \cos \varphi) \tag{2.5}$$

where ε is an integration constant corresponding to an additional phase modulation at $\varphi = 2k\pi$, $k \in \mathbb{Z}$. For simplicity, ε will be set to 0, which means wherever the atoms lie in the minima of the substrate potential ($\varphi = 2k\pi$, $k \in \mathbb{Z}$), there is no additional phase modulation ($\frac{d\varphi}{dx} = 0$). The corresponding solution will then have most of its atoms in the minima of the substrate potential. From the above equation, one gets:

$$\frac{\mathrm{d}\varphi}{\mathrm{d}x} = \pm\frac{1}{l} \sin \frac{\varphi}{2} \tag{2.6}$$

In the following, the ± sign is included inside l. This sign corresponds to positive or negative mismatch δ, *i.e.* to a chain with $a > b$ or $a < b$ respectively. This last equation can be integrated into the so-called misfit dislocation solution:

$$\varphi(x) = 4 \arctan \left(e^{x/2l}\right) \tag{2.7}$$

where the choice $\varphi(0) = \pi$ has been made for simplicity. This solution is plotted on Fig. 2.13 (left, in blue). As a first comment, it clearly reminds of the soliton solution seen for polyacetylene. It indeed corresponds to a solution joining the two degenerate

---

[11] In the continuum limit, abrupt variations of φ_n induced by sharp minima of the substrate potential are excluded. Such minima would lock the atoms to given positions and act as a pinning potential. This effect will be considered later in a different context.

vacua $\varphi(x) = 0$ and $\varphi(x) = 2\pi$. Besides, in this context, the term "soliton" also comes from the fact it is a non-dispersive solution of the non-linear Sine-Gordon equation (2.4).

When getting back to the atomic structure underlying this soliton, it corresponds to a misfit dislocation. In the solution (2.7), the $+2\pi$ jump between $-\inf$ and $+\inf$ indicates an atom is missing, as sketched on Fig. 2.13 (right, in blue). Depending on the sign of l, one atom is either added or removed, thus giving rise to a kink or an antikink.

Furthermore, the parameter l finds a new meaning here. Its definition sets it as the ratio between elastic and potential energies. In Equation (2.7), it also sets the width of the soliton. Indeed, if $l \ll 1$, it is favourable to put as many atoms in the substrate potential minima as possible, resulting in a soliton in the shape of a sharp step. Alternatively, when $l \gg 1$, the atomic chain rigidity forces a smooth evolution of φ, resulting in a soliton with a large width.

As a final remark about this solution, a lattice of such kinks or antikinks is possible (by setting $\varepsilon \neq 0$ [50]). For a lattice of well separated kinks, the solution with a single kink derived here is a suitable approximation. These kink and antikink lattices are solutions corresponding to a chain where the lattice mismatch induces respectively compressive or tensile strain, and introduced earlier as the soliton incommensurate phase and drawn on Fig. 2.14. One may wonder what difference lies between this kind of incommensurate phase and a commensurate phase of sufficiently order to hold the same strain. A first answer is now going to be provided by investigating the transition between a commensurate and an incommensurate phase. A complementary answer will be provided on thermodynamic grounds in the next section.

2.3.3 Commensurate-incommensurate transition

This question motivates the determination of the critical values of l and δ inducing the transition between the strictly commensurate phase and this incommensurate phase. In this regard, it is worth noting that the differentiation leading to the Sine-Gordon equation (2.4) removes all reference to the mismatch δ. Determining critical parameters for the transition then requires to get back to the total energy (2.2). From it, the force exerted by the springs on the atoms is derived as:

$$F = \mu\left(x_{n+1} - x_n - a\right) = \frac{\mu b}{2\pi}\left(\varphi_{n+1} - \varphi_n - \delta\right) = 2\pi\frac{Vl^2}{b}\left(\frac{\mathrm{d}\varphi}{\mathrm{d}x} - \delta\right)$$

Using Equation (2.6), one gets:

$$F = 2\pi\frac{Vl^2}{b}\left(\frac{1}{l}\sin\frac{\varphi}{2} - \delta\right) \tag{2.8}$$

From this, the energy required to add a misfit dislocation can be deduced as:

$$W = \int_0^{2\pi} F\mathrm{d}\varphi = \frac{2\pi l^2 V}{b}\int_0^{2\pi}\left(\frac{1}{l}\sin\frac{\varphi}{2} - \delta\right)\mathrm{d}\varphi = \frac{8\pi l^2 V}{b}\left(\frac{1}{l} - \frac{\pi\delta}{2}\right)$$

Misfit dislocations are added to a strictly commensurate phase if $W \leqslant 0$, which is achieved when l is in absolute value larger than a critical l_c given by the misfit δ.

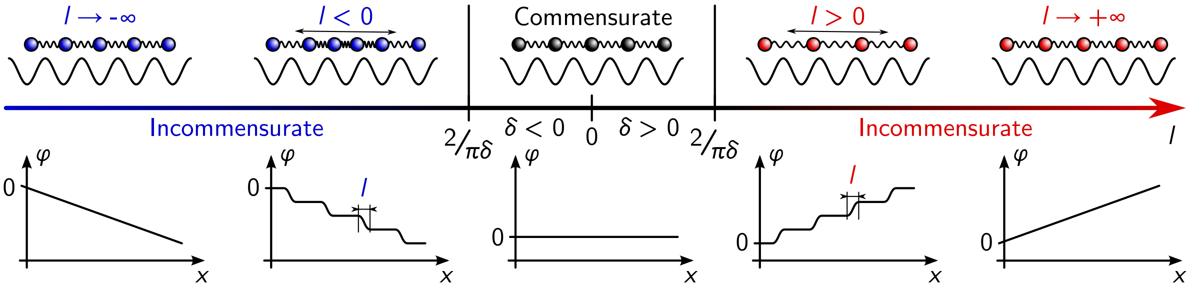

Figure 2.14: **Phase diagram of the 1D atomic chain.** For a given mismatch δ, depending on the energy ratio l, the atomic chain undergoes a commensurate-incommensurate transition, as schematically indicated with either a drawing (top) or a phase plot (bottom). **Left and right:** for $|l| > \left|\frac{2}{\pi\delta}\right|$, the elastic energy overcomes the potential energy, so an incommensurate lattice of solitons is favoured. **Middle:** for $|l| < \left|\frac{2}{\pi\delta}\right|$, the substrate potential forces the atoms to sit on its minima, leading to a strictly commensurate phase.

Alternatively, the transition to an incommensurate phase occurs as soon as the misfit δ gets larger than δ_c given by l, as:

$$l_c = \frac{2}{\pi\delta} \text{ and } \delta_c = \frac{2}{\pi l} \tag{2.9}$$

The Frank and van der Merwe 1D model gives therefore a qualitative description of the system. The competition at stake between the elastic and potential energies is quantified by the value of l. Depending on its value with respect to $\frac{2}{\pi\delta}$, the competition results in two possible regimes: either a strictly commensurate phase, or an incommensurate phase comprising a lattice of solitons of width l. This situation is schematically presented on Fig. 2.14. For small enough $|l|$, the system lies in the stability domain of the commensurate phase, and it turns into an incommensurate phase when $|l| > |l_c|$. It can be noted that for an infinite $|l|$ (respectively an infinitely small substrate potential), all solitons of the lattice overlap each other, and the naive incommensurate phase is recovered. Hereafter, no distinction will be made between this naive incommensurate (I) and the soliton incommensurate (S) phases.

To assess whether the commensurate-incommensurate transition is continuous or not, the continuity of the soliton density at the transition should be assessed. It is rather straightforward that the soliton density equals the average mismatch $\bar{\delta} = 2\pi\frac{\bar{a}-b}{b}$, with $\bar{a}$ the average lattice parameter of the chain. One can also get an intuitive idea of its evolution with respect to δ. Indeed, for $\delta < \delta_c$, no soliton is found, so $\bar{\delta} = 0$. As for the situation of very large δ, it is equivalent to very large l. As pictured on Fig. 2.14, one then expects $\bar{a} = a$, so $\bar{\delta} = \delta$. The exact evolution between the two is continuous and plotted on Fig. 2.15 (left).[12]

---

[12] The proof is quite simple, and requires to solve Equation (2.5) for any value of ε, as performed in [50].

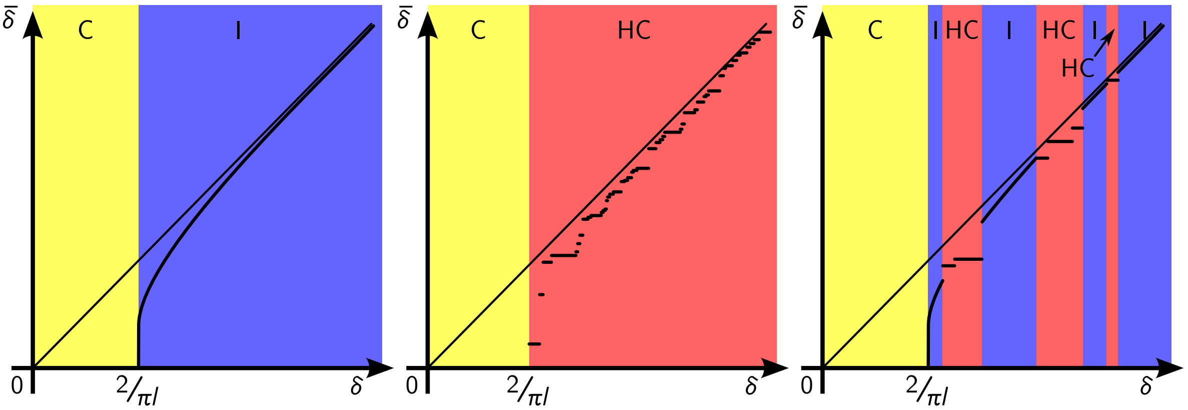

Figure 2.15: **Dynamics of commensurate and incommensurate lattices.** Beyond the commensurate-incommensurate transition, three typical situations depict the evolution of the soliton density $\bar{\delta}$ under the change of an external parameter, chosen to be the mismatch δ. **Left:** for an incommensurate (I) phase, no locking ever occurs, so its is also called a floating phase. **Middle:** transitions through an infinite number of high order commensurate (HC) phases leads to a quasi-continuous evolution of $\bar{\delta}$ called the devil's staircase. **Right:** a behaviour alternating between these two situations is referred to as the incomplete devil's staircase.

Although simple, this model contains the single necessary physical concept to anticipate the commensurate-incommensurate transition: the competition between two energy scales and their associated length scales.[13]

It could be argued, however, that high order commensurate phases are not accounted for. In this perspective, the smooth variation of $\bar{\delta}$ on Fig. 2.15 (left) translates the independence of the chain from the substrate potential, as it does not lock on any high order commensurate. Based on this independence, the incommensurate phase is also called the floating phase.

The Frank and van der Merwe model can actually be adapted by replacing the strict commensurate relation $b = a$ with any higher order relation $Nb = Ma$ [3]. The associated calculation can be found in [192], and results in a condition on l and δ similar to Equation (2.9). It defines a stability domain for the high order commensurate phase whose width is of the order of $\delta_{c,(M,N)} \sim \delta_c^{M/2}$.

One then expects the system to lock on successive high order commensurate phases. If l is small, the width of each stability domain is large enough, so the evolution $\bar{\delta}$ goes through a series of plateaus, as illustrated on Fig. 2.15 (middle). If the number of such plateaus is infinite, the evolution is an almost-continuous devil's staircase, in analogy to Cantor's function. For larger values of l, each stability domain shrinks, and their total sum is small enough to promote transitions through incommensurate phases. The

---

[13] A more complete discussion is provided in the original publication [49,50], as well as a generalization to two dimensions in a later work [200].

variation of $\bar{\delta}$ switches from a smooth evolution to discrete jumps, called an incomplete devil's staircase, as depicted on Fig. 2.15 (right).

Getting back to the question motivating this discussion, the difference between a high order commensurate phase and the floating incommensurate phase lies in their dynamics. Over a variation of an outside parameter, a floating phase adapts its average lattice parameter $\bar{a}$ continuously, whereas for a high order commensurate phase, $\bar{a}$ is locked to the commensurate relationship with the substrate. This key-difference has been used experimentally to investigate the transition between the two in the case of Kr atoms lying on Pt(111) [93].

In summary, the Frank and van der Merwe model provides a simple framework to overview the structural phases of supported graphene systems and their dynamics. It includes naturally the solitons to its phase diagram, which decomposes into two kinds of phases: commensurate (strictly or high order) and incommensurate. Transitions between these phases gives rise to smooth, discontinuous or almost-continuous evolutions, the latter of which corresponds to a fractal pattern analogous to a devil's staircase.

The classification between commensurate and incommensurate phases raises the issue of sorting the variety of supported graphene systems introduced earlier. As already mentioned, only graphene supporting on Ni(111) unambiguously matches a strictly commensurate phase. On the other hand, the very large majority of systems displaying moiré superlattices may either be sufficiently high order commensurate phases, or incommensurate lattices of solitons.

To elaborate further, a deeper understanding of phase transitions, and in particular of the commensurate-incommensurate transition is necessary. Besides, determining whether supported graphene can host topological defects with peculiar properties also requires the introduction of these notions, which are now going to be addressed.

2.4 Phase transitions and topological defects

So far, a 2D material supported by a substrate has been described using an intuitive model that resorts to classical mechanics. Although simple, this model enables to anticipate the more modern concept of phase transition. In the following, the early theories proposed by Ehrenfest and Landau will first be briefly reminded. From that, more attention will be devoted to the concept of order parameter, which will prove useful to introduce topological defects. A few examples will be given, in particular of topological defects in graphene and supported graphene systems. Finally, to get more insight on the incommensurate phase and the phase transitions occurring in 2D, the so-called Berezinskii-Kosterlitz-Thouless transition and Hohenberg-Mermin-Wagner theorem will be presented.

2.4.1 Classification of phase transitions

A phase transition of a system is the abrupt change of its state and properties upon the continuous variation of an outside parameter. Many examples correspond to this description: the freezing of water below 0°C at ambient pressure, displacive transitions in crystals upon application of pressure, or the suppression of the superconducting state by a sufficiently large magnetic field. This concept is ubiquitous in physics, and a large variety of phase transitions exist, thus calling for a classification.

One of the earliest classifications was formulated by Paul Ehrenfest in 1933, and relies on thermodynamic grounds. As the system at equilibrium undergoes a phase transition, its thermodynamic potential evolves continuously, but one of its derivatives is discontinuous. The order of the phase transition is then given by the lowest derivative of the thermodynamic potential that is discontinuous at the transition. As an example, the transition from a liquid to a gas can be shown to be of first order. Its elementary change of Gibbs free enthalpy G upon variation of temperature T and pressure p states as:

$$\mathrm{d}G = -S\mathrm{d}T + V\mathrm{d}p$$

with S and V the entropy and molar volume, respectively. This relation is valid for both phases labelled A and B, and in particular along the transition line in a (p, T) diagram, one has $dG_A = dG_B$. This translates into the Clapeyron relation:

$$\left(\frac{\mathrm{d}p}{\mathrm{d}T}\right)_{\text{transition}} = \frac{S_B - S_A}{V_B - V_A} = \frac{L}{T}\,\frac{1}{\Delta V}$$

where $L = T\Delta S$ is the latent heat at the phase transition. It translates a discontinuity both in S and in V, which are first derivatives of G. This is therefore a first-order transition.

The Ehrenfest classification has been introduced only to illustrate that multiple classifications of phase transitions exist. The most relevant to the problem exposed here has been proposed by Lev Landau in 1937, and is based on symmetry groups. Each phase of a system has a symmetry group, which contains all the symmetry operations that leave the system invariant. These symmetry operations are translations, rotations, space inversion, time reversal, etc.

For a phase transition between two phases A and B, their symmetry groups Γ_A and Γ_B are most likely different. The Landau theory applies in the case when Γ_B is a subgroup of Γ_A (or vice-versa). This means the B phase is less symmetric, and needs more variables than the A phase to be fully described. This additional information is stored inside the so-called order parameter. For symmetry reasons, the order parameter equals zero in the high symmetry phase (A), and is non-zero in the low symmetry phase (B).[14]

---

[14] This needs not be the case. For the liquid-gas transition mentioned earlier, both phases have the same symmetries. Moreover, a phase transition can occur between two crystalline phases where no

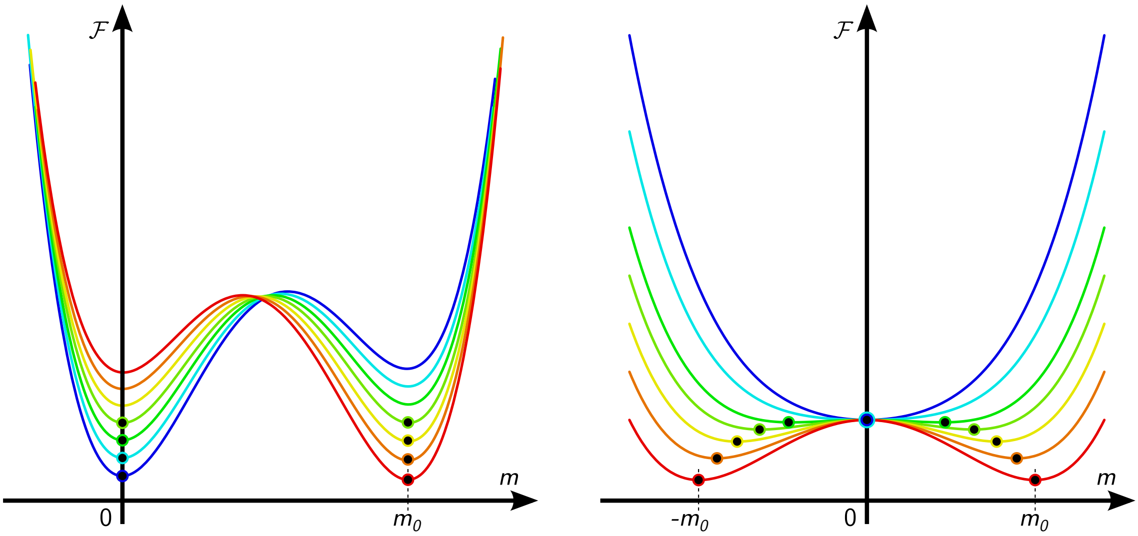

Figure 2.16: **First and second order transitions.** The free energy density functional $\mathcal{F}$ is expanded with respect to the order parameter m close to the transition. Each curve corresponds to $\mathcal{F}$ at a given value of the parameter driving the transition (from blue to red). The stable configuration is given by the minimum of $\mathcal{F}$ (identified by a circled black dot) and determines the value of m. **Left:** when m is discontinuous from 0 to m_0, the transition is of first order. **Right:** when m is continuous at the transition, the transition is of second order.

A simple example is the transition of a crystal like α-iron from a paramagnetic to a ferromagnetic state. In the paramagnetic state, because the nuclear magnetic moments are randomly distributed, all the directions of space are equivalent. Below the Curie temperature, magnetic moments align, so iron spontaneously magnetizes. A specific direction of magnetization $\mathbf{M}$ is chosen by the system, so the equivalence of all directions is lifted. In this example, it is intuitive that by lowering the temperature, the rotation symmetry has been broken, and the additional information needed to describe the system is encoded in the magnetization direction. Magnetization appears therefore as a suitable order parameter.

This example illustrates the meaning of the term "order parameter". Indeed, the lower symmetry phase is the ferromagnetic state, as the rotational symmetry is broken, but it is also an ordered phase. Indeed, the existence of a global magnetization emerges from the ordering of the individual magnetic moments at a local scale. The order parameter thus translates the degree of order that arises in the system.

The concept of order parameter is central to the Landau classification. Phase transitions are indeed sorted depending on the continuity of the order parameter at the

---

symmetry group is the subgroup of the other. In both situations, there is no order parameter associated with the phase transition.

transition. If the order parameter m jumps abruptly from 0 to a finite value m_0, the transition is of first order. On the contrary, if m grows gradually from 0 to m_0, it is of second order. Second order transitions are also referred to as continuous. Both situations are schematically represented on Fig. 2.16.

The Landau theory actually goes beyond this classification. The equilibrium state of a system indeed corresponds to the minimum of its free energy F in phase space. Close to the phase transition, the dependence of F with respect to the order parameter m must then be of importance. Following this, Landau's idea consists in defining a free energy density functional $\mathcal{F}$ that depends on the order parameter configuration $m(\mathbf{r})$. Landau imposed that $\mathcal{F}$ is both invariant under the symmetries of the system, and analytical and expandable in powers of m close to the phase transition.[15] These strong assumptions enable to exclude certain terms from the expansion of $\mathcal{F}$ in powers of m, and to deduce qualitative properties about phase transitions. It should be noted that F is a thermodynamic quantity, whereas $\mathcal{F}$ is a functional that depends on the considered micro-state. Calculating F requires to calculate the partition function based on $\mathcal{F}$, which is beyond the scope of this thesis. For further reading, one can refer to [79, 182], from which this introduction to phase transitions is inspired.

Back to the focus of this Chapter, the density of solitons $\bar{\delta}$ seems an appropriate order parameter for the commensurate-incommensurate transition described in the framework of the Frank and van der Merwe model. From this perspective, the continuity of $\bar{\delta}$ illustrated on Fig. 2.15 (left) indicates it is a second order transition. On the contrary, a transition between adjacent commensurate phases is of first order.

From these considerations, it is clear that although the phases at stake hold very strong similarities, different phase transitions occur between them. It is worth defining more formally the order parameter.

2.4.2 Order parameter space

Landau classification is based on symmetry groups, so the order parameter appears as the quantity describing the symmetry breaking in the ordered phase. The larger the breaking, the larger the space of order parameter. As a first example, the distortion of polyacetylene reduces translational invariance by doubling the size of the unit cell. All the translations by an odd number of unit cells are no longer symmetry operations in the distorted state. The associated order parameter is the elongation of the bonds between each pair of A and B neighbouring atoms, noted u on Fig. 2.11. As seen earlier, the possible values of u are limited to ± 1 – to this extent, the free energy density profile of Fig. 2.16 (right) fits the situation of polyacetylene, with $m_0 = 1$.

This example calls for two comments. First, one should notice the symmetry breaking is rather "small", as only a numerable number of symmetry operations is broken, that is why the space on which the order parameter is defined is minimal: $\{-1, 1\}$. Secondly, all the symmetry operations that are broken are also those who transform the $u = -1$

---

[15] The schematic plots of Fig. 2.16 are drawn in the spirit of this theory.

state into the $u = +1$ state (and vice-versa). These two comments indicate a direct correspondence between the order parameter space and the more intuitive ensemble of broken symmetries.

The paramagnetic-ferromagnetic transition can be considered as a second example. As explained above, the rotational symmetry along an infinite number of axes is reduced to a rotational symmetry along the single axis given by the magnetization direction. In other words, the symmetry breaking is "larger", as an infinite number of symmetry operations has been broken in the ferromagnetic state. Consistently, the order parameter is the magnetization $\mathbf{M}$, which is a vector defined in 3D space. Here again, there is an intuitive proportionality between the extent of the broken symmetry and the order parameter space. Moreover, here too, none of the broken rotations leave the direction of $\mathbf{M}$ unchanged.

Those two striking features actually arise from more formal considerations. Let us consider a phase transition between a high symmetry disordered phase of symmetry group G, and a low symmetry ordered phase of symmetry group H. The order parameter space is given by the quotient group G/H [139]. This means that all the symmetry operations of H act as equivalence relations between the elements of G. G/H is then the group of the associated equivalence classes. For instance, the equivalence class of the identity, noted [Id], contains all the symmetry operations of G equal to Id modulo a symmetry operation of H. Therefore, [Id] is H itself. The broken symmetry operations of G are all contained in the other equivalence classes of G/H. Many illustrations and a more mathematically accurate discussion can be found in Section IV of [139].

Polyacetylene shall now be reconsidered in the light of the quotient group. Since the reduction of translational invariance is at stake, only translations need to be considered in G and H. G is the symmetry group of the undistorted chain, and its translations can be indexed with an integer in $\mathbb{Z}$. On the other hand, H is the symmetry group of the distorted chain, and due to the doubling of the unit cell, the allowed translations are those indexed with an even number in $2\mathbb{Z}$. The resulting quotient group G/H is therefore isomorphic to the cyclic group $(\mathbb{Z}/2\mathbb{Z}, +)$, which is the additive group of integers modulo 2. This is written $G/H \cong (\mathbb{Z}/2\mathbb{Z}, +)$. For simplicity, the operation of the group will be implicit in the following. $\mathbb{Z}/2\mathbb{Z}$ contains two equivalence classes: $[0]$, which contains all even numbers ($[0] = 2\mathbb{Z}$), and $[1]$, which contains all odd numbers ($[1] = 2\mathbb{Z} + 1$). This matches the situation of polyacetylene, where the translations are indexed either with an even or with an odd number. Finally, here, one can check that the order parameter space of the Peierls distortion of polyacetylene $\{-1, 1\}$ is indeed isomorphic to G/H. In general, one notes $G/H \cong \mathbb{Z}_2$.

Similarly, the paramagnetic-ferromagnetic transition can be reconsidered. In the paramagnetic phase, all rotations are symmetry operations, so $G \cong \mathrm{SO}(3)$, the group of rotations in 3D, whereas only one rotation axis remains in the ferromagnetic phase, so $H \cong \mathrm{SO}(2)$, the group of rotations in 2D. As a result, the order parameter space is isomorphic to $\mathrm{SO}(3)/\mathrm{SO}(2)$, which can be proved to be isomorphic to S^2, the sphere in

2D. This is consistent with the magnetization taking any direction on the sphere S^2.

So far, formally introducing the order parameter space has not brought more information than what intuition could provide. However, it is critical to properly define it when dealing with topological defects, as it is now going to be presented.

2.4.3 Topological defects

Topological defects have been introduced earlier when discussing the properties of polyacetylene, in Sect. 2.2.4. In this particular case, the topological defect is an unpaired electron on the chain, which induces different dimerization patterns on its sides. This can be interpreted as a spatial distribution of $u(x)$ containing a singularity: a point in space where u is not defined. Because of this singular character, the topological defect cannot be removed by a continuous transformation of the u field. Here, one would need to abruptly change u from -1 to 1 on half of the 1D space.

In the previous section, u has been proved to be a suitable order parameter for the Peierls distortion of polyacetylene. From this example, it is intuitive to extend the definition of a topological defect. One then has to consider a continuous spatial distribution of order parameter $m(\mathbf{r})$ in a space of dimensionality d within the system. The vacuum solution, or topologically trivial state, is a uniform distribution $m(\mathbf{r}) = m_0$. On the contrary, in presence of a topological defect, the system is in a topologically nontrivial state, which means it is in a distinct state where the distribution $m(\mathbf{r})$ cannot be continuously deformed into the vacuum solution. A topological defect then corresponds to a singular region of dimensionality $d' \leqslant d-1$ in the spatial distribution of order parameter.

The essence of a topological defect is its non-equivalence to the vacuum solution under continuous transformation. This means that its existence is independent of its detailed geometrical configuration. No matter how exactly the order parameter field is distributed around such a defect, the singularity cannot be removed. This also means that the presence of a topological defect can be deduced “from afar” by looking at the order parameter distribution $m(\mathbf{r})$.

In the case of polyacetylene, the boundary conditions $u(-\infty) = -1$ and $u(+\infty) = +1$ imply the presence of a kink topological defect somewhere on the chain, as illustrated on Fig. 2.17 (left). A more complicated example consists in a dislocation in graphene, as represented on Fig. 2.17 (right). By performing a contour around the dislocation and counting the number of unit cells, one can see an additional vector has to be added to close the contour. This additional vector characterizes the dislocation, and is called its Burgers vector, noted $\mathbf{b}$, and the contour is a Burgers contour.[16] No matter how far from the dislocation this contour is drawn, as long as it circles around it, it will not be able to close.

---

[16] These names refer to the Dutch physicist Jan Burgers for his pioneering work on dislocations in crystals [17].

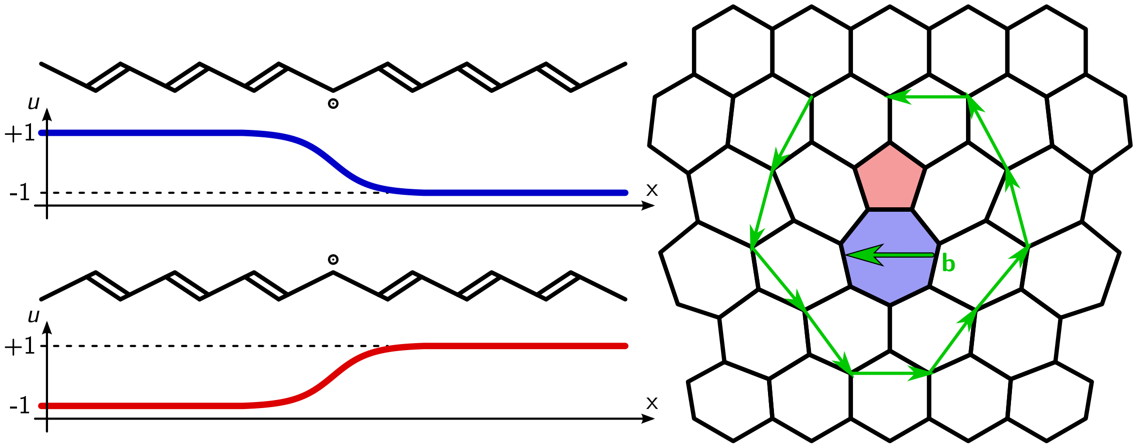

Figure 2.17: **Topological defects in polyacetylene and graphene. Left:** in polyacetylene, a change in the dimerization pattern induces a kink (blue, top) or an antikink (red, bottom), which is related to a non-trivial distribution of $u(x)$. **Right:** a pentagon-heptagon pair in graphene is a dislocation. A contour around it does not close unless the Burgers vector $\mathbf{b}$ of the dislocation is added.

As seen in these examples, there are two fundamental properties of topological defects. First, they induce a peculiar distribution of order parameter around them, which is why they are inequivalent to the topologically trivial state. For the kink in polyacetylene, this is the step-like function in $u(x)$, and for the dislocation, it is the strain field created around it. Secondly, topological defects can always be assigned an integer quantity that characterizes them. For polyacetylene, the kink and anti-kink create a Δu jump which is either $+2$ or -2. For dislocations, the coordinates of the Burgers vector in the Bravais lattice of the crystal give two integers. Since the detailed geometrical configuration of a topological defect does not matter, this integer quantity – called the winding number – is all one needs to know.

These properties have an underlying origin, which are the homotopy groups of the order parameter space, noted $\pi_n(G/H)$, $n \in \mathbb{N}$. Before using them on a few examples, they are first going to be briefly introduced. For a more accurate definition than what is presented below, one can refer to [139].

Homotopy groups

The definition of homotopy groups rely on the homotopy equivalence of paths. Two paths connecting two points A and B are homotopic if they can be continuously deformed into each other. The same can be said about loops, which are paths with identical initial and termination points M. This homotopy equivalence is illustrated on Fig. 2.18 (left). In the following, only loops will be considered.

Based on this equivalence, one can define equivalence classes, which regroup all homotopic loops of a given space X. For instance, the $[0]$ class consists of all the loops

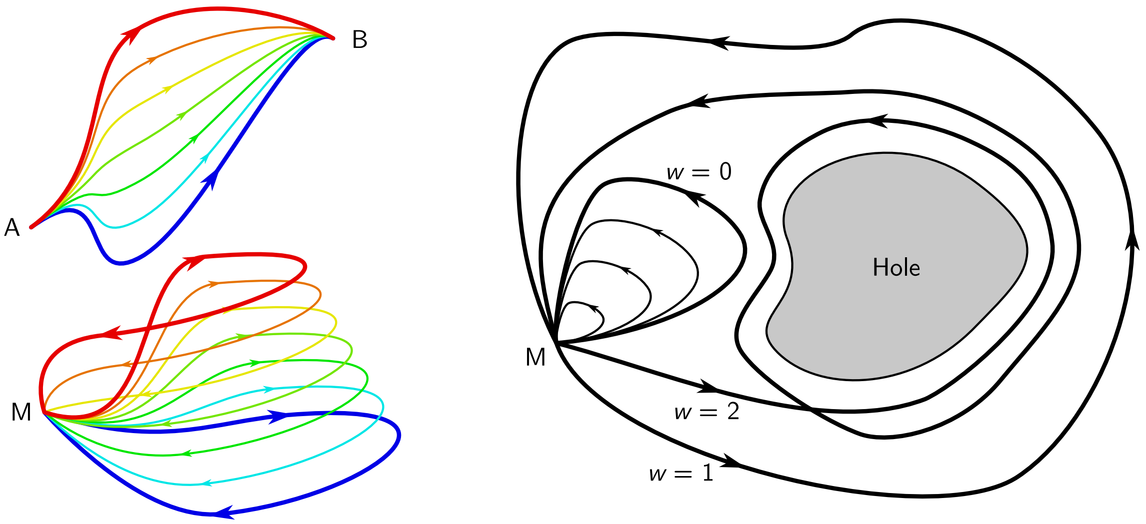

Figure 2.18: **Homotopy equivalence and classes. Top left:** the red and blue paths connecting the points A and B are homotopic, as they can be distorted into one another. **Bottom left:** similarly, the red and blue loops are homotopic. **Right:** in presence of a hole, different classes of loops can be found, depending on their winding number w, that is, the number of times they circle around the hole. Only loops with $w = 0$ can be deformed into a point.

that can be deformed into a point, as drawn on 2.18 (right). For a space containing a hole, the loops circling around this hole cannot be reduced to a point, and therefore are not part of the [0] class. Depending on the number of times they circle around the hole, they can be sorted into classes: [1] for loops circling once, [2] for those circling twice, [−1] for those circling once in opposite direction, etc. This number, noted w, is literally a winding number. The ensemble of all loops can then be separated into classes, here indexed by the winding number w.

When this ensemble is endowed with the summation law which consists in concatenating loops, it forms a group, called the 1^{st} homotopy group $\pi_1(X, M)$ of X. In this case, M is the point from where all loops depart, and the index 1 specifies that 1D loops are considered. This group is also known as the fundamental group. For a connected space X, reference to M is not necessary, and the 1^{st} homotopy group is simply noted $\pi_1(X)$. Other homotopy groups can be defined by extending the definition of a loop to other dimensions. $\pi_0(X)$ is the homotopy group for equivalence between 0-loops, or points, and $\pi_2(X)$ is the homotopy group associated to 2-loops, or closed surfaces. In general, the n^{th} homotopy group $\pi_n(X)$ is the group of homotopy classes of n-loops in X.

At this point, one can already sense a strong similarity between the homotopy classes and the topological defects. Like topological defects, loops within the same homotopy class defer in their geometric aspect, but hold the same winding number. Moreover, while a loop from the [0] class can be deformed to the trivial point-like loop, a loop from another homotopy class cannot. This would require to cut it somewhere and reconnect it somewhere else. This property is analogous to the impossibility to remove a topological defect from a medium by a continuous transformation of the order parameter field. One then has the intuition that the vacuum order parameter distributions correspond to the elements of the [0] class, while topological defects with a given winding number w have an associated homotopy class $[w]$.

This correspondence is actually a strict isomorphism. Topological defects of dimensionality d' in a medium of dimensionality d are given by the elements of the $(d-d'-1)^{\text{th}}$ homotopy group of the order parameter space $\pi_{d-d'-1}(G/H)$ [139]. A few examples are now going to be reviewed.

Kinks in polyacetylene

Once again, the simple 1D case of polyacetylene distortion can be discussed. It has been shown in the previous section that the order parameter space G/H is isomorphic to $\mathbb{Z}_2$. This group contains two elements, which stand for the two possible dimerization patterns.

Since $d = 1$, only 0D defects are at stake, so $d' = 0$ is the only option. One then has to evaluate $\pi_0(\mathbb{Z}_2)$, which is the homotopy group of points. Since $\mathbb{Z}_2$ is made of two elements, there are only two disjoint points, so $\pi_0(\mathbb{Z}_2) \cong \mathbb{Z}_2$. This means that there are also two elements in $\pi_0(\mathbb{Z}_2)$. The neutral element stands for all the configurations equivalent to the vacuum solution, which is the uniformly distorted chain. This includes chains containing kink-antikink pairs. The other element contains all configurations equivalent to the chain containing a single kink or antikink.

It is worth noting no distinction is made between the kink and the antikink. Indeed, they correspond to two symmetrical situations, which are therefore equivalent. There is no difference between the two on topological grounds. The result obtained based on homotopy groups is thus consistent with previous discussions.

Dislocations in graphene

Determining the existence of topological defects in the structure of graphene is a more complicated task. Indeed, the procedure used so far is straightforward once the order parameter space is defined. The challenge then consists in identifying properly the symmetry groups of the ordered and disordered phases, so as to find the possible topological defects.

Here, a solid-liquid transition is going to be considered, so the high symmetry disordered phase is a liquid, whereas the low symmetry ordered phase is a solid. This situation actually pushes the use of homotopy groups to its limits. Indeed, the order parameter field is continuous, which is at odds with the discrete nature of crystals. A naive extension to this situation can be used, with some limitations pointed out by David Mermin [139]. Still, it successfully anticipates dislocations, which is what is going to be presented here.

A second major objection that can be raised when dealing with crystalline order in 2D is the so-called Hohenberg-Mermin-Wagner theorem [138, 140]. It states that crystalline ordering is impossible in 1D and 2D, so long-range order is replaced by so-called quasi-long-range order. The term "solid" will then be used instead of "crystal", and its underlying meaning will be addressed later in this thesis.

As it freezes, a liquid gets the rotational and translational orders of a solid. Here, only the translational invariance will be retained. This means that instead of taking the full Euclidian group $E(2)$ as the symmetry group G of the liquid phase, only the group of continuous planar translations $T(2)$ will be considered. Consistently, the solid phase symmetry group H contains only the discrete planar translations. With these strong assumptions, one can consider the translations of G can be indexed by the two real coordinates of their vector. This implies that $G \cong \mathbb{R}^2$. Following the same principle, the translations of H are those permitted by the Bravais lattice of graphene, so $H \cong \mathbb{Z}^2$.

From this, the order parameter space can be deduced as $G/H \cong \mathbb{R}^2/\mathbb{Z}^2$. This group contains the equivalence classes of pairs of real numbers modulo a pair of integer numbers. This equivalence is well-known as the congruence relation. It is quite familiar that any real number is equal to a number within $[0, 1]$ modulo an integer, with 0 and 1 superimposed. This coincides with the circle S^1. In other words, the quotient group $\mathbb{R}/\mathbb{Z} \cong S^1$. For the same reasons, $\mathbb{R}^2/\mathbb{Z}^2 \cong S^1 \otimes S^1 = T^2$. As a result, the order parameter space is isomorphic to the torus: $G/H \cong T^2$.

Beside this mathematical approach, the order parameter space can be made more intuitive by proceeding as follows. If one imagines building the solid phase atom per atom, once the first one is placed, the origin of space $(0, 0)$ is set. As a consequence, all other atoms are placed deterministically by translational invariance at (m, n) positions, with m and n integers. Setting the absolute coordinates of the first atom is therefore the choice of order parameter. Its coordinates are unique modulo a Bravais lattice vector, so the choice reduces to a point in the Bravais unit cell. Due to the periodic boundary conditions on this unit cell, the space on which the point is chosen is indeed isomorphic to a torus T^2. The order parameter then corresponds to a two-component phase – called geometric phase – indicating the position of the crystal with respect to the origin of space.

In fact, the order parameter of the solid phase consists of the peaks in its structure factor.[17] The peak positions are determined by the lattice parameter and the absolute orientation of the solid.[18] The absolute position of the solid lies in the phase reference of the peaks. In 2D, two peaks are needed to define translational invariance, so two phases are set when choosing this order parameter. Since the space for these two phases is $[0, 2\pi] \times [0, 2\pi]$, with 0 and 2π superimposed, one finds again it is isomorphic to a torus T^2.

---

[17] For a crystal, those are Bragg peaks.

[18] The choice of the absolute orientation is related to the rotational order of the crystal that has not been considered here.

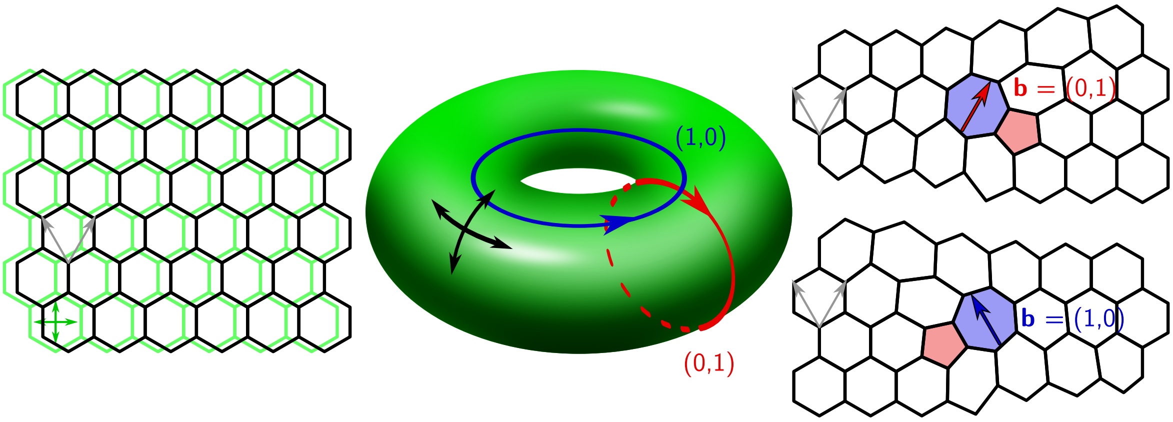

Figure 2.19: **Dislocations as topological defects in graphene. Left:** like all solids, graphene has a lateral positioning degree of freedom, illustrated by green arrows. **Middle:** this degree of freedom is that of the order parameter of the liquid-solid transition, which is then defined on a torus. Topological defects are then sorted by homotopy classes of loops on the torus. **Right:** They can circle through (red) and around (blue) its hole, which therefore corresponds to different topological defects, here dislocations.

The topological defects in graphene are then given by the homotopy groups of T^2. As graphene is a 2D material, its dimensionality is $d = 2$. Topological defects can then either be 1D or 0D ($d' = 1$ and $d' = 0$), so $\pi_0(T^2)$ and $\pi_1(T^2)$ should be considered respectively. As T^2 is a connected space, all points are equivalent, so $\pi_0(T^2) \cong \{0\}$. Consequently, there is no 1D topological defect in the structure of graphene.

For 0D topological defects, loops homotopy classes on the torus have to be considered. The hole of the torus reminds of that seen on Fig. 2.18, so non-homotopic loops can be expected. Indeed, as drawn on Fig. 2.19, two kinds of loops are possible: those circling around the hole (blue), and those circling through it (red). Two integers are then necessary to count each kind of rounds. Additionally, the order in which the rounds are performed does not matter, so $\pi_1(T^2)$ is abelian. Altogether, $\pi_1(T^2) \cong (\mathbb{Z}^2, +)$. This means 0D topological defects carry a couple of integer numbers as a winding number. This clearly corresponds to the integer coordinates of the Burgers vector of a dislocation, as represented on Fig. 2.17 (right).

With these two examples, homotopy groups appear to provide a general tool to anticipate and classify topological defects. Graphene systems more relevant to this thesis are now going to be briefly reviewed with this scheme.

Semenoff and Kekulé insulators

In the previous Chapter, the Semenoff and Kekulé gaps have been presented as typical consequences of the graphene-substrate interaction. Such gaps were underlined to open due to a symmetry breaking. The associated order parameter space and topological defects they can host are now going to be presented.

The Semenoff insulator can first be treated as a 2D analogue of polyacetylene. It has indeed been emphasized earlier the added staggered potential μ can be considered as the order parameter of the transition from graphene to the Semenoff insulator. The associated broken symmetry is the discrete space inversion symmetry. For this reason, the order parameter space is $G/H \cong \mathbb{Z}_2$, consistent with the fact that μ can be chosen either positive or negative.

As for the possible topological defects, graphene has $d = 2$ dimensions, so they can have $d' = 0$ or $d' = 1$ dimension. For $d' = 0$, topological defects are sorted along the homotopy classes of loops on $\mathbb{Z}_2$. As $\mathbb{Z}_2$ is a discrete space, loops are reduced to points on each of its 2 elements, which we call e and a. As a result, $\pi_1(\mathbb{Z}_2, e) = \pi_1(\mathbb{Z}_2, a) \cong \{0\}$, so no topological line point defect exists in the Semenoff insulator.

The situation is different for $d' = 1$, since $\pi_0(\mathbb{Z}_2) \cong \mathbb{Z}_2$. The underlying algebra shows this 1D defect is analogous to the kink in polyacetylene. This line defect separates two semi-infinite regions of the 2D space with opposite Semenoff mass m_S. This topological soliton is then a metallic wire where m_S equals zero [181, 219].

Realizing experimentally such a system proves challenging, as one would need to only influence graphene with a Semenoff term. It has been claimed in the case of a line defect in graphene on a Ni(111) surface [108]. However, it was noted that the underlying metal would shunt the transport properties of this 1D metal. Actually, strong $\pi - d$ hybridization dopes graphene by about 2 eV, and opens a gap at the Dirac cone [203], so this system does not correspond to a Semenoff insulator.

To achieve the needed decoupling from the substrate, Bernal-stacked bilayer graphene systems have been proposed [131, 199, 229] and realized [87, 115, 223]. In this case, the Semenoff insulator model is insufficient, as both graphene sheets have to be accounted for. Still, the underlying $\mathbb{Z}_2$ space inversion-related order parameter holds, because bilayer graphene under a transverse electric field is insulating [21]. The sign of the gap changes sign depending either on the direction of the applied electric field, or equivalently, on the AB or BA stacking of the bilayer. A 1D domain wall between two regions with opposite gaps have therefore been proposed, relying either on the direction of the electric field [131, 229], or on the stacking sequence [199, 229]. Both propositions have been realized experimentally, and the properties of the 1D topological wire have then been probed by quantum transport [87, 115] and STM [223], as illustrated on Fig. 2.20.

As a final comment, one should be aware that although this 1D domain wall is topological, its transport properties are very "fragile". Indeed, like in the Semenoff insulator, they suppose intervalley scattering is absent, which requires very high quality samples. Any localized defect could promote scattering between K and K' valleys, against which the "topological protection" granted by space-inversion symmetry breaking is useless.[19]

---

[19] To this extent, the deliberate use of terms such as "quantum valley Hall insulators" and "valley Chern numbers" is misleading [199, 229].

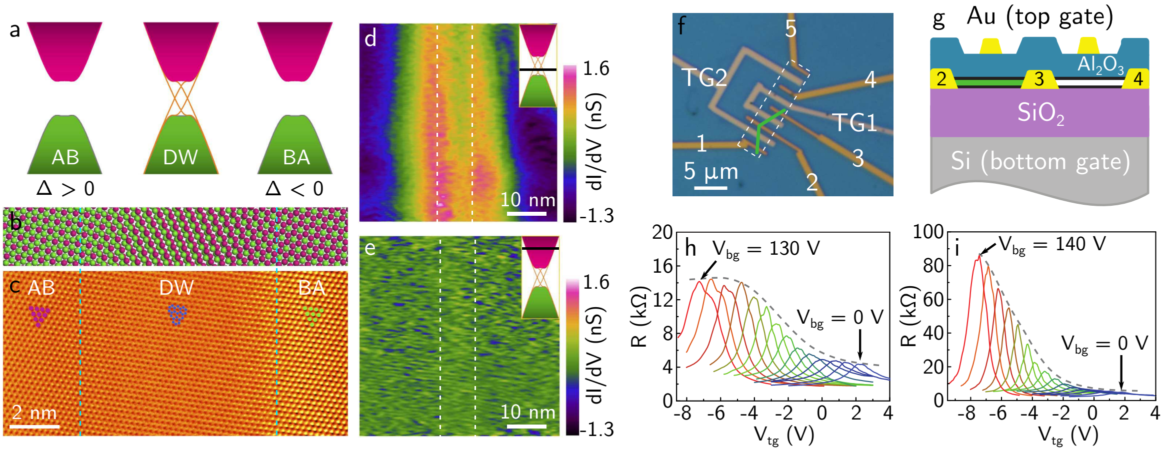

Figure 2.20: **Topological gapless channels at a bilayer graphene domain wall.** (**a**) Under a transverse electric field, the band structure of bilayer graphene has a gap Δ, which changes sign upon reversing of stacking AB to BA. At the interface between AB and BA domains, topological states lie at the Fermi level. (**b-c**) Ball model and STM topograph ($V_b = 0.4$ V, $I_t = 0.25$ nA) of such a domain wall. The dashed line indicates its edges. (**d**) $\mathrm{d}I/\mathrm{d}V$ map of the domain wall at $V_b = 30$ mV, showing the location of the conducting channels at the domain wall edges. (**e**) They are no longer visible for $V_b = 300$ mV as the Fermi level lies in the conduction band. Adapted from [223]. (**f**) Optical image of a dual-gated field effect transistor of bilayer graphene. White dashed lines denote the bilayer flake, and a green line indicates the domain wall. (**g**) Side-view of the device. Gate-dependent resistance is measured with (**h**) and without (**i**) a domain wall. The resistance peak indicates the energy of the Dirac point. Applying a backgate voltage induces a transverse electric field that opens a band gap, thus increasing the resistance at the Dirac point. The lower resistance in (**i**) indicates the presence of the 1D conducting channel. Adapted from [87].

Now turning to the Kekulé insulator, it is a phase of graphene with a lowered translational invariance. In analogy to polyacetylene, one may expect the order parameter space to be $G/H \cong \mathbb{Z}_3$, because of the tripled unit cell of the Kekulé-distorted graphene. This implies that under the distortion, carbon atoms move only along their chemical bonds. It actually neglects the bond angle degree of freedom, which, if taken into account, results in $G/H \cong S^1$ [23]. This means there is an infinity of Kekulé dimerization patterns, which can be indexed by a parameter φ parametrizing S^1.

In the previous Chapter, the Kekulé order parameter introduced in the low-energy effective hamiltonian of graphene was a 2-component vector $\mathbf{\Delta}$. When taken in polar coordinates, its modulus $\Delta = |\mathbf{\Delta}|$ is related to how much the atoms are displaced from their positions in a honeycomb lattice. Δ then indicates the amplitude of the Kekulé band gap. On the other hand, the phase of $\mathbf{\Delta}$ is φ, which corresponds to the chosen dimerization pattern.

When considering topological defects, homotopy groups of S^1 should be considered.

For $d' = 1$, as S^1 is a connected space, one finds $\pi_0(S^1) \cong \{0\}$, so no 1D topological defect exists. On the contrary, $\pi_1(S^1) \cong \mathbb{Z}$. Indeed, loops on a circle belong to different homotopy classes depending on how many rounds they make. 0D topological defects in a Kekulé insulator are thus possible, and correspond to vortices in their field of dimerization pattern [78].

No report of an experimental realization of such topological defects could be found. Indeed, as discussed earlier, the realization of a Kekulé insulator is already challenging. Still, a theoretical proposal has been put forward based on artificial graphene made of CO molecules on Cu(111) [8].

As a conclusion, domain walls in Semenoff insulators and vortices in Kekulé distorted-graphene are topological defects one can expect in the electronic properties of supported graphene. They can be expected in more realistic systems. Furthermore, moiré superlattices have been presented as a phenomenon arising from the superposition of graphene on its substrate. The Frank and van der Merwe model has also proved a possible transition from commensurate to incommensurate superstructures. Topological defects associated with these structural aspects can also be expected.

Graphene moiré superlattices

Topological defects in moiré superlattices can be considered on a two-fold basis. As explained in Section 2.2, moiré superlattices influence graphene's electronic properties by breaking inversion and translational symmetries. The order parameter resulting from inversion symmetry breaking results is a Semenoff gap, which will be considered first. Reducing translational invariance to the moiré superperiodicity yields other topological defects that will be considered afterwards.

Due to the varying stacking sequence of graphene on its substrate, a moiré superlattice can to some extent be considered as an insulating phase of graphene with a superperiodically modulated order parameter. This possibility has been suggested in the case of a Semenoff mass field. Other such terms can be added to the low-energy effective hamiltonian of graphene. It has indeed been generalized with effective scalar and vector potential terms V_{eff} and $\mathbf{A}_{\text{eff}}$ for twisted bilayer graphene [95] and graphene on h-BN [96].

In the light of possible topological defects in Semenoff insulators, moiré superlattices could then be expected to display a periodic array of 1D conducting channels, where $m_S = 0$. For a twisted bilayer graphene, the symmetry between AB and BA stackings implies this array is a percolating triangular lattice, hence of metallic character. On the contrary, for graphene on h-BN, the conducting channels form individual loops due to the asymmetry between B and N atoms, making the system insulating. Such situations are sketched on Fig. 2.21, and remain valid as long as the twist angle between the two layers is sufficiently small [96].

It should be reminded that the theoretical approach underlying these effects requires preservation of the Dirac cone and marginal doping from the substrate. Substrates such

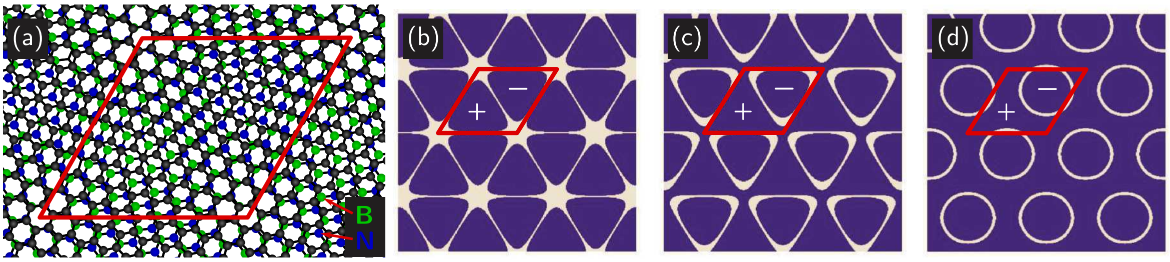

Figure 2.21: **1D $\mathbb{Z}_2$-topological defects array in moiré superlattices.** (**a**) A twisted layer of graphene on a weakly interacting substrate such as h-BN is considered as a model system. Due to the different stacking configurations within the moiré supercell (red rhombus), inversion symmetry is broken, giving rise to a $\mathbb{Z}_2$ order parameter. 1D conduction is achieved wherever this order parameter is zero. (**b**) When graphene lies twisted on another layer of graphene, the AB and BA stackings lead to exactly opposite order parameters, so a percolating array of conducting channels arise. (**c-d**) For graphene on h-BN, asymmetric B and N atoms induce individual conducting loops, which are more separated (d) when the asymmetry is stronger. Adapted from [96].

as h-BN or Au(111) appear as suitable candidates.

A second type of topological defects can be found in a moiré superlattice, this time related to its superperiodicity. It assumes a high-order commensurate relation between graphene and its substrate. For simplicity, the situation when $n \times n$ cells of graphene match $p \times p$ cells of substrate will be considered. The moiré unit cell is then given by unit vectors $\mathbf{a_{m,1}} = n\ \mathbf{a_{gr,1}}$ and $\mathbf{a_{m,2}} = n\ \mathbf{a_{gr,2}}$. Generalizing what has been detailed for polyacetylene, the order parameter space is $G/H \cong (\mathbb{Z}/n\mathbb{Z})^2$. The additional square is due to the 2D character of the moiré. Using properties of cyclic groups, one can rewrite $G/H \cong \mathbb{Z}/n^2\mathbb{Z}$. In other words, there are n^2 different but equivalent ways of designing such a moiré, which are due to discrete translations of vector $\mathbf{t} = i\ \mathbf{a_{gr,1}} + j\ \mathbf{a_{gr,2}}$, with $i, j \in \llbracket 0, n-1 \rrbracket^2$. This is sketched on Fig. 2.22 (top).

Loops on $\mathbb{Z}/n^2\mathbb{Z}$ are all reduced to points on individual subsets, so no 0D defect exists. As for points, $\pi_0(\mathbb{Z}/n^2\mathbb{Z}) \cong \mathbb{Z}/n^2\mathbb{Z}$, so there are $n^2 - 1$ different types of 1D topological defects. They are domain walls between shifted moiré domains, as illustrated on Fig. 2.22 (bottom).

This section has provided many examples of topological defects. Their definition relies on the notion of order parameter, which originates from the context of phase transitions. They indeed correspond to non-trivial spatial distributions of order parameter. As it is now going to be presented, it appears they also play a fundamental role in phase transitions, as was predicted by 2016 Nobel laureates John M. Kosterlitz and David J. Thouless.

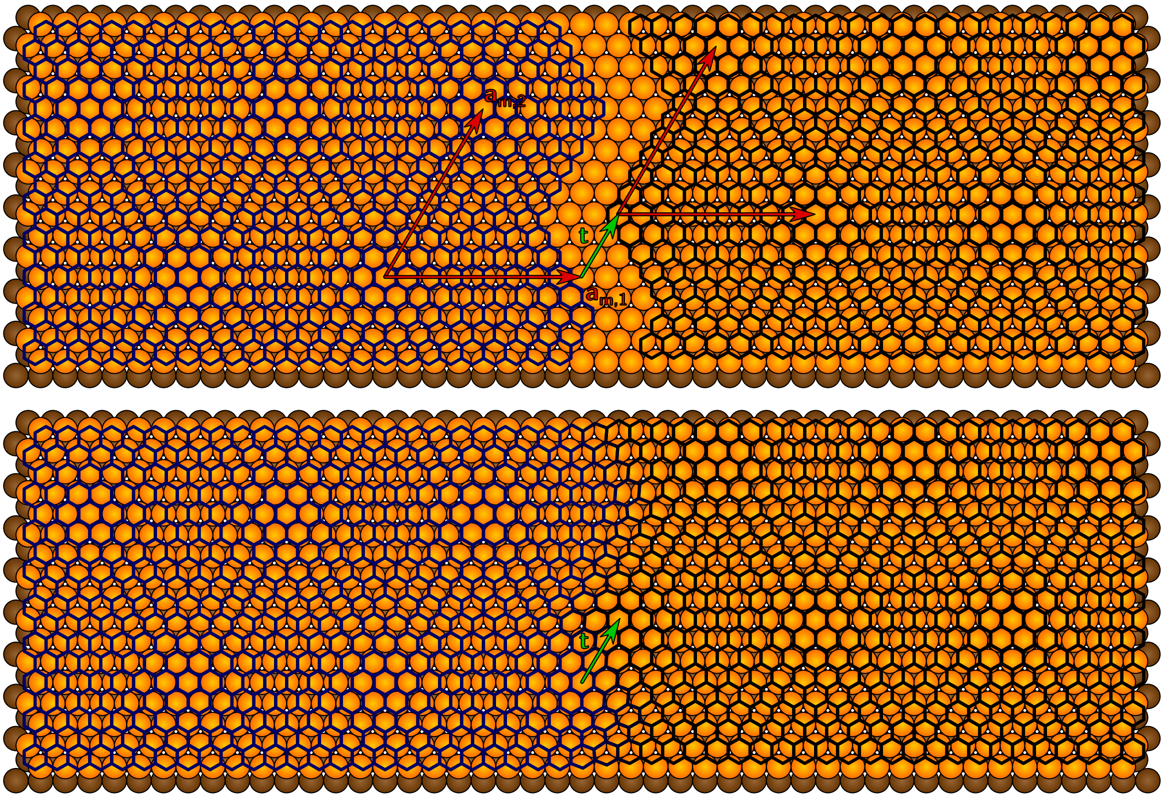

Figure 2.22: **1D $\mathbb{Z}/\mathbf{n^2}\mathbb{Z}$-topological defect in a moiré superlattice.** A moiré superlattice of unit vectors $\mathbf{a_{m,1}}, \mathbf{a_{m,2}}$ corresponding to 9×9 cells of graphene stacked on 8×8 cells of substrate is considered. **Top:** two domains (blue and black) are shifted with respect to each other by a vector $\mathbf{t}$ (green arrow). **Bottom:** the coordinates of $\mathbf{t}$ are the winding numbers of the topological domain wall between the two domains.

2.4.4 Berezinskii-Kosterlitz-Thouless transition

A system containing a single topological defect is in a non-trivial state that cannot be continuously deformed to the state free of defects, or vacuum state. Equivalently, it is impossible to add topological defects to a system continuously one by one. Nonetheless, one can imagine adding pairs of topological defects with opposite winding numbers. This corresponds to a kink-antikink pair in polyacetylene, or to a dislocation pair with opposite Burgers vectors in solids.

In 1972, Kosterlitz and Thouless proved that in 2D, pairs of topological defects could actually unbind above a critical temperature [102]. The underlying mechanism applies with generality to multiple systems: the XY model of spins in 2D, superfluid helium films, or 2D solids. The driving mechanism can be justified by a simplified explanation involving the free energy F of a single topological defect. On the one hand, the topological defect has an energetic cost U – for a dislocation in graphene, this cost corresponds to the strain induced in the layer. U grows as:

$$U = U_0 \ln\left(\frac{A}{A_0}\right)$$

where U_0 is a typical energy related to the system under consideration, A is the size of the 2D system, and A_0 is the typical size of the topological defect.

On the other hand, since this topological defect can be placed anywhere in the system, the number of configurations Ω is proportional to the size of the system. The associated entropy S then writes as:

$$S = k_B \ln \Omega = k_B \ln\left(\frac{A}{A_0}\right)$$

Importantly, the entropy also grows logarithmically with the sample size. As a result, when considering the free energy, one gets:

$$F = U - TS = U_0 \ln\left(\frac{A}{A_0}\right) - k_B T \ln\left(\frac{A}{A_0}\right) \tag{2.10}$$

A critical temperature $T_c = {}^{U_0}/_{k_B}$ defines the change of sign of F. For $T < T_c$, the energetic cost of a topological defect overcomes the disorder favoured by the entropic term. But for $T > T_c$, it becomes preferable to create topological defects. This gives a simple explanation for the Kosterlitz-Thouless transition to occur. It should be noted it neglects the interaction between topological defects though, as well as the renormalization of the system's constants they induce.[20] A more thorough account of these effects can be found elsewhere [79, 103].

While John M. Kosterlitz and David J. Thouless predicted this transition in 1972, Vadim Berezinskii pointed out in 1970 the importance of weak and local external fields in the phase diagram of 2D systems at low temperature [7]. The work of Berezinskii was of important inspiration for Kosterlitz and Thouless to formulate their theory, as they attributed such local external fields to topological defects. The transition triggered by topological defects pairs unbinding at $T = T_c$ is therefore called the Berezinskii-Kosterlitz-Thouless (BKT) transition.

Following the BKT transition theory, developments in the case of 2D solids have led to a microscopic picture of their melting into 2D liquids [69, 148], referred to as the Kosterlitz-Thouless-Halperin-Nelson-Young theory [186]. Two BKT transitions indeed occur. First, dislocation pairs unbind, which fully breaks translational invariance. The system is no longer a solid, but rather an anisotropic liquid called a liquid crystal, which preserves some rotational correlations. In a second stage, individual dislocations break up in pairs of disclinations. Disclination pairs unbinding constitute the second BKT transition that brings the system to a liquid state.

The BKT transition has a rather peculiar status among phase transitions. Indeed, from the point of view of thermodynamics, it can be shown that no discontinuity occurs

---

[20] For instance, a high concentration of dislocations induces considerable strain in a 2D solid, and therefore reduces its shear modulus K, which in turn reduces U_0.

in any of the thermodynamic potential derivatives. As such, it is a transition of infinite order in the Ehrenfest classification [79]. As far as the Landau classification is concerned, the BKT transition cannot be sorted, as no symmetry is actually broken across it. Equivalently, this means no order is destroyed or created at the BKT transition.

This last statement may appear counter-intuitive. In the case of graphene, the honeycomb arrangement of its atoms leaves the impression it displays crystalline long-range order. Actually, because of its 2D character, no such order can occur, and graphene should display a so-called quasi-long-range order that preserves the continuous translational symmetry. This explains why no symmetry is broken across the BKT transition, and it is the consequence of the so-called Hohenberg-Mermin-Wagner theorem [140]. Its origin and its consequences for graphene are now going to be introduced.

2.4.5 Goldstone mode and quasi-long-range order

Before considering the specificities of a 2D system, the concept of Goldstone mode is first going to be introduced briefly. Its name originates from Jeffrey Goldstone, who theorized this collective excitation that emerges following a phase transition that breaks a continuous symmetry [60]. An illustrative example of historical importance [140] is going to be considered.

Goldstone theorem

This example is the so-called 2D XY model. It considers a 2D lattice of spins whose directions are confined to the plane coupled to each other via a ferromagnetic interaction. Because of this interaction, one would naively expect that below a certain temperature T_c, a transition from a paramagnetic to a ferromagnetic state occurs. Due to the Goldstone mode and to the specific $d = 2$ dimensionality of the system, this actually does not occur [140].

In the paramagnetic-ferromagnetic transition, a rotational symmetry is broken. Indeed, as all spins $\mathbf{s}_i$ align and acquire an average value $\mathbf{s}$, a global magnetization $\mathbf{M}$ emerges. Here, $\mathbf{s}$ will be regarded as the order parameter. As $\mathbf{s}$ can take any direction in the plane, it is intuitive that the order parameter space is the circle S^1, that is why this transition involves a continuous symmetry breaking.

To investigate this further, following Landau theory, a free energy functional $\mathcal{F}$ can be expanded as a Taylor series in powers of $\mathbf{s}$ near $T = T_c$, as:

$$\mathcal{F}(\mathbf{s}, T) - \mathcal{F}(\mathbf{0}, T) = \frac{a}{2}(T - T_c)\ \mathbf{s} \cdot \mathbf{s} + \frac{b}{4}\ (\mathbf{s} \cdot \mathbf{s})^2 \tag{2.11}$$

with a and b positive coefficients. For $T > T_c$, $\mathbf{s} = \mathbf{0}$ minimizes $\mathcal{F}$, which is consistent with a zero order parameter in the high symmetry phase. For T just below T_c, this Equation (2.11) yields the so-called "Mexican hat" potential, represented on Fig. 2.23 (a). $\mathcal{F}$ is then minimized for $|\mathbf{s}| = \sqrt{\frac{a(T_c - T)}{b}} = s_0$. This means $\mathbf{s}$ takes any value on the red circle indicated on Fig. 2.23 (a). This result is consistent with the S^1 order parameter space.

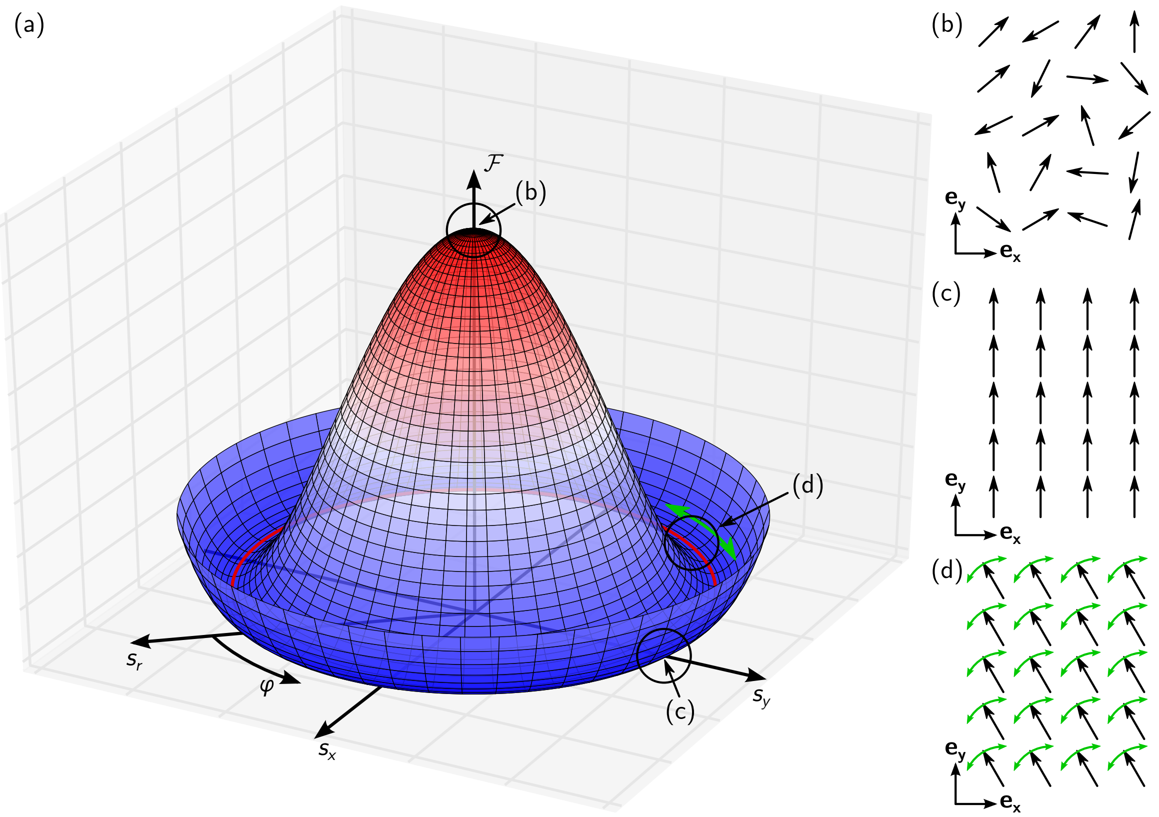

Figure 2.23: **Goldstone mode with a "Mexican hat" free energy functional.** (**a**) The free energy landscape of the low temperature phase of the XY model is plotted with respect to its order parameter $\mathbf{s}$. (**b**) The ground state of the disordered phase corresponds to an unstable extremum of free energy. (**c**) One possible ground state of the ordered state has its spins aligned, for instance in the y direction. (**d**) Due to the ground state degeneracy, a continuous rotation of all spins does not cost any energy. The associated Goldstone mode has a vanishing frequency at infinite wavelength.

It is clear that the ground state is infinitely degenerate on all the angles φ that parametrize S^1. As indicated with a green arrow on Fig. 2.23 (a), a rotation of the order parameter $\mathbf{s}$ does not cost any energy. It is equivalent to a uniform rotation of the spins $\mathbf{s}_i$, as drawn on Fig. 2.23 (d). For the same reason, a non-uniform rotation of the spins with smooth spatial variation will be long to relax. This corresponds to a long wavelength mode with low energy, called a spin wave or a magnon. For an infinitely long wavelength, the energy of this mode is vanishingly small.

The Goldstone theorem generalizes this last statement to any broken continuous symmetry, to which is associated such a mode, thus called a Goldstone mode. This theorem has been introduced in a context of field theory, so the term Goldstone boson is also used [60].[21] Because of its infinitely small frequency, the Goldstone mode is excited

---

[21] The existence of this Goldstone mode is not always guaranteed. When it interacts with a gauge field,

at any non-zero temperature, and induces fluctuations of the order parameter. In the previous example, this means the average spin direction $\mathbf{s}$ wiggles because of thermally excited spin waves.

The small energy cost of a Goldstone mode with $\mathbf{q} \neq \mathbf{0}$ is due to the gradients of order parameters it creates. In other words, there is some resistance of the spins to wiggle collectively. This behaviour is analogous to the rigidity of a solid material, which opposes an elastic deformation. Following Landau theory, one can define a generalized rigidity K in an additional elastic free energy term of the form:

$$\mathcal{F}_{el} = \frac{1}{2} \int_V \mathrm{d}^d\mathbf{r}\ K\ (\nabla\varphi(\mathbf{r}))^2 \tag{2.12}$$

with V the volume of the system. In reality, K depends of the order parameter distribution $\varphi(\mathbf{r})$, but this effect will not be discussed at this point. Consequently, K will be treated as a thermodynamic constant.[22]

There are also Goldstone modes in 2D solids. When considering topological defects in graphene, it was shown its order parameter space is T^2. In fact, the order parameter is the two-component geometric phase indicating the position of the crystal with respect to the origin of space. In analogy to the XY model, it should then have two Goldstone modes associated with each component. Indeed, two in-plane acoustic phonons make the atoms wiggle around their average position. For low values of q, they induce long wavelength fluctuations of the geometric phase with a vanishing frequency, since $\omega = c_{ph}q$, with c_{ph} the celerity of the phonons. Besides, in this context, the generalized rigidity K corresponds to the solid shear modulus.

Hohenberg-Mermin-Wagner theorem

Between 1966 and 1968, David Mermin, Herbert Wagner and Pierre Hohenberg underlined in a succession of papers the crucial role of Goldstone modes in 1D and 2D systems [77,138,140]. While the original paper of Mermin and Wagner focused on the XY model [140], it was generalized to superfluids and superconductors by Hohenberg [77], and to 2D solids by Mermin [138]. The generality of this result is now commonly known as the Hohenberg-Mermin-Wagner (HMW) theorem. It states that because of the reduced dimensionality, thermal fluctuations associated with the Goldstone modes

---

the Goldstone boson becomes an additional component of the gauge boson (it gets "eaten"). This is the so-called Higgs mechanism, which makes the gauge boson massive. It is famous for the Higgs boson, which makes the W and Z gauge bosons massive. In condensed matter, superconductivity provides a similar example. A superconductor breaks the continuous electromagnetism gauge symmetry, so one would expect a Goldstone mode. Actually, it interacts with the photon, hence "gets eaten", making the photon massive. As a consequence of this mass, the photon field decays exponentially inside a superconductor: this is known as the Meissner effect.

[22] The energy cost of a topological defect U_0 introduced earlier originates from the elastic energy term (2.12) integrated over a contour enclosing the defect. For a topological defect of winding number w, one then has $U_0 = \pi w^2 K$.

hinder long-range order at $T \neq 0$. That appears counter-intuitive given the existence of graphene, which could be taken as a counter-example of a 2D crystal.

To understand its implications, the HMW theorem requires to remind what short and long-range orders are. Order is a notion introduced earlier as opposed to symmetry. It relies on the (equal-time) correlation function $g(\mathbf{r})$, normalized here as:

$$g(\mathbf{r}) = \frac{\langle m(\mathbf{0}) m(\mathbf{r})\rangle}{\langle m(\mathbf{r})\rangle^2} \tag{2.13}$$

where $\langle\ \rangle$ indicates the average on configurations of $m(\mathbf{r})$. Clearly, the correlation function indicates how much the order parameter at a certain position $m(\mathbf{r})$ is the same as that at the origin $m(\mathbf{0})$. It is related by Fourier transform to the structure factor $S(\mathbf{q})$, which is accessible experimentally by diffraction techniques. It expresses as:

$$S(\mathbf{q}) = \frac{1}{V}\int_V \mathrm{d}^d\mathbf{r}\ e^{-i\mathbf{q}\cdot\mathbf{r}}\ g(\mathbf{r}) \tag{2.14}$$

where V is the volume of the system, and d its dimensionality. In the following, the order parameter m will be the direction given by φ, with φ the phase corresponding for instance to the direction of a spin in the XY model, or to one component of the geometric phase of a 2D solid.

For a system with short-range order, like a gas or a liquid, no correlation subsists at large distances, so for $|\mathbf{r}|$ sufficiently large, one has:

$$g(\mathbf{r}) \simeq \frac{1}{r^{2-d+\eta}} e^{-r/\xi} \text{ and } S(\mathbf{q}) = \sum_{\mathbf{G}} \frac{A_{\mathbf{G}}}{1/\xi^2 + |\mathbf{q}-\mathbf{G}|^2} \tag{2.15}$$

where ξ is the correlation length, η a critical exponent that depends on the transition, and $A_{\mathbf{G}}$ the peak amplitude. $S(\mathbf{q})$ appears as a series of lorentzian peaks, whose widths are given by the correlation length $1/\xi$. Such $g(\mathbf{r})$ and $S(\mathbf{q})$ are plotted on Fig. 2.24 (left). When approaching the transition, ξ diverges as $\frac{1}{(T-T_c)^\nu}$, with ν another critical exponent. This has two consequences. First, when close to T_c, the lorentzian peaks in $S(\mathbf{q})$ get sharper and sharper, which is consistent with a transition to a set of Bragg peaks. Secondly, the exponential term in $g(\mathbf{r})$ vanishes, so exactly at the transition, one has $g(\mathbf{r}) \simeq \frac{1}{r^{2-d+\eta}}$. In this case, correlations scale following the critical exponent η, which characterizes the universality class of the transition.

In a system with long-range order, correlations extend to infinite distance. For example, in a crystal, the positions of the atoms are given by translational invariance up to infinite distances. In diffraction, this results in a structure factor composed of Bragg peaks. It can be shown to express as:

$$g(\mathbf{r}) \simeq e^{-2W} \text{ and } S(\mathbf{q}) = \sum_{\mathbf{G}} e^{-2W}\ \delta(\mathbf{q}-\mathbf{G}) \tag{2.16}$$

where $\mathbf{G}$ are the vectors in the reciprocal lattice and e^{-2W} is the Debye-Waller factor. It is the impact of thermal fluctuations on the structure factor. The role of the

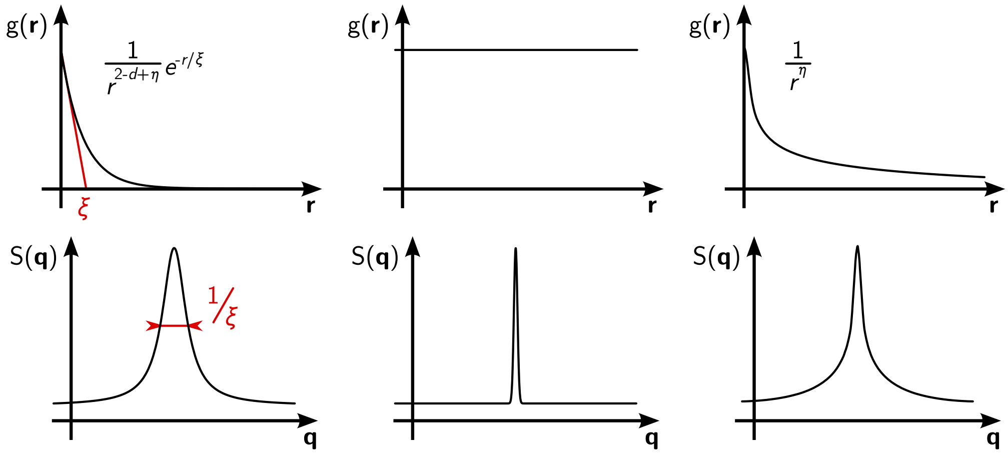

Figure 2.24: **Correlation function g(r) and structure factor S(q) for different kinds of order. Left:** short-range order shows an exponential decay of correlations on a typical correlation length ξ, yielding lorentzian peaks in the structure factor. **Middle:** for a system with long-range order, correlations preserve a finite value up to infinite distances, hence having a structure factor composed of Bragg peaks. **Right:** for quasi-long-range order, this correlation length extends to infinity, so correlations decay as a power-law of exponent η, giving rise to peaks following a power-law of exponent $-2+\eta$.

Goldstone mode lies therefore in this term. It relates to the generalized rigidity K and to temperature T through:

$$W = \frac{k_B T}{2} \int_0^\Lambda \frac{\mathrm{d}^d \mathbf{q}}{(2\pi)^d} \frac{1 - e^{i\mathbf{q}\cdot\mathbf{r}}}{K q^2} \tag{2.17}$$

where Λ is the cut-off wave vector corresponding to the edge of the first Brillouin zone. The integration in Equation (2.17) depends critically on the dimensionality d. For $d > 2$, it converges to a finite value, as expected for long-range order:

$$W \simeq \frac{k_B T}{2} \frac{\Lambda^{d-2}}{K(d-2)} \tag{2.18}$$

For $d = 2$, W can be seen to diverge, so the system is disordered. A direct integration of Equation (2.17) actually gives:

$$W \simeq \frac{k_B T}{2\pi K} \ln(\Lambda\, r) \tag{2.19}$$

The reduced dimensionality of the phase space on which is performed the integration is key to this result. It leads to thermal fluctuations of the order parameter which grow logarithmically with the size of the sample. This also leads to a power law dependence of the correlation function and structure factor:

$$g(\mathbf{r}) \simeq \frac{1}{r^{\eta(T)}} \text{ and } S(\mathbf{q}) = \sum_{\mathbf{G}} |\mathbf{q} - \mathbf{G}|^{-2+\eta(T)}, \text{ with } \eta(T) = \frac{k_B T}{2\pi K} \tag{2.20}$$

Except for $T = 0$, correlations do not have a finite value at infinity. This is the clear signature that thermal fluctuations destroy long-range order in 2D. These fluctuations correspond to the low-energy Goldstone modes. Nevertheless, although long-range order is absent, correlations do not decrease exponentially with distance, but as a power law. In a diffraction experiment, the measured structure factor should display peaks with a power-law dependence, rather than Bragg peaks or lorentzian peaks. This intermediate situation between short and long-range order is called quasi-long-range order.[23] As a side note, this situation is somehow similar to the critical case mentioned above, but with a temperature-dependent exponent η, thus not related to a universality class.

The description of quasi-long-range order gives a better understanding of 2D solids like graphene. A naive description would consider it as a 2D crystal where translational symmetry is broken. Two in-plane acoustic phonon branches play the role of Goldstone modes associated with the broken continuous symmetry. In virtue of the HMW theorem, the thermal fluctuations of the acoustic phonons actually exclude long-range crystalline order. Atoms in a 2D solid therefore sit on average positions, but fluctuate around it with amplitudes growing as the logarithm of the sample size $\ln L$.

Moreover, although graphene is an example of 2D solid, it is worth noting it exists in a 3D world. The out-of-plane dimension should further impede long-range order, as the out-of-plane acoustic phonon – so-called ZA phonon, or flexural mode – is very soft: it has a frequency dependence $\omega \propto q^2$. This would lead to out-of-plane fluctuations that grow as L^2, which are responsible for the so-called ripples in suspended graphene samples. Rippling of graphene has been observed by TEM measurements [141], and the associated power-law dependence in q of the structure factor has been confirmed by Monte-Carlo simulations [45]. This first approach should be nuanced, as strain-induced renormalization of mechanical constants and anharmonic coupling of the in-plane and out-of-plane acoustic phonons result in a change of the exponents involved in power-laws and in fluctuation amplitudes [90]. As a final remark about pristine graphene, accounting for $\sim 1\%$ strain is enough to both suppress the anharmonic coupling and renormalize the ZA phonon dispersion, blocking graphene's spontaneous rippling [175].

When supported by a substrate, one can wonder whether quasi-long-range order is preserved in graphene. The Frank and van der Merwe model introduced earlier provides a qualitative answer. In a commensurate phase, graphene locks its periodicity to a commensurate relation with the substrate, and therefore acquire long-range order. In this case, 1D topological solitons analogous to kinks in polyacetylene can be expected between shifted domains. On the contrary, in the incommensurate phase, quasi-long-range order is maintained, giving rise to a floating incommensurate order. Without long-

---

[23] It has originally been referred to as "topological order" [102, 103], but this expression has taken a different meaning that goes beyond the Landau theory of phase transitions.

range order, the 1D solitons are no longer topological, but a mere signature of thermal fluctuations. They are Goldstone modes analogous to acoustic phonons, which are called phasons. One can then wonder on which side of the commensurate-incommensurate transition supported graphene sits.

Chapter 3

Experimental techniques and methods

3.1 Scanning Tunneling Microscopy (STM)

In 1981, Gerd Binnig and Heinrich Rohrer invented scanning tunneling microscopy (STM), and developed the first scanning tunneling microscope with Christopher Gerbel and Edmund Weibel. Soon later, it enabled them to resolve the atomic structure of the (7×7)-reconstructed surface of Si(111) [9], which had been a long-standing puzzle. In the following years, they have invented many other microscopes, such as the atomic force microscope (AFM), the scanning near-field optical microscope (SNOM) and the magnetic force microscope (MFM). For all of them, a very sharp probe is scanned above a surface to measure its local properties with atomic resolution. Data is collected at each point of a grid, and then converted to an image representing the physical property measured at each point. That is why this family of microscopes is called scanning probe microscopy. For all these contributions, Binnig and Rohrer shared the Nobel Prize in Physics in 1986.

In the following, an elementary introduction is given about STM. Further information can be found in dedicated books and reviews, among which [26] and [48].

3.1.1 Working principle

Quantum tunneling

The physical phenomenon at stake in STM is quantum tunneling. In STM, the metallic tip and the conducting sample are separated by vacuum over a small distance, of the order of few Å. When a voltage bias is applied between the two, the absence of tip-sample contact means no current should flow according to classical accounts of electrodynamics. From a quantum mechanical point of view, however, electrons are similar to waves, and can be described as wave functions indicating their probability amplitude distribution in space. In particular, at the end of the STM tip and at the surface of the sample, wave functions decay exponentially like evanescent waves. Due to the small distance between the two, there is a non-zero overlap of the electronic wave functions, and therefore a non-zero probability for electron transfer between the tip and sample. This mechanism is known as quantum tunneling, and results in a tunnel current I_t that

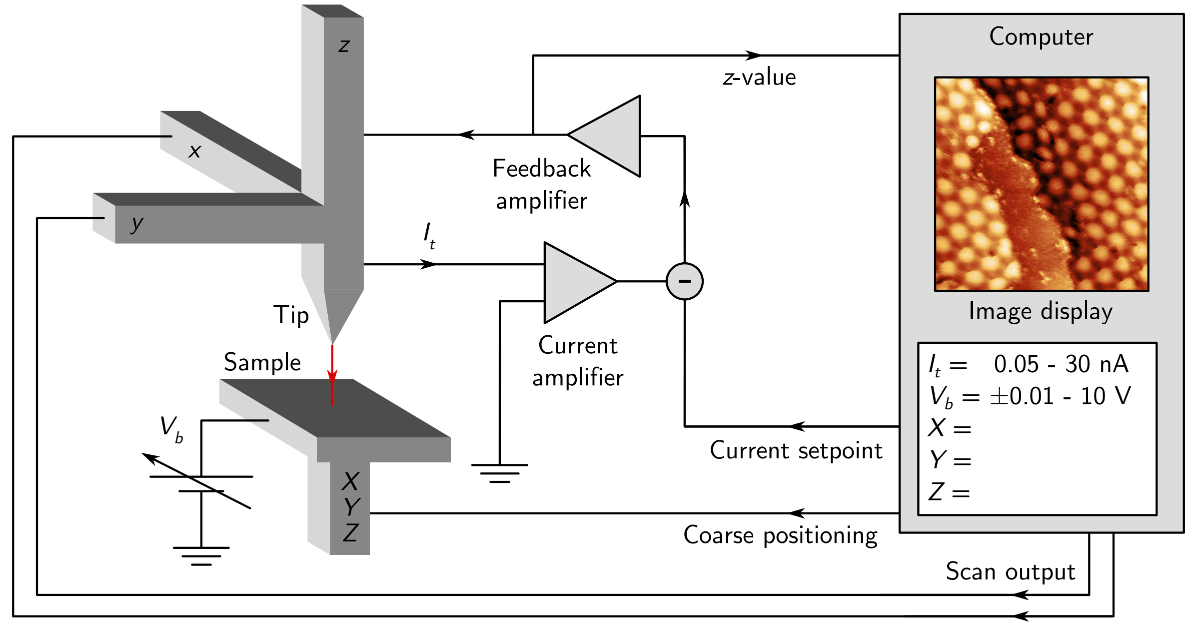

Figure 3.1: **Basic principle of a scanning tunneling microscope:** a tip is scanned using three piezoelectric actuators (x, y, z) above a sample positioned by inertial motors (X, Y, Z). During the scan, a voltage bias V_b is set between the sample and tip, so a tunnel current I_t can be measured. A feedback loop compares the measured current to a setpoint value, so their difference drives the z piezoelectric actuator to maintain a constant tip-sample distance. The imposed z displacement is displayed as a topograph on the control computer.

depends exponentially on the tip-sample distance d [26, 48]:

$$I_t \propto e^{-2\kappa d}, \text{ with } \kappa = \sqrt{\frac{2m\phi}{\hbar^2}} \tag{3.1}$$

with m the electron free mass, and ϕ the work function of the tip and sample. For a metal, $\phi \sim 5$ eV, so $\kappa \sim 1$ Å^{-1}, so variation of d of only 1 Å would result in an order of magnitude variation of I_t. This exponential dependence is at the origin of the very high vertical resolution of STM, whose experimental aspects are now introduced.

STM principle

STM relies on quantum tunneling to probe the topography of a surface. Its elementary principle consists in maintaining a constant tunnel current I, called current setpoint, so the tip-sample distance is kept constant. While scanning the tip, adjustments of its vertical position z then directly translate the topography of the sample surface. This method is known as the constant-current imaging mode, which provides topographs $z(x, y)$.

It is also possible to scan the tip while maintaining a setpoint tip position z. This is known as the constant-height imaging mode. The variations of tunnel current are then acquired during the scan, providing $I_t(x, y)$ maps. In the following, only the constant-current imaging mode will be discussed.

With this basic principle, the experimental apparatus of an STM has the following requirements and components:

- Scanning, approaching and retracting the STM tip with Å resolution. This requirement is met by three-dimensional piezoelectric actuators, which enable very fine positioning using voltage biases.
- Coarse positioning of the STM tip with respect to the sample, in order to approach it down to the to a distance where a tunnelling current becomes measurable. It is realized using inertial piezoelectric motors, with various possible configurations depending on STM design.
- Measuring the tunnel current, which relies on a current-voltage amplifier. It converts the tunnel current of the order of $0.05 - 30$ nA into a voltage with a typical gain of 10^8 V/A.
- Maintaining the tunnel current to its setpoint value. For this, a feedback system compares the measured current to the setpoint value, and amplifies the difference to drive the z piezoelectric actuator. The feedback is negative, so a too large (resp. small) current implies retracting (resp. approaching) the tip.

This basic apparatus is sketched on Fig. 3.1, where the role of each component is summarized.

Topographic and electronic contributions

In the simple explanation given so far, STM gives access to the topography of the surface. Nevertheless, it relies on a quantum electronic effect, which can affect non-trivially the measured topographs. In this short section, an introductory account of this effect is given.

From an experimentalist point of view, STM offers a long list of tunable parameters. The most elementary parameters are the tunnel current setpoint I_t and bias voltage V_b (here applied to the sample), which play a fundamental role.[1]

As far as the current setpoint is concerned, it is related to the tip-sample distance. Setting a high current setpoint requires the tip to be close to the sample, so electrons are likely to tunnel between the two. On the other hand, the role of V_b is more subtle. The tunneling hamiltonian [4] clarifies it.

---

[1] Other parameters affect the measurements, such as the feedback loop gains, which relate to the tip-sample distance stability.

For a tunnel junction between two normal metals separated by an insulating layer, the tunnel current I expresses in this formalism as a function of the bias voltage V_b as:

$$I(V_b) = \frac{4\pi e}{h} |M|^2 \int \mathrm{d}\epsilon \; \rho_{\mathrm{tip}}(\epsilon)\rho_{\mathrm{sample}}(\epsilon + eV_b) \; [f_{\mathrm{tip}}(\epsilon) - f_{\mathrm{sample}}(\epsilon + eV_b)] \tag{3.2}$$

where the integration runs on all the electronic energies, $|M|^2$ is the tunneling parameter (related to the tip-sample distance), $f(E)$ is the Fermi-Dirac distribution, and ρ the electronic density of states. It means that a at a given energy ϵ, electrons that tunnel from the tip to the sample have to leave a filled state of the tip to enter an empty state of the sample. The number of such electrons is thus proportional to the density of states of the tip and sample at that energy, and their filled/empty character is given by the Fermi-Dirac distribution.

As a consequence, in a STM measurement, the tunnel current is proportional to the product of tip and sample electronic densities of states over an energy window set by V_b. It is often assumed that the tip has a constant density of states for energies around its Fermi energy, which appears a legitimate approximation for common metallic tips made of W or PtIr. The tunnel current is then directly proportional to the integrated density of states of the sample. When V_b is raised, I_t increases due to the additional states that can be probed in the electronic density of states. Due to the spatial dependence of these electronic states, some areas of the sample may appear higher or lower. This is commonly referred to as an electronic density of states effect, and it plays an important role in the apparent morphology of supported graphene samples.

3.1.2 Experimental setup

In the experimental data presented in this thesis, STM measurements were performed at room temperature under UHV, using a commercial Omicron UHV-STM 1, with a W chemically etched tip. In particular, when studying moiré superlattices (see Chapter 4), thermal drift and miscalibrations have been corrected before analysing STM images.

In that chapter, a STM topograph of multilayer graphene grown on C-face SiC is also presented. It has been measured in a different home-made He-cooled STM at 4 K, using a commercial PtIr tip bought from Bruker.

3.2 Ultra High Vacuum (UHV) techniques

3.2.1 Multi-purpose UHV system

UHV techniques are absolutely necessary to prepare samples in a clean and controllable environment. In the work presented here, a UHV system encompassing four chambers connected to each other by a transfer tunnel shown on Fig. 3.2 has been employed. At the end of this tunnel, a chamber kept at $\sim 10^{-8}$ mbar is used to introduce samples. Samples are mounted onto molybdenum Omicron plates, which are adapted to

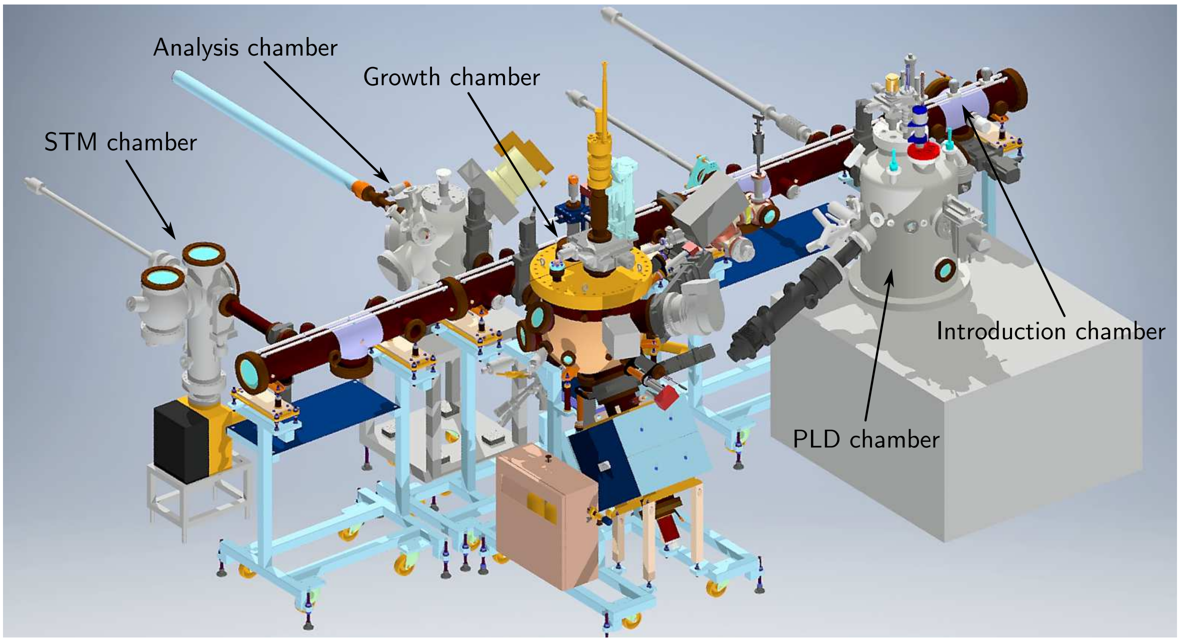

Figure 3.2: **Multi-purpose UHV system:** The UHV system is composed of 4 chambers arranged around a transfer tunnel. From left to right, the STM chamber, the analysis chamber, the growth chamber and the PLD chamber.

either single crystals or to thin films. These plates are themselves held onto 1-inch large molybdenum blocks that are transferred from chamber to chamber with magnetic transfer rods. Among the four chambers, two have been used extensively: one is dedicated to STM measurements, whereas the other is used to grow 2D materials like graphene. This second chamber is now going to be quickly presented.

To perform graphene growth in this chamber, Omicron plates are transferred onto a heating stage, where they can be heated radiatively up to ∼ 400°C, and by an electron beam up to ∼ 1300°C. Temperature was controlled using both an infra-red pyrometer, and a thermocouple mounted on the heating stage and in contact with the Omicron plate. A gas line is connected to the UHV system by a leak valve, so various gases can be controllably introduced, such as C_2H_4 or O_2. Purity of the introduced gases was systematically checked with a quadrupole mass spectrometer.

Single crystal preparation was also performed in this chamber using Ar^+ ion sputtering, both for the Re(0001) and Ir(111) surfaces presented. Argon was introduced with a dedicated valve and gas line, and bombardment was performed using a Gen 2 (Tectra GmbH) plasma source. The Re single crystal cut in the (0001) surface purchased from Surface Preparation Laboratory was cleaned by cycles with 2 keV ion energy at 750 °C and subsequent annealing at ∼ 1300 °C. As for the Ir single crystal cut in the (111) surface purchased from Surface Preparation Laboratory, it was cleaned by cycles with 1 keV ion energy and subsequent annealing at 1200 °C.

The growth chamber is also equipped with an electron gun and a phosphor screen,

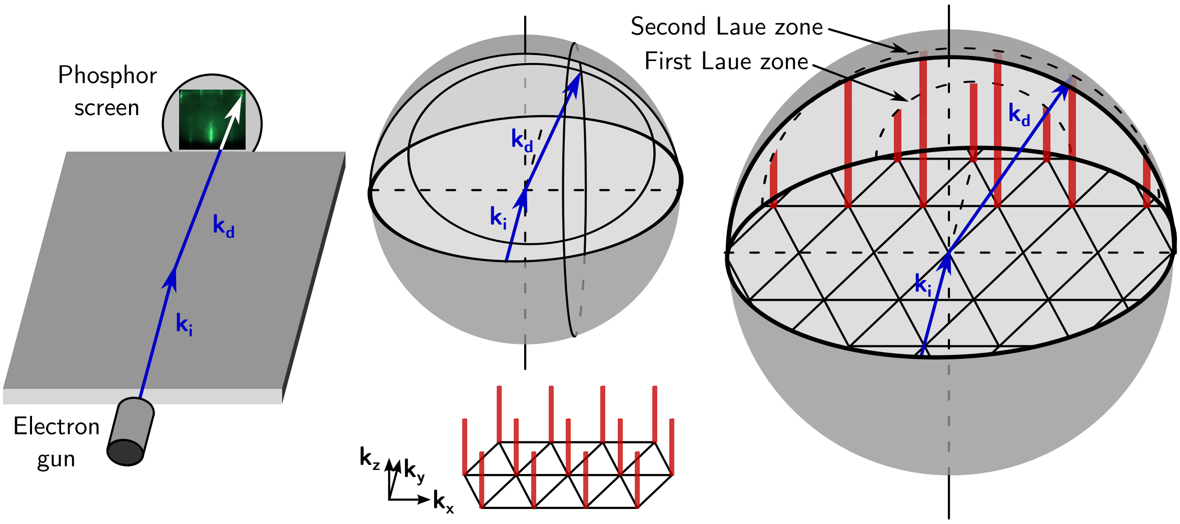

Figure 3.3: **RHEED setup. Left:** Geometry of a typical RHEED setup. A monochromatic beam of electrons is aimed at the sample surface in grazing incidence, resulting in a diffraction pattern made of streaks observed on the screen. **Top middle:** Energy conservation implies wave vector conservation, which is equivalent to the Ewald's sphere construction. **Bottom middle:** The structure factor probed by RHEED is made of truncation rods that extend along k_z. **Right:** Intersections of the Ewald's sphere with the crystal truncation rods indicate the wave vectors taken by diffracted electrons. Successive rows of truncation rods define the successive Laue zones. For clarity, the radius of the Ewald's sphere is reduced by an order of magnitude.

so as to perform reflection high energy electron diffraction (RHEED), as is now going to be presented.

3.2.2 Reflection High Energy Electron Diffraction (RHEED)

RHEED is a surface science technique commonly used to characterize and monitor thin films growth. It is indeed popular for *in operando* studies. Unfortunately, few reviews are dedicated to it. Here, [124] has been mainly used, as it delivers an intuitive description, which is summarized here.

Experimental setup

RHEED uses high-energy electrons, typically a few 10 keV ($E = 10$ keV for all RHEED patterns shown in Chapter 5) produced by thermionic emission, accelerated and focused with electrostatic lenses. In normal incidence, such electrons penetrate deep inside matter, but in RHEED, the scattering geometry corresponds to grazing incidence and exit (typically $\sim 1°$), so the sample is probed only over a few atomic planes in depth. The larger the incident angle, the more electrons probe the bulk of the sample. For a surface-sensitive analysis, the incident angle should then be chosen as small as possible. The schematic geometry of a RHEED setup is illustrated on Fig. 3.3 (left).

Due to this peculiar scattering geometry, electrons are mostly sensitive to the periodicity of the atomic rows lying parallel to the incident beam of electrons. Diffraction of electrons by parallel rows of atoms is analogous to the diffraction of visible light by an optical grating. A RHEED diffraction pattern thus consists of a set of streaks whose separation is inversely proportional to the distance between adjacent rows. With a single RHEED pattern, only a cut through the 2D reciprocal lattice is measured. By rotating the sample with respect to its z axis, different azimuths can be probed, so the full 2D reciprocal lattice can be deduced. For this reason, the heating stage can be rotated so as to probe different azimuths with different incident angles, and moved in all three directions of space to facilitate alignment of the electron beam, sample, and screen.

For a more precise understanding of this surface diffraction technique, the kinematic theory of diffraction applied to the RHEED geometry is now presented.

Kinematic theory of diffraction

In kinematic theory, only elastic single scattering events are considered. This two-fold hypothesis is going to be detailed. First, elastic scattering means that electrons have the same energy before and after scattering. Following Equation (1.11), the electron energy expresses as $E = \sqrt{m^2c^4 + \hbar^2k^2c^2}$, with m the free electron mass, and c the celerity of light. Conservation of energy then implies conservation of its wave vector k. Second, with only one scattering event, only two wave vectors have to be considered: those of the incident and diffracted electrons.

Using both hypotheses, diffraction can be simply explained using the so-called Ewald's sphere construction. Due to energy conservation, if the incident electron has a wave vector $\mathbf{k_i}$, the diffracted electron has a wave vector $\mathbf{k_d}$ of equal modulus k. When setting the center of reciprocal space at the apex of $\mathbf{k_i}$, this means $\mathbf{k_d}$ defines a sphere of modulus k known as the Ewald's sphere, and represented on Fig. 3.3 (top middle). A condition is fixed on $\mathbf{k_d}$ by energy conservation: its apex has to sit on the Ewald's sphere.

The second condition is set by the crystal reciprocal lattice. RHEED is a surface sensitive technique which probes the few topmost layers of a sample. This means that within the coherence length of the electron beam, a perfect crystal is indeed sensed by the electrons as a system with long-range x and y translational invariance, but short range z invariance. Hence the structure factor shows narrow intensity maxima in the (k_x, k_y) plane, and broad maxima in the k_z direction. This is illustrated in the case of a triangular lattice, disregarding the z periodicity for simplicity, on Fig. 3.3 (bottom middle). In a first-order approximation the position of these maxima match that of the Bragg peaks of the bulk sample, yet surface relaxation effects usually slightly shift the position of the maxima in the k_z direction with respect to the bulk case.

The wave vectors $\mathbf{k_d}$ taken by diffracted electrons have to fulfil both conditions, and then correspond to the intersection of the Ewald's sphere with the truncation rods. This is shown on Fig. 3.3 (right). The kinematic theory therefore accounts for the position of the streaks observed on a RHEED pattern and will be used to deduce precisely lattice parameters based on streak positions.

However, many other features of RHEED patterns are not explained by the above simple description. On the one hand, some effects are related to imperfections of the RHEED scheme. For instance, the electron beam is not strictly monochromatic, so the Ewald's sphere is rather a shell with non-zero thickness. The intersection of the crystal truncation rods with this shell are thus the observed streaks rather than points. Another imperfection originates from the slight divergence of the electron beam, which blurs out the origin of the reciprocal space, and therefore the Ewald's sphere position.

On the other hand, some features are directly related to necessary refinements of the kinematic theory. For example, when surface roughness is below the electron beam coherence length (of the order of 10 nm), sharp mounds are present on the surface, so grazing incidence electrons can penetrate inside them from their side. Instead of reflective, diffraction is then transmissive, hence sensitive to the crystal bulk. As a result, the truncation rods are replaced by a set of Bragg peaks, and RHEED patterns display dots instead of streaks. Similarly, when the beam incident angle is raised, surface sensitivity of RHEED is reduced, and the bulk contribution is more important. The truncation rods then become strongly modulated along k_z, as the probed sample depth is intermediate between a 2D and a 3D crystal. Furthermore, for samples composed of structurally coherent domains smaller than the coherence size of the beam, the diffraction signal is broadened by finite-size effects.

In practice, kinematic theory is satisfactory to understand the (k_x, k_y) position of the diffraction peaks, hence to extract average lattice parameters, and provides a qualitative information regarding the width of the diffraction peaks, which relates to strain fields and/or finite size effects. A comprehensive quantitative interpretation of the RHEED diffraction patterns would require a careful account of the geometry effects, and to go beyond the kinematic theory framework. A dynamical theory is actually needed to take multiple scattering events into account. Within this framework, the broad curved lines across the RHEED patterns of highly crystalline samples, called Kikuchi lines, are also understood.

RHEED data analysis

For an accurate determination of streak positions, a systematic RHEED pattern fitting procedure has been developed. In short, specific parts of the RHEED pattern are averaged to define line profiles. A well-suited fitting function is then selected, and a least-squares fitting procedure gives access to the streak intensity, position and width. A graphical user interface has also been designed for user-friendly batch-analysis of RHEED patterns and movies. Details about each step of this procedure are now given.

First, when RHEED patterns are obtained on the phosphor screen, they are captured using a CCD camera, which provides images with 1280×960 pixels, with the intensity on each pixel $I(x, y)$ coded on 10 bits (from 1 to 1024). To maximize the signal to noise ratio, intensity is adjusted with the camera shutter. Moreover, to analyse each streak

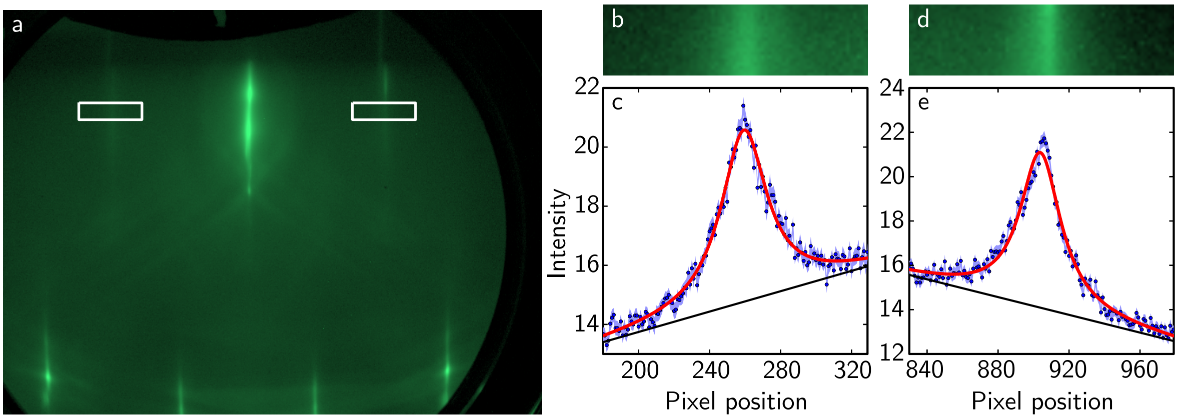

Figure 3.4: **RHEED pattern analysis.** (**a**) RHEED pattern obtained for a clean Re(0001) surface. The central intense specular streak lies in between two less intense Re streaks in the first Laue zone, on which white rectangles define regions of interest. At the bottom of the pattern, four shorter streaks correspond to Re streaks in the second Laue zone. (**b-d**) Close-up views of the regions of interest. Line profiles are extracted from them by line averaging along the vertical direction. (**c-e**) Extracted profiles (blue points, error bars are a blue shade) are fitted by lorentzian peaks on a linear background. Low intensity rods have been chosen so error bars are visible.

with the maximum signal to noise ratio, a different image is taken for each streak with its intensity adjusted just below the camera saturation level.

Second, to perform fits, one needs to define a statistical model. The intensity of each pixel $I(x, y)$ is assumed to be random, and since it takes large values (> 20), it is modelled with a normal law: $I(x, y) \sim \mathcal{N}(\tilde{I}(x), \tilde{\sigma}^2)$, with $\tilde{I}(x)$ and $\tilde{\sigma}$ the physical intensity and its intrinsic standard deviation. Rectangular regions of interest are selected on the RHEED pattern, as represented with white rectangles on Fig. 3.4a. Its height is set so all lines are close to identical. As a consequence, each line can be considered as an independent measurement of $\tilde{I}(x)$. Its unbiased estimator $\bar{I}(x)$ is given by the mean of $I(x, y)$ along the y direction, so line averaging is performed in the vertical direction over the N lines of the region of interest. This translates as:

$$\bar{I}(x) = \frac{1}{N} \sum_{y=1}^{N} I(x, y) \tag{3.3}$$

$\bar{I}(x)$ then follows a normal law $\bar{I}(x) \sim \mathcal{N}(\tilde{I}(x), {}^{\tilde{\sigma}^2}\!/_{N})$, so its standard deviation is ${}^{\tilde{\sigma}}\!/_{\sqrt{N}}$. Getting an unbiased estimator of the standard deviation $\tilde{\sigma}$ is more challenging. Nevertheless, as a normal law is used here, the so-called rule-of-thumb applies [16], and the corrected biased estimator $\bar{\sigma}(x)$ writes:

$$\bar{\sigma}(x) = \sqrt{\frac{1}{N-1.5}\sum_{y=1}^{N}\left(I(x,y) - \bar{I}(x)\right)^2} \tag{3.4}$$

This estimator is slightly biased, but the bias is below 0.1 % for $N > 9$ lines. For the regions of interest magnified on Fig. 3.4b,d, $\bar{I}(x)$ and $\bar{\sigma}(x)$ correspond to the blue data points and error bars of Fig. 3.4c,e.

Third, and finally, a fitting function is picked and fitted to the data using a least-squares algorithm. Lorentzian profiles appear to provide satisfactory fits, although this choice is difficult to justify on physical grounds. As for the background, typical shapes are used: flat, linear, quadratic or lorentzian. The origin of this background is usually the intense specular streak or Kikuchi lines, which are both well-fitted with lorentzian profiles.

Using this method, streak positions can easily be determined with sub-pixel resolution, which typically translates into lattice parameter uncertainty in the range of few 0.001 Å.

As a side note, when RHEED patterns of high quality epitaxial graphene on a metal are investigated, the moiré superperiodicity gives rise to a succession of evenly-separated rods sharing the same width, as can be seen on Fig. 5.1. Dedicated fitting functions fulfilling these conditions have been designed for such profiles.

3.2.3 Graphene growth on Re(0001)

While the properties of graphene epitaxially grown on various metals have been discussed in Chapter 2, its preparation has been omitted. In all cases, it requires to expose the clean metallic surface to a carbon-containing precursor at sufficiently high temperature.[2] If the carbon precursor is a molecule, the growth technique is commonly referred to as chemical vapour deposition (CVD), because chemical reactions implying cracking of this molecule are involved in graphene growth. When the precursor is atomic carbon, it is then called physical vapour deposition (PVD), as no chemical reaction is needed and thermal energy is brought only to activate the mobility and attachment of carbon atoms. More information about the different growth techniques and underlying mechanisms can be found in dedicated review publications [5, 191]. In the following, only CVD will be introduced in order to discuss the particular case of graphene on Re(0001).

Three typical CVD recipes can be distinguished. The first one consists in covering the surface with precursor molecules at room temperature first, then interrupt its exposition to the precursor, and finally anneal it, so only the adsorbed species react and form graphene patches. Since the final annealing step is the one triggering graphene

---

[2] Graphene preparation on SiC is usually different, as at high temperature, Si sublimates from the SiC crystal and C atoms rearrange at the surface to form graphene layers [42, 47].

formation, this method is called temperature-programmed growth (TPG). It can be employed to obtain a partial graphene coverage [32, 114, 209], or to use the patches as seeds to grow high quality graphene [84].

A second recipe consists in exposing the surface to the precursor when it is already at high temperature. This way, as the growth takes place, new molecules are continuously provided by the gas phase. This second method is called CVD by specialists, as in this case, chemical reactions occur while the gaseous and solid phases coexist. It is the most well-known one, because it is widely employed on polycrystalline Cu without UHV requirement [116], as well as in various systems under UHV [191].

To understand the third method, it should be specified that in the above-described CVD, graphene growth competes with other processes, such as carbon dissolution and precursor desorption. Indeed, thermodynamics shows that solubility of atomic carbon in metals increases exponentially with temperature. For metals of sufficiently high solubility, purposeful dissolution of carbon atoms can be achieved at high temperature, so when the sample is slowly cooled down, carbon segregates at the surface and forms graphene. This has for example been achieved with polycrystalline Ni [225] and single crystal Ru(0001) [135, 170].

With this distinction in mind, details about graphene preparation on Re(0001) are now going to be given. Few works are devoted to graphene supported by this substrate [1, 142, 158, 193], and only one to its growth [143]. As a general trend, interaction of carbon with rhenium results in three competing processes depending on temperature: graphene growth, bulk dissolution, and carbide formation. To avoid the two latter, relatively low temperatures have to be used, resulting in a non-trivial growh process, with many competing reaction paths, as will discussed in Chapter 5.

Applying a TPG method to Re(0001) with annealing temperature between 850 and 1100 K does not lead to graphene, but to a surface carbide [143], with a $(7 \times \sqrt{19})$ structure that has been reported by LEED studies [143, 232] illustrated on Fig. 3.5d. Besides, this carbide is stable at high temperature, so it does not convert to graphene, contrary to other systems like Ni(111) [109,161]. On the contrary, graphene on Re(0001) converts into this surface carbide at temperatures above 1200 K [143]. Above 1350 K, this carbide dissolves into the bulk of the Re crystal [143].

Graphene growth then requires to avoid high temperature carbide formation. One growth recipe is a hybrid TPG-CVD method, which consists in a succession of rapid annealing cycles between 300 and 1100 K, in a C_2H_4 background [142, 143]. At each cycle, *in operando* LEED studies have proved graphene's crystalline quality to improve, as visible on Fig. 3.5a-b. This method was therefore used to produce the full layer graphene sample presented in Chapters 4 and 5. An additional sample partially covered with graphene is studied in Chapter 5, and has been obtained following a simple TPG method at 800 K.

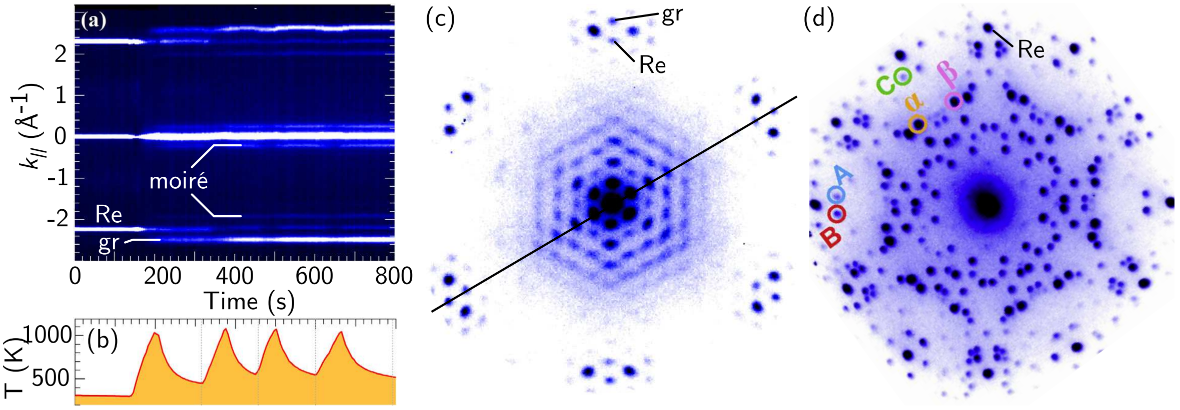

Figure 3.5: **Graphene and carbide formation on Re(0001).** (**a**) LEED line profile evolution during graphene growth on Re(0001), following annealing-cooling cycles indicated by the temperature evolution (**b**). (**c**) LEED pattern for high quality graphene on Re(0001), with the cut taken for the profile (**a**). Spots due to graphene, rhenium are indicated, while all the others are due to the moiré superlattice. (**d**) LEED pattern of the surface carbide, with six-fold symmetry due to the coexistence of rotated carbide domains. Adapted from [143].

3.3 Simulation

3.3.1 Density functional theory (DFT)

Calculations shown in Chapters 4 and 5 have been performed in the framework of Density Functional Theory (DFT). The used code – VASP – enables to relax the atomic structure, so as to determine the equilibrium atom positions, and calculate the system electronic band structure. Solving the Schrödinger equation of a complex system with interacting electrons is a difficult task, which requires many steps and levels of approximation.

The first step separates the electronic and ionic parts of the problem. Indeed, the mass ratio between an electron and the lightest of all ions (H^+) is of 1/1832. This small ratio results in different typical time scales for electrons and ions, so electrons can be considered to react instantly to any ion displacement. In other words, for any ionic behaviour, electrons can be considered as in their ground state. This means that the electronic part and ionic parts can be decoupled, and is known as the Born-Oppenheimer approximation.

The ionic part is treated by classical equations of movement, and their positions define the electric potential experienced by the N electrons of the system. Their configuration is deduced from the electronic Schrödinger equation. Some approaches are based on the electronic wave functions, but even for slightly complex systems, this requires very large computation time and memory. Hohenberg and Kohn have suggested a different approach based on the charge density. They have first proved that every term of the Schrödinger equation, including the electron-ion interaction, are a functional of the charge density. Solving the Schrödinger equation is then equivalent to minimize the energy with respect to the charge density functional – a problem that can efficiently be solved numerically. The obtained energy minimum and associated charge density are that of the ground state.

Still, calculating the charge density is a difficult problem for a system of N interacting electrons. To achieve this, Kohn and Sham have re-introduced an approach based on atomic orbitals, which consists in building the system wave function on a basis of one-electron orbitals. The electronic Schrödinger equation then rewrites as a set of one-electron Schrödinger-like equations, known as the Kohn-Sham equations [100]. They contain an additional term accounting for electron-electron interactions, called the exchange-correlation potential, to which the exchange-correlation energy is associated.

Except for very simple systems, calculating the exchange-correlation term is too complex, so the exact theory explained so far has to be simplified using some approximation. One is the local density approximation (LDA), which is based on a homogeneous electron gas. At each point $\mathbf{r}$ of the system, the charge density expresses as $n(\mathbf{r})$. The exchange-correlation energy of the system at $\mathbf{r}$ is then set equal to that of a homogeneous electron gas with density $n(\mathbf{r})$ [100]. This crude approximation provides very good results, and its successes have made DFT famous. As it is based on a homogeneous electron gas, it tends to simulate the system more homogeneous than what it really is, underestimating interatomic distances and overestimating binding energies. For this reason, corrections have been proposed, such as the generalized gradient approximation (GGA), which not only takes the density $n(\mathbf{r})$ into account, but also its gradient $\nabla n(\mathbf{r})$ [163].

With the description provided so far, the total energy of the system can be derived. From that, it is possible de calculate its variations upon atomic displacements, and to deduce the forces applied to these atoms. By minimizing the forces, the equilibrium atomic structure can be deduced.

As for the electronic structure, its calculation relies on the Kohn-Sham orbitals. They are in principle intermediates in the derivation of the charge density. Indeed, the Kohn-Sham equations are Schrödinger-like equations whose eigenenergies and eigenvectors are those of an effective electronic system with same charge density as the real system. Given the formalism of DFT, only the total energy and Fermi level are meaningful. Nonetheless, the dispersion of these quantities in the Brillouin zone is often very relevant to the band structure of the real system.

In the calculations presented in this thesis, the Vienna Ab initio Simulation Package (VASP) code has been used. As one might guess, it has been developed in the Technical University of Vienna, in Austria. It relies on a basis of plane waves, and the electron-ion interaction is described using the projected augmented wave (PAW) formalism [106]. This well-optimised approach enables to deal with relatively large systems like surfaces or interfaces.

This feature is valuable, as VASP can only calculate periodic systems. For systems with broken translational invariance, such as defects or surfaces, large supercells are then needed. The defect is put at the center of a unit cell, and surrounded with a certain number of additional cells, constituting one large supercell. As an example, the graphene on Re(0001) supercell contains a few Re planes, on which is set a graphene plane, as well as a vacuum slab. This design is chosen to compensate for the periodic boundary conditions in the vertical direction of space. Indeed, the central Re plane should have properties similar to a bulk crystal, and the vacuum slab prevents from spurious interactions between graphene and the backside Re.

In all calculations shown, five planes of Re have been chosen, as well as a vacuum slab of at least 25 Å. These calculations are based on the GGA approach with Perdew–Burke–Ernzerhof (PBE) functional, which is well-suited to surfaces and interfaces [164]. Van der Waals interactions are also taken into account semi-empirically using Grimme approach [64].

3.3.2 Parametrized atomistic potentials

When larger systems on larger time scales have to be considered, DFT calculations become intractable in terms of computational time. One can then turn to molecular dynamics (MD), which solves the classical equation of atomic motion using empirical interatomic potentials. As such potentials are analytical, and depend only on interatomic distances, calculating the forces exerted to atoms can be done efficiently. However, they contain empirically adjusted parameters and correction terms. This implies this method must not be used in a situation deviating too much from the one used to adjust these potentials.

Here, a Brenner bond-order potential (BOP) has been used and adjusted for Ru-C systems [52]. BOP is a class of empirical potentials that is based on the Pauling concept of bond order, which means the strength of a bond depends on its local environment. Highly-coordinated atoms indeed establish weak bonds, as opposed to lowly-coordinated atoms. Thus, BOP can efficiently describe different bonding states of an atom. Within the BOP class, the specificity of a Brenner BOP is to account well for some carbon properties, such as the formation of radicals, and the difference between conjugated and non-conjugated systems [14].

To give an elementary picture of the potential form, the Brenner BOP decomposes into two parts: one repulsive and one attractive. Both have an exponential form with adjustable parameters, so the total potential has a Morse-like expression. In this formulation, the bond order is the weight attributed to the attractive part of the potential: the more coordinated the bond is, the more attractive it is. The bond order also contains an angular dependence in order to account for the bending rigidity of the bonds. Finally, lower and upper smooth cutoff distances are set in the model, consistent with the local environment dependence.

Three kinds of bonds have to be parametrized: Ru-Ru, Ru-C and C-C. For Ru-Ru, the BOP can be brought back to the second moment approximation to the tight-binding scheme, which has been parametrized for Ru. For C-C, the original BOP has been used. As for the Ru-C bond, its parameters have been fitted to values obtained by DFT calculations. Finally, as the BOP depends on the local environment only, an additional correction is needed for van der Waals forces. Here, the empirical Grimme D2 correction is added as a non-bonding interaction term, with parameters taken from [64]. The nonadditive character of the van der Waals forces is also taken into account.

Overall, the parametrized atomistic potentials presented here obtain very good agreement with DFT results of bare graphene on Ru(0001), therefore justifying its use in situations where DFT would be too demanding [52].

In the context of Chapter 5, configurations inferred from STM observations of graphene on Re(0001) are calculated in the case of graphene on Ru(0001). Two reasons support the validity of this modification. Indeed, Ru(0001) and Re(0001) both have a tendency for strong graphene-metal interaction, giving rise to large moiré corrugations [193, 213]. Moreover, the defect reported in Chapter 5 for graphene on Re(0001) has been observed on Ru(0001) as well in similar situations [129, 146, 209].

These results, presented on Fig. 5.19, have been obtained in the context of a collaboration. Many possible configurations have been provided to Daniel Förster and Florent Calvo, who performed the calculation using parametrized atomistic potentials.

Chapter 4

Classification of commensurate graphene moiré superlattices

The 2D character of free-standing graphene is the reason for its non-crystalline state, called a floating order, where the atoms fluctuate in position with a logarithmic dependence on sample size. When supported, one can wonder if this floating order survives the irruption of a 3D substrate, or if graphene tends to lock with a (high-order) commensurate relation to the substrate. In the framework of the Frank and van der Merwe model, these are the two sides of the commensurate-incommensurate transition. If incommensurate, one would expect to observe Goldstone modes as a signature of thermal fluctuations. If otherwise commensurate, a given translational superperiodicity in the structure should be detectable. In this Chapter, a method to identify by STM and analyse with very high precision the commensurate structure is presented and exemplified [1].

The usual structural model used to describe moiré superlattices assumes (Fig. 4.1, top left) that a single moiré beating occurs within a moiré period and that the graphene and moiré lattices are commensurate (integer multiples of their lattice parameters can be found to make them match). This superlattice model was for instance often used to describe graphene on Ir(111), but eventually proved too restrictive, as the variety of situations observed in experiments [72,76,84,120,136,205] depends critically on growth conditions [10] and sample history [73,84]. Accordingly, more general models have been proposed. Some simply assume that the graphene and moiré lattices are incommensurate [147]. Others assume commensurability, yet without the constraint of a single moiré beating within the moiré unit cell. This situation is sketched in Fig. 4.1 (bottom left) and accounts for experimental data obtained with graphene on Ru(0001) and on Ir(111), for which four beatings were proposed in case of the zigzag rows of graphene aligning the close-packed ones of the metal [10,81,84,134] and even more for graphene whose zigzag rows are $\sim 30°$ rotated [120].

There are many ways the above assumption for commensurability can be fulfilled, as can be shown by considering strains and rotation of the graphene with respect to its substrate [137]. For substrates exerting a weak bonding with graphene, rotations readily occur [120,190]. Strain, on the contrary, is more energetically costly in reason of the high mechanical stiffness of graphene [111]. It appears that strains beyond few percents are not achievable in graphene synthesized on a substrate. Formal treatments of strain so far exclusively assumed biaxial strain. One noticeable exception is the description given by Hermann [75]. This description relates geometrical transformations

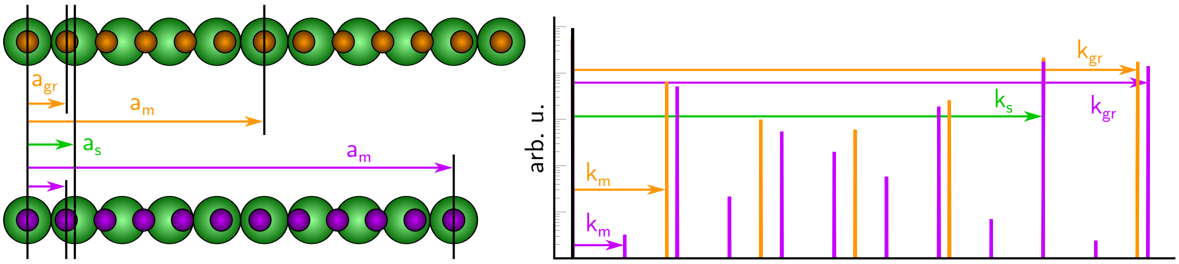

Figure 4.1: **Moiré superlattice and beatings. Left:** ball model of a chain of (small) carbon atoms in graphene on top of a chain of (large) atoms from the support, both having different lattice parameters a_{gr} and a_{s}, whose commensurability define a moiré superlattice with period a_{m}. **Right:** Corresponding fast Fourier transform (FFT). For 6 graphene periods matching 5 support periods (orange), a single beating occurs within the moiré period, and the FFT reveals a fundamental harmonic defined by $k = {}^{(k_{\mathrm{gr}}-k_{\mathrm{s}})}/_{(6-5)}$. For 11 graphene periods matching 9 support periods (purple), two beatings occur within the moiré period, with similar stacking configurations at the edges and at the middle of the ball model. The corresponding FFT reveals a fundamental harmonic at $k = {}^{(k_{\mathrm{gr}}-k_{\mathrm{s}})}/_{(11-9)}$.

to a set of indices characterizing the commensurability between two triangular lattices. Among the transformation considered in Hermann's work is a shear strain, applied with a similar magnitude for the two lattices. No account for the recently observed case of sheared graphene onto a rigid lattice [10], such as a metallic substrate whose deformations induced by graphene can be neglected, has been found.

Here the straightforward extension of Hermann's formalism to the latter case is presented. Besides, the relationships that establish the consistency between this formalism and another one are derived. This other formalism has been recently presented by Zeller and Günther to describe the number of beatings a moiré can comprise [228]. Overall, with the help of geometrical transformations, a fully-consistent description of the full complexity of commensurate moiré superlattices is provided, relating the graphene, substrate, and moiré, for the general case of an arbitrary strain (including shear, uniaxial, biaxial) and of superlattices having any number of beating. This transformation is expressed within a matrix formalism and in an extension of the so-called Wood's notation, which gives the angles formed between the unit cell vectors of graphene and the moiré as well as the ratio between these vectors' length. The latter notation is used to construct maps of the possible commensurate moiré superlattices and to revisit previously published analysis of experimental observations. It shows supported graphene is subjected to strain levels far below what is usually assumed.

This description is applied to resolve the structure of the moiré superlattices in graphene on multilayer graphene prepared on SiC, and in monolayer graphene grown on Re(0001) and Ir(111). For this purpose, STM is used in both direct and reciprocal (Fourier) space, in the latter case achieving better than 0.1 pm precision on the lattice parameter determination, owing to distortion-less imaging with atomic resolution across several 10 nm fields of view. Rotated and sheared moiré superlattices are found. Similarly to the rotation, shear appears more obviously in the moiré than in the graphene, as confirmed by DFT calculations. Some of these moirés comprise several beatings in the case of metal substrates. Strikingly, commensurability between graphene and moiré superlattices provides a fine description of even very large moiré supercells, comprising above $1,000$ carbon atoms.

4.1 General framework

In this section, the (sometimes heavy) algebra underlying the interpretation of the STM results is detailed. In short, graphene will always be considered uniform, and a high order commensurate relation with its substrate will be assumed. Under this assumption, a general analysis scheme can be used on both diffraction patterns and Fourier-transformed atomically-resolved images to extract the commensurate relation. One can then relate it to other parameters such as a Wood's notation or strain levels. The reader is warned that until the end of subsection 4.1.3, this section is rather heavy in terms of algebra and mathematical details. All details are included, so all necessary equations to analyse moiré superlattices are provided to the reader. The essential formulae that will most often be sufficient to interpret experimental results are given in Equations (4.5), (4.15a–4.15d) and (4.16a–4.16d), and (4.32).

In most cases, supported graphene and its substrate do not share the same lattice parameter and/or graphene lies twisted by some angle with respect to its support. Assuming commensurability between the two lattices, a supercell can be defined which comprises the smallest integer numbers of unit cells of both graphene and the support. This supercell defines the moiré superlattice. Formally, in a 1D picture, the moiré superlattice parameter a_m is an integer number times graphene's (a_gr) or the support's (a_s) lattice parameters: $a_\mathrm{m} = i\ a_\mathrm{gr} = m\ a_\mathrm{s}$, with i and m two coprime integers.

Still in 1D, the reciprocal space unit vectors of the moiré superlattice (k_m), of graphene (k_gr) and of the support (k_s) hence fulfil $i\ k_\mathrm{m} = k_\mathrm{gr}$ and $m\ k_\mathrm{m} = k_\mathrm{s}$. It should be emphasized that these two equations constitute the general definition of a moiré superlattice. On the contrary, the definition usually proposed in the literature is that of the beating period (a_b), $k_\mathrm{b} = k_\mathrm{gr} - k_\mathrm{s}$, which does not require commensurability. $k_\mathrm{m} = k_\mathrm{b}$ can be obtained in the particular case of a commensurate system, with $i - m = 1$, *i.e.* with i and m two consecutive integer numbers. This particular case is sketched in Fig. 4.1 (top left). Figure 4.1 (bottom left) shows a different situation with $i - m = 2$. Strikingly, at first sight the two moiré superlattices in Fig. 4.1 are very similar. Indeed, at the middle of both linear ball models, the stacking of the carbon atoms onto the substrate ones is similar. In an analogy with optics, beatings between the two lattices seem to occur at the same location. Careful inspection however reveals that, for the $i - m = 1$ moiré (Fig. 4.1, top left), the central carbon atom sits exactly on top of the atom underneath, while for the $i - m = 2$ moiré (Fig. 4.1, bottom left), the coincidence is only approximate. The difference is most often subtle in a scanning probe microscopy experiment [81] (similar graphene/support stackings yield similar signals), and usually overlooked, so the $i-m=2$ is generally (erroneously) described as a $i-m=1$ moiré.

In fact it has a richer Fourier spectrum than the latter, as can be seen on Fig. 4.1 (right). The fundamental Fourier harmonic of the $i-m=2$ moiré is $k_{\mathrm{m}} = {}^{(k_{\mathrm{gr}}-k_{\mathrm{s}})}/_{(i-m)} = {}^{(k_{\mathrm{gr}}-k_{\mathrm{s}})}/_{2}$, and not $(k_{\mathrm{gr}}-k_{\mathrm{s}})$ as is the case for the $i-m=1$ moiré. The predominant intensity of the second harmonic $(k_{\mathrm{gr}}-k_{\mathrm{s}})$ translates nothing else than the close (but not exact) lattice coincidence observed at the beating period (Fig. 4.1, bottom left). The Fourier description of moiré superlattices naturally makes the distinction between both, the $i-m=1$ moiré containing only one beating, and the $i-m=2$ comprising two distinct ones. For this reason, experimental data will be analysed in Fourier space.

In 2D, the generalization of the above relations resorts to (2×2) matrices. For example, the unit cell of graphene is related to that of its substrate as:

$$\begin{pmatrix} \mathbf{a_{gr_1}} \\ \mathbf{a_{gr_2}} \end{pmatrix} = \begin{pmatrix} a & b \\ c & d \end{pmatrix} \begin{pmatrix} \mathbf{a_{s_1}} \\ \mathbf{a_{s_2}} \end{pmatrix} \tag{4.1}$$

This translates into reciprocal space as:

$$\begin{pmatrix} \mathbf{k_{s_1}} \\ \mathbf{k_{s_2}} \end{pmatrix} = \begin{pmatrix} a & c \\ b & d \end{pmatrix} \begin{pmatrix} \mathbf{k_{gr_1}} \\ \mathbf{k_{gr_2}} \end{pmatrix} \tag{4.2}$$

where (a,b,c,d) are four numbers with no assumption made on a possible high order commensurate relation. The existence of such a relation is actually not always assumed, *i.e.* the sole beating phenomenon is sometimes considered [221,228]. To avoid any confusion, a distinction is going to be made between the beating period, which corresponds to the strongest contribution in the Fourier transform, and the moiré superperiodicity, which is the translational invariant.

Besides, graphene is generally assumed to be six-fold D_{6h} symmetric, yielding $c=-b$ and $d=a-b$. In this case, a rather simple formalism is used to interpret the structure of a moiré superlattice, which is going to be summarized first.

4.1.1 Moiré superlattices without commensurability

With no commensurability hypothesis and assuming unsheared structures, the plane transformations relating graphene and its support is a rotation-scaling:

$$\begin{pmatrix} \mathbf{k_{gr_1}} \\ \mathbf{k_{gr_2}} \end{pmatrix} = \mathrm{P} \begin{pmatrix} p & 0 \\ 0 & p \end{pmatrix} \begin{pmatrix} \cos\varphi & -\sin\varphi \\ \sin\varphi & \cos\varphi \end{pmatrix} \mathrm{P}^{-1} \begin{pmatrix} \mathbf{k_{s_1}} \\ \mathbf{k_{s_2}} \end{pmatrix} \tag{4.3}$$

With $\mathrm{P} = \begin{pmatrix} 1 & 0 \\ -1/2 & \sqrt{3}/2 \end{pmatrix}$ the matrix that links a hexagonal to an orthonormal basis, and $p = \dfrac{a_{\mathrm{gr}}}{a_{\mathrm{s}}}$ defined as the scaling factor. p is related to biaxial strain ε_{b} in graphene.

Moreover, in reciprocal space, the beating has the visible Fourier component with lowest frequency, and its wave vector along one direction usually corresponds to the wave vector mismatch:

$$\mathbf{k_{b_1}} = \mathbf{k_{gr_1}} - \mathbf{k_{s_1}} \tag{4.4}$$

Using Equations (4.3) and (4.4), $\mathbf{k_{b_1}}$ is decomposed on the support reciprocal basis $(\mathbf{k_{s_1}}, \mathbf{k_{s_2}})$, which gives:

$$\begin{aligned}\mathbf{k_{b_1}} &= \mathbf{k_{gr_1}} - \mathbf{k_{s_1}}\\ &= \left(p\ \cos\varphi - \frac{p\sqrt{3}}{3}\sin\varphi - 1\right)\mathbf{k_{s_1}} + \frac{2p\sqrt{3}}{3}\sin\varphi\ \mathbf{k_{s_2}}\end{aligned}$$

From which the beating period $a_\mathrm{b} = \dfrac{4\pi\sqrt{3}}{3\sqrt{\mathbf{k_{b_1}}\cdot\mathbf{k_{b_1}}}}$ is extracted and expressed as a function of a_s, p and φ:

$$a_\mathrm{b} = a_\mathrm{s}\sqrt{\frac{1}{1 - 2p\ \cos\varphi + p^2}}$$

This relation is the most commonly used one [221]. Assuming there are N beatings per moiré supercell ($\sqrt{N}\ \mathbf{k_{m_1}} = \mathbf{k_{b_1}}$), it can be extended straightforwardly to the moiré period:

$$a_\mathrm{m} = a_\mathrm{s}\sqrt{\frac{N}{1 - 2p\ \cos\varphi + p^2}} \tag{4.5}$$

This simple model has also been extended to account for more general situations [228]. Indeed, the beating arises from a mismatch between two spatial frequencies. Higher order Fourier components[1] than in Equation (4.4) may be considered as well and the reciprocal lattice unit vectors along one direction of the first three of them (2^nd to 4^th order) are defined by:

$$\begin{aligned}\sqrt{N}\ \mathbf{k_{m_1}} &= \mathbf{k_{b_1}} = \mathbf{k_{gr_1}} + \mathbf{k_{gr_2}} - 2\mathbf{k_{s_1}}\\ \sqrt{N}\ \mathbf{k_{m_1}} &= \mathbf{k_{b_1}} = \mathbf{k_{gr_1}} + 2\mathbf{k_{gr_2}} - 3\mathbf{k_{s_1}}\\ \sqrt{N}\ \mathbf{k_{m_1}} &= \mathbf{k_{b_1}} = \mathbf{k_{gr_1}} + 3\mathbf{k_{gr_2}} - 4\mathbf{k_{s_1}}\end{aligned}$$

Using these particular relations for higher order beatings, one gets:

---

[1] This term reminds the high order commensurate relations of the Frank and van der Merwe model. In that context, it corresponds to the integers i and m defining the moiré superlattice. On the contrary, for beatings, “high order” refers to the order of the taken harmonics. These numbers are not related.

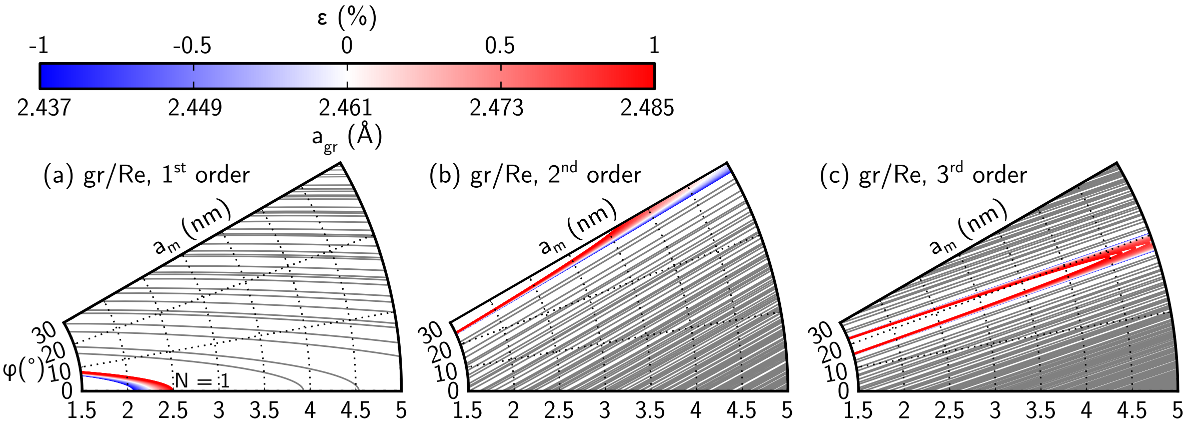

Figure 4.2: **Moiré superperiodicity for beatings of each Fourier order.** Depending on the definition chosen for a beating, the relation between the moiré superperiodicity a_m, the twist angle φ, and the strain level ε (given by colour for a $N = 1$ moiré superlattice) changes drastically. $N > 1$ moiré superlattices are indicated by only a gray line. **Left:** 1st order beating (see Equation (4.5)) with maximum of a_m at $\varphi = 0°$. **Middle:** 2nd order beating (see Equation (4.6)) with a maximum of a_m at $\varphi = 30°$. **Right:** 3rd order beating (see Equation (4.7)) with a maximum of a_m at $\varphi \sim 19°$.

$$2^{\text{nd}}\ \text{order} : a_\mathrm{m} = a_\mathrm{s}\sqrt{\frac{N}{4 - 6p\ \cos\varphi + 2p\sqrt{3}\ \sin\varphi + 3p^2}} \tag{4.6}$$

$$3^{\text{rd}}\ \text{order} : a_\mathrm{m} = a_\mathrm{s}\sqrt{\frac{N}{9 - 12p\ \cos\varphi + 6p\sqrt{3}\ \sin\varphi + 7p^2}} \tag{4.7}$$

$$4^{\text{th}}\ \text{order} : a_\mathrm{m} = a_\mathrm{s}\sqrt{\frac{N}{16 - 20p\ \cos\varphi + 12p\sqrt{3}\ \sin\varphi + 13p^2}}$$

For a substrate with given a_s, these Equations express the dependence of a_m on the twist angle φ, the scaling factor p and the number of beatings N. Examples of this dependence are given on Fig. 4.2 for moirés of graphene on Re(0001) with beatings defined with Fourier components of 1st, 2nd and 3rd orders.

Following this method, any beating order can be accounted for. The most general case can then be considered, with a relation such as $\sqrt{N}\ \mathbf{k_{m_1}} = \mathbf{k_{b_1}} = g_1\mathbf{k_{gr_1}} + g_2\mathbf{k_{gr_2}} + s_1\mathbf{k_{s_1}} + s_2\mathbf{k_{s_2}}$. According to this convention, beatings defined with 1st and 2nd orders components correspond respectively to $(g_1, g_2, s_1, s_2) = (1, 0, -1, 0)$ and $(g_1, g_2, s_1, s_2) =$

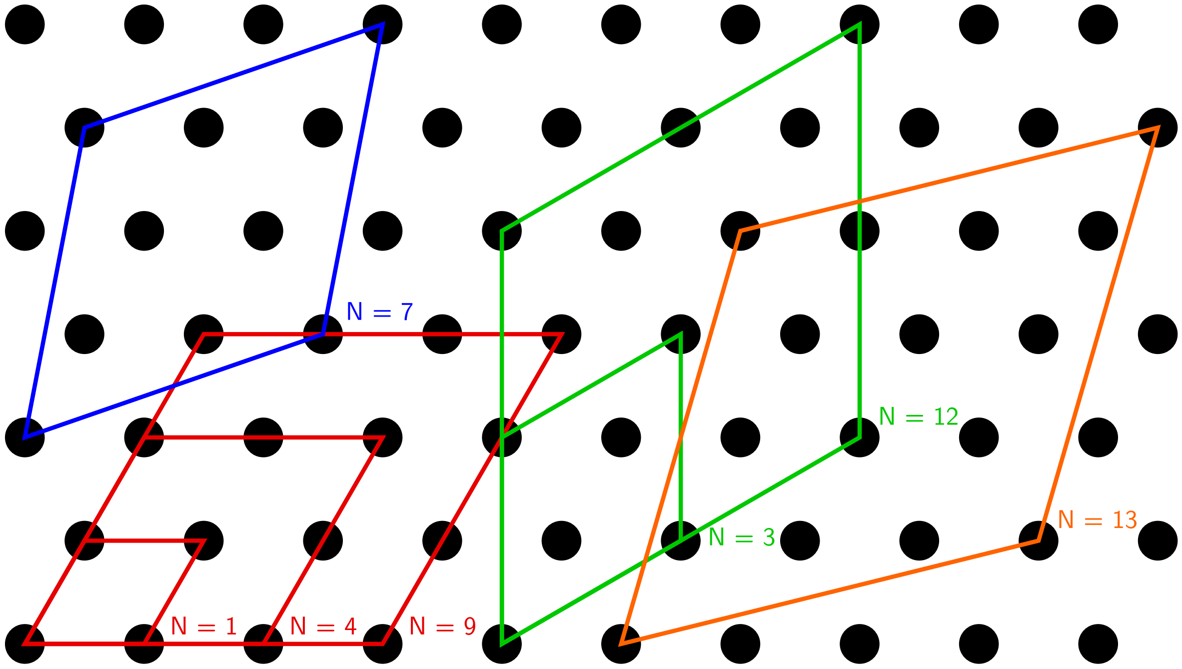

Figure 4.3: **Possible numbers of beatings.** Scheme enumerating the hexagonal moiré cells for an increasing value of beatings N per moiré unit cell. Each beating is displayed as a black circle. For isotropic superlattices, only solutions of the Diophantine equation $a^2 + b^2 - ab = N$, $a, b \in \mathbb{N}$, are allowed.

$(1, 1, -2, 0)$. In the general case, the period a_m is:

$$a_\mathrm{m} = a_\mathrm{s}\sqrt{\frac{N}{(s_1^2 + s_2^2 + s_1 s_2) + (2(g_1 s_1 + g_2 s_2) + g_1 s_2 + g_2 s_1)p\,\cos\varphi + (g_1 s_2 - g_2 s_1)p\sqrt{3}\,\sin\varphi + (g_1^2 + g_2^2 + g_1 g_2)p^2}} \tag{4.8}$$

The integer values taken by N are constrained by the hexagonal lattice through the following Diophantine equation: $a^2 + b^2 - ab = N$, where a and b are integers. A geometrical picture of this problem is given on Fig. 4.3.

4.1.2 Moiré superlattice with commensurability

The use of two integers i and m in 1D to express the commensurate relation, as on Fig. 4.1, can be generalized to the 2D case. In order to account for its structural complexity, a set of eight integers (i, j, k, l, m, n, q, r), which are determined through atomically-resolved microscopy, is then necessary (only four are needed to describe graphene maintaining the D_{6h} symmetry, *i.e.* when it is only strained biaxially and rotated).

The commensurate relation then expresses in the matrix form as:

$$\begin{pmatrix} \mathbf{a_{m_1}} \\ \mathbf{a_{m_2}} \end{pmatrix} = \underbrace{\begin{pmatrix} i & j \\ k & l \end{pmatrix}}_{= M_{\text{gr}}} \begin{pmatrix} \mathbf{a_{gr_1}} \\ \mathbf{a_{gr_2}} \end{pmatrix} = \underbrace{\begin{pmatrix} m & n \\ q & r \end{pmatrix}}_{= M_{\text{s}}} \begin{pmatrix} \mathbf{a_{s_1}} \\ \mathbf{a_{s_2}} \end{pmatrix} \tag{4.9}$$

This translates into reciprocal space as:

$$\begin{pmatrix} \mathbf{k_{gr_1}} \\ \mathbf{k_{gr_2}} \end{pmatrix} = \underbrace{\begin{pmatrix} i & k \\ j & l \end{pmatrix}}_{= M_{\text{gr}}^{\text{T}}} \begin{pmatrix} \mathbf{k_{m_1}} \\ \mathbf{k_{m_2}} \end{pmatrix} \text{ and } \begin{pmatrix} \mathbf{k_{s_1}} \\ \mathbf{k_{s_2}} \end{pmatrix} = \underbrace{\begin{pmatrix} m & q \\ n & r \end{pmatrix}}_{= M_{\text{s}}^{\text{T}}} \begin{pmatrix} \mathbf{k_{m_1}} \\ \mathbf{k_{m_2}} \end{pmatrix} \tag{4.10}$$

The (i, j, k, l, m, n, q, r) integers used here correspond to the decomposition of the superstructure lattice vectors $\mathbf{a_{m_1}}$ and $\mathbf{a_{m_2}}$ into the basis formed by the graphene lattice vectors (i, j, k, l), and the supporting material lattice vectors (m, n, q, r), as sketched on Fig. 4.4 (left). This decomposition is in practice performed more conveniently but equivalently in reciprocal space (Equation (4.10)).

When a structure is isotropic, the commensurability relation simplifies. Instead of eight integer parameters (i, j, k, l, m, n, q, r), only four of them (i, j, m, n) are sufficient, since both directions $\mathbf{a_{m_1}}$ and $\mathbf{a_{m_2}}$ are identical. Matrices in Equations (4.9) and (4.10) then become:

$$M_{\text{gr}} = \begin{pmatrix} i & j \\ -j & i-j \end{pmatrix}, \; M_{\text{s}} = \begin{pmatrix} m & n \\ -n & m-n \end{pmatrix} \tag{4.11}$$

$$\text{and } M_{\text{gr}}^{\text{T}} = \begin{pmatrix} i & -j \\ j & i-j \end{pmatrix}, \; M_{\text{s}}^{\text{T}} = \begin{pmatrix} m & -n \\ n & m-n \end{pmatrix} \tag{4.12}$$

Although using a set of eight integers is efficient to describe a moiré superlattice, it is a relatively cumbersome notation that does not give an immediate picture of the structure. A clearer formulation of such sheared structures is then desirable. In the following, two complementary pictures are going to be presented. First, a rather intuitive one is based on the Wood's notation commonly used in surface science. Secondly, the commensurate relation will be decomposed into elementary geometrical deformations, so strain levels can be extracted from them.

Generalized Wood's notation

In the simple case of graphene experiencing only deformations preserving its pristine D_{6h} symmetry, the Wood's notation provides a straightforward image of the structure. It describes the length and orientation of the superstructure lattice vectors compared to that of graphene or its supporting material. In the more general case addressed here, where the lattice vectors are allowed to vary in length and orientation independently as a result of shear and/or uniaxial strains, an extension of the Wood's notation is required, which is derived here. As depicted on Fig. 4.4 (middle), $\mathbf{a_{gr_1}}$ and $\mathbf{a_{gr_2}}$ are rescaled (resp.

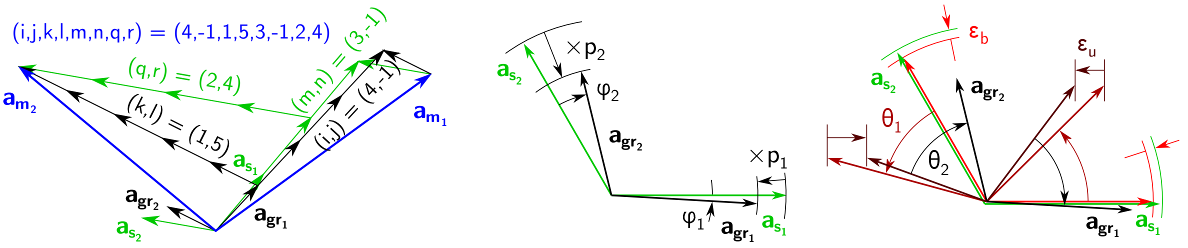

Figure 4.4: **Structural interpretation of a moiré superlattice. Left**: the lattice vectors of the moiré superlattice decompose into both graphene and support bases, giving $(i, j, k, l, m, n, q, r) = (4, -1, 1, 5, 3, -1, 2, 4)$. **Middle:** corresponding extended Wood's notation: $(p_1\ \mathrm{R}\varphi_1 \times p_2\ \mathrm{R}\varphi_2)$, where p_1 and p_2 are scaling factors, and φ_1 and φ_2 are rotation angles. **Right:** the transformation relating graphene lattice vectors ($\mathbf{a_{gr_1}}$,$\mathbf{a_{gr_2}}$) to those of its support ($\mathbf{a_{s_1}}$,$\mathbf{a_{s_2}}$) can be decomposed into four steps. (**1**) Graphene vectors are isotropically rescaled with respect to those of the support (light red). (**2**) Graphene is rotated with respect to its support (red), in order to determine the direction in which (**3**) a horizontal rescaling is applied (dark red). (**4**) A final rotation is applied (black).

rotated) with respect to $\mathbf{a_{s_1}}$ and $\mathbf{a_{s_2}}$ by factors p_1 and p_2 (resp. angles φ_1 and φ_2). The extended Wood's notation reads as $(p_1\ \mathrm{R}\varphi_1 \times p_2\ \mathrm{R}\varphi_2)$. This notation straightforwardly captures the graphene-substrate relation, and pictures how sheared it is by comparing p_1 and p_2, and φ_1 and φ_2. Once again, these quantities relate to the (i, j, k, l, m, n, q, r) integers.

The core idea of the relation between the generalized Wood's notation and the (i, j, k, l, m, n, q, r) integers is to express the graphene-substrate commensurate relation in both pictures, and then to relate the two.

A direct relation between the lattice vectors of graphene and its support is deduced from the above Equation (4.9) as:

$$\begin{pmatrix} \mathbf{a_{gr_1}} \\ \mathbf{a_{gr_2}} \end{pmatrix} = \frac{1}{il - jk} \begin{pmatrix} lm - jq & ln - jr \\ -km + iq & -kn + ir \end{pmatrix} \begin{pmatrix} \mathbf{a_{s_1}} \\ \mathbf{a_{s_2}} \end{pmatrix} = \begin{pmatrix} a & b \\ c & d \end{pmatrix} \begin{pmatrix} \mathbf{a_{s_1}} \\ \mathbf{a_{s_2}} \end{pmatrix} \tag{4.13}$$

On the other hand, the (2×2) matrix that links $(\mathbf{a_{gr_1}}, \mathbf{a_{gr_2}})$ and $(\mathbf{a_{s_1}}, \mathbf{a_{s_2}})$ can be written in the formalism of an extended Wood's notation. For a $(p_1\ \mathrm{R}\varphi_1 \times p_2\ \mathrm{R}\varphi_2)$, and assuming a hexagonal support lattice, this matrix rewrites as:

$$\begin{pmatrix} \mathbf{a_{gr_1}} \\ \mathbf{a_{gr_2}} \end{pmatrix} = \begin{pmatrix} p_1 \left(\cos\varphi_1 + \frac{\sin\varphi_1}{\sqrt{3}} \right) & \frac{2p_1}{\sqrt{3}} \sin\varphi_1 \\ -\frac{2p_2}{\sqrt{3}} \sin\varphi_2 & p_2 \left(\cos\varphi_2 - \frac{\sin\varphi_2}{\sqrt{3}} \right) \end{pmatrix} \begin{pmatrix} \mathbf{a_{s_1}} \\ \mathbf{a_{s_2}} \end{pmatrix} \tag{4.14}$$

To extract the values of parameters p_1, p_2, φ_1 and φ_2, the matrices from Equations (4.13) and (4.14) are identified. This gives rise to two non-linear systems of two equations with two unknowns each. It can be solved by considering:

$$\frac{a}{b} = \frac{\sqrt{3}}{2}\frac{1}{\tan\varphi_1} + \frac{1}{2} \quad \Longrightarrow \quad \varphi_1 = \arctan\left(\frac{b\sqrt{3}}{2a-b}\right)$$

In order to get p_1, the expression of φ_1 is inserted into that of b so:

$$b = \frac{2p_1}{\sqrt{3}}\sin\left(\arctan\left(\frac{b\sqrt{3}}{2a-b}\right)\right) \quad \Longrightarrow \quad p_1 = \sqrt{a^2+b^2-ab}$$

Similarly, one can express p_2 and φ_2 as functions of c and d. The commensurability relation of any anisotropic superstructure can then translated into an extended Wood's notation. The same can be done to relate the moiré unit vectors to those of the support, as (P_1 RΦ_1 × P_2 RΦ_2). This is summarized as:

$$\begin{cases} p_1 = \sqrt{a^2+b^2-ab} & (4.15a) \\ \varphi_1 = \arctan\left(\dfrac{b\sqrt{3}}{2a-b}\right) & (4.15b) \\ p_2 = \sqrt{c^2+d^2-cd} & (4.15c) \\ \varphi_2 = \arctan\left(\dfrac{c\sqrt{3}}{c-2d}\right) & (4.15d) \end{cases} \quad \text{and} \quad \begin{cases} P_1 = \sqrt{m^2+n^2-mn} & (4.16a) \\ \Phi_1 = \arctan\left(\dfrac{n\sqrt{3}}{2m-n}\right) & (4.16b) \\ P_2 = \sqrt{q^2+r^2-qr} & (4.16c) \\ \Phi_2 = \arctan\left(\dfrac{q\sqrt{3}}{q-2r}\right) & (4.16d) \end{cases}$$

When a structure is isotropic, the commensurability relation simplifies into Equations (4.11) and (4.12). In this case, all equations detailed above can be taken with $c = -b$ and $d = a - b$, and the Wood's notation gets back to its usual form $(p \times p)\mathrm{R}\varphi$ and $(P \times P)\mathrm{R}\Phi$, with:

$$\begin{cases} p = \sqrt{\dfrac{m^2+n^2-mn}{i^2+j^2-ij}} & (4.17a) \\ \varphi = \arctan\left(\dfrac{(in-jm)\sqrt{3}}{2(im+jn)-(in+jm)}\right) & (4.17b) \end{cases} \quad \text{and} \quad \begin{cases} P = P_1 & (4.18a) \\ \Phi = \Phi_1 & (4.18b) \end{cases}$$

Strain levels in a moiré superlattice

So far, the analysis of the moiré superlattices has been performed by expressing the moiré superlattice unit vectors as function of those of the graphene and support unit cells. The analysis is now going to be expressed as function of elementary geometrical deformations.

In the most general case, graphene is twisted, strained and sheared with respect to its substrate. The combination of all these contributions can be separated into four elementary geometrical transformations represented on Fig. 4.4 (right):

- An isotropic rescaling by a factor p_{iso} corresponding to biaxial strain (1),
- An anisotropic rescaling by a factor p_{an} in a direction given by an angle θ_1 (2-3),
- An additional rotation by an angle θ_2 (4).

These transformations translate in mechanical terms as biaxial strain ε_{b} (1), uniaxial strain in a given direction ε_{u} (2 and 3), and a rotation (4) of the graphene layer. It can be noted that the so far overlooked shearing contribution is taken into account by combining a rotation, biaxial and uniaxial strains. The impact of such a combination on a moiré has only been predicted [75].

In the following calculations, ε_{b} and ε_{u} are going to be determined. Setting HOPG as a reference of zero-strain (an arbitrary one, in fact), they are defined as:

$$\begin{cases} \varepsilon_{\text{b}} = \dfrac{a_{\text{gr}_{\min}} - a_{\text{HOPG}}}{a_{\text{HOPG}}} = \dfrac{a_{\text{s}}}{a_{\text{HOPG}}} p_{\text{iso}} - 1 & \text{(4.19a)} \\ \varepsilon_{\text{u}} = \dfrac{a_{\text{gr}_{\max}} - a_{\text{gr}_{\min}}}{a_{\text{HOPG}}} = \dfrac{a_{\text{s}}}{a_{\text{HOPG}}} p_{\text{iso}} \left(p_{\text{an}} - 1\right) & \text{(4.19b)} \end{cases}$$

As can be seen, they depend straightforwardly on p_{iso} and p_{an}, θ_1 and θ_2. Here again, to relate these four parameters to (i, j, k, l, m, n, q, r), the (2×2) matrix that links $(\mathbf{a_{gr_1}}, \mathbf{a_{gr_2}})$ and $(\mathbf{a_{s_1}}, \mathbf{a_{s_2}})$ is going to be identified with that of Equation (4.13). Considering this matrix as a plane transformation, one gets:

$$\begin{aligned} \begin{pmatrix} \mathbf{a_{gr_1}} \\ \mathbf{a_{gr_2}} \end{pmatrix} &= \mathrm{P} \underbrace{\begin{pmatrix} \cos\theta_2 & \sin\theta_2 \\ -\sin\theta_2 & \cos\theta_2 \end{pmatrix} \begin{pmatrix} p_{\text{an}} & 0 \\ 0 & 1 \end{pmatrix} \begin{pmatrix} \cos\theta_1 & \sin\theta_1 \\ -\sin\theta_1 & \cos\theta_1 \end{pmatrix} p_{\text{iso}}} \mathrm{P}^{-1} \begin{pmatrix} \mathbf{a_{s_1}} \\ \mathbf{a_{s_2}} \end{pmatrix} \\ &= p_{\text{iso}} \begin{pmatrix} p_{\text{an}}\cos\theta_1\cos\theta_2 - \sin\theta_1\sin\theta_2 & p_{\text{an}}\sin\theta_1\cos\theta_2 + \cos\theta_1\sin\theta_2 \\ -p_{\text{an}}\cos\theta_1\sin\theta_2 - \sin\theta_1\cos\theta_2 & -p_{\text{an}}\sin\theta_1\sin\theta_2 + \cos\theta_1\cos\theta_2 \end{pmatrix} \end{aligned} \tag{4.20}$$

With $\mathrm{P} = \begin{pmatrix} 1 & 0 \\ -1/2 & \sqrt{3}/2 \end{pmatrix}$ the matrix that links a hexagonal to an orthonormal basis.

Identifying Equations (4.20) with (4.13) leads to a non-linear system of four equations with four unknowns. By linearly combining them, one gets:

$$\begin{cases} \cos\left(\theta_1 + \theta_2\right) p_{\text{iso}} \left(p_{\text{an}} + 1\right) = a + d & \text{(4.21a)} \\ \sin\left(\theta_1 + \theta_2\right) p_{\text{iso}} \left(p_{\text{an}} + 1\right) = \dfrac{-a + 2b - 2c + d}{\sqrt{3}} & \text{(4.21b)} \\ \cos\left(\theta_1 - \theta_2\right) p_{\text{iso}} \left(p_{\text{an}} - 1\right) = a - b - d & \text{(4.21c)} \\ \sin\left(\theta_1 - \theta_2\right) p_{\text{iso}} \left(p_{\text{an}} - 1\right) = \dfrac{a + b + 2c - d}{\sqrt{3}} & \text{(4.21d)} \end{cases}$$

$\theta_1 + \theta_2$ and $\theta_1 - \theta_2$ can readily be extracted from Equations $\dfrac{(4.21\text{b})}{(4.21\text{a})}$ and $\dfrac{(4.21\text{d})}{(4.21\text{c})}$, which are then linearly combined to get:

$$\begin{cases} \tan(2\theta_1) = -\sqrt{3} + \dfrac{2\sqrt{3}((a^2+c^2+ac)-(b^2+d^2+bd))}{2(a^2+c^2+ac)-(b^2+d^2+bd)-2(ab+cd)-(ad+bc)} \\ \tan(2\theta_2) = \sqrt{3} - \dfrac{2\sqrt{3}((a^2+b^2-ab)-(c^2+d^2-cd))}{(a^2+b^2-ab)-2(c^2+d^2-cd)-2(ac+bd)+(ad+bc)} \end{cases}$$

Moreover, the determinants of the matrices from Equations (4.20) and (4.13) also have to be equal as:

$$p_{\text{iso}}^2 p_{\text{an}} = ad - bc \tag{4.22}$$

This latter equation relates p_{iso} and p_{an} directly. In order to get another relation relating p_{iso} to p_{an}, one can calculate Equations (4.21a) × (4.21c) + (4.21b) × (4.21d) and (4.21b) × (4.21c) − (4.21a) × (4.21d) as:

$$\begin{cases} p_{\text{iso}}^2\left(p_{\text{an}}^2-1\right)\cos(2\theta_2) = \dfrac{2}{3}\big((a^2+b^2-ab)-2(c^2+d^2-cd) \\ \qquad\qquad +(ad+bc)-2(ac+bd)\big) & \text{(4.23a)} \\ p_{\text{iso}}^2\left(p_{\text{an}}^2-1\right)\sin(2\theta_2) = \dfrac{-2}{\sqrt{3}}\big((a^2+b^2-ab)-(ad+bc)+2(ac+bd)\big) & \text{(4.23b)} \end{cases}$$

And then combine them as Equation $\sqrt{(4.23\text{a})^2+(4.23\text{b})^2}$:

$$p_{\text{iso}}^2\left(p_{\text{an}}^2-1\right) = \frac{2}{3}\sqrt{\begin{array}{l}[a^2+b^2-ab+c^2+d^2-cd+4(ac+bd)-2(ad+bc)]^2 \\ +3\left[a^2+b^2-ab+c^2+d^2-cd\right]^2\end{array}} \tag{4.24}$$

Another relation is obtained using Equation $(4.21\text{a})^2+(4.21\text{b})^2$:

$$p_{\text{iso}}^2\left(p_{\text{an}}+1\right)^2 = \frac{4}{3}\left[(a^2+b^2-ab)+(c^2+d^2-cd)+ac+ad-2bc+bd\right] \tag{4.25}$$

Using $p_1 = \sqrt{a^2+b^2-ab}$ and $p_2 = \sqrt{c^2+d^2-cd}$ and $A = 2(ac+bd)-(ad+bc)$, these two latter relations can be rewritten as Equation ½(4.25) + ½(4.24) − (4.22):

$$p_{\text{iso}}^2 p_{\text{an}}^2 = \frac{2(p_1^2+p_2^2)+A}{3}\left(1+\sqrt{1+3\frac{A^2-4p_1^2p_2^2}{(2(p_1^2+p_2^2)+A)^2}}\right) \tag{4.26}$$

Finally, p_{iso} and p_{an} can be calculated as Equations $\sqrt{(4.26)-(4.24)}$ and $\sqrt{\dfrac{(4.26)}{(4.26)-(4.24)}}$:

$$\begin{cases} p_{\mathrm{iso}} = \sqrt{\dfrac{2(p_1^2+p_2^2)+A}{3}}\sqrt{1-\sqrt{1-3\dfrac{4p_1^2p_2^2-A^2}{(2(p_1^2+p_2^2)+A)^2}}} \\ p_{\mathrm{an}} = \dfrac{2(p_1^2+p_2^2)+A}{\sqrt{3(4p_1^2p_2^2-A^2)}}\left(1+\sqrt{1-3\dfrac{4p_1^2p_2^2-A^2}{(2(p_1^2+p_2^2)+A)^2}}\right) \end{cases}$$

Using $B = \dfrac{2(p_1^2+p_2^2)+A}{3}$ and $C = \sqrt{\dfrac{4p_1^2p_2^2-A^2}{3}}$, this can be written simply as:

$$\begin{cases} p_{\mathrm{iso}} = \sqrt{B-\sqrt{B^2-C^2}} \\ p_{\mathrm{an}} = \dfrac{B+\sqrt{B^2-C^2}}{C} \end{cases}$$

One can deduce biaxial and uniaxial strain levels ε_{b} and ε_{u} using Equations (4.19a) and (4.19b):

$$\begin{cases} \varepsilon_{\mathrm{b}} = \dfrac{a_{\mathrm{s}}}{a_{\mathrm{HOPG}}}\sqrt{B-\sqrt{B^2-C^2}}-1 & (4.27a) \\ \varepsilon_{\mathrm{u}} = \dfrac{a_{\mathrm{s}}}{a_{\mathrm{HOPG}}}\left(\sqrt{B+\sqrt{B^2-C^2}}-\sqrt{B-\sqrt{B^2-C^2}}\right) & (4.27b) \end{cases}$$

In other words, graphene is strained anisotropically, and the strain level ranges from $\varepsilon = \varepsilon_{\mathrm{b}}$ to $\varepsilon = \varepsilon_{\mathrm{b}} + \varepsilon_{\mathrm{u}}$ depending on the in-plane direction. Although cumbersome, these formulae relate directly the commensurate relation to the uniform strain fields in graphene, and are hence of practical interest.

For an isotropic structure, there cannot be any anisotropic strain ($\varepsilon_{\mathrm{u}} = 0$), and isotropic strain ε_{b} is simply given by Equation (4.27a) with $c = -b$ and $d = a - b$:

$$\varepsilon_{\mathrm{b}} = \frac{a_{\mathrm{s}}}{a_{\mathrm{HOPG}}}p - 1 = \frac{a_{\mathrm{s}}}{a_{\mathrm{HOPG}}}\sqrt{\frac{m^2+n^2-mn}{i^2+j^2-ij}} - 1 \tag{4.28}$$

4.1.3 Number of moiré beatings

Moiré superlattices have been considered either as some supercell comprising a certain number of beatings, or as a commensurate supercell defined by a set of integers (i, j, k, l, m, n, q, r). No link has been established between the two, and in fact, it lies in the number of beatings N per moiré supercell. In anisotropic moiré superlattices, the number of beatings along $\mathbf{a_{m_1}}$ and $\mathbf{a_{m_2}}$ may be different, and will be noted N_1 and N_2, with $N \simeq N_1 N_2$. For simplicity, one will assume the commensurability along each direction can be approximated by that of isotropic moiré superlattices with indices (i, j, m, n) and (k, l, q, r).

To calculate them, one has to combine the two approaches developed so far. Indeed, the Fourier components defining the beating $\mathbf{k_{b_1}}$ (resp. $\mathbf{k_{b_2}}$) also define the number of beatings N_1 (resp. N_2), and relate $\mathbf{k_{b_1}}$ to elementary wave vectors $\mathbf{k_{gr_1}}$, $\mathbf{k_{gr_2}}$, $\mathbf{k_{s_1}}$ and $\mathbf{k_{s_2}}$. Additionally, these vectors are linked to the moiré wave vector $\mathbf{k_{m_1}}$ (resp. $\mathbf{k_{m_2}}$) through the integers (i, j, m, n) (resp. (k, l, q, r)). Combining these two relations gives access to N_1 (resp. N_2).

Based on the definition of a beating, the number of beatings of any order N_1 along the first moiré direction is simply obtained with:

$$N_1 = \frac{|g_1\mathbf{k_{gr_1}} + g_2\mathbf{k_{gr_2}} + s_1\mathbf{k_{s_1}} + s_2\mathbf{k_{s_2}}|}{|\mathbf{k_{m_1}}|} \tag{4.29}$$

The commensurability relation can be expressed in reciprocal space, as in Equation (4.10). It can be seen as a decomposition of $\mathbf{k_{gr_1}}$, $\mathbf{k_{gr_2}}$, $\mathbf{k_{s_1}}$ and $\mathbf{k_{s_2}}$ on the $(\mathbf{k_{m_1}}, \mathbf{k_{m_2}})$ basis using integer values. Injecting this into Equation (4.29), the number of beating N_1 of any moiré order given by (g_1, g_2, s_1, s_2) is:

$$\begin{aligned} N_1 = &\sqrt{(g_1 i + g_2 j + s_1 m + s_2 n)^2} \\ &\overline{+ (g_1 j - g_2(i-j) + s_1 n - s_2(m-n))^2} \\ &\overline{- (g_1 i + g_2 j + s_1 m + s_2 n)(g_1 j - g_2(i-j) + s_1 n - s_2(m-n))} \end{aligned} \tag{4.30}$$

In particular, for the aforementioned beatings based on 1st, 2nd, 3rd and 4th order Fourier components, this results in:

$$\begin{cases} N_1 = \sqrt{(i-m)^2 + (j-n)^2 - (i-m)(j-n)} \\ N_1 = \sqrt{(i+j-2m)^2 + (2j-2n-i)^2 - (i+j-2m)(2j-2n-i)} \\ N_1 = \sqrt{(i+2j-3m)^2 + (3j-3n-2i)^2 - (i+2j-3m)(3j-3n-2i)} \\ N_1 = \sqrt{(i+3j-4m)^2 + (4j-4n-3i)^2 - (i+3j-4m)(4j-4n-3i)} \end{cases}$$

Equivalent relations can be written for N_2 by substituting (k, l, q, r) to (i, j, m, n).[2]

As a final remark, Equation (4.30) can be used to calculate the number of beatings for any order of the Fourier components defining the beating. Nevertheless, from the electronic point of view, the 1st order beating contribution is the one that dominates in the modulation of the potential the electrons are subjected to. They are given by:

---

[2] It can be noted that for each of these relations, the number of beatings N_1 is different. For instance, the so-called R30 phase of graphene on Ir(111) ($(i, j, m, n) = (14, 9, 12, 2)$) contains $N = 39$ beatings in a 1st order beating picture, but $N = 1$ beating using the 2nd order beating relation, which enabled its identification [120].

$$\begin{aligned} N_1 &= \sqrt{(i-m)^2+(j-n)^2-(i-m)(j-n)} \text{ and} \\ N_2 &= \sqrt{(k-q)^2+(l-r)^2-(k-q)(l-r)} \end{aligned} \quad (4.32)$$

Beatings defined with higher order Fourier components can be considered as small corrections to this modulation. Equation (4.30) gives the number of moiré cells N that a correction of n^{th} order has in the moiré unit cell.

4.1.4 Precision on the structure determination

The geometrical developed so far proves necessary to properly interpret the refined twist angles and shearings observed in atomically-resolved microscopy images. The experimental uncertainty on the identification of the (i,j,k,l,m,n,q,r) integers is here discussed to justify this necessity.

Quantitatively, the uncertainty on (i,j,k,l) can be lowered by precisely determining $(\mathbf{k_{gr_1}},\mathbf{k_{gr_2}})$ and $(\mathbf{k_{m_1}},\mathbf{k_{m_2}})$. In practice, the distance between the moiré spots and the graphene spots in the Fourier transform image (each spot corresponding to a Fourier component) is measured. Due to the moiré periodicity, such spots are expected to be evenly separated. The sharpness of the spots is inversely proportional to the size of the atomically resolved image, and the number of spots increases with the contrast of the moiré with respect to the atomic lattice. The former effect sets a precision in the determination of the spacing between two spots of 6% in the case of graphene on Ir(111) that will be discussed later, for which an image with a field of view of $\sim$ 500 nm^2 has been used. The latter effect translates into an uncertainty as low as $1/\sqrt{50} \times 6\% \sim 1\%$ in the case of graphene on Ir(111). Indeed, around the center of the reciprocal space, there are $\sim$ 60 Fourier components, which corresponds to $\sim$ 50 Fourier component spacings along one direction. The same is true around the graphene harmonics, so overall, in our example, the precision over k_{m} and k_{gr} is $\sim$ 1%. For (i,j,k,l), this precision translates through propagation of uncertainty into 2%.

The above described determination of (i,j,k,l,m,n,q,r) is liable to put shears in evidence. At first thought, atomic resolution imaging can artificially produce sheared images. Such shears may result from imaging artefacts, for instance, in the case of scanning probe microscopy, thermal drift of the piezoelectric scanners or inequivalent calibration of these scanners along the two scan directions. However, these artefacts have no influence on the decomposition of $\mathbf{k_{gr_1}}$ and $\mathbf{k_{gr_2}}$ onto $\mathbf{k_{m_1}}$ and $\mathbf{k_{m_2}}$.

In the following, STM topographs of graphene on C-face SiC, Re(0001) and Ir(111) are exposed. For multilayer graphene on C-face SiC, STM measurements were performed at 4 K. For graphene on Re(0001) and Ir(111), STM measurements were performed at room temperature under UHV. Before analysing STM images, thermal drift and miscalibrations have been corrected.

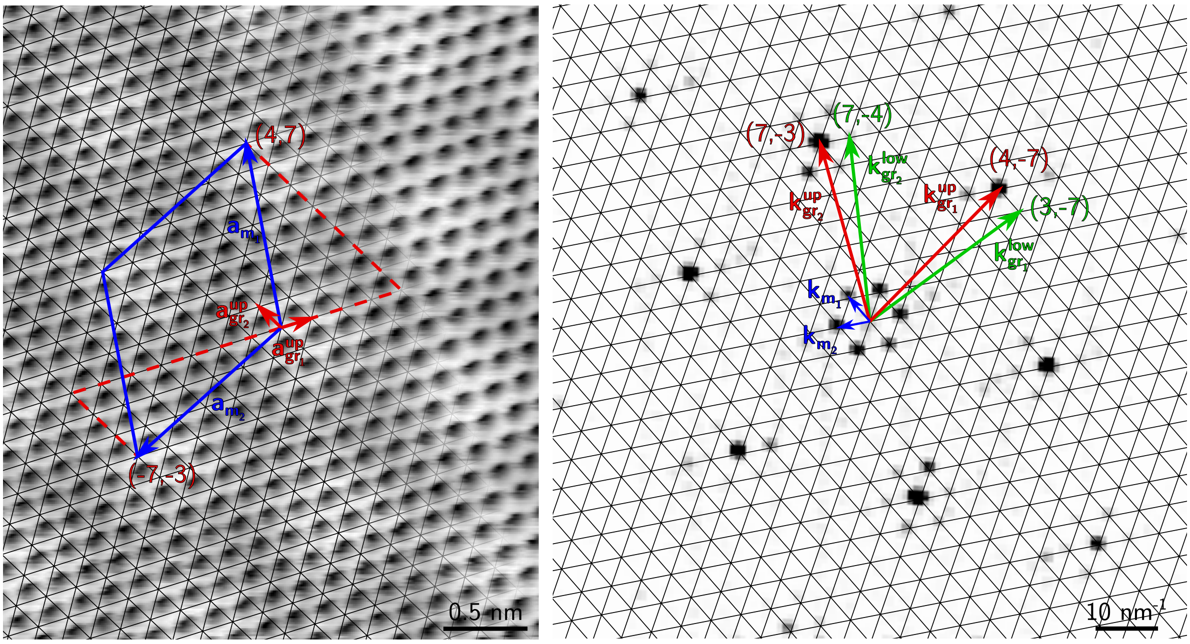

Figure 4.5: **STM analysis of multilayer graphene on C-face SiC. Left**: (3.2×3.8 nm^2) STM topograph ($I_{\text{tunnel}} = 10$ nA, $V_{\text{bias}} = 100$ mV) with emphasized upper graphene lattice (black), moiré superlattice cell (blue rhombus) and lattice vectors of upper graphene and moiré (red and blue respectively). **Right:** corresponding FFT-image with emphasized moiré reciprocal lattice (black) and lattice vectors of moiré and upper and lower layers of graphene (blue, red and green respectively).

4.2 Experimental results

4.2.1 Twisted graphene bilayer

First, the case of multilayer graphene on the C-face of SiC sample is considered. It has been grown on undoped double-polished 4H-SiC(000$\bar{1}$), purchased from Novasic and cut into 5×5 mm^2 pieces. The growth has been performed in a RF-furnace following the recipe in Ref. [42]. SiC surface was first cleaned in H$_2$ and Ar atmosphere at $1,560$ °C, and subsequently annealed in Ar atmosphere at the same temperature.

On Fig. 4.5 (left), a moiré with ~ 1.5 nm beating is observed. In the present case, the relationship between the lattice vectors of the upper graphene layer and of the moiré can be read on the fast Fourier transform (FFT) of the STM image shown on Fig. 4.5 (right) to deduce matrix $M^{\text{T}}_{\text{gr}_{\text{up}}}$. Here, this matrix indicates the coincidence of the graphene and moiré lattices in reciprocal space. In direct space, this means that the moiré has only one beating per unit cell, so $N = 1$. For a $N = 1$ moiré, $\mathbf{k_{m_1}} = \mathbf{k^{up}_{gr_1}} - \mathbf{k^{low}_{gr_1}}$, as the lower layer of graphene is the support material. From this, the matrix $M^{\text{T}}_{\text{gr}_{\text{low}}}$ between the lattice vectors of the lower graphene layer and of the moiré is obtained. Transposing matrices $M^{\text{T}}_{\text{gr}_{\text{up}}}$ and $M^{\text{T}}_{\text{gr}_{\text{low}}}$ gives access to $M_{\text{gr}_{\text{up}}}$ and $M_{\text{gr}_{\text{low}}}$, which hold the decomposition of the moiré unit vectors on the upper and lower graphene lattices in direct space:

$$M^{\mathrm{T}}_{\mathrm{gr_{up}}} = \begin{pmatrix} 4 & -7 \\ 7 & -3 \end{pmatrix} \text{ and } M^{\mathrm{T}}_{\mathrm{gr_{low}}} = \begin{pmatrix} 3 & -7 \\ 7 & -4 \end{pmatrix}$$
$$\text{so } M_{\mathrm{gr_{up}}} = \begin{pmatrix} 4 & 7 \\ -7 & -3 \end{pmatrix} \text{ and } M_{\mathrm{gr_{low}}} = \begin{pmatrix} 3 & 7 \\ -7 & -4 \end{pmatrix}$$

This commensurability relation gives a complete structural description, by decomposing the moiré lattice vectors in the basis of each graphene layer, using the set of integers $(i, j, k, l, m, n, q, r) = (4, 7, -7, -3, 3, 7, -7, -4)$. Using Equations (4.15a), (4.15b), (4.15c) and (4.15d), such a structure can be analysed as two graphene layers sharing the same lattice parameter $a^{\mathrm{up}}_{\mathrm{gr}} = a^{\mathrm{low}}_{\mathrm{gr}}$ $(p_1 = p_2 = 1)$, and rotated by $\varphi = \varphi_1 = \varphi_2 = \arctan\left({}^{7\sqrt{3}}/_{73}\right) \sim 9.43°$ with respect to each other. This falls in the regime where the two graphene layers interact weakly, leading to Fermi velocity renormalization around the Dirac cones [122, 154, 194].

4.2.2 Graphene on Re(0001)

The case of multilayer graphene on C-face SiC has shown a situation where a moiré superlattice is related to a single structural parameter: the twisting angle φ. Now we report a situation where graphene is not only twisted, but also strained and sheared with respect to the substrate, a Re(0001) surface. A full monolayer of graphene forms on Re(0001) through a self-limiting process [143], and the dominant Fourier component is found to correspond to a beating with $\sim$ 2.2 nm period.

Here, graphene was grown on a Re(0001) single crystal following the recipe presented in Section 3.2.3, by saturating the surface with C_2H_4 at room temperature (introduced with a $3 \cdot 10^{-8}$ mbar pressure), and two subsequent cycles of flash-annealing/cooling at 750 °C with a $5 \cdot 10^{-7}$mbar C_2H_4 pressure.

A direct analysis of the STM topograph along the same lines as for Fig. 4.5 is here challenging. Fig. 4.6 (left) highlights two additional phenomena, which have been discussed in the context of graphene on metals [38, 129].

First, depending on the position within the moiré superlattice, the apparent height accessed by STM shows a varying number of visible C: in a valley, only 3 atoms out of a 6-C ring are seen, whereas on a hill, all 6 are observed. This is due to the sites occupied by the C atoms on the terminal metallic layer, which are either atop, hcp or fcc (see Section 2.1). In a valley, the sites occupied by the C atoms are either atop and hcp, or atop and fcc. The overlap of the p_z-like orbital of a C atom in atop position with the d-like orbitals of the underlying metal atom is then maximal. Consequently, the local electronic density of states is modified, making it appear low in STM [213]. This explains why, for strongly-interacting substrates, only half the C atoms appear as protrusions in a moiré valley, while all of them can be identified on top of a moiré hill (see Refs. [129, 134, 157, 230] for graphene on Ru(0001), Ref. [207] for graphene on Rh(111), and Ref. [193] for graphene on Re(0001)).

Second, the apparent atomic rows of C oscillate with the same periodicity as the beatings. This phenomenon has been reported and discussed in the case of graphene on

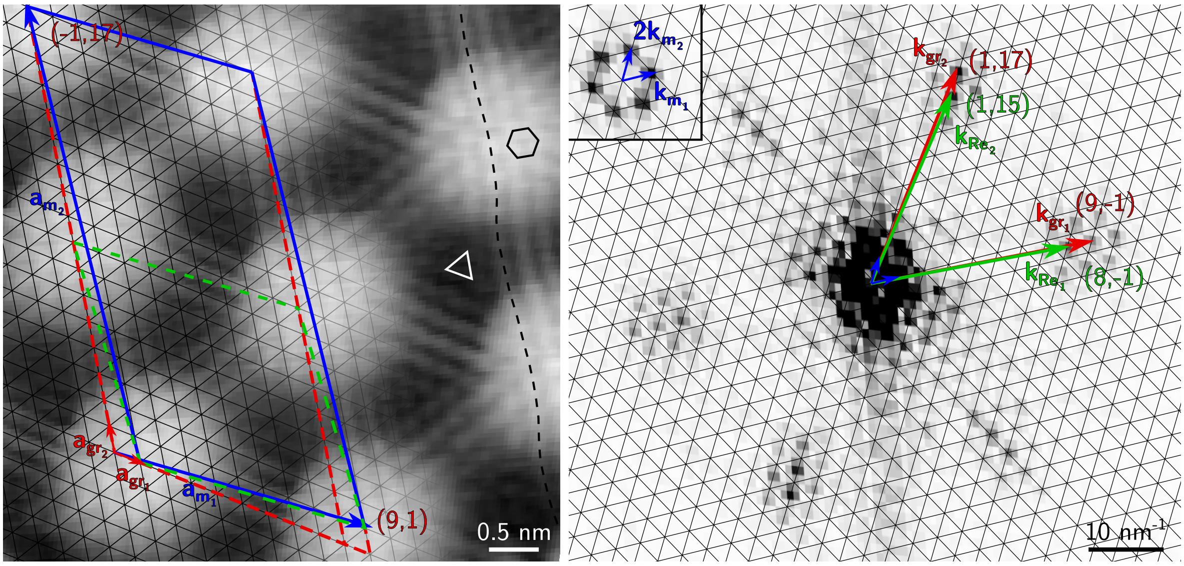

Figure 4.6: **STM analysis of graphene on Re(0001).** **Left**: (5.6×5.2 nm^2) STM topograph ($I_{\text{tunnel}} = 6$ nA, $V_{\text{bias}} = 30$ mV) with overlaid graphene lattice (black), and lattice vectors of graphene and $N = 2$ superlattice (red and blue arrows respectively). Moiré cell (blue full line) and its closest unsheared approximation with $N = 1$ beating (green dashed line), with the coordinates of its corners in the graphene basis. The "odd-even" transition along lines of carbon atoms is also emphasized, as well as the either 6 or 3 C atoms observed in a moiré hill or valley. **Right**: corresponding FFT-image with emphasized moiré reciprocal lattice (black) and lattice vectors of moiré, graphene and Re (blue, red and green respectively). Inset shows the $\mathbf{k_{gr}} - \mathbf{k_{Re}}$ harmonics surrounding the center of the FFT-image with improved contrast.

Ru(0001) [129], and observed as well in many instances before and since then. A detailed account of this effect has been published after the work presented here [38]. Still, it is known since the 1990s as the "odd-even transition" in the case of graphite [144,153,156]. Its origin is well illustrated in the case of the two distinctive moiré valleys. Indeed, they differ only in the site of the remaining visible C atom: hcp or fcc. Depending on whether the site is hcp or fcc, the corresponding C atom belongs to sub-lattice A or B of graphene. As a consequence, when moving from one beating to the other, the C atoms that are observed switch continuously from one sub-lattice to the other. This induces an apparent oscillation of the rows of C atoms. Therefore, these two effects are related to a modulation of the electronic density of states on the two sub-lattices of graphene, which is correlated with the moiré periodicity.

Density functional calculations have been performed in order to provide a qualitative interpretation of the effect of shear strain, in the case of graphene on Re(0001), on the observed STM images. The large size of the $N > 1$ beatings moiré superlattice observed experimentally is not affordable for DFT calculations, due to a too large number of atoms. A smaller moiré superlattice was hence considered, comprising only one beating.

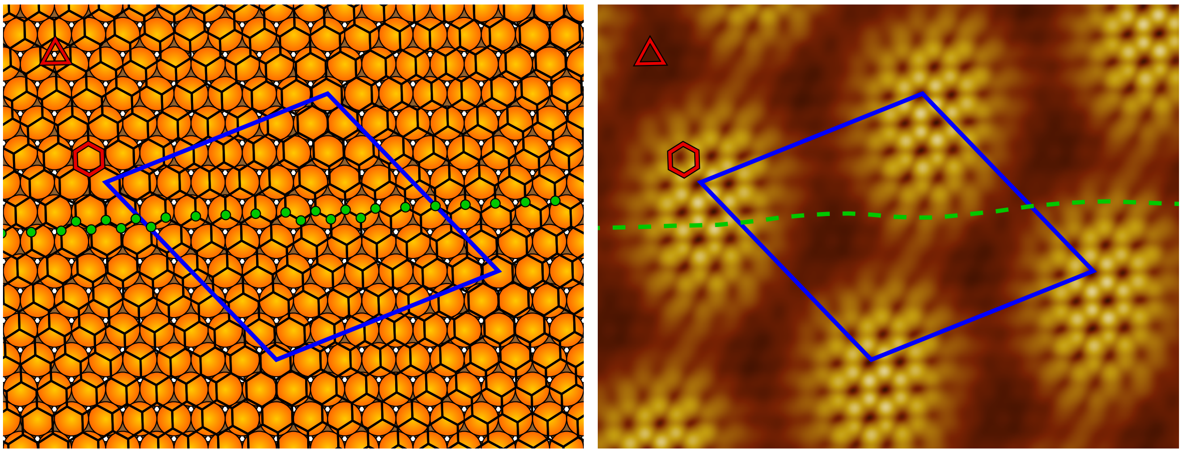

Figure 4.7: **DFT simulation of graphene on Re(0001). Left:** schematic view of the $(i, j, k, l, m, n, q, r) = (9, 3, -2, 7, 8, 3, -2, 6)$ $N = 1$ moiré superlattice used for DFT calculations. **Right:** cross-section of the square modulus of the converged wavefunction integrated between E_F and $E_F + 0.5$ eV. On both images, the superlattice unit cell is emphasized with a blue rhombus. In both moiré valleys, only one C out of two is seen (right), contrary to the moiré hill, as indicated by red triangle and hexagon. This alternative appearance of either one C sub-lattice or the other gives rise to an effective C row oscillation (green dots, left), emphasized by a green dotted line (right).

A cross-section in the electronic density map, computed from the relaxed structure, integrated between Fermi level and 0.5 eV above it, is shown on Fig. 4.7.

DFT calculations were performed using the VASP code, with the projector augmented wave (PAW) approach [105,106]. The exchange correlation interaction is treated within the general gradient approximation parameterized by Perdew, Burke and Ernzerhof (PBE) [164]. The Methfessel Paxton method is used to calculate the total energy with a smearing of 0.2. The cut-off energy is of 400 eV. The supercell consists in four Re layers and one C layer with an empty space of 9 Å to avoid spurious interactions. Re atoms are kept fixed in the bottom second Re layer, all other atoms are allowed to relax. Due to the size of the supercell, calculations are performed using the K point only. After convergence, residual forces are lower than 0.03 eV/Å.

Using DFT calculations, the two effects explained above have been reproduced in the case of a sheared and twisted $N = 1$ moiré superlattice of graphene on Re(0001), comprising a sufficiently small number of atoms to be treated numerically. This moiré is characterized by the set $(i, j, k, l, m, n, q, r) = (9, 3, -2, 7, 8, 3, -2, 6)$. On Fig. 4.7 (right), one can see that the moiré reproduces the two anomalies described above. Only one C sub-lattice is observed in each moiré valley. Within the unit cell, this causes an effective oscillation of the atomic C row, which is actually related to the varying contribution of each sub-lattice to the electronic density, as can be checked on Fig. 4.7 (left).

On Fig. 4.7 (right), it can be noted that the hills of the beating are not circular, but appear rather elliptical. This is attributed to the small shearing that graphene undergoes in this superstructure, whose effect is enhanced on the moiré. Similar non-circular hills can be observed on Fig. 4.6a, which is another clue that indicates graphene structure is sheared on this STM topograph.

Fig. 4.6 displays an analysis taking the two STM electronic effects into account. The FFT image is analysed similarly to Fig. 4.5 (right), although the situation is different. Indeed, in two directions, the graphene spots do not superimpose with the extrapolated reciprocal space lattice paved with the $\mathbf{k_{gr_1}} - \mathbf{k_{Re_1}}$ and $\mathbf{k_{gr_2}} - \mathbf{k_{Re_2}}$ vectors. This means that the moiré is not a $N = 1$ superlattice (cf. Fig. 4.1 bottom). Moreover, the positions of the graphene spots with respect to the moiré reciprocal network vary for the three main directions. Consequently, based on the reciprocal space analysis, the moiré structure considered here is sheared. The commensurability relation of this structure reads as:

$$M_{\mathrm{gr}}^{\mathrm{T}} = \begin{pmatrix} 9 & -1 \\ 1 & 17 \end{pmatrix} \text{ and } M_{\mathrm{Re}}^{\mathrm{T}} = \begin{pmatrix} 8 & -1 \\ 1 & 15 \end{pmatrix}$$
$$\text{so } M_{\mathrm{gr}} = \begin{pmatrix} 9 & 1 \\ -1 & 17 \end{pmatrix} \text{ and } M_{\mathrm{Re}} = \begin{pmatrix} 8 & 1 \\ -1 & 15 \end{pmatrix}$$

Therefore $(i, j, k, l, m, n, q, r) = (9, 1, -1, 17, 8, 1, -1, 15)$ is the corresponding set of integers. As a signature of the anisotropy, the moiré cell contains a different number of beatings $N_1 = 1$ and $N_2 = 2$ in each of its main directions, as can be deduced from Equation (4.32). This analysis is displayed in direct space on top of the original STM topograph on Fig. 4.6 (left), where the superstructure lattice vectors are explicitly decomposed on the graphene lattice.

To get a more simple grasp of this structure, the moiré can be described using the $(P_1 \text{ R}\Phi_1 \times P_2 \text{ R}\Phi_2)$ extended Wood's notation, with $P_1 = \sqrt{8^2 + 1^2 - 1 \times 8} \sim 7.55$, $P_2 = \sqrt{(-1)^2 + 15^2 - (-1) \times 15} \sim 15.52$, $\Phi_1 = \arctan\left(\sqrt{3}/15\right) \sim 6.59°$, and $\Phi_2 = \arctan\left(\sqrt{3}/31\right) \sim 3.20°$, as deduced from Equations (4.16a), (4.16b), (4.16c) and (4.16d). This notation makes clear the twice larger size of the moiré compared to a $N = 1$ superlattice, comprising 308 carbon atoms, as well as a sizeable shear. The corresponding shear of the graphene lattice is obvious in the corresponding extended Wood's notation $(p_1 \text{ R}\varphi_1 \times p_2 \text{ R}\varphi_2)$. Using Equations (4.15a), (4.15b), (4.15c) and (4.15d), one gets $p_1 = \sqrt{137^2+2^2-2\times137}/154 \sim 0.883$, $p_2 = \sqrt{(-1)^2+136^2+1\times136}/154 \sim 0.886$, $\varphi_1 = \arctan\left(\sqrt{3}/136\right) \sim 0.73°$ and $\varphi_2 = \arctan\left(\sqrt{3}/271\right) \sim 0.36°$. This is summarized as (0.883 R0.73° × 0.886 R0.36°). This structure is close but different from the previously reported assignment of a (7 × 7)R0° $N = 1$ moiré [193].

Overall, the structure is a superlattice both sheared and twisted with $N_1 = 1$ beating in one direction and $N_2 = 2$ in the other, giving rise to $N = 2$ beatings in the moiré cell. This is significantly more complex than the $N = 1$ twisted superlattices discussed in many reports, and even than the $N = 4$ untwisted superlattices reported in graphene on Ir(111) [11] and graphene on Ru(0001) [134], or than a solely sheared superlattice [75].

A more physical description of such a structure is given by comparing the graphene

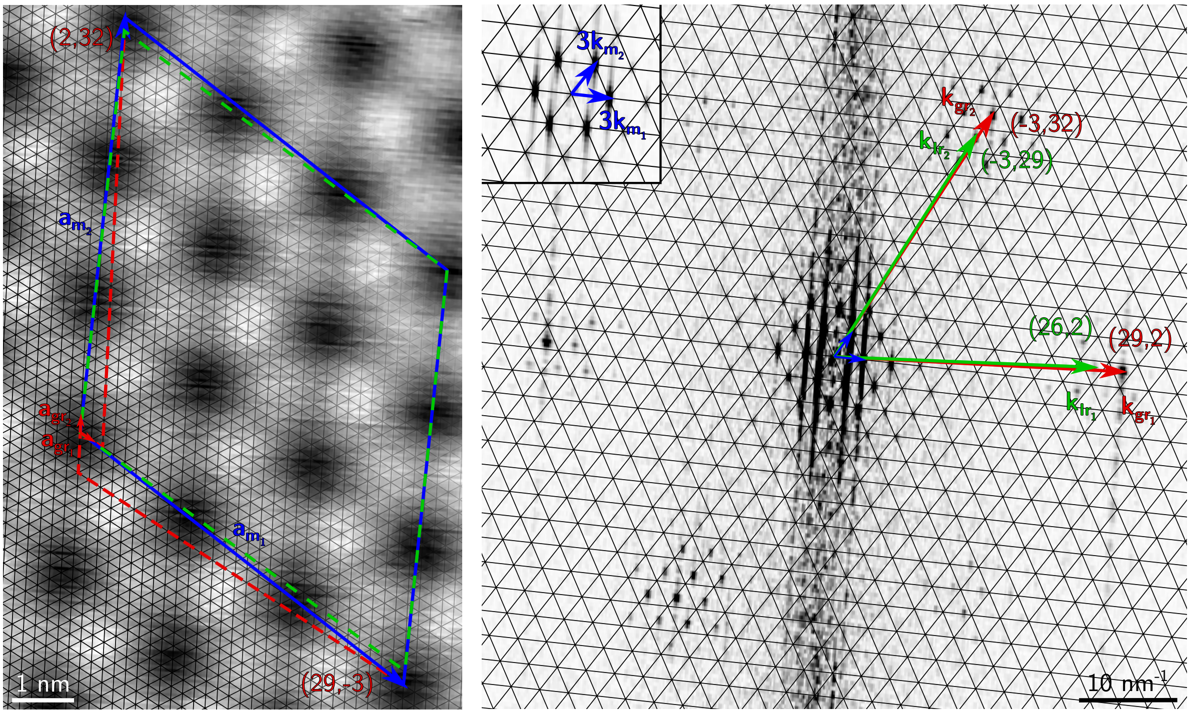

Figure 4.8: **STM analysis of graphene on Ir(111). Left:** (13.5×7.4 nm^2) STM topograph ($I_{\text{tunnel}} = 20$ nA, $V_{\text{bias}} = 60$ mV) with highlighted graphene lattice (black), and lattice vectors of graphene and $N = 9$ moiré (red and blue arrows respectively). Moiré cell (blue line) with the coordinates of its corners in the graphene basis, and its closest unsheared approximation (green dashed line). It should be noted the contrast is inverted compared to Fig. 4.6, so hills appear as dark. **Right:** FFT-image obtained from a 15.6×30 nm^2 STM topograph, and overlaid with the lattice paved with $\mathbf{k_{gr}} - \mathbf{k_{Ir}}$ vectors, and lattice vectors of moiré, graphene and Ir (blue, red and green respectively). Inset shows moiré spots surrounding the center of the FFT-image with improved contrast.

overlayer with its HOPG counterpart, and decomposing the strain in terms of a uniaxial and a biaxial contributions. Using Equations (4.27a) and (4.27b) in the case of graphene on Re(0001), graphene is biaxally compressed by $\varepsilon_{\text{b}} \sim -0.14\%$ and uniaxially compressed by $\varepsilon_{\text{u}} \sim -0.84\%$. This shows that a moiré is actually related to a non-trivial distortion of the graphene lattice.

4.2.3 Graphene on Ir(111)

The anisotropy of the graphene and moiré lattices is also encountered when the graphene-substrate interaction is much weaker, *e.g.* for graphene on Ir(111). The graphene on Ir(111) was prepared by exposing to 10^{-8} mbar of C_2H_4 at $1,000$ °C for 15 minutes.

Similarly to graphene on Re(0001), the FFT-image of Fig. 4.8 (right) shows the graphene spots do not superimpose with the extrapolated reciprocal lattice paved with

$\mathbf{k_{gr_1}} - \mathbf{k_{Ir_1}}$ and $\mathbf{k_{gr_2}} - \mathbf{k_{Ir_2}}$, which means the moiré comprises more than a single beating ($N > 1$). In addition, the position of the graphene spots with respect to the moiré reciprocal lattice is not the same in each main direction, which means the structure is sheared. Actually, along the close-to-horizontal direction in reciprocal space (center-right in Fig. 4.8 right), the set of harmonics around $\mathbf{k_{gr_1}}$ are for instance found right at the center of mass of the triangles defined by the extrapolated lattice. On the contrary, for the second direction (top-right in Fig. 4.8 right), the set of harmonics around $\mathbf{k_{gr_2}}$ lie in between two nodes of the extrapolated reciprocal lattice. This translates into the commensurability relation as:

$$M_{\mathrm{gr}}^{\mathrm{T}} = \begin{pmatrix} 29 & 2 \\ -3 & 32 \end{pmatrix} \text{and } M_{\mathrm{Ir}}^{\mathrm{T}} = \begin{pmatrix} 26 & 2 \\ -3 & 29 \end{pmatrix}$$

$$\text{so } M_{\mathrm{gr}} = \begin{pmatrix} 29 & -3 \\ 2 & 32 \end{pmatrix} \text{and } M_{\mathrm{Ir}} = \begin{pmatrix} 26 & -3 \\ 2 & 29 \end{pmatrix}$$

This description of the superlattice can be summarized with $(i, j, k, l, m, n, q, r) = (29, -3, 2, 32, 26, -3, 2, 29)$, as interpreted in Fig. 4.8 (left). Such a moiré comprises three beatings in each direction (Equation (4.32)), in total $1,868$ carbon atoms. In the extended Wood's notation, this superlattice is described with $(P_1 \ \mathrm{R}\Phi_1 \times P_2 \ \mathrm{R}\Phi_2)$, with $P_1 = \sqrt{26^2 + (-3)^2 + 26 \times 3} \sim 27.62$, $P_2 = \sqrt{2^2 + 29^2 - 2 \times 29} \sim 28.05$, $\Phi_1 = \arctan\left(^{-3\sqrt{3}}/_{55}\right) \sim -5.40°$, and $\Phi_2 = \arctan\left(^{-\sqrt{3}}/_{28}\right) \sim -3.54°$, as deduced from Equations (4.16a), (4.16b), (4.16c) and (4.16d). This is very close but still different from the so-called incommensurate $(9.32 \ \times 9.32)$ R0° structure [147]. The graphene structure is similarly described with $(p_1 \ \mathrm{R}\varphi_1 \times p_2 \ \mathrm{R}\varphi_2)$, with $p_1 = \sqrt{838^2+(-9)^2-838\times(-9)}/934 \sim 0.902$, $p_2 = \sqrt{6^2+847^2-6\times847}/934 \sim 0.904$, $\varphi_1 = \arctan\left(^{-9\sqrt{3}}/_{1685}\right) \sim -0.53°$, and $\varphi_2 = \arctan\left(^{-3\sqrt{3}}/_{844}\right) \sim -0.35°$, as deduced from Equations (4.15a), (4.15b), (4.15c) and (4.15d). These values are in excellent agreement with the 0.903 ratio recently measured by means of surface X-ray scattering [85].

Using Equations (4.27a) and (4.27b), this shearing translates into a combination of biaxial compression $\varepsilon_{\mathrm{b}} \sim -0.29\%$ and uniaxial compression $\varepsilon_{\mathrm{u}} \sim -0.41\%$ (expressed using HOPG as a reference for unstrained graphene). Shear and strain of such extents have already been reported before [10], but no quantitative analysis was provided.

4.3 Moiré superlattice classification

Table 4.1 gives the list of moiré superlattices that have been explicitly reported for graphene on Ir(111) and Pt(111). These structures cover the full $0 - 30°$ range for $\varphi = (\mathbf{a_s}, \mathbf{a_{gr}})$. Similarly, the strain level $\varepsilon = {}^{(a_{\mathrm{gr}} - a_{\mathrm{HOPG}})}/_{a_{\mathrm{HOPG}}}$ goes up to 4.5%. Given the high number of degrees of freedom epitaxial graphene has to relax strain, it appears unrealistic to consider interpreted superlattices with $\varepsilon \gtrsim 1\%$. Instead, more complex superlattices, with greater moiré periods a_{m}, and numerous moiré cells should be considered.

Three support lattices have been considered so far, revealing that a moiré structure can be rotated, strained and sheared. It also demonstrates that moiré superlattices

Figure 4.9: **Moiré lattice constant a_{m} versus angle φ between graphene and its support**. Each point corresponds to a commensurate superlattice of given a_{m} and φ, with its colour indicating the strain level of graphene. The full lines indicate the superlattices containing N beatings within the moiré cell. The coloured ones add a strain information, and for clarity are only shown for the $N = 1$ case. Graphene on (**a**) Ir(111), (**b**) Pt(111) , (**c**) Re(0001) (with lattice parameters $a_{\mathrm{Ir}} = 2.7147$ Å, $a_{\mathrm{Pt}} = 2.7744$ Å, and $a_{\mathrm{Re}} = 2.7609$ Å, see Ref. [97]). For graphene on Ir(111) and Pt(111), black stars index reported unsheared structures, while for graphene on Re(0001), they index the sheared structure analysed here.

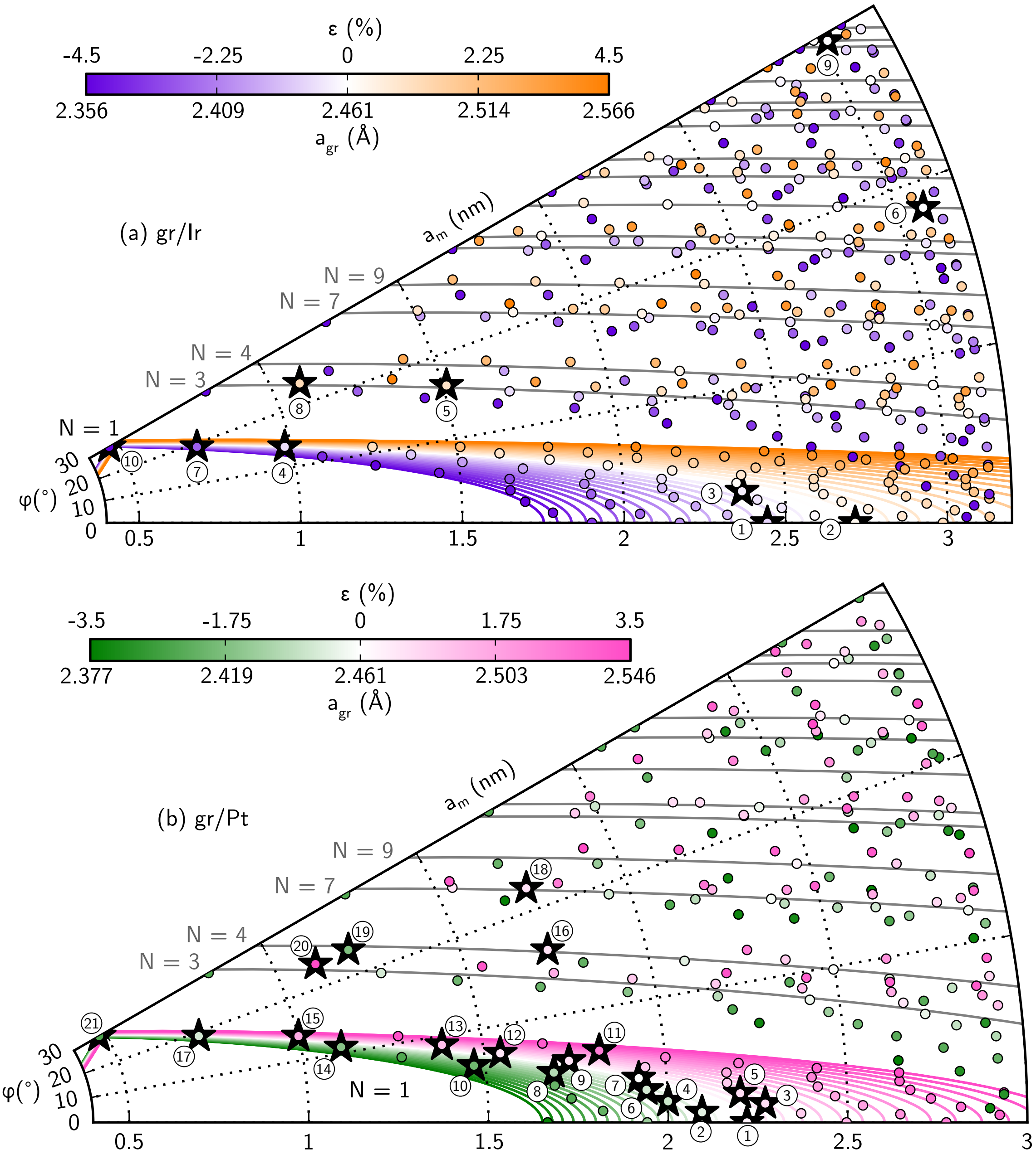

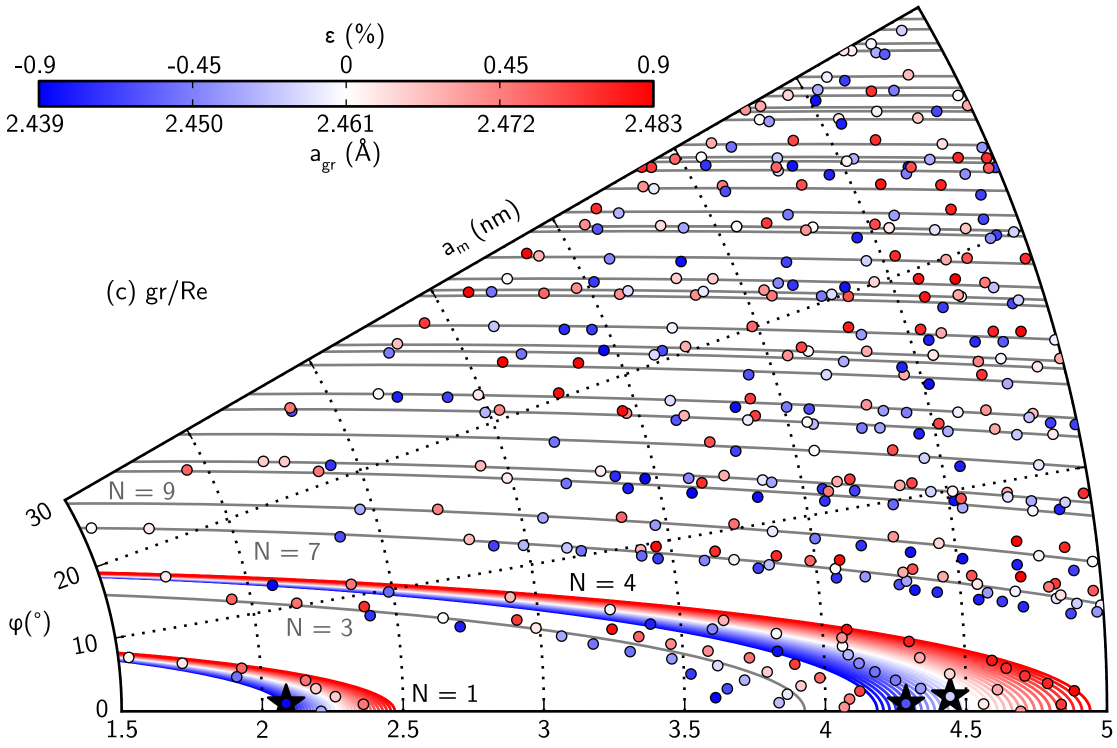

comprising more than one beating are commonly encountered. Three equivalent ways have been presented to describe moiré superlattices with ease:

- Using an extended Wood's notation for a pictorial description using two scaling factors and two angles,
- In more physical terms with rotation angles, and uniaxial and biaxial strains,
- With eight integers that decompose independently the two moiré lattice vectors onto those of graphene and of its support.

The use of eight integers proves necessary for a universal description of all moiré superlattices, in particular of $N > 1$ beatings superlattices, and of sheared superlattices, which both display specific properties. $N > 1$ beatings superlattices indeed exhibit inequivalent moiré hills [81]. Additionally, the geometrical description of a moiré superlattice has a direct link with the position of its replica bands and mini-gaps in reciprocal space. Angle-resolved photoemission spectroscopy [154, 166] and Raman spectroscopy [19, 20] probe the former, while conductance measurements [35, 80, 168] are a precise mean to measure the latter. If sufficiently sensitive and resolved, these techniques will detect the fundamental component of $N > 1$ beatings superlattices.

As for sheared superlattices, their broken three-fold symmetry reshapes the Brillouin zone, which shifts K and K' points, and therefore the position of the graphene Dirac cones [30]. Upon large shear strains, they are predicted to merge, so a band gap opens. Additionally, even marginal shear strain should shift the position of the superlattice mini-gaps in k. As a consequence, for twisted bilayer graphene, this broken-symmetry

gr/Ir	(i, j, m, n)	φ (°)	N	a_{m} (nm)	a_{gr} (Å)	ε (%)	Reference
1	$(10, 0, 9, 0)$	0	1	2.44	2.4432	−0.73	[136, 227]
2	$(11, 0, 10, 0)$	0	1	2.71	2.4679	0.27	[10]
	$(21, 0, 19, 0)$	0	4	5.16	2.4562	−0.20	[10]
3	$(11, 4, 10, 4)$	2.4	1	2.37	2.4541	−0.29	[84]
4	$(4, 0, 4, 1)$	13.9	1	0.98	2.4470	−0.58	[120, 136, 227]
5	$(7, 3, 6, 1)$	16.3	1	1.51	2.4849	0.96	[136]
6	$(13, 1, 13, 5)$	18.5	16	3.08	2.4607	−0.02	[120]
7	$(3, 0, 3, 1)$	19.1	1	0.72	2.3941	−2.73	[136, 227]
8	$(5, 2, 4, 0)$	23.4	1	1.09	2.4912	1.22	[136]
9	$(14, 9, 12, 2)$	29.6	37	3.02	2.4601	−0.04	[120]
10	$(2, 0, 2, 1)$	30	1	0.47	2.3510	−4.48	[136]

gr/Pt	(i, j, m, n)	φ (°)	N	a_{m} (nm)	a_{gr} (Å)	ε (%)	Reference
1	$(9, 0, 8, 0)$	0	1	2.22	2.4661	0.20	[110, 137]
2	$(9, 1, 8, 1)$	0.8	1	2.09	2.4516	−0.39	[43, 55, 137]
3	$(10, 2, 9, 2)$	1.3	1	2.27	2.4778	0.67	[137]
4	$(9, 2, 8, 2)$	1.7	1	2.00	2.4442	−0.69	[110, 137]
5	$(10, 3, 9, 3)$	2.1	1	2.20	2.4776	0.67	[137]
6	$(9, 3, 8, 3)$	2.7	1	1.94	2.4468	−0.59	[43, 137]
7	$(9, 4, 8, 4)$	3.7	1	1.92	2.4611	−0.004	[43, 55, 133, 137]
8	$(8, 4, 7, 3)$	4.7	1	1.69	2.4358	−1.03	[137, 220]
9	$(8, 3, 7, 2)$	5.7	1	1.73	2.4752	0.57	[190]
10	$(7, 3, 6, 2)$	6.2	1	1.47	2.4135	−1.94	[55]
11	$(8, 2, 7, 1)$	6.3	1	1.82	2.5229	2.51	[43]
12	$(7, 2, 6, 1)$	7.2	1	1.54	2.4735	0.50	[137]
13	$(6, 1, 5, 0)$	8.9	1	1.39	2.4915	1.23	[43, 137]
14	$(5, 1, 4, 0)$	10.9	1	1.11	2.4217	−1.60	[137, 196]
15	$(4, 0, 4, 1)$	13.9	1	1.00	2.5008	1.61	[55, 137, 195]
16	$(7, 0, 7, 2)$	16.1	4	1.73	2.4752	0.57	[137]
17	$(3, 0, 3, 1)$	19.1	1	0.73	2.4468	−0.59	[43, 55, 133, 137] [190, 196, 220]
18	$(8, 5, 7, 2)$	22.1	7	1.73	2.4752	0.57	[137]
19	$(5, 0, 5, 2)$	23.4	4	1.21	2.4187	−1.73	[43, 63]
20	$(5, 2, 4, 0)$	23.4	3	1.11	2.5460	3.45	[43]
21	$(2, 0, 2, 1)$	30	1	0.48	2.4027	−2.38	[55, 110, 137]

Table 4.1: **Noticeable graphene on Ir(111) and Pt(111) moiré superlattices:** each considered superlattice is labelled with its (i, j, m, n) integers, and the corresponding graphene-substrate angle (φ), graphene and moiré lattice constants (a_{gr} and a_{m}), and biaxial strain (ε) are indicated. Indices correspond to those appearing in Fig. 4.9.

is predicted to give rise to multiple Van Hove singularities in the electronic density of states [149]. The geometrical analysis presented here is thus a tool towards the quantitative prediction of such effects.

The notation relying on eight integers enables to enumerate all the possible structures by combining every possible value for each integer. The system can further be treated by addressing two independent directions separately, *i.e.* by considering two sets of four integers, (i, j, m, n) and (k, l, q, r), which obey the same equations. One can then rely on the equations established in Sect. 4.1 for isotropic structures. In particular, the commensurability is given by Equations (4.11) and (4.12), the Wood's notation by Equations (4.17a) to (4.18b), and the biaxial strain by Equation (4.28).

With increasing values of (i, j, m, n), it is then possible to enumerate every possible structure. Using a limited set of parameters such as ε and φ allows for a graphical representation of the strain of every possible moiré superlattice in a given direction. Fig. 4.9 gives this representation in the case of graphene on dense-packed surfaces of Ir, Pt and Re. Fig. 4.9 also displays the parametrized curves associated with a first order beating. They correspond to the one-dimensional formula $\sqrt{N}k_m = k_b = k_{gr} - k_s$, and they are defined by Equation (4.5). This series of parametrized curves highlights moiré superlattices with increasing numbers of beatings N.

In the case of graphene on Pt(111), the interpretation in terms of sub-3 nm period superlattices corresponds to suspiciously high strains for a system with such a weak interaction between graphene and the metal. For instance, the phases indexed as 11, 19, 20 and 21 on Fig. 4.9 have been interpreted as moiré superlattices with respectively $\epsilon = 2.51\%$ (11), $\epsilon = -1.73\%$ (19) and $\epsilon = 3.45\%$ (20), and $\epsilon = -2.38\%$ (21). Higher number of beatings are in fact probable for such structures. Such a high number of beatings was determined in the case of the so-called R30 phase of graphene on Ir(111) [120]. A combined micro-spot low energy electron diffraction (μ-LEED) and STM study showed that within a moiré unit cell of ~ 3.02 nm lattice parameter, $N = 39$ beatings separated by ~ 0.47 nm occur ($N_1 = N_2 = \sqrt{39}$). This $N = 39$ moiré is described with $(i, j, m, n) = (14, 9, 12, 2)$ (indexed as 9 on Fig. 4.9), which corresponds to $\epsilon = -0.04\%$. This moiré was also described as a $N = 1$ moiré [136] with $(i, j, m, n) = (2, 0, 2, 1)$ (indexed as 10 on Fig. 4.9a), for which $\epsilon = -4.48\%$, which is questionable. Similarly, the so-called R18.5 of graphene on Ir(111) was interpreted as either $(i, j, m, n) = (13, 1, 13, 5)$, $\varepsilon = -0.02\%$ [120], or $(i, j, m, n) = (3, 0, 3, 1)$, $\varepsilon = -2.73\%$ [227], respectively labelled as 6 and 7 on Fig. 4.9.

The analysis performed here demonstrates the rich variety of moiré superlattices to be expected for graphene on a substrate, well beyond the simple case of $N = 1$ unsheared cases. Although many structures are possible from the geometrical point of view, few of them have actually been reported in the literature. This state of fact can be interpreted in two different ways: either differentiating some very similar structures has not been considered or is not possible due to too limited space resolution, or only a few of them are stable enough to actually exist.

Graphene on Ir(111) and Pt(111) are typical of the first situation. Numerous moiré phases have been reported for them, as shown on Fig. 4.9. The majority of them is identified as $N = 1$ moiré superlattices, nevertheless, this description appears sometimes unrealistic. For graphene on Re(0001), like on Ru(0001) and Ni(111), graphene tends to align its zigzag rows to the close-packed rows of the metal ($\varphi \sim 0°$), even in growth conditions quite far from thermodynamic equilibrium. Presumably, the strong bonds of covalent character between carbon and metal atoms inside the growing flake are not readily broken, as would be required for twisting.

Although large-angle twists are almost prohibited for graphene on Re(0001), slightly twisted graphene phases coexist. These numerous very similar structures can be assumed to be local minima in the energy landscape. Their coexistence then implies a high activation energy between each of them, so the formation of a large-scale uniform graphene phase is kinetically limited. In other words, graphene needs to be heated to high enough temperature to rearrange into the most stable phase of graphene on Re(0001). However, at high temperature, graphene growth competes with bulk dissolution and carbide formation, so the growth is performed by annealing cycles [143]. Over each cycle, graphene's crystallinity progressively improves, which supports this simple kinetic scenario. To go further, one can compare this situation with that of graphene on Ru(0001), where domains slightly rotated around $\varphi \sim 0°$ can be grown, as observed in STM [146] and μ-LEED [126]. By tuning the growth to higher temperature, large domains of one specific structure tend to form [146, 157], which has been analysed as a $N = 4$ ($N_1 = N_2 = 2$) superlattice ($(i, j, m, n) = (25, 0, 23, 0)$) using surface x-ray diffraction [134]. Such similar behaviours may lead to the conclusion that the mechanism presented here is common to every system where graphene is in strong interaction with its substrate.

Graphene on C-face SiC grows with rotational disorder between the adjacent graphene layers [71], so the terminal layers exhibit many possible twisted phases [201]. Even though all kinds of twists are encountered in experiments, it seems that certain twist angles are preferential. It is very likely that these twist angles correspond to commensurate moiré superlattices such as the one reported here. Since both graphene layers share the same lattice parameter, the situation can be depicted with two integers (i, j), such that $(i, j, m, n) = (i, j, -j, i - j)$. For instance, $(i, j) = (4, 7)$ in the present work, and $(i, j) = (4, 1)$ in Ref. [71]. It should be noted that the observation, with diffraction techniques, of a continuum of twist angles (e.g. see Ref. [71]) does not necessarily imply that the twist angle can take random values. Indeed, the existence of a multitude of commensurate superlattices discretely spanning the $0 - 60°$ twist range could as well account for the observation due to the finite size of the diffraction spot (set by the domain size or the instrumental resolution) that they yield. Further pushing this idea suggests to revisit the so-called van der Waals epitaxy. This concept has been introduced decades ago [101], and is attracting a renewed interest in the context of 2D materials growth one onto another, so as to describe the preferential alignment of two lattices "without the need of lattice coincidence". In fact, van der Waals epitaxy seems to be nothing more than a standard epitaxy characterised by a large supercell that does not always appear straightforwardly in experiments.

In conclusion, different supported graphene systems have been studied with STM. A consistent analysis of moiré superlattices involving both direct and FFT STM images has been presented. The geometry of the superlattices, as apparent in STM images, has been rationalized by calculating electronic density maps derived from DFT calculations. A spatial precision of a tenth of 1 pm is achieved, revealing that graphene lying on a substrate is actually twisted, strained and sheared, which breaks its rotational symmetry. A geometrical model enables to classify all moiré superlattices. This model gives a global picture assuming commensurability between graphene and its substrate (and consequently between graphene or the substrate, and the moiré), yielding various numbers of beatings. While a very large number of structures is possible, only a few have actually been reported. In the case of strong graphene-substrate interaction, it is unlikely that all predicted superlattices are discovered, since for instance phases corresponding to a substantial rotation of graphene with respect to the substrate do not tend to form. For low interaction graphene-substrate systems, the complexity of the moiré superlattices has been undetected or overlooked, leading to possibly simplified interpretations.

Surprisingly, no matter how strong the interaction between graphene and its substrate, no clear preferential commensurate structure seems to be observed. This apparently contradicts the Frank and van der Merwe model, which predicts that a strongly-interacting substrate should have large stability domains for commensurate structures. In particular, graphene on Re(0001) displays a very large number of possible orientations, where graphene undergoes complex strain fields such as the shearing identified here. The reason for this apparent paradox is explained in the next Chapter.

Chapter 5

Competing structural orders in graphene on Re(0001)

When suspended, graphene would behave, if it were not held at its edge (like is usually the case in experiments), as a pristine 2D solid with quasi-long-range order, owing to the HMW theorem (see Section 2.4.5). This state of matter exhibits a characteristic power-law decay over distance in the correlations of its order parameter, here atomic displacements with respect to their rest positions. In reciprocal space, this translates into power-law peaks in the structure factor. In direct space, it means that although graphene has local translational order, there is no coherence of this order at larger distances. In other words, due to the 2D character of graphene, there is no absolute reference for the positions of its C atom positions, and their thermally-induced displacements diverge at any non-zero temperature.

When supported by a substrate, an explicit reference is set to C atoms, so one naively expects them to lock on the substrate crystalline order. However, the lattice parameter mismatch and the graphene-substrate interaction play a critical role that can be qualitatively understood with the Frank and van der Merwe model (see Section 2.3.1). Two possible structural orders are expected as possible ground states of this model: a (possibly high-order) commensurate phase where graphene is locked on the long-range order of the substrate, and an incommensurate phase where its own quasi-long-range order survives.

In the previous Chapter, the STM-observation and analysis of moiré superlattices have been interpreted as a signature of complex high-order commensurate phases, submitted to non-trivial strain fields. Here, the study of larger-scale STM images shows static disorder is also present in graphene on Re(0001) samples. Although both commensurate and incommensurate phases can display disorder, neither of them accounts fully for the reported observations. Graphene on Re(0001) rather corresponds to a metastable so-called chaotic phase, where static disorder is quenched, as if it were in a frozen, glassy configuration, due to the large number of local minima in the free energy landscape.

The origin of this peculiar state is rationalized through a detailed analysis of the species and processes involved in the growth of graphene on Re(0001). Growing graphene on a substrate interacting strongly with carbon such as Re is revealed to be kinetically blocked. As a result, multiple reaction paths compete. In particular metastable carbon nanoclusters form, and prove difficult to incorporate in graphene due to high activation energies. This gives rise to the static defects and disorder underlying the chaotic phase. The atomic structure of both the carbon nanoclusters and resulting defects in graphene are presented exhaustively for the first time, with consistency between STM and DFT.

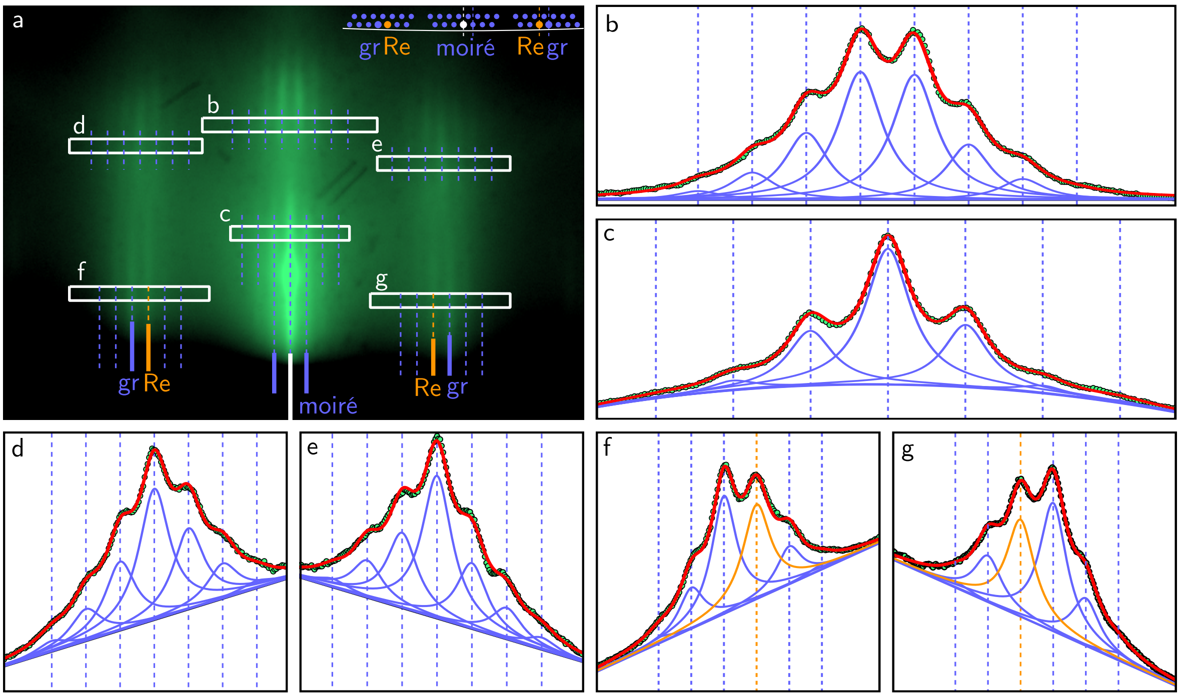

Figure 5.1: **Periodic features in the final steps of graphene growth.** (**a**) RHEED pattern of the graphene-covered Re(0001) surface with $[11\bar{2}0]$ incident azimuth. Coloured lines indicate the specular rod (white), as well as the position of Re (orange), graphene and moiré (blue) truncation rods. Inset shows a schematic top view of the reciprocal space with all observed rods and a cut of the Ewald's sphere in white. (**b-g**) Profiles extracted from the rectangular cuts are fitted with lorentzian peaks on a flat (**b**), quadratic (**c**) or linear (**d-g**) background.

5.1 Metastable chaotic phase

To investigate this structural order, graphene was grown on a Re(0001) single crystal, following the method described in Chapter 3. The sample studied here is the same as the one of Section 4.2.2, and the presented STM topographs have been acquired during the same experimental run. To assess the kind of order of the obtained graphene, electron diffraction measurements have been performed, and show an overall good structural quality. Complementary atomically-resolved STM investigation reveals that some disorder is actually still present at the local scale. When qualifying this type of disorder, it appears graphene on Re(0001) corresponds neither to a commensurate, nor to an incommensurate layer, but is in a chaotic state.

5.1.1 Experimental observation of static disorder

Sharp truncation rods attributed to Re, graphene and moiré periodicities are typical of RHEED patterns taken at the end of graphene growth, as visible on Fig. 5.1a. In the

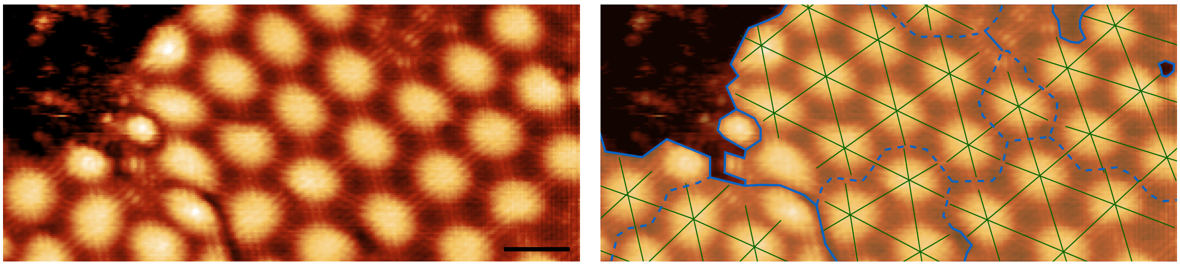

Figure 5.2: **Coexisting moiré superlattices. Left:** STM topograph (V_b = 20 mV and I_t = 10 nA, scale bar 2 nm) of graphene on Re(0001) displaying domains of different moiré superlattices. **Right:** corresponding interpretation, where green lines following the moiré hills show the difference between adjacent domains. Blue lines indicate two types of domain walls: either grain boundaries (solid) where the honeycomb structure is disrupted, or continuous domain walls (dashed) across which the structural coherence of graphene is preserved.

first Laue zone (Fig. 5.1f,g), sharp lorentzian profiles match the Re and graphene rods, with additional equidistant lorentzian contributions sharing the width of the graphene rod and related to the moiré superperiodicity. Their sharpness translates the large size of graphene crystallites. Besides, the large number of equidistant moiré-related rods observed in the first (Fig. 5.1c,f,g) and second Laue zone (Fig. 5.1b,d,e) is a signature of the large-scale moiré regularity.

As RHEED probes mm^2-areas of the sample, the rods fitted positions give access to average lattice parameters. Assuming the Re substrate as unstrained ($a_{\mathrm{Re}} = 2.7609$ Å [97]), the lattice constant of graphene is found to be $a_{\mathrm{gr}} = 2.481 \pm 0.002$ Å, corresponding to a lattice extension of 0.8 ± 0.1 % with respect to HOPG ($a_{\mathrm{HOPG}} = 2.4612$ Å [97]). The average moiré superperiodicity is then $a_{\mathrm{m}} = 2.44 \pm 0.02$ nm, which corresponds to an average commensurability of 9.85 graphene cells on 8.85 Re cells.

When considering the fitted amplitudes, since RHEED is a surface-sensitive probe, one would expect the graphene rod to be more intense than that of Re. This is indeed the case, consistently with a high graphene coverage. In short, RHEED measurements indicate graphene covers most of the surface with rather high crystalline quality and a regular moiré superperiodicity.

These results are consistent with atomically-resolved STM imaging, a typical example of which is given on Fig. 5.2 (left). A monolayer of graphene covers the Re(0001) surface, giving rise to a $a_{\mathrm{m}} \sim 2.4$ nm moiré superlattice, except on the bare top-left hand corner. However, close inspection of the beating periodicity and orientation reveals slight variations, emphasized with green lines on Fig. 5.2 (right). These variations seem to follow domains identified with blue lines, which are either grain boundaries (full lines) between graphene crystallites, or domain walls (dashed lines) between different moiré phases. Grain boundaries disrupt the carbon lattice, featuring holes and defective structures, as can be seen on the bottom of Fig. 5.2. On the contrary, no such discon-

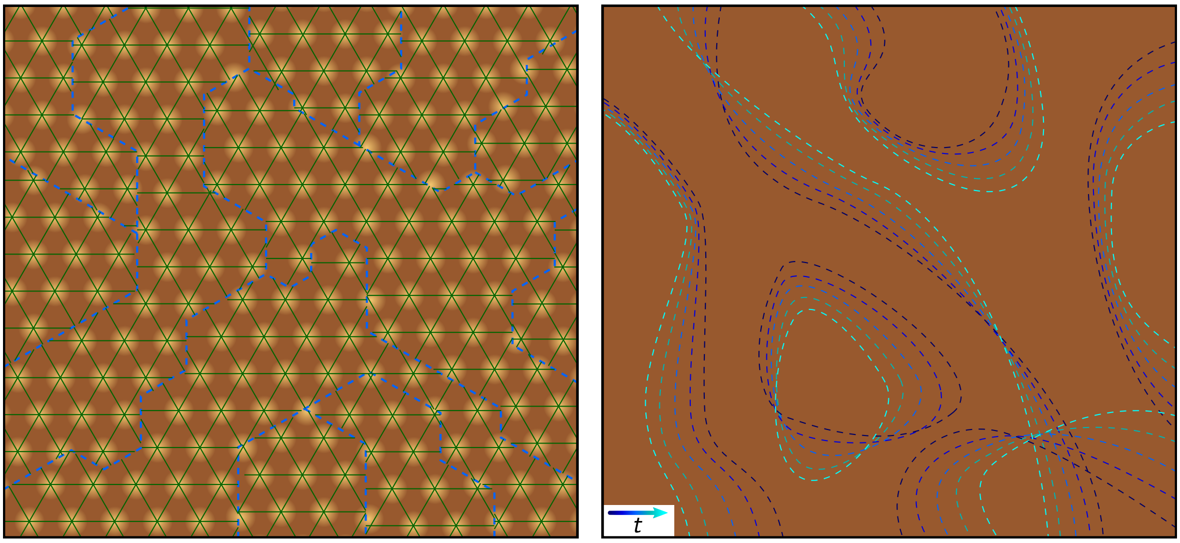

Figure 5.3: **Disorder in commensurate and incommensurate phases. Left:** For a commensurate phase, disorder manifests itself as degenerate domains shifted with respect to each other, as indicated by green lines. The domain walls (dotted blue lines) are static and correspond to topological defects in the commensurate order. **Right:** For an incommensurate phase, thermal fluctuations generate zero-mass phasons (dotted blue lines), which upon propagation make C atoms wiggle. This phase is disordered in itself, and disorder is dynamic.

tinuity can be identified along domain walls, which therefore preserve the honeycomb lattice coherence. Between two adjacent domains, the beatings are rotated of at most 5 °, and variations of a_m stay within ± 0.1 nm.

As the beating arises from the superposition of graphene and its Re substrate (see previous Chapter), the observed slight variations originate from even slighter modulations in the structure of graphene and/or Re. Since the beating periodicity is about 10 times that of graphene, the rotations and lattice parameter variations are $\lesssim 0.5°$ and 0.1 Årespectively.

5.1.2 Disorder in commensurate and incommensurate phases

Beyond this order of magnitude estimation, a more detailed structural analysis is desirable to evaluate whether graphene is commensurate or incommensurate on Re(0001). Both phases can host disorder, but of two different kinds, as illustrated on Fig. 5.3.

Let us first consider a commensurate phase. In such a phase, graphene locks on a specific commensurate relation with the substrate, which is the absolute minimum in its free energy landscape. This relation corresponds to a single moiré superlattice, while other possible moiré superlattices are at best metastable. Still, even with a single possible moiré superlattice, disorder is possible, as a domain of graphene can be shifted with respect to another one. The interface between two such domains is a domain wall, and constitutes a topological defect in the commensurate order (see Section 2.4.3). Therefore, for a commensurate phase, domain walls can be expected between shifted domains of the same moiré superlattice, as illustrated on Fig. 5.3 (left) with blue dotted lines.

On the contrary, thermal fluctuations play a key-role in an incommensurate phase, as the C atom displacements they induce prohibit graphene from locking to a commensurate relation. In other words, there is no long-range order, so the concepts of domain and domain wall are ill-defined. This absence of long-range order can be seen as arising from Goldstone modes called phasons (see end of Chapter 2), whose thermally-induced generation and propagation cause C atoms to wiggle. In this case, disorder is dynamic, so the blue dotted lines on Fig. 5.3 (right) bend and move continuously over time, and correspond to propagating phasons.

With this distinction in mind, one can wonder whether the variations observed on Fig. 5.2 mimic domain walls between degenerate commensurate domains, or phasons in an incommensurate solid. Due to the small size of the identified domains, an analysis similar to the one detailed in the previous Chapter is impossible, because a small field of view would lack resolution, whereas a large one would average out different domains.

Still, elliptic moiré hills associated to shear can be observed on Fig. 5.2 (left). This means non-trivial strain fields are distributed over the entire field of view. Moreover, no specific high-order commensurate structure is observed in more occurrences than any other, which contradicts the existence of a single stable commensurate phase of graphene on Re(0001). In these conditions, continuous domain walls do not correspond to topological defects between degenerate domains of this stable phase. They are rather domain walls between non-degenerate metastable phases of graphene on Re(0001).

Intuitively, the absence of a privileged commensurate phase supports the scenario of incommensurate graphene. However, the observed disorder is static, and therefore does not correspond to dynamic disorder expected from an incommensurate phase. Indeed, no change of the moiré superlattices could be detected in the course of STM imaging or in between two STM topographs, which means no movement in the underlying atomic structure takes place. It can be argued that the typical time scale of atomic displacements is well shorter than the acquisition time scale of conventional STM, so the effect of fluctuations should be averaged out. Here, one can exclude thermal fluctuations of the atomic positions in the Å-range, which would prevent to even define average atomic positions at all, according to the HMW theorem applied to an incommensurate phase.

In the end, the observations correspond neither to a commensurate, nor to an incommensurate configuration. Commensurability is excluded, because disorder is such that no unique stable phase of graphene on Re(0001) can be identified. This does not exclude the existence of such a stable phase in other circumstances, but simply means that many metastable features are instead observed here. It is not incommensurate either, as the observed disorder is static rather than dynamic. This does not exclude graphene could be incommensurate, but implies that fluctuations are pinned to the Re lattice because of the strong graphene-substrate interaction. These two alternative descriptions – highly disordered commensurate and frozen incommensurate – are the two faces of the same coin: a kind of intermediate state called the chaotic phase [3].

A chaotic phase in supported 2D solids has been discussed in two contexts. On the one hand, appropriate tuning of interaction strengths in the system can lead to frustration. In the discrete 1D Frank and van der Merwe model (see Section 2.3.1), elastic and potential energy terms compete, so a given configuration of the system cannot in general satisfy both at the same time.[1] With the right tuning of parameters, chaotic metastable solutions can be found [2], where either compressive or tensile phasons are randomly pinned to the lattice [15]. The chaotic character of these solutions can be understood when considering their spatial evolution as a time evolution. Following the relative atomic positions along the chain is then equivalent as studying its time evolution. As there is no periodicity along the chain, the situation is analogous to a chaotic time evolution. The frustration at the origin of this behaviour is analogous to the anisotropic next-nearest-neighbour Ising model, where competition between ferromagnetic nearest-neighbour and antiferromagnetic next-nearest neighbour can also give rise to chaotic phases [3]. In this model too, chaotic phases appear as kinks randomly pinned by the Peierls potential [86]. In this context, chaos originates from frustration in the interactions.

On the other hand, a chaotic phase can also be stabilized upon a temperature quench of a liquid into a (disordered) glass. In that case, even though a crystalline phase is favoured at low temperature, the out-of-equilibrium evolution of the system quenches disorder in the low temperature phase. Quenched disorder is then metastable. For 2D solids, the transition is the commensurate-incommensurate transition (see Section 2.3.3), where the disordered phase is the incommensurate one, and the ordered phase is the commensurate solid. Disorder is due to the phasons (see Section 2.4.5). If abruptly cooled down from the incommensurate to the commensurate phase, quenched disorder should be expected as phasons with frozen dynamics: this corresponds to the chaotic phase. It has for instance been reported as a “soliton glass” in surface X-ray diffraction experiments of Pb atoms adsorbed on Cu(110) when varying temperature and coverage [117]. In this situation, chaos relates to quenched disorder resulting from an abrupt phase transition.

Although the final state observed is much alike a glass, scenarios of the kind involved in the liquid-to-glass and incommensurate-to-“phason glass” transitions are not at play here. As it is now going to be presented, the static disorder on Fig. 5.2 is due to growth constraints. Indeed, this chaotic disorder is kinetically blocked as graphene grows on Re(0001).

---

[1] In Section 2.3.2, the continuum approximation removes the discrete character, thereby avoiding issues of frustration, and providing simple analytical solutions. This approximation relies on the hypothesis of smooth variation of phase φ, which is no longer valid for frustrated configurations.

5.2 Kinetically blocked disorder in graphene

To understand the static disorder observed in a full layer of graphene, the first steps of the growth will have to be addressed. Instead of a Re single crystal, here a 50 nm thick Re(0001) film has been used. It has been deposited by molecular beam epitaxy (MBE) on a polished α-Al_2O_3(0001) single crystal, which had been previously cleaned by annealing under UHV for 5 h at $T = 573$ K. Rhenium deposition was performed at 773 K with a rate of 8 Å/min. The obtained Re(0001) film has its $\langle 1\bar{1}00 \rangle$ crystallographic directions aligned with the $\langle 11\bar{2}0 \rangle$ ones in α-Al_2O_3. After deposition, its crystalline quality has been checked by RHEED and AFM.

To grow graphene, it has then been exposed to air, and transferred to another UHV system via a bottle under static vacuum. A sub-monolayer coverage of graphene has been obtained by annealing at $T = 800$ K for 4 h (base pressure $4 \cdot 10^{-10}$ mbar). The carbon precursor is attributed to airborne adsorbates as well as possible residual CO of the UHV chamber.

5.2.1 Species coexistence

After annealing, RHEED patterns of the Re(0001) surface have been acquired at two different incident angles, as shown on Fig. 5.4a,b. Fig. 5.4a displays streaks revealing truncation rods associated with the Re and graphene periodicities. Fitting their position and using Re's lattice constant as a reference, the lattice constant of graphene is extracted: $a_{\mathrm{gr}} = 2.479 \pm 0.006$ Å, corresponding to a lattice extension of 0.7 ± 0.3 % with respect to HOPG. This value is consistent with the lattice constant measured in the final steps of graphene growth. As for the fitted amplitudes, due to the low graphene coverage, the Re rod is more intense even at fairly low incident angle, as visible on Fig. 5.4c-d.

Moreover, at more grazing incidence, intermediate streaks can be identified halfway between the specular and the Re streaks on Fig. 5.4b. This is consistent with either a (2×2) or a (2×1) superstructure, attributed to C adatoms (see below). Two main reasons support a (2×2) superstructure. First, in a (2×1) superstructure, C atoms are arranged on neighbouring Re sites. However, no such neighbouring atoms are observed on STM topographs. Besides, DFT calculations performed for various coverages of C atoms on Rh(111), another metal surface known for its high affinity to carbon, show there is a repulsion energy between C atoms [215]. Preliminary DFT results obtained for Re(0001) not shown here support a similar trend, therefore favouring a (2×2) over a (2×1) superstructure.

Although those (2×2) rods are difficult to notice on the raw RHEED pattern on Fig. 5.4b, the average line profiles on Fig. 5.4e-f show they are actually hidden by the tail of the lorentzian-fitted specular rod. Their fitted width is larger than those of graphene and Re on Fig. 5.4c-d, which can attributed to a disordered arrangement of carbon adatoms. This ordering is consistent with DFT calculations published earlier [67].

In situ STM corroborates the interpretation of RHEED patterns. It reveals three

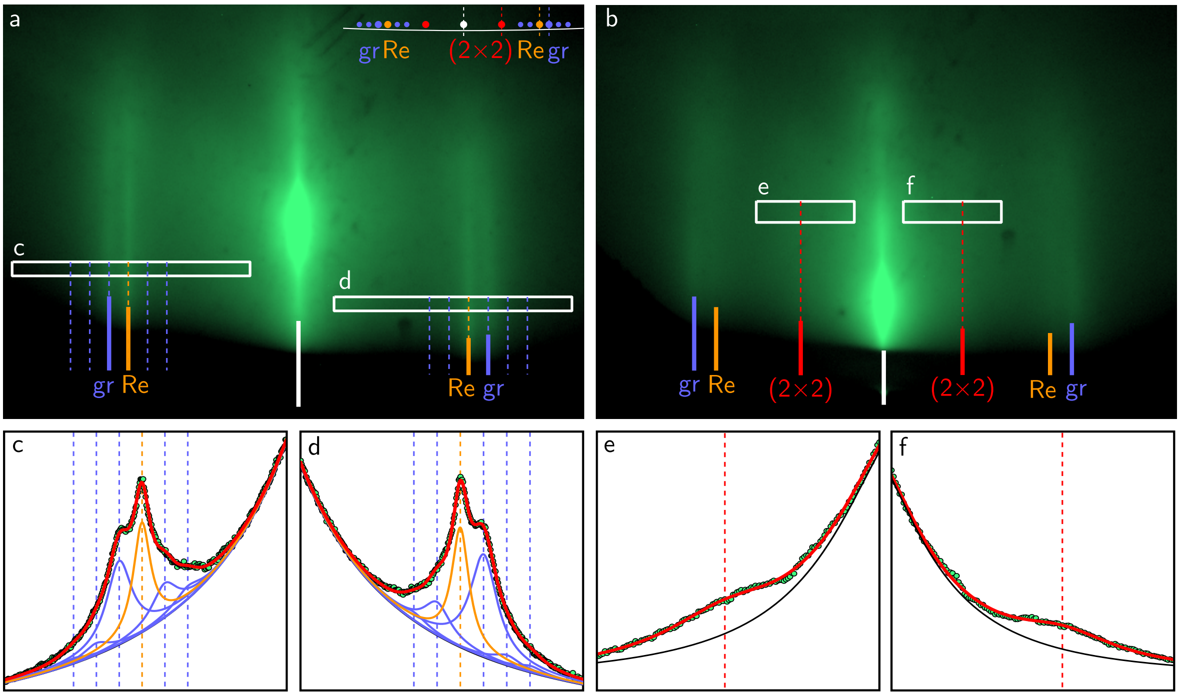

Figure 5.4: **Periodic features in the first steps of growth.** (**a-b**) RHEED patterns of the Re(0001) surface after 800 K annealing, with $[11\bar{2}0]$ incident azimuth, at two different incidence angles. Coloured lines indicate the specular rod (white), as well as the position of Re (orange), graphene (blue) and the carbon adatoms (2×2) superstructure (red) truncation rods. Inset shows a schematic top view of the reciprocal space with all observed rods and the Ewald's sphere in white. (**c-f**) Profiles extracted from the rectangular cuts are fitted with lorentzian peaks on a lorentzian background.

kinds of species, as visible on Fig. 5.5 (left). Graphene flakes with several nanometers of extension are readily identified by their typical moiré superlattice. In addition to these flakes, smaller objects are observed, which have the size of molecules. The smallest dimer-like ones will be disregarded. Their aspect strongly changes depending on imaging conditions, as shown on Fig. 5.6, and at present the (already high) lateral resolution obtained in the STM images only allows for speculations regarding their nature. The other molecule-like objects remind of similar ones, which have been observed on other metal surfaces following the breaking of carbon molecules [33, 121] or during chemical vapour deposition [34, 107, 215]. While it is accepted that they consist of sp^2-hybridised carbon, and form strong bonds at their edges with the metal surface, their structure and their binding geometry remain unclear. These details are however crucial to understand the disorder quenching during further stages of graphene preparation.

A small detour is now taken to reach such degree of detail, focusing on the third kind of species present at the surface. Close inspection of Fig. 5.5 (left) reveals a dilute, partially ordered phase of even smaller features of atomic size around the molecules and graphene islands. They provide the key that has been missing to unambiguously

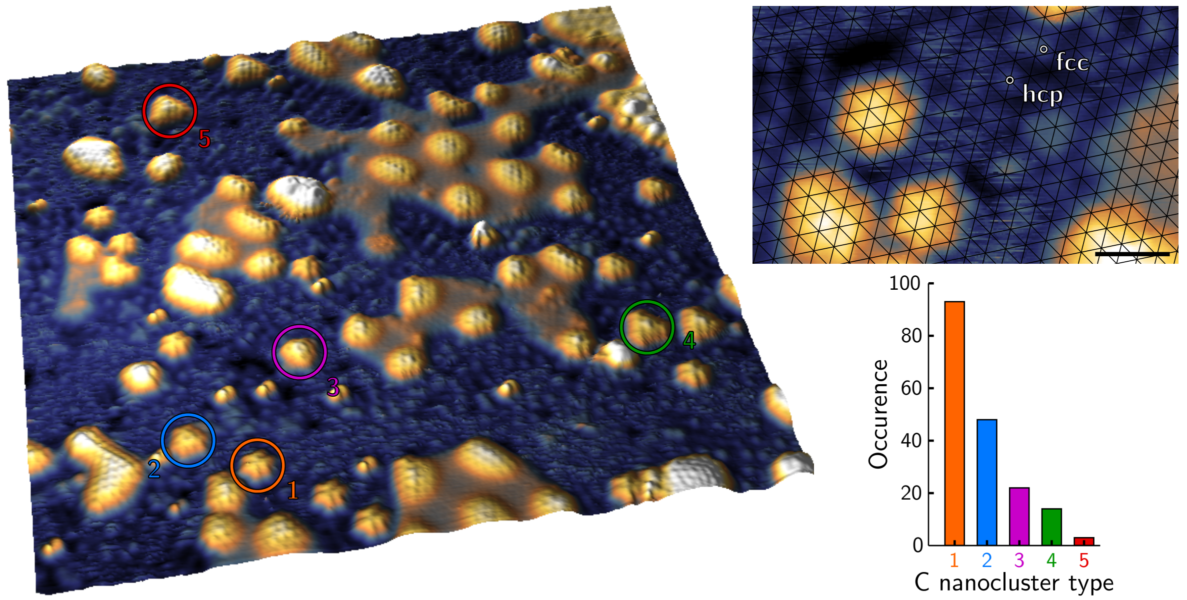

Figure 5.5: **Carbon species formed on Re(0001). Left:** 3D STM topograph ($V_b = -2$ V and $I_t = 1$ nA, 20×20 nm^2) of graphene on Re(0001) revealing three kinds of species: graphene islands, carbon adatoms, and carbon nanoclusters. The latter are numbered from 1 to 5 by increasing size. **Top right:** close-up view (scale bar 1 nm), overlaid with a triangular grid whose vertices are hcp sites. The locations of hcp and fcc sites are indicated. **Bottom right:** number of occurrences for each graphene nanocluster.

elucidate the nature and bonding of the nanoclusters in previous works.

5.2.2 Carbon adatoms

Upon annealing at 800 K in UHV, only few atomic species can still be expected on a Re(0001) surface. Indeed, H_2 desorbs completely after an annealing at 800 K [40]. On the contrary, S atoms stick to Re(0001) for temperatures up to 1600 K [92], even if isolation from outdoors atmosphere makes exposure to sulfur-compounds unlikely. Molecular adsorption of N_2 on Re(0001) is possible, but it is fully removed at 200 K [66]. As for dissociative adsorption of N_2, although N atoms desorption requires 1200 K annealing, it has a sticking coefficient below 10^{-5} [66]. At room temperature, O_2 adsorbs dissociatively [39]. Similarly, CO_2 molecules adsorb dissociatively into CO and O fragments at room temperature [162]. As for CO molecules, they are known to bind at any temperature, and dissociate at temperatures above 450 K [41]. In the end, only individual C and O atoms are reasonable candidates for these atomic features.

DFT studies predict they both bind preferentially on hcp hollow sites to form a (2×2) superstructure [67, 88]. This is consistent with the disordered (2×2) arrangement of atoms observed by both RHEED (Fig. 5.4b) and STM (Fig. 5.5a). Since most atoms

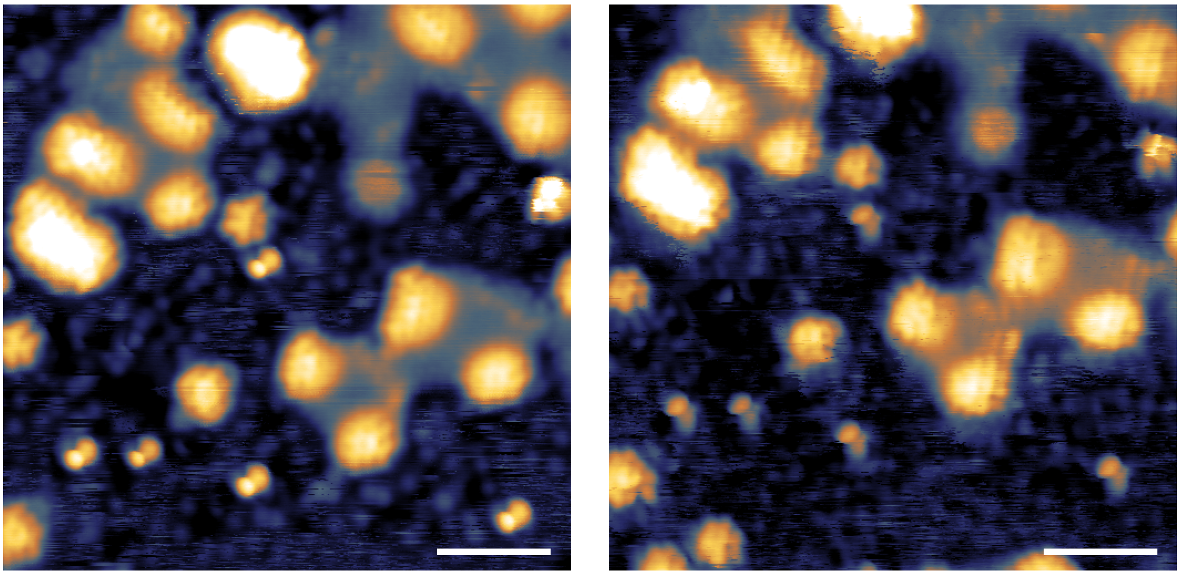

Figure 5.6: **STM tip artefact.** Successive STM topographs ($V_b = -2$ V and $I_t = 1$ nA, scale bar 2 nm) taken in the same scanning direction before (left) and after (right) a tip change.

should sit on hcp hollow sites, a triangular mesh extrapolating the adatoms can be superimposed on STM images, as illustrated on Fig. 5.5b and 5.7c-e. Most atoms are found on the nodes of this mesh, which therefore correspond to hcp sites of the substrate (see Section 2.1 for site denomination). The second preferred site for C and O adatoms is the fcc hollow site, which is thus attributed to the fraction of atoms found not to match the nodes of the mesh. Consistently with DFT calculations, no individual atom is found on top sites, although few multimers sometimes comprise atoms on top sites, as can be seen on Fig. 5.7c,e. The number of occurrences for each type of site is reported on Fig. 5.7b, and shows in particular a ratio between atoms in fcc and hcp sites of 0.13 ± 0.03.

This ratio provides strong hints concerning the nature of the atoms bound to the surface, C or O. Indeed, the binding energy difference $\Delta E_{\mathrm{hcp-fcc}}$ between hcp and fcc hollow sites is ~ 0.1 eV for C and ~ 0.6 eV for O [67]. It is reasonable to assume atoms can diffuse on the Re(0001) surface at 800 K, so their distribution on hcp and fcc sites should follow a Maxwell-Boltzmann distribution. The ratio of atoms in fcc and hcp sites should then be of the order of $\exp\left(^{-\Delta E_{\mathrm{hcp-fcc}}}/_{k_B T}\right)$. For C, this yields a fcc/hcp ratio of ~ 0.2, whereas this ratio is $\sim 10^{-4}$ for O. The dilute atom phase is hence identified as a phase of C atoms.

The attribution of hcp, fcc and top sites is further confirmed using the STM contrast of the graphene moiré superlattice. A moiré superlattice contains three typical stacking configurations that correspond to the moiré hill and valleys (see Section 2.1), easily distinguished on STM topographs. Indeed, both topographic and electronic effects con-

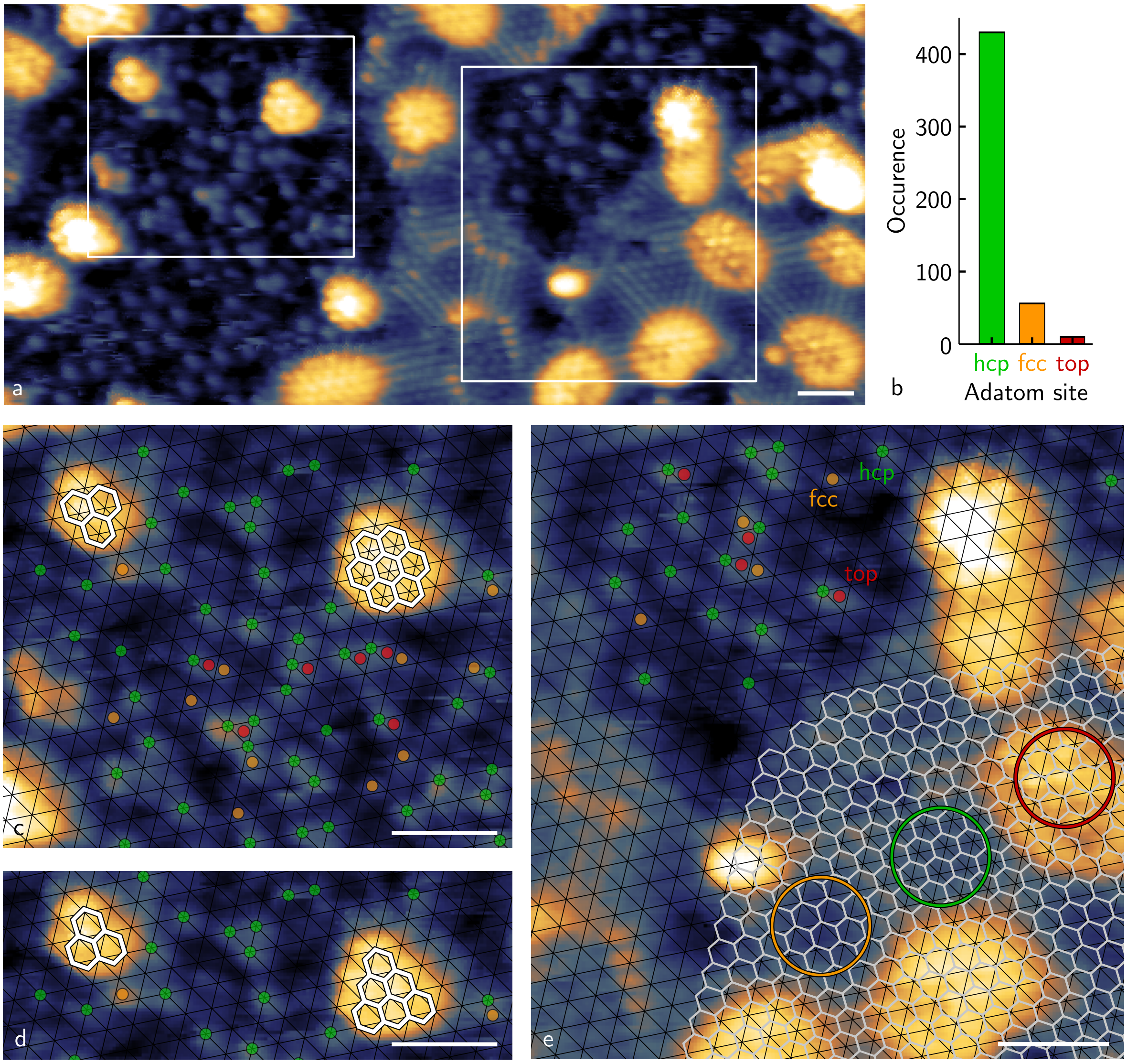

Figure 5.7: **Substrate extrapolation.** (**a**) STM topograph ($I_\mathrm{t} = 5$ nA, $V_\mathrm{b} = 0.5$ V, all scale bars 1 nm) of coexisting carbon adatoms, carbon nanoclusters, and nanometer-size graphene islands. (**b**) Number of occurrences of adatom adsorption sites. (**c-e**) Close-up views of (**a**), where adatoms on hcp (green), fcc (orange) or top (red) sites are indicated. A black mesh is extrapolated from them and used to interpret the adsorption sites of H- (**c**) or T- (**d**) carbon nanoclusters. The consistency of this analysis is checked on (**e**) by confronting the extrapolated mesh to the circled typical areas of the moiré pattern, where graphene (grey honeycomb lattice) adopts top-hcp (orange), top-fcc (green) and hcp-fcc (red) local stackings.

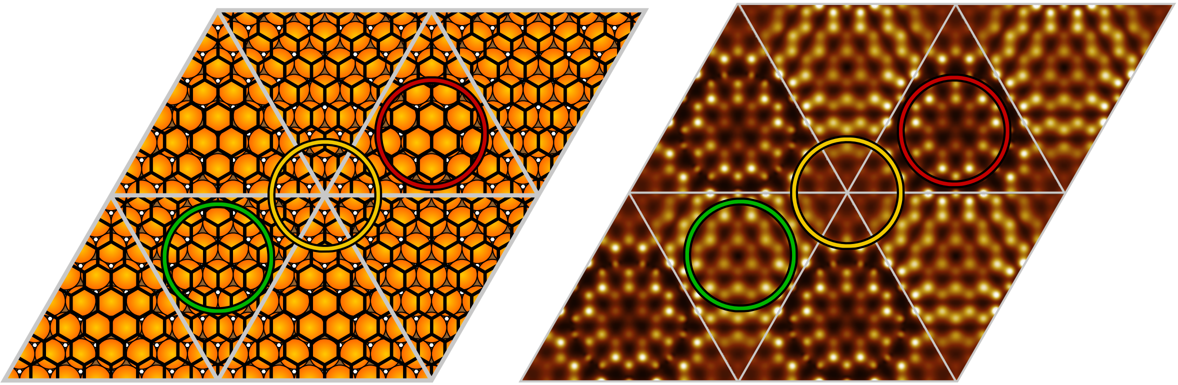

Figure 5.8: **Calculated valley contrast. Left:** ball model of 4 moiré supercells, as emphasized by gray lines. For each supercell, 8 cells of graphene match 7 cells of Re. The three typical areas of the moiré superlattice are circled depending on their local stacking configuration: top-hcp (orange) and top-fcc (green) for the valleys, and hcp-fcc (red) for the hill. **Right:** cross-section just above the valley atoms of the square modulus of the corresponding electronic wave function integrated from $E_F - 0.25$ eV to E_F. A difference in electronic density between the two valleys is responsible for the contrast between the dark top-hcp valley (circled in orange) and the brighter top-fcc valley (circled in green). Such contrast could be reproduced no matter the height where the cross-section was taken, or what energy window was chosen for the integration. Here, the cross-section is taken close to the atoms in the moiré valleys, so because of graphene corrugation, it is below the atoms in the moiré hill. Therefore, this cross-section does not simulate the moiré hill correctly.

tribute to make moiré hills look bright and moiré valleys appear dark.[2] The top-hcp and top-fcc valley areas partially bond to Re, so they lie close to the substrate, and due to $\pi - d$ hybridization, their electronic density of states above the Fermi level is depleted. Unlike them, the hcp-fcc hill area lies further apart from Re with a relatively intact density of states. One can then use the STM contrast to extrapolate the underlying substrate sites.

While the attribution of the top sites is rather straightforward in link with the moiré hills, distinguishing hcp from fcc sites requires to distinguish the top-hcp from top-fcc valleys of the moiré. To this end, DFT calculations of a moiré cell of graphene on Re(0001) have been performed. The moiré cell consists of 8 graphene cells aligned with 7 cells of rhenium and contains 5 layers of rhenium. In the converged structure, carbon atoms are closer to Re in the top-hcp valley than in the top-fcc one. Beside, cuts in the electronic density show top-hcp areas are depleted in electrons with respect to top-fcc areas, as illustrated on Fig. 5.8. For both reasons, the top-hcp valley appears lower (darker) than the top-fcc valley in STM topographs of graphene on Re(0001). It is also

---

[2] Contrary to graphene on Ir(111) [147], no inversion of the moiré contrast of graphene on Re(0001) has been observed in experiments.

known that top-hcp areas tend to appear lower by STM on the similar system graphene on Ru(0001) [213]. This attribution confirms the identification of hcp and fcc sites, as detailed on Fig. 5.6e.

In short, the smallest features observed on Fig. 5.5a are C adatoms forming a disordered (2×2) superstructure, and sitting preferentially on hcp hollow sites. Due to the relatively small binding energy difference between hcp and fcc sites, they also occupy fcc sites in non-negligible proportions. Not only does this feature distinguish C from O atoms, it also provides a way to extrapolate the atomic structure of the Re(0001) substrate. This extrapolation will be the key to analyse the identified carbon nanoclusters.

5.2.3 Carbon nanoclusters

Turning back to the carbon nanoclusters, their structural analysis is going to be detailed in four steps. First, their epitaxial character is going to be justified. Then, size and symmetry constraints will show only two families of configurations can match the STM features. Using the disordered (2×2) C superstructure, the adsorption sites of each possible configuration will be deduced. Finally, confrontation of those interpretations with DFT simulations will provide the details of the atomic structures.

First, the nanoclusters observed on Fig. 5.5 (left) are systematically found on the surface (yet their observation has long been hampered by the difficult imaging conditions), with always the same shape and orientation. The associated statistics are displayed on Fig. 5.5 (bottom right). This systematics in the observation of the nanoclusters shows they have a well-defined structure in epitaxial relation with the Re(0001) substrate.

Another proof of the epitaxial relation between the carbon nanoclusters and their substrate is given on Fig. 5.9, where carbon nanoclusters observed on one side of an atomic step all look like the symmetric of those observed on the other side of this step. Since they are all observed on the same STM topograph, this symmetry is neither an electronic density of state effect nor a tip effect. It is actually well accounted for on crystallographic grounds. Indeed, Re is a hcp crystal, *i.e.* it is a stacking of close-packed atom planes along the [0001] direction, indexed as ABABAB... At an atomic step edge, the lower terrace can be labelled as an A plane, whereas the upper terrace is a B plane. This different labelling translates the two-fold rotation symmetry that relates an A plane to a B plane. Essentially, it inverts the hcp and fcc hollow sites, as pictured on Fig. 5.9 (bottom). As a consequence, going through an atomic step is equivalent to applying a 180°-rotation operation to the substrate. Since the carbon nanoclusters are epitaxially attached to it, they are also rotated by 180° when going through an atomic step, as observed on Fig. 5.9 (top). This observation is thus consistent with the fact that carbon nanoclusters have a well-defined structure epitaxially formed on Re(0001).

Close-up views of the nanoclusters indexed 1, 2, 4, 5, on Fig. 5.5 (left) are displayed on Fig. 5.10a. The structure of nanocluster 3 will be discussed later on Fig. 5.12.

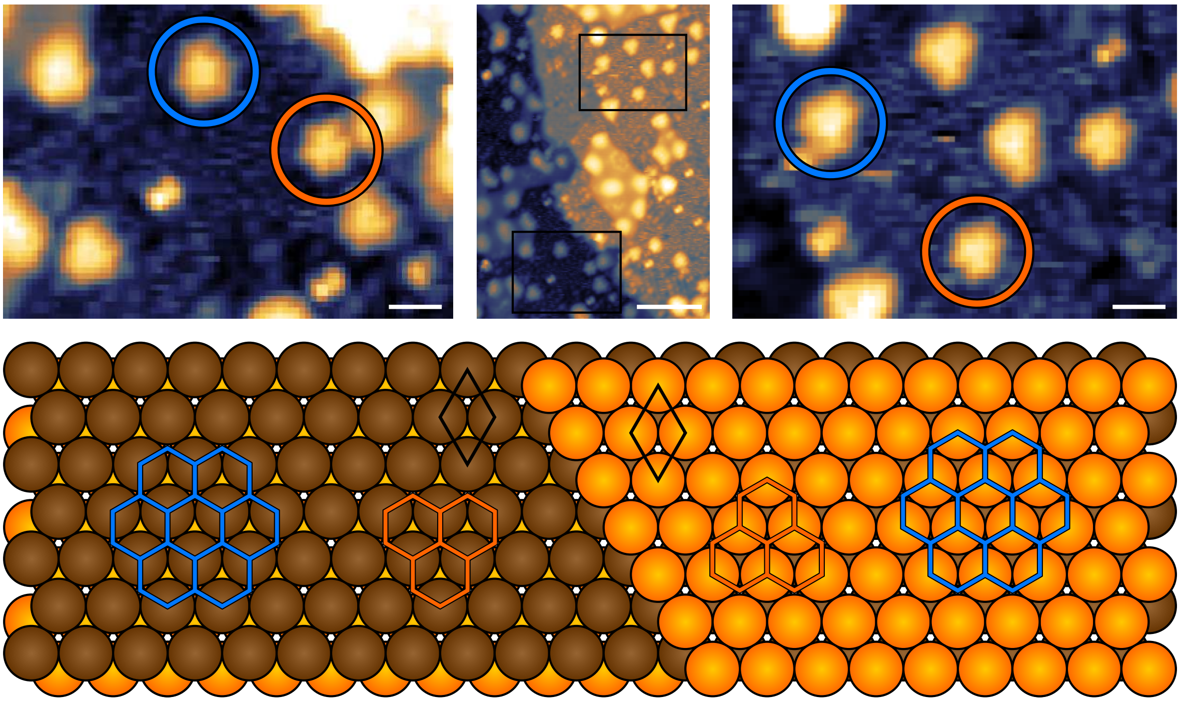

Figure 5.9: **Carbon nanocluster inversion through an atomic step. Top:** STM topographs ($I_\mathrm{t} = 1$ nA, $V_\mathrm{b} = -2$ V) of carbon nanoclusters observed on each side of an atomic step. **Top middle:** (scale bar 5 nm) black rectangles indicate areas of lower and upper terraces displayed with better contrast on each side. **Top left and right:** (scale bars 1 nm) Both the shape and the atomic structure of the carbon nanoclusters look inverted. **Bottom** : ball model clarifying this inversion based on the substrate atoms stacking. Two black rhombi indicate the hcp and fcc hollow sites are inverted, so the epitaxial carbon nanoclusters are also inverted.

On STM topographs, carbon nanoclusters appear as bright protusions with an atomically resolved apparent structure, as visible on Fig. 5.10,1-5,a. To make this atomic structure more visible as on Fig. 5.10,1-5,b, a paraboloidal background has been systematically fitted and subtracted.

STM does not give direct access to atomic structures, but probes the electronic wave function integrated over an energy window. In general, these protusions cannot be straightforwardly interpreted as atoms, and require comparison with DFT calculations as will be detailed later on. Nevertheless, it can be reasonably argued that the observed three-fold symmetry of all carbon nanoclusters is inherited from the symmetrical structure of their stacking onto the substrate. The possible structures are therefore constrained by size and symmetry arguments.

Given these constraints of symmetry and size, only two options can reasonably be considered for each observed carbon nanoclusters. This leads to two families represented

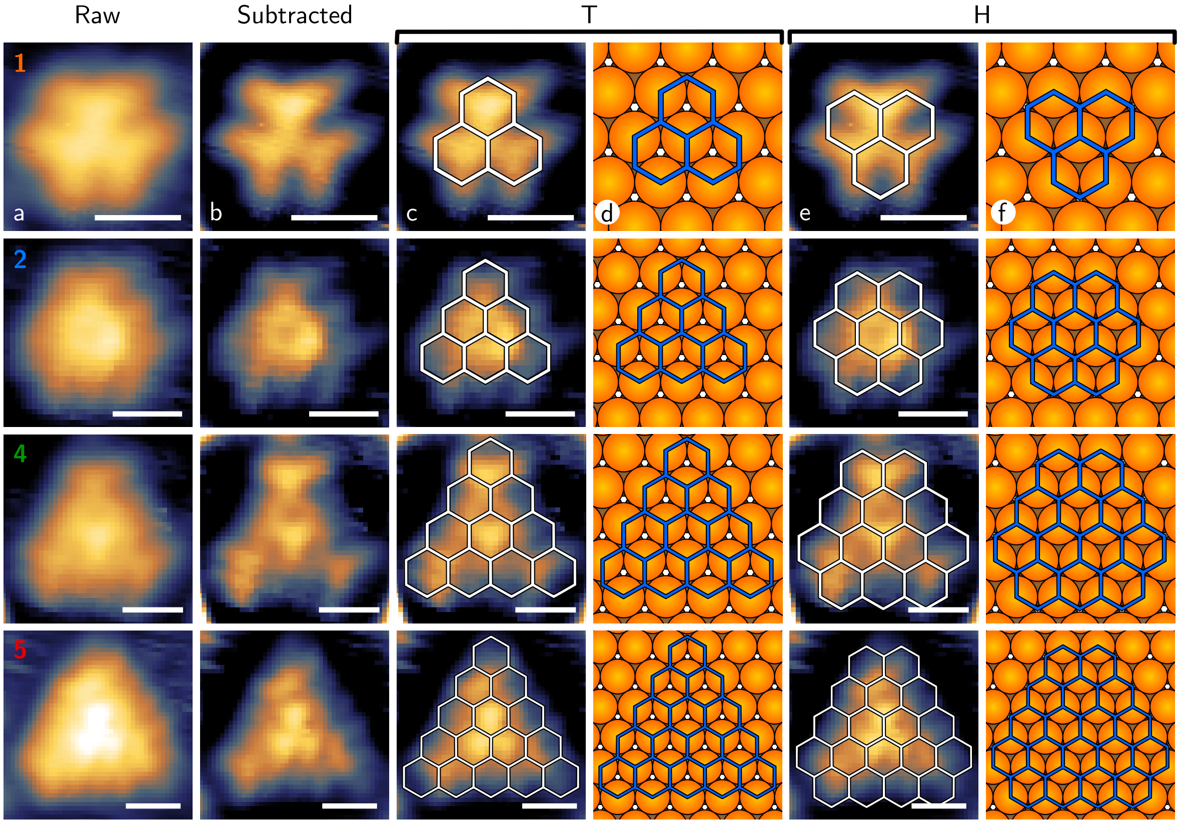

Figure 5.10: **Two possible sets of interpretations of carbon nanoclusters on Re(0001).** Raw (**1-5,a**) and background-subtracted (**1-5,b**) STM topographs (I_t = 1 nA, V_b = −2 V, all scale bars 0.5 nm) of carbon nanoclusters indexed from 1 to 5 sorted by increasing size, either interpreted as T-nanoclusters (**1-5,c**) or H-nanoclusters (**1-5,e**). Their corresponding ball and stick models (respectively **1-5,d** and **1-5,f**) show their attachment sites are systematically top and fcc, and top and hcp. Note that for T- and H-series, a fcc (bright) and a hcp (dark) site respectively lays beneath the center of a carbon ring.

on Fig. 5.10. All carbon nanoclusters of the first one have the shape of triangles (hereafter labelled T), with sharp apices each constituted of a single six-membered carbon ring (C6 ring). The second possible family is also composed of carbon nanoclusters with the shape of triangles, but with apices made of two C6 rings. Due to this more hexagonal shape, they will then be labelled H. These structures overlay the experimental images on Fig. 5.10,1-5,c and 1-5,e.

Using the disordered superstructure of C adatoms, the substrate atomic structure can be extrapolated, in order to identify the adsorption sites of each carbon nanocluster. An example of this process is illustrated on Fig. 5.7. On Fig. 5.7a, the two smallest carbon nanoclusters (labelled 1 and 2 on Fig. 5.5) are identified on the left part of the image. Their two possible configurations are superimposed on Fig. 5.7c,d in white. Using the triangular mesh extrapolated from the C adatoms and the moiré superlattice, the atomic sites of the substrate can also be deduced. Confronting the T- and H-configurations to the mesh reveals their adsorption sites are respectively top and hcp, and top and fcc. This process has been repeated on multiple STM topographs, yielding equivalent results for each configuration of the family. The results are summarized in the ball models shown on Fig. 5.10,1-5,d and 1-5,f.

In order to confront these two interpretations, DFT calculations have been performed. The apparent height contrast within the clusters clearly supports H-configurations. Obviously, this assertion only holds if the height contrast mainly translates the carbon-rhenium bonding, and not the spatial modulations of a truly molecular orbital, *i.e.* a collective state of an object that would be decoupled from the metal surface. DFT calculations unveil strong hybridization between carbon and rhenium, ruling out the latter possibility.

The largest carbon nanoclusters cannot be considered, as they would require very large unit cells and thus prohibitively long computation times. Every possible symmetric configuration of the smallest graphene nanocluster (indexed as 1 earlier) has then be calculated. The obtained results are summarized on Fig. 5.11, in particular the H- and T-configurations (d and e respectively) interpreted from STM topographs are tested. Their relative stability will be commented later. Strong structural differences can be observed from configuration to configuration. In particular, the side-views of the converged hcp-fcc configurations (a,b) show a pronounced dome-like shape, with their central atom lying further apart from Re. This dome-like shape is also marginally found in the H-configuration (d), while all three remaining configurations (c,e,f) are rather flat. For the four latter configurations, all C atoms then lie close to the Re surface. These qualitative differences due to different adsorption sites are similar to that calculated on Rh(111) [215]. In general, whatever the considered configuration, carbon atoms seem to bond strongly to Re, as indicated by the short C-Re distances.

The resulting integrated electronic density of states is consistent with this interpretation. For each configuration, all observed features are indeed in one-to-one correspondence with the atomic structure. This is in sharp contrast with STM measurements of isolated molecules on an insulating substrate [172]. They are featureless for bias voltages

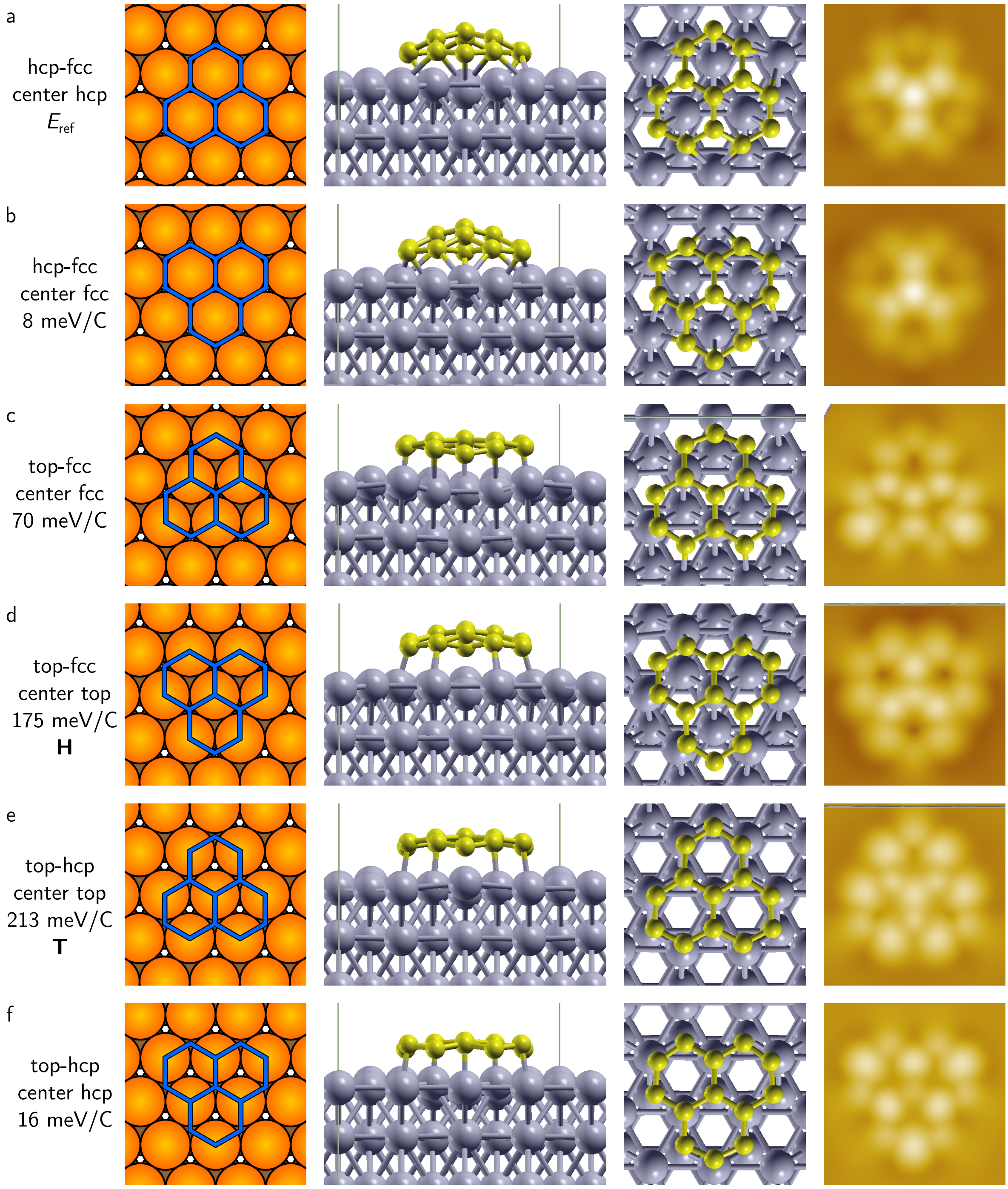

Figure 5.11: **DFT results for the smallest nanocluster on Re(0001).** A nanocluster made of three fused benzene rings has in principle six possible configurations on Re(0001), which have been calculated by DFT. For each (**a-f**), the total energy per C atom, schematic atomic structure, side and top-views of the converged structure, and deduced electronic density are displayed. The energy indicated uses the most stable configuration (**a**) as a reference, and the cut in electronic density is taken above the highest atom and integrated between E_F and $E_F + 0.25$ eV.

in between the highest occupied and lowest unoccupied molecular states, and display features similar to molecular orbitals of the free molecule for large bias voltages. This important difference strongly suggests that the observed carbon nanoclusters lose their molecular electronic spectrum due to their strong bonding to the Re surface. As the observed bright protusions in STM topographs are directly related to the molecular shape, orientation and atomic structure, DFT calculations therefore support H-configurations.

Although scarce, contradictory literature can be found on carbon nanoclusters. Nanoclusters 1 and 2 have been invoked without much justifications in STM studies on Ru(0001) [33,121], while nanocluster 2 has been discussed in detail on Rh(111) [215]. In the latter case, their structure was interpreted as symmetric molecules made of fused C6 rings,[3] as done here. However, those conclusions were later put into question by DFT calculations and STM image simulations [53,54,226]. The simulations indeed show that for any number of carbon atoms, carbon nanoclusters containing C5 or C7 rings are more stable by several eV. In particular, nanocluster 2 is not interpreted as a molecule composed of seven fused C6 rings, with its zigzag rows aligned with the metal dense-packed rows (see Fig.5.10,2f). It is instead assigned to a curved molecule where three of the edge C6 rings are replaced by C5 rings, rotated by 30° with respect to the substrate. They also attribute the STM data to electronic density of states effects [226]. As will be explained later, important arguments were lacking to give full credit to this DFT-based view.

The electronic density of states effects in STM images are disproved for Re(0001) by the DFT calculations performed here. Nonetheless, the greater stability of the C5-containing carbon nanocluster is confirmed. It is not attributed to nanocluster 2, as claimed by the authors [226] on Rh(111), but to another one indexed 3 on Fig. 5.5. In fact, its atomic structure can be extracted from the STM topograph, as detailed on Fig. 5.12a-c. Using the same method as before, its adsorption sites are interpreted as shown on Fig. 5.12d. DFT calculations complement this analysis, as they reveal a strong distortion of the molecule edges, so its constituting atoms all adopt a hcp hollow site. A dome-like shape of the nanoclusters is also evident on the side-view of the atomic structure. Moreover, when comparing Fig. 5.12a and e, a very good agreement is found. Only the positions of the C6 and C5 rings at the periphery of the nanocluster look inverted based on their apparent heights. Nonetheless, the larger shape of the C6 rings is observed on both the STM image and the calculated electronic density image. As a result, a one-to-one correspondence between STM features and atomic structure is concluded for this nanocluster too.

5.2.4 Growth process

Two extreme scenarios can explain the coexistence of the carbon nanoclusters and graphene. On the one hand, as depicted on Fig. 5.13 (top), the carbon nanoclusters can be thought to act as intermediate building blocks. As suggested by Loginova *et al.*

---

[3] The discussion on adsorption sites in the literature, however, is either missing or questionable.

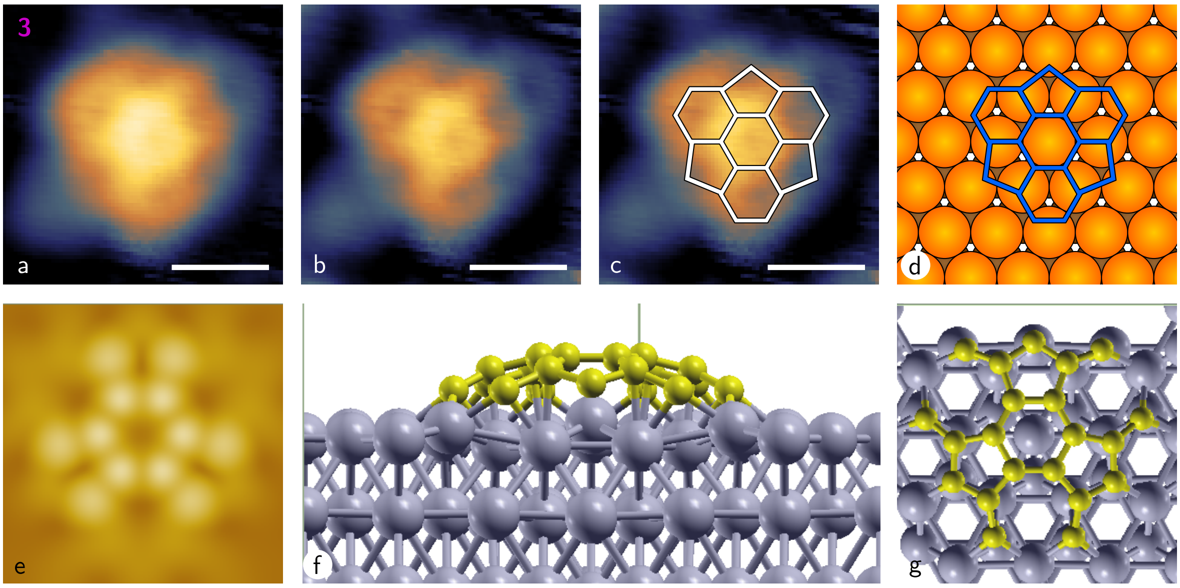

Figure 5.12: **Strongly-bound nanocluster 3 on Re(0001).** Raw (**a**) and background-subtracted (**b**) STM topographs ($I_\mathrm{t} = 1$ nA, $V_\mathrm{b} = -2$ V, all scale bars 0.5 nm) of carbon nanocluster indexed 3. It is interpreted as a molecule made of four C6 rings and three C5 rings arranged with three-fold symmetry (**c**), with adsorption sites shown on the corresponding ball model (**d**). The electronic wave function (**e**) of the DFT-converged structure integrated between $E_F - 0.25$ eV and E_F is in good agreement with STM measurement. Side-view (**f**) of the structure shows a dome-like shape of the nanocluster, with short C-Re bonds. Top-view (**g**) reveals large distortions of the molecule edge structure so all edge C atoms sit on hcp hollow sites.

in a LEEM study of graphene growth on Ru(0001) [119], direct integration of carbon adatoms into graphene flakes may be unfavourable, so mobile 5-atom carbon species have been interpreted from a kinetic model as the necessary intermediates. This argument seems to hold generality for other metal surfaces. It proved right on Ir(111) [120], a surface with much lower affinity to C than Ru(0001), and it may well apply to Rh(111) and Re(0001), which are of similar structure and have, like Ru(0001), good affinity with C. Yet, that LEEM study could not provide a direct observation of such clusters at the atomic scale, and the observation of carbon nanoclusters on Rh(111) was later claimed as their identification [215]. In this case, the single carbon adatoms would first assemble into carbon nanoclusters, which would then diffuse on the surface and attach to each other, thus forming a graphene layer.

On the other hand, the coexistence of graphene and carbon nanoclusters can be seen as the result of their competitive formation, as schematically represented on Fig. 5.13 (bottom). Then, carbon adatoms can either assemble into graphene or carbon nanoclusters, but the incorporation of the latter into graphene is hindered due to its prohibitively high activation energy.

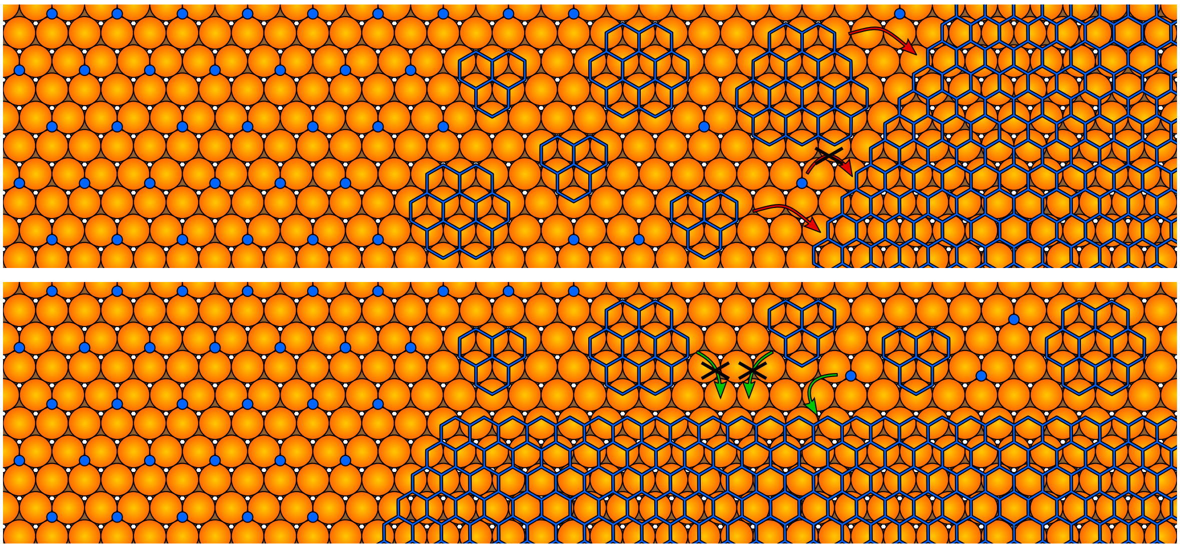

Figure 5.13: **Growth scenarios:** ball and stick models representing the two typical growth scenarios, with chronological order from left to right. **Top:** carbon nanoclusters as intermediates. Carbon adatoms first form a (2×2) superstructure, then assemble into carbon nanoclusters, which act as necessary intermediates in the growth of a graphene layer. **Bottom:** carbon nanoclusters as competitors. Carbon adatoms, initially in a (2×2) arrangement, form simultaneously carbon nanoclusters and graphene. However, the carbon nanoclusters are kinetically blocked from incorporating the graphene layer.

Three different reasons tend to support the second scenario over of the first one. First, the surface mobility of carbon nanoclusters is presumably very limited, even at high temperature. Indeed, they establish strong C-Re bonds, as indicated by DFT calculations. It is more likely carbon nanoclusters do not diffuse on the surface, and are not able to assemble into graphene.

Second, the model used by Loginova *et al.* indicated the intermediate carbon cluster would have a typical size of 5 carbon atoms [119]. Yet, all reported carbon nanoclusters are at least made of 13 carbon atoms (up to 51 for the largest identified in the present work). This discrepancy suggests that another type of carbon species is involved in the growth of graphene, such as carbon chains, as suggested in the case of graphene on Ni(111) [27]. Following this idea, DFT calculations have been performed in order to compare the relative stability of carbon adatoms, carbon nanoclusters, carbon chains, and graphene, but are not shown here as this work is ongoing.

Third, direct experimental evidence contradicts the first scenario. This brings back to the first sample presented on Fig. 5.1 and 5.2, for which a full layer of graphene is grown. In the final steps of graphene growth, graphene and carbon nanoclusters are found coexisting, as on Fig. 5.14a, where graphene completely surrounds two small carbon nanoclusters. If such carbon nanoclusters were mobile intermediates in the growth of graphene, they would have been incorporated into the graphene layer surrounding them,

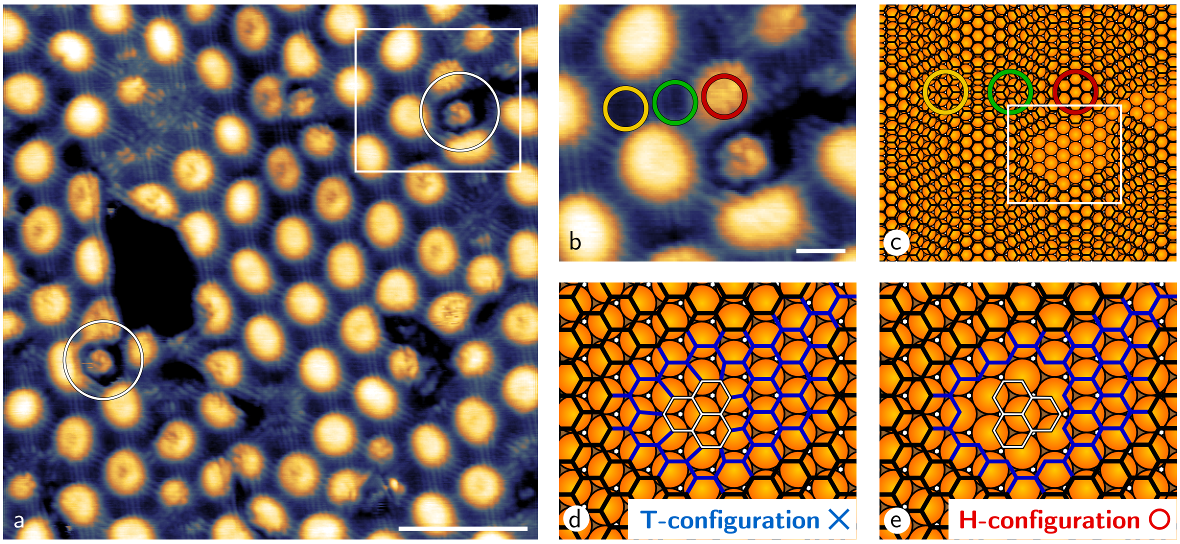

Figure 5.14: **Carbon nanocluster incorporation.** (**a**) STM topograph ($V_b = 30$ mV and $I_t = 6$ nA, 20×20 nm^2) showing two of the smallest carbon nanoclusters (circled) surrounded with a continuous graphene layer. (**b**) Close-up view of one of the nanocluster, where the typical hcp-fcc, top-fcc and top-hcp of the moiré superlattice are circled respectively in red, green and orange. (**c**) Ball and stick interpretation of the graphene and substrate atomic structures. (**d-e**) Tentative incorporation of either T- or H-configured nanocluster. Only the H-configuration yields the observed blocked incorporation.

and should not be observed at this stage.

This leads to the conclusion that the observed carbon nanoclusters compete with graphene growth, and that nanocluster incorporation is a limiting step in the growth of high quality graphene.

As a complementary comment, interpretation of this blocked situation can be pushed to the atomic scale to support the identified nanocluster structure. Using the moiré superlattice, one can extrapolate the substrate atomic lattice, as schematically done on Fig. 5.14c. When fitting the possible T- and H-configurations of the observed nanocluster, its registry can be compared with the surrounding graphene layer. It appears the T-configuration could be easily incorporated in the graphene layer, as indicated by the smooth extrapolation of blue sticks from graphene to the nanocluster on Fig. 5.14d. On the contrary, the H-configuration is considerably shifted with respect to the graphene registry, as visible on Fig. 5.14e. Bridging it to the surrounding graphene would then require either unrealistic strain fields in graphene, or a huge shift of its attachment sites from top-fcc to top-hcp, which is unlikely due to its strong bonding to the surface hindering its mobility. In short, this situation is blocked owing to the off-registry of the carbon nanocluster with respect to surrounding graphene. This picture is consistent with the interpreted growth scenario, further supporting H-configurations as the correct atomic structures.

Although the competition of graphene growth with nanocluster formation explains the observed species coexistence, the question of their nucleation remains to be addressed. Indeed, a graphene island expands starting from a small seed, which should be made of a few C6 rings. Then, what is the difference between a graphene seed and a carbon nanocluster?

The answer to that question lies in the adsorption sites. To discuss graphene seeds, the smallest nanocluster (labelled 1) is the logical object to consider. Due to its small size, all its six possible configurations have been calculated by DFT, as presented on Fig. 5.11. Earlier discussion concluded the experimentally observed configuration is the one on Fig. 5.11d. However, its total energy is shockingly higher than most other configurations. In particular carbon nanoclusters lying on hcp-fcc sites (Fig. 5.11a,b) have similar energies, more than 2 eV below the H-configuration.

This apparent paradox has also been mentioned for carbon nanoclusters on Rh(111), although not discussed [215]. Actually, it is the key-difference between a graphene seed and a blocked nanocluster. Indeed, the more stable hcp-fcc configurations correspond to graphene seeds, whereas the less stable H-configuration is a carbon nanocluster whose lateral extension is blocked. Consequently, hcp-fcc configurations are not observed experimentally, because they evolve into larger size graphene islands. On the contrary, carbon nanoclusters with lower stability can be identified because their evolution is kinetically blocked. It should therefore be emphasized that the species experimentally observed by STM are not the most stable ones, but the metastable ones whose dynamics is the slowest.

All these considerations can be summarized in an elementary energetic model, where multiple reaction paths of C species on Re(0001) compete. At this point, a distinction should be made between thermodynamically and kinetically controlled reactions. Under thermodynamic control, the reaction passes through the most stable species no matter how high the activation energies. On the contrary, under kinetic control, metastable products with the lowest activation energies are formed. Some reaction paths followed in this system are sketched on Fig. 5.15.

At low concentration, isolated adatoms in hcp hollow sites are the most stable C form. At higher concentration, their stability is reduced, as C adatoms interact repulsively. Chains of $N\times$ C atoms then form. They can assemble following different reaction paths. The one displayed in green is that of graphene growth. It involves graphene seeds in the form of nanoclusters in hcp-fcc registry, whose stability increases with size, as they extend into a graphene layer. The activation energies involved along this path are bound to 800 K. This means that in the experimental conditions chosen here, none of the intermediates is kinetically blocked, and therefore observed.

Two other paths are also shown in red. One in the background forms the series of metastable nanoclusters in top-fcc registry. Although they have high energy, low activation energies favour their formation at lower temperature. As such, it is under kinetic control. For higher carbon density, incorporation of carbon nanoclusters into

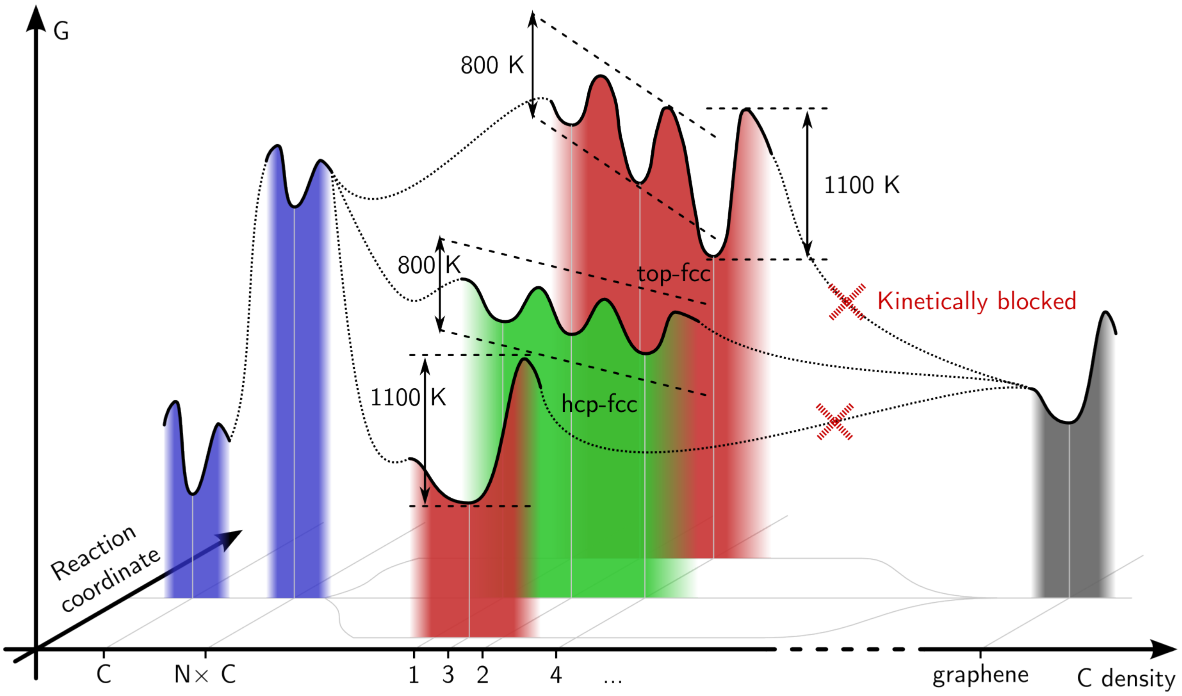

Figure 5.15: **Possible reaction paths for carbon on Re(0001).** Multiple reaction paths are sketched in a Gibbs free energy G diagram, where one axis stands for the C concentration on the surface, and the other is a reaction coordinate axis. Full lines are portions of the G landscape, while dotted lines merely indicate possible reaction paths. Indicated local minima of G correspond to local minima in DFT calculations, while activation energies account for the observation or absence of species at the surface. At low concentration, isolated adatoms and chains of $N\times$ C atoms (blue) are the most stable C forms, which assemble following different reaction paths. The green one leads to graphene seeds in hcp-fcc registry, which grow into graphene (grey) as the carbon concentration is raised. Red paths lead to metastable carbon nanoclusters (see main text). When carbon concentration is raised, their stability decreases, but their transformation into graphene is kinetically blocked (red dotted crosses).

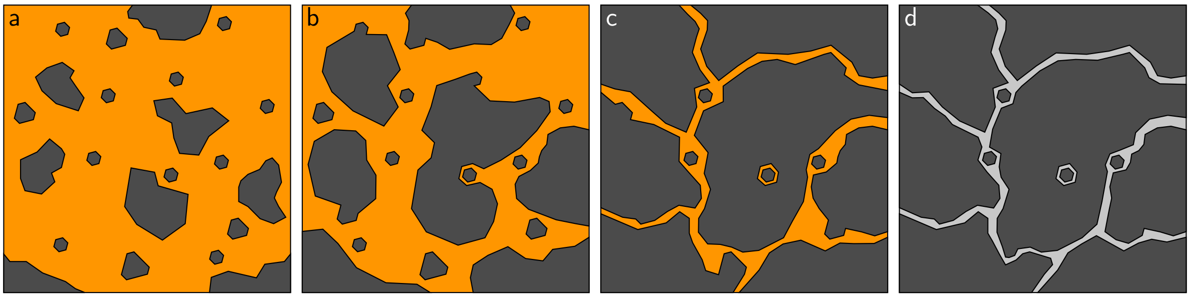

Figure 5.16: **Schematic graphene growth on Re(0001).** Growth of graphene proceeds in four steps pictured from left to right with grey carbon species on an orange Re substrate. (**a**) Graphene islands and carbon nanoclusters form. (**b**) Graphene islands grow, and incorporate some nanoclusters. (**c**) As graphene covers almost all the surface, its growth is blocked at some remaining nanoclusters and grains boundaries, leaving nm-scale gaps on the surface. (**d**) Gap bridging is a limiting step which can produce defective structures (light grey).

graphene has such a high activation energy that they are kinetically blocked. Few blocked nanoclusters are observed at the end of graphene growth on Re(0001). The activation energies can then be inferred to be of the order of growth temperature, so around 1100 K.

Another red path is represented in the foreground, and leads to a stable carbon nanocluster, which has been discussed on Fig. 5.12 as nanocluster 3. Its energy per C atom is found lower than the hcp-fcc graphene seeds, so under thermodynamic control, it should be the majority product. However, above some critical carbon density, this carbon nanocluster should become less stable than graphene patches (green reaction path). At this point, thermodynamic control supports a transformation of nanocluster 3 into the more stable graphene patches in hcp-fcc registry. In experimental conditions chosen here, such transformation is likely kinetically blocked. Additionally, like nanoclusters in top-fcc registry, the incorporation of this nanocluster into graphene is also kinetically blocked.

Finally, special emphasis is put on the fact that on Re(0001), graphene has to be grown at relatively low temperature to avoid surface carbide formation [143]. This makes activation energies large with respect to thermal energy. Hence, the kinetically controlled paths are favoured, leading to carbon nanoclusters, rather than graphene. Growth of large area uniform graphene would require higher temperatures, which are not attainable for Re. As a result, long growth durations are necessary so thermodynamics drive the incorporation of nanoclusters into graphene.

Now that the formation of metastable species on Re(0001) is rationalized, their transformation into more stable graphene has to be considered. This process is not necessarily seamless, and in fact produces typical defects, which underlay the quenched disorder of the chaotic phase. In the following and final section, those defects are going

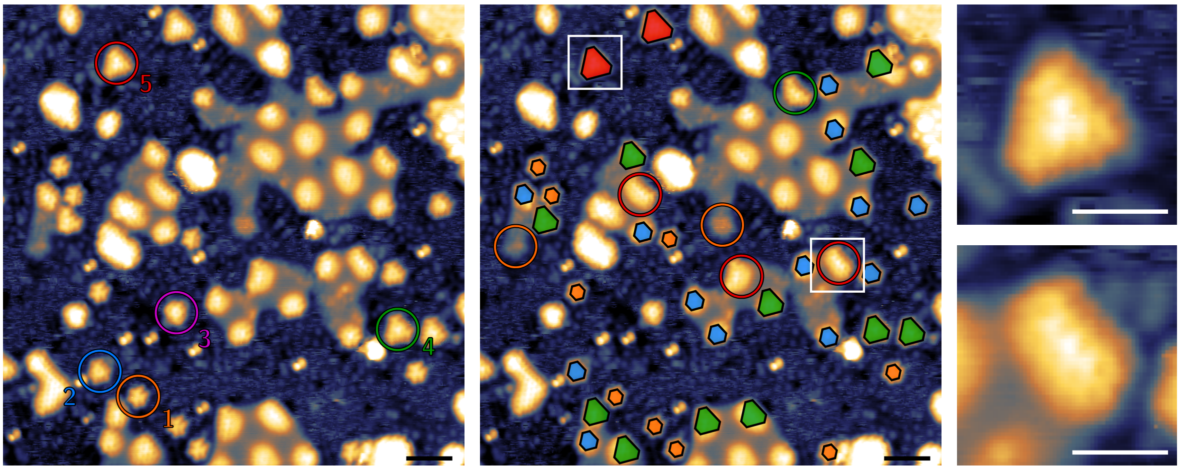

Figure 5.17: **Easier incorporation of carbon nanoclusters in early steps of graphene growth. Left:** STM topograph ($V_b = -2$ V and $I_t = 1$ nA, 20×20 nm^2) of the three coexisting species: graphene islands, carbon adatoms, and carbon nanoclusters. The latter are numbered from 1 to 5 by increasing size. **Middle:** Same topograph where nanoclusters are outlined with coloured frames. Similar frames are added at the edges of some graphene islands, where the shapes and apparent heights of nanoclusters 2, 4 and 5 can be recognized. Other colour-circled nanoclusters are identified at the edges of graphene flakes due to their shape, but have their apparent height partially or completely altered. **Right:** Close-up views (scale bars 1 nm) on the largest isolated nanocluster (top), and its counterpart found at the edge of a graphene island (bottom). Once incorporated, the apparent height of the nanocluster decreases to equal that of the low-lying part of the graphene layer.

to be addressed.

5.2.5 Quenched disorder

Based on the growth process presented above, many defects can be expected, as illustrated on Fig. 5.16. It summarizes graphene growth in four steps, which are now detailed. First, graphene and carbon nanoclusters are formed on the surface depending on which reaction path is locally taken. The exact process at stake is difficult to determine. Short carbon chains appear as a likely intermediate in the formation of larger carbon species.

Second, graphene seeds expand, while nanoclusters are kinetically blocked and bound to the surface. In this step, incorporation of carbon nanoclusters into graphene is not a critical step, as the free edges of graphene can support strain to some extent. Supporting this claim, the STM topograph shown on Fig. 5.5 can be re-interpreted, focusing now on the graphene islands edges. As indicated on Fig. 5.17, their shape, their atomic contrast, and their apparent height are all reminiscent of the neighbouring nanoclusters. The deformed or absence of moiré superlattice surrounding these regions is also a signature

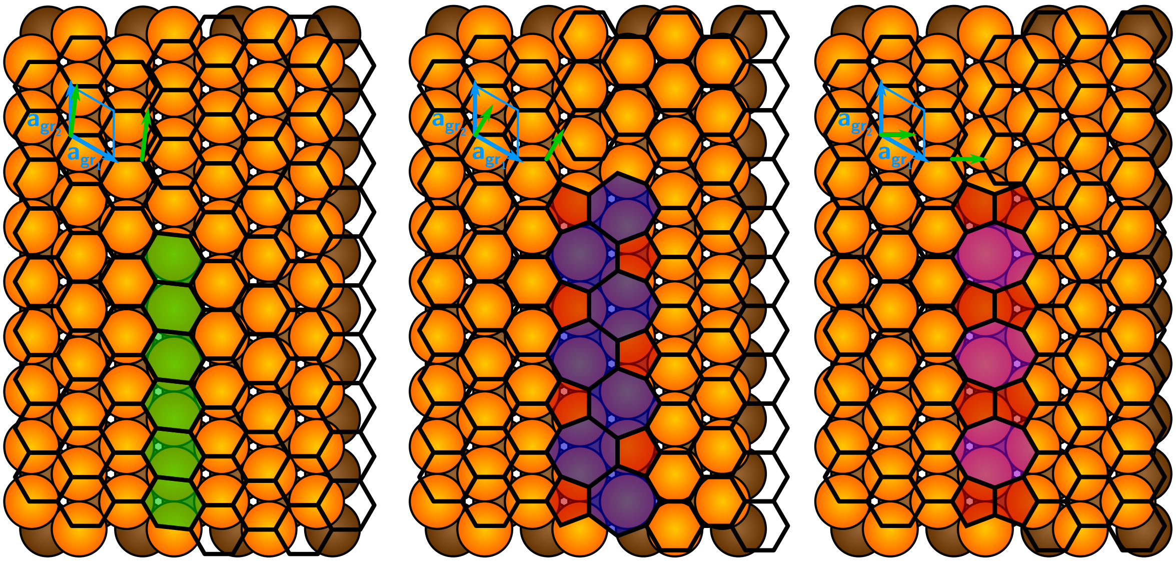

φ~(0,2π) φ=(2π/3,4π/3) φ=(4π/3,2π/3)

Figure 5.18: **Grain boundary structure.** Two degenerate graphene flakes sharing the same commensurability with Re are shifted with respect to each other. For each configuration, the shift is analysed as a two-component phase. **Left:** a slight shift only strains the honeycomb lattice of graphene. **Middle:** a Stone-Wales defect-line results in a $\varphi = (\frac{2\pi}{3}, \frac{4\pi}{3})$ grain boundary. **Right:** a defect-line made of series of octagon and double-pentagon defects gives rise to a $\varphi = (\frac{4\pi}{3}, \frac{2\pi}{3})$ grain boundary.

of the strain field needed to incorporate the nanocluster.

Third, graphene flakes grow up to the point the edges of each flake meets either a remaining nanocluster or the edge of another flake. Considering as an example the central nanocluster of Fig. 5.16, it is surrounded by graphene, similar to what is observed on Fig. 5.14. In that case, the atomic structure depicted on Fig. 5.14e shows that the nanocluster and graphene layer are too shifted for the incorporation to take place. A similar situation can be imagined at a grain boundary between two graphene flakes, when they are shifted with respect to each other for example by half a graphene unit vector. In short, the limiting step of growth occurs in its final steps and is attributable to shifted species, and leaves gaps between them.

Eventual bridging of the gaps may occur in a fourth and final step. Fig. 5.18 considers the simplified 1D case of two adjacent zigzag-edged graphene flakes holding the same commensurate relation with Re. Their relative shift is given by a vector indicating the translation needed to superimpose both domains. An analogy can be made between this shift between two domains of identical periodicity in space, and a delay between two signals of same frequency in time. This delay is commonly interpreted in terms of phase shift. Similarly, a geometric phase $\varphi = (\varphi_x, \varphi_y)$ can be defined to characterize the grain boundary, where two components are needed to account for the shift in x and y directions of space. Here, the geometric phase has been introduced on geometrical grounds, but it has also been introduced in Section 2.4.3 when discussing topological defects.

For small shifts ($\varphi \sim (0,0)$), the honeycomb lattice of graphene can be preserved accounting for a static strain field at the interface, as illustrated on Fig. 5.18 (left). Larger shifts require to break the honeycomb topology of the lattice and to resort to defective structures. Among them, two are of particular relevance, as they are reminiscent of previously reported defects. The first one is composed of so-called Stone-Wales defects, which are pairs of upside-down heptagon-pentagon pairs, as drawn on Fig. 5.18 (center). Stone-Wales defects have been observed in TEM studies [113], which enable to determine the phase shift of this grain boundary as $\varphi = (\frac{2\pi}{3}, \frac{4\pi}{3})$. The second one is made of octagons and pairs of pentagons of carbon atoms, as has been observed in STM [108] and TEM works [174], corresponding to a $\varphi = (\frac{4\pi}{3}, \frac{2\pi}{3})$ shift. Due to their particular phase shift, they will be referred to as $\frac{2\pi}{3}$- and $\frac{4\pi}{3}$-grain boundaries in the following.

The simple image of a 1D grain boundary presented here actually is not directly relevant for graphene on Re(0001). Indeed, no such defective grain boundary is observed on STM images. Instead, Fig. 5.2 shows gaps between graphene islands and continuous domain walls. It is likely the formation energy of an extended defect line is too high here. Instead, large strain fields created at the interface between shifted domains extend over few nm distances. This description corresponds to the phasons with frozen dynamics discussed earlier. This alternative description then not only explains an aspect of the quenched disorder in graphene on Re(0001), but also justifies why a sheared moiré superlattice could be analysed in the previous Chapter.

Beside the strain fields distributed over the sample, another kind of defect is commonly found, which has been reported in many STM works on graphene on strongly-interacting metals, such as Ru(0001) [129] or Re(0001) [193]. It is easily identified in continuous graphene samples as a “missing hill” in the moiré superlattice, as exemplified on Fig. 5.19. As often in STM imaging, direct determination of the atomic configuration is made difficult by the local electronic density of state effects. Yet, as visible on the close-up view shown on Fig. 5.19, the core of the defect seems to comprise carbon rings whose zigzag rows align those of the surrounding graphene lattice.

To clarify the atomic structure of this defect, a preliminary comment can be made based on Fig. 5.17, illustrating carbon nanocluster incorporation in the early stage of graphene growth. Most of the nanoclusters identified along the edges of graphene islands are the larger ones (indexed 2 and 4), but never correspond to the smallest and most often observed nanocluster 1 (see statistics on Fig. 5.5b) reported so far. As nanocluster 3 is 30°-rotated with respect to the substrate, it is expectable that its incorporation into a graphene layer aligned with the substrate is limited.

This striking feature can be understood by inspecting the incorporated nanoclusters circled on Fig. 5.17. Contrary to those highlighted with coloured frames, their apparent height differs from their isolated counterpart. In particular, two close-up views compare nanoclusters in an isolated state of incorporated at an edge on Fig. 5.17 (right). At

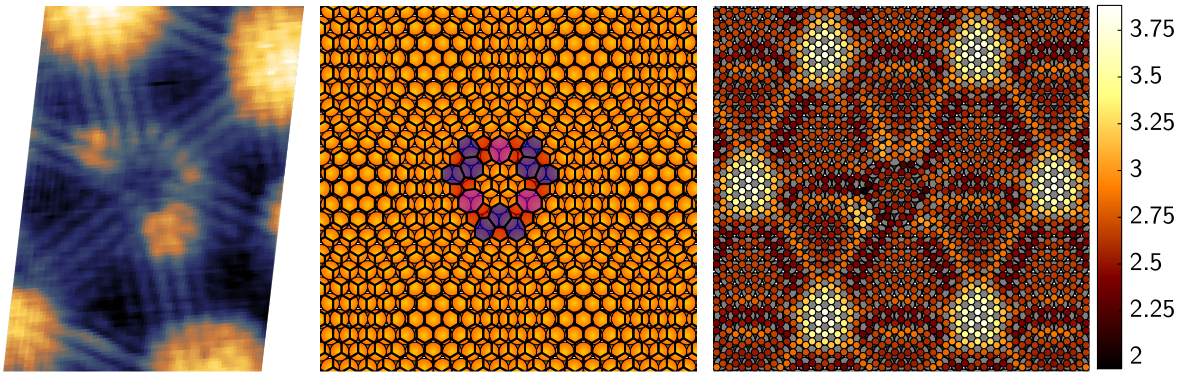

Figure 5.19: **Missing hill defect. Left:** STM topograph ($V_b = 30$ mV and $I_t = 6$ nA, scale bar 1 nm) of full layer graphene with a defect positioned where a moiré hill is expected, lowering its apparent height. **Middle:** interpreted atomic structure of this kind of defect, where a grain boundary loop stabilizes the core of the defect on top-fcc sites instead of the hcp-fcc registry of intact neighbouring moiré hills. **Right:** atomic structure converged by atomistic simulations of a large unit cell containing 1 defective missing hill and 15 intact moiré hills. Carbon atoms are coloured depending on their z position (taken from substrate, in Å), revealing the atoms in the missing hill lie close to the substrate.

their edge facing the bare Re substrate, they display the bright signature of an isolated nanocluster, while at the edge connected to the graphene island, the apparent height is similar to the low-lying continuous graphene. Given the small length scales at stake, this change of contrast cannot be assigned to a change in the carbon atom registry. In other words, the apparently lower area of the incorporated nanocluster still lies on top-fcc adsorption sites. This alteration of the apparent height therefore relates to an electronic density of states effect.

The density of states change is due to the transition from an isolated top-fcc nanocluster to a top-fcc moiré valley. The key-difference is the modification of the edge carbon atoms coordination as the nanocluster is incorporated. When isolated, DFT calculations show all its edge atoms establish strong C-Re bonds. As they have two neighbouring carbon atoms, their stable adsorption sites are the highly coordinated sites of Re, *i.e.* hcp and fcc hollow sites. This line of reasoning is supported by Fig. 5.10, on which the hcp-fcc nanoclusters are the most stable, and adopt a dome-like structure indicative of high coordination of edge carbon atoms with Re. Upon incorporation, the situation changes drastically. At the edge of the nanocluster, some C-Re bonds are broken, and new C-C bonds are created with the host graphene flake. The corresponding edge atoms then have three neighbours in a sp^2 configuration, so C-Re bonds are oriented out of the plane and are sp^3-like. As a result, the attachment site between C and Re switches from hollow to top. In other words, even when they both sit on top-fcc sites, a nanocluster and graphene do not bind to Re in the same way, because of a difference in carbon coordination. Stronger binding of the nanocluster to the surface results in a different electronic density of states, which explains the change in apparent STM height observed upon nanocluster incorporation.

The missing hill defect is now analysed. As we will see, even if the real height might not be measured by STM, a true topographic picture is relevant here. Instead of the high-lying (bright) hill with hcp-fcc registry, this defect shows an apparent height similar to a moiré valley with top-hollow registry. This change is not attributable to a coordination issue. Indeed, no interruption similar to a vacancy where graphene would bind to Re can be seen. Instead, the STM topograph on Fig. 5.19 (left) points to a continuous layer with a depression at the position where a moiré hill is expected. Furthermore, at the very core of the defect, few C6 rings having their zigzag rows aligned with those of graphene can be identified.

A different atomic registry then appears as a suitable explanation for the observed depression. Replacing the hcp-fcc configuration of a moiré hill with the top-fcc registry of a nanocluster in principle results in a short graphene-metal distance, while keeping the zigzag rows in the same direction. It also suggests that this defect originates from the limiting final step of graphene growth, when isolated nanoclusters are incorporated and shifted graphene flakes are bridged.

The atomic structure of the defect is difficult to infer from STM images, which seem to reveal strong local electronic density variations not obviously related to height variations. The previous considerations about grain boundaries are now going to prove relevant. Indeed, in order to bridge a nanocluster in top-fcc sites to a graphene flake where atoms in hcp-fcc registry are expected, $\frac{2\pi}{3}$- and $\frac{4\pi}{3}$-grain boundaries are needed. A schematic model is shown in Fig. 5.19 (middle). It features a loop of such grain boundaries surrounding a carbon nanocluster of type 2 placed where a moiré hill would be expected. This structure is continuous and dense, and it satisfies the stacking constraint at the core of the defect.

To check the stability of this defect, DFT calculations are not suited, since prohibitively large ensembles of atoms would be needed to rule out interactions between defects associated with the periodic boundary conditions. Instead atomistic simulations accounting for covalent bonding based on bond-order-potentials have been used. The bond-order potentials are parametrised against DFT calculations (see Section 3.3.2), and take into account a correction for dispersion forces that have been carefully adjusted for graphene on Ru(0001) [52].[4] The similarity of graphene on Ru(0001) and Re(0001), both exhibiting the same kind of defects, and governed by carbon-metal interactions of similar magnitude [193, 213], gives confidence in the relevance of the comparison between the experimental results obtained on graphene on Re(0001) and the simulations performed for graphene on Ru(0001). The lowest-energy configuration of a possible defect is shown in Fig. 5.19 (right). The simulation reproduces the decreased height at the defect location, which is, as expected, only occurring when the defect replaces a hcp-fcc

---

[4] Parametrised potentials have not yet been optimised for the C-Re system. This represents a considerable effort and will become more legitimate when more experimental data with complementary approaches will be available.

region of the pristine graphene.

Other similar configurations have been tested, yielding similar results, but not shown here. Supercells containing one defective missing hill and 8 intact moiré hills were found sufficiently large to avoid substantial interactions due to boundary conditions. For each configuration, calculations were performed with and without dispersion forces correction, which provided a similar trend in both cases. Both top-fcc and top-hcp defect cores have been investigated, reproducing similar low C-Re distances at the defect core. This suggests there is not a single possible structure for this kind of defect, but rather a family of structures, which share the common feature to stabilize a defect core in a top-hollow registry.

The present investigation gives a detailed atomic structure for an almost 0D defect observed commonly at the surface of strongly-interacting metals. This atomic structure proves to host defective structures such as Stone-Wales defects. Such structures break the topology of the honeycomb lattice, and therefore constitute topological defects similar to dislocations (see Section 2.4.3). But contrary to the frozen phasons considered earlier, which relate to the possible commensurate order of graphene on Re(0001), missing hills are topological defects which may be regarded as native to the graphene layer itself (they would still be relevant if the graphene layer would be transferred and suspended for instance). Two ways exist for such defects to be removed: either diffuse to a graphene edge, or annihilate when groups of them with zero total winding number merge. Both mechanisms require them to diffuse inside graphene. At moderate temperatures, this process may be time-consuming. Consequently, growth constraints not only prevent graphene on Re(0001) to reach its ground state (either commensurate or incommensurate), but they are also an obstacle to the formation of a defect-free graphene layer.

In conclusion, the kinetic barriers to chemical processes at stake during graphene growth have a critical and non-trivial impact on the degree of order of the final graphene layer. Due to the relatively low temperature required to avoid carbide formation, reactions at the surface of Re(0001) are under kinetic control, leading to multiple competitive reaction paths.

Among them, it is shown that graphene flakes grow out of seeds – namely carbon nanoclusters in hcp-fcc registry with respect to the metallic surface. A family of other metastable species – carbon nanoclusters in top-fcc registry – are also identified. For the first time, their atomic structure, adsorption sites, and relative stabilities have been rationalized self-consistently by DFT calculations and atomically-resolved STM measurements performed at different stages of growth.

Beyond the study of the coexisting carbon species on Re(0001), it is shown that the high activation energies at stake result in various types of defects. On the one hand, nanocluster incorporation into graphene can lead to a type of defect here referred to as a “missing moiré hill”, which corresponds to loops of defects that break the topology of the graphene lattice. In the growth conditions studied here, such topological defects are a serious obstacle to the formation of a high quality graphene layer. On the other hand, coalescence of different graphene flakes gives rise to 1D domain walls where strain is stored. This leads to a non-uniform distribution of strain in graphene.

Finally, understanding the origin and atomic structure of these defects provides new insight on the very essence of supported graphene systems. While it is usually assumed they are in their ground state, leading to a debate over their commensurate or incommensurate nature, it appears the defects formed because of the growth maintain the system in a metastable state. In particular, the non-uniform strain field distributed on the surface corresponds to an array of phasons with frozen dynamics. Due to this peculiar static disorder, graphene on Re(0001) is not in its ground state, but in a metastable chaotic phase.

This conclusion opens new questions. One can indeed wonder whether graphene on Re(0001) can be brought to its ground state, or if it is truly a “phason glass” that will always be disordered to some extent. Generalization of the considerations developed here to other systems where a 2D material may or may not interact as much with its substrate could also be of general interest to fully grasp the diversity of phases specific to 2D systems.

Conclusion

In this manuscript, the nature of graphene supported by a crystal has been discussed. Graphene is known both as a 2D material and as semi-metal with exceptional electronic properties. It has been explained that the effect of a substrate not only modifies both, but that the induced modifications are deeply correlated. In other words, the electronic properties can only be understood in the light of a fine structural analysis.

Indeed, the tight-binding model presented in Chapter 1 accommodates to the effects of a substrate with the Semenoff and Kekulé insulator models. In Chapter 2, a completely different approach is taken, where placing graphene on a substrate deforms its structure. This can be interpreted as a phase transition from pristine to deformed graphene. When it comes to the electronic properties, the order parameter of this phase transition is a combination of the Semenoff and Kekulé masses, showing the consistency of both approaches.

Going further, topological defects associated to those structural phase transitions should have an electronic counterpart. As an example, 1D strain kinks in bilayer graphene have been proved to behave as 1D metallic wires. Extending this equivalence to moiré superlattices and structural defects, exotic electronic properties are anticipated for graphene supported by weakly interacting substrates, and constitute a perspective of this thesis.

In the case of graphene on Re(0001), strong $\pi - d$ hybridization disrupts graphene's band structure, so no such effect can be expected. Still, focusing on structural aspects, the commensurate-incommensurate transition is a fundamental problem, which – surprisingly – is seldom discussed in the graphene community. Indeed, it is often assumed graphene has a commensurate relation to its substrate, but little experimental evidence supports this claim. Hence, it is worth wondering whether supported graphene locks on a commensurate relation to its substrate, or preserves its quasi-long-range order in an incommensurate phase.

In the experimental work presented in Chapter 4, the commensurability hypothesis has been tested by atomically-resolved STM measurements. A FFT-based analysis developed for this purpose gives quantitative analysis of strain fields distributed in the interpreted moiré superlattices. Using this method, it is worth noting shearing strain is reported for the first time. Such six-fold symmetry breaking strain is unexpected from the superposition of two six-fold symmetric solids, and casts doubt on the commensurability hypothesis.

When pushing this hypothesis even further, it is possible to extrapolate all the possible commensurate phases, and to classify them. This classification has two consequences. The first one puts into question past interpretations where graphene is strained up to 4 % with respect to a HOPG reference. Considering there are possible commensurate phases with two orders of magnitude lower strain calls for a re-examination of those interpretations using the methodology provided here. The second consequence is related to the commensurability hypothesis. Indeed, if it is true, the ground state of a supported graphene system would be one given commensurate phase among an infinitely large number of closely related metastable phases. In that case, it would be very difficult to stabilize the ground state.

The experimental data presented in Chapter 5 strongly support this claim. Indeed, the static disorder observed on STM images correspond to the coexistence of different moiré superlattices. In the commensurate scenario, this means metastable phases are still present, questioning the validity of the commensurability hypothesis. Moreover, the incommensurate scenario is not compatible either with this situation, as in this case, its Goldstone modes have frozen dynamics. Graphene on Re(0001) is therefore interpreted as a metastable chaotic phase.

It is finally proved that the chaotic phase originates from growth constraints. A detailed STM and numerical study reveals it features competing reaction paths, some of which are favoured because of low activation energies. However, they lead to metastable carbon nanoclusters that are kinetically blocked from incorporating graphene at the end of its growth. This can result in nanoscale defects called "missing moiré hills", whose atomic structure is provided for the first time. This growth scenario also gives a prototypical example of how graphene forms at moderate temperature on strongly-interacting substrates.

The main question addressed in this manuscript deals with the structural ground state of supported graphene systems. Two scenarios have been put forward, but neither of them fits experimental results, which support metastable configurations. In the end, this conclusion does not rule out either scenarios, but claims the ground state of graphene on Re(0001) is not reached in the conditions investigated here. Further improvements of the growth recipe could provide more insight, although it is likely some minor disorder may always be present.

A more promising perspective would rely on *in operando* studies at varying temperature. Indeed, commensurate and incommensurate phases are easily distinguished by their dynamic properties. For instance, measuring the coefficients of thermal expansion of graphene and its substrate simultaneously can inform on the chosen phase [93]. Indeed, for a commensurate phase, locking of graphene on its substrate yields identical coefficients, whereas an incommensurate phase implies two different coefficients. Based on previous works [11], *in operando* RHEED measurements could provide a satisfying resolution.

Bibliography

[1] A. Artaud, L. Magaud, T. Le Quang, V. Guisset, P. David, C. Chapelier, and J. Coraux. Universal classification of twisted, strained and sheared graphene moiré superlattices. *Sci. Rep.*, 6:25670, May 2016.

[2] S. Aubry. The twist map, the extended Frenkel-Kontorova model and the devil's staircase. *Physica D*, 7(1):240–258, May 1983.

[3] P. Bak. Commensurate phases, incommensurate phases and the devil's staircase. *Rep. Prog. Phys.*, 45(6):587–629, 1982.

[4] J. Bardeen. Tunnelling from a Many-Particle Point of View. *Phys. Rev. Lett.*, 6(2):57–59, 1961.

[5] M. Batzill. The surface science of graphene: Metal interfaces, CVD synthesis, nanoribbons, chemical modifications, and defects. *Surf. Sci. Rep.*, 67(3-4):83–115, Mar. 2012.

[6] C. Bena and G. Montambaux. Remarks on the tight-binding model of graphene. *New J. Phys.*, 11(9):095003, Sept. 2009.

[7] V. L. Berezinskii. Destruction of long-range order in one-dimensional and two-dimensional systems having a continuous symmetry group. *JETP*, 32(3):493–500, 1971.

[8] D. L. Bergman. Realization of a vortex in the Kekule texture of molecular graphene at a Y junction where three domains meet. *Phys. Rev. B*, 87(3):035422, Jan. 2013.

[9] G. Binnig, H. Rohrer, C. Gerber, and E. Weibel. 7×7 reconstruction on Si (111) resolved in real space. *Phys. Rev. Lett.*, 50(2):120, 1983.

[10] N. Blanc, J. Coraux, C. Vo-Van, A. T. N'Diaye, O. Geaymond, and G. Renaud. Local deformations and incommensurability of high-quality epitaxial graphene on a weakly interacting transition metal. *Phys. Rev. B*, 86(23):235439, Dec. 2012.

[11] N. Blanc, F. Jean, A. V. Krasheninnikov, G. Renaud, and J. Coraux. Strains induced by point defects in graphene on a metal. *Phys. Rev. Lett.*, 111(8):085501, Aug. 2013.

[12] B. Borca, S. Barja, M. Garnica, M. Minniti, A. Politano, J. M. Rodriguez-García, J. J. Hinarejos, D. Farías, A. L. V. d. Parga, and R. Miranda. Electronic and geometric corrugation of periodically rippled, self-nanostructured graphene epitaxially grown on Ru(0001). *New J. Phys.*, 12(9):093018, Sept. 2010.

[13] R. Brako, D. Šokčević, P. Lazić, and N. Atodiresei. Graphene on the Ir(111) surface: from van der Waals to strong bonding. *New J. Phys.*, 12(11):113016, Nov. 2010.

[14] D. W. Brenner. Empirical potential for hydrocarbons for use in simulating the chemical vapor deposition of diamond films. *Phys. Rev. B*, 42(15):9458–9471, 1990.

[15] D. A. Bruce. Discrete lattice effects in incommensurate systems. *J. Phys. C: Solid State Phys.*, 13(25):4615, 1980.

[16] R. M. Brugger. A Note on Unbiased Estimation of the Standard Deviation. *Am. Stat.*, 23(4):32–32, Oct. 1969.

[17] J. M. Burgers. Geometrical considerations concerning the structural irregularities to be assumed in a crystal. *Proc. Phys. Soc.*, 52(1):23, 1940.

[18] C. Busse, P. Lazić, R. Djemour, J. Coraux, T. Gerber, N. Atodiresei, V. Caciuc, R. Brako, A. T. N'Diaye, S. Blügel, J. Zegenhagen, and T. Michely. Graphene on Ir(111): physisorption with chemical modulation. *Phys. Rev. Lett.*, 107(3):036101, July 2011.

[19] V. Carozo, C. M. Almeida, E. H. M. Ferreira, L. G. Cançado, C. A. Achete, and A. Jorio. Raman signature of graphene superlattices. *Phys. Rev. B*, 11(11):4527–4534, Nov. 2011.

[20] V. Carozo, C. M. Almeida, B. Fragneaud, P. M. Bedê, M. V. O. Moutinho, J. Ribeiro-Soares, N. F. Andrade, A. G. Souza Filho, M. J. S. Matos, B. Wang, M. Terrones, R. B. Capaz, A. Jorio, C. A. Achete, and L. G. Cançado. Resonance effects on the Raman spectra of graphene superlattices. *Phys. Rev. B*, 88(8):085401, Aug. 2013.

[21] E. V. Castro, K. S. Novoselov, S. V. Morozov, N. M. R. Peres, J. M. B. L. dos Santos, J. Nilsson, F. Guinea, A. K. Geim, and A. H. C. Neto. Biased Bilayer Graphene: Semiconductor with a Gap Tunable by the Electric Field Effect. *Phys. Rev. Lett.*, 99(21):216802, Nov. 2007.

[22] J. Cayssol. Introduction to Dirac materials and topological insulators. *C. R. Physique*, 14(9-10):760–778, Nov. 2013.

[23] C. Chamon. Solitons in carbon nanotubes. *Phys. Rev. B*, 62(4):2806, 2000.

[24] V. Cheianov, V. Fal'ko, O. Syljuåsen, and B. Altshuler. Hidden Kekulé ordering of adatoms on graphene. *Solid State Commun.*, 149(37-38):1499–1501, Oct. 2009.

[25] V. V. Cheianov, O. Syljuåsen, B. L. Altshuler, and V. I. Fal'ko. Sublattice ordering in a dilute ensemble of monovalent adatoms on graphene. *Europhys. Lett.*, 89(5):56003, Mar. 2010.

[26] C. J. Chen. *Introduction to scanning tunneling microscopy.* Oxford University Press New York, 1993.

[27] D. Cheng, G. Barcaro, J.-C. Charlier, M. Hou, and A. Fortunelli. Homogeneous Nucleation of Graphitic Nanostructures from Carbon Chains on Ni(111). *J. Phys. Chem. C*, 115(21):10537–10543, June 2011.

[28] C. K. Chiang, C. R. Fincher Jr, Y. W. Park, A. J. Heeger, H. Shirakawa, E. J. Louis, S. C. Gau, and A. G. MacDiarmid. Electrical conductivity in doped polyacetylene. *Phys. Rev. Lett.*, 39(17):1098, 1977.

[29] F.-C. Chuang, W.-H. Lin, Z.-Q. Huang, C.-H. Hsu, C.-C. Kuo, V. Ozolins, and V. Yeh. Electronic structures of an epitaxial graphene monolayer on SiC(0001) after gold intercalation: a first-principles study. *Nanotechnology*, 22(27):275704, July 2011.

[30] G. Cocco, E. Cadelano, and L. Colombo. Gap opening in graphene by shear strain. *Phys. Rev. B*, 81(24):241412(R), June 2010.

[31] J. Coraux, A. T. N‘Diaye, C. Busse, and T. Michely. Structural Coherency of Graphene on Ir(111). *Nano Lett.*, 8(2):565–570, Feb. 2008.

[32] J. Coraux, A. T. N'Diaye, M. Engler, C. Busse, D. Wall, N. Buckanie, F.-J. M. z. Heringdorf, R. v. Gastel, B. Poelsema, and T. Michely. Growth of graphene on Ir(111). *New J. Phys.*, 11(2):023006, 2009.

[33] Y. Cui, Q. Fu, H. Zhang, and X. Bao. Formation of identical-size graphene nanoclusters on Ru(0001). *Chem. Commun.*, 47(5):1470–1472, 2011.

[34] D. Curcio, L. Omiciuolo, M. Pozzo, P. Lacovig, S. Lizzit, N. Jabeen, L. Petaccia, D. Alfè, and A. Baraldi. Molecular Lifting, Twisting, and Curling during Metal-Assisted Polycyclic Hydrocarbon Dehydrogenation. *J. Am. Chem. Soc.*, 138(10):3395–3402, Mar. 2016.

[35] C. R. Dean, L. Wang, P. Maher, C. Forsythe, F. Ghahari, Y. Gao, J. Katoch, M. Ishigami, P. Moon, M. Koshino, T. Taniguchi, K. Watanabe, K. L. Shepard, J. Hone, and P. Kim. Hofstadter's butterfly and the fractal quantum Hall effect in moiré superlattices. *Nature*, 497(7451):598–602, May 2013.

[36] C. R. Dean, A. F. Young, I. Meric, C. Lee, L. Wang, S. Sorgenfrei, K. Watanabe, T. Taniguchi, P. Kim, K. L. Shepard, and J. Hone. Boron nitride substrates for high-quality graphene electronics. *Nature Nanotech.*, 5(10):722–726, Oct. 2010.

[37] K. Donner and P. Jakob. Structural properties and site specific interactions of Pt with the graphene/Ru(0001) moiré overlayer. *J. Chem. Phys.*, 131(16):164701, 2009.

[38] Q. Dubout, F. Calleja, G. Sclauzero, M. Etzkorn, A. Lehnert, L. Claude, M. Papagno, F. D. Natterer, F. Patthey, S. Rusponi, A. Pasquarello, and H. Brune. Giant apparent lattice distortions in STM images of corrugated sp^2-hybridised monolayers. *New J. Phys.*, 18(10):103027, Oct. 2016.

[39] R. Ducros, M. Alnot, J. J. Ehrardt, M. Housley, G. Piquard, and A. Cassuto. A study of the adsorption of several oxygen-containing molecules (O_2, CO, NO, H_2O) on Re(0001) by XPS, UPS and temperature programmed desorption. *Surf. Sci.*, 94:154–168, 1980.

[40] R. Ducros, J. J. Ehrardt, M. Alnot, and A. Cassuto. Hydrogen and deuterium adsorption on polycristalline Re surfaces; effect of C and O coadsorption. *Surf. Sci.*, 55:509–522, 1976.

[41] R. Ducros, J. Fusy, J. Jupille, P. Pareja, and S. Tatarenko. CO adsorption on rhenium single crystal surfaces: characterization of molecular and dissociated states and influence of structural defects. *Appl. Surf. Sci.*, 29:179–193, 1987.

[42] K. V. Emtsev, A. Bostwick, K. Horn, J. Jobst, G. L. Kellogg, L. Ley, J. L. McChesney, T. Ohta, S. A. Reshanov, J. Röhrl, E. Rotenberg, A. K. Schmid, D. Waldmann, H. B. Weber, and T. Seyller. Towards wafer-size graphene layers by atmospheric pressure graphitization of silicon carbide. *Nat. Mater.*, 8(3):203–207, Mar. 2009.

[43] M. Enachescu, D. Schleef, D. F. Ogletree, and M. Salmeron. Integration of point-contact microscopy and atomic-force microscopy: Application to characterization of graphite/Pt (111). *Phys. Rev. B*, 60(24):16913, 1999.

[44] C. Enderlein, Y. S. Kim, A. Bostwick, E. Rotenberg, and K. Horn. The formation of an energy gap in graphene on ruthenium by controlling the interface. *New J. Phys.*, 12(3):033014, Mar. 2010.

[45] A. Fasolino, J. H. Los, and M. I. Katsnelson. Intrinsic ripples in graphene. *Nat. Mater.*, 6(11):858–861, Nov. 2007.

[46] A. C. Ferrari, F. Bonaccorso, V. Fal'ko, K. S. Novoselov, S. Roche, P. Bøggild, S. Borini, F. H. L. Koppens, V. Palermo, N. Pugno, J. A. Garrido, R. Sordan, A. Bianco, L. Ballerini, M. Prato, E. Lidorikis, J. Kivioja, C. Marinelli, T. Ryhänen, A. Morpurgo, J. N. Coleman, V. Nicolosi, L. Colombo, A. Fert, M. Garcia-Hernandez, A. Bachtold, G. F. Schneider, F. Guinea, C. Dekker, M. Barbone, Z. Sun, C. Galiotis, A. N. Grigorenko, G. Konstantatos, A. Kis, M. Katsnelson, L. Vandersypen, A. Loiseau, V. Morandi, D. Neumaier, E. Treossi, V. Pellegrini, M. Polini, A. Tredicucci, G. M. Williams, B. Hee Hong, J.-H. Ahn, J. Min Kim, H. Zirath, B. J. van Wees, H. van der Zant, L. Occhipinti, A. Di Matteo, I. A. Kinloch, T. Seyller, E. Quesnel, X. Feng, K. Teo, N. Rupesinghe, P. Hakonen, S. R. T. Neil, Q. Tannock, T. Löfwander, and J. Kinaret.

Science and technology roadmap for graphene, related two-dimensional crystals, and hybrid systems. *Nanoscale*, 7(11):4598–4810, 2015.

[47] P. N. First, W. A. de Heer, T. Seyller, C. Berger, J. A. Stroscio, and J.-S. Moon. Epitaxial graphenes on SiC. *MRS Bulletin*, 35(4):296–305, 2010.

[48] Ø. Fischer. Scanning tunneling spectroscopy of high-temperature superconductors. *Rev. Mod. Phys.*, 79(1):353–419, 2007.

[49] F. C. Frank and J. H. van der Merwe. One-Dimensional Dislocations. I. Static Theory. *Proc. R Soc. A*, 198(1053):205–216, Aug. 1949.

[50] F. C. Frank and J. H. van der Merwe. One-Dimensional Dislocations. II. Misfitting Monolayers and Oriented Overgrowth. *Proc. R Soc. A*, 198(1053):216–225, Aug. 1949.

[51] Y. I. Frenkel and T. Kontorova. On the theory of plastic deformation and twinning. *Zh. Eksp. Teor. Fiz.*, 8:89–95, 1938.

[52] G. D. Förster, F. Rabilloud, and F. Calvo. Atomistic modeling of epitaxial graphene on Ru(0001) and deposited ruthenium nanoparticles. *Phys. Rev. B*, 92(16):165425, Oct. 2015.

[53] J. Gao, Q. Yuan, H. Hu, J. Zhao, and F. Ding. Formation of Carbon Clusters in the Initial Stage of Chemical Vapor Deposition Graphene Growth on Ni(111) Surface. *J. Phys. Chem. C*, 115(36):17695–17703, Sept. 2011.

[54] J. Gao and J. Zhao. Carbon clusters near the step of Rh surface: implication for the initial stage of graphene nucleation. *Eur. Phys. J. D*, 67(3), Mar. 2013.

[55] M. Gao, Y. Pan, L. Huang, H. Hu, L. Z. Zhang, H. M. Guo, S. X. Du, and H.-J. Gao. Epitaxial growth and structural property of graphene on Pt(111). *Appl. Phys. Lett.*, 98(3):033101, 2011.

[56] I. Gierz, T. Suzuki, R. T. Weitz, D. S. Lee, B. Krauss, C. Riedl, U. Starke, H. Höchst, J. H. Smet, C. R. Ast, and K. Kern. Electronic decoupling of an epitaxial graphene monolayer by gold intercalation. *Phys. Rev. B*, 81(23):235408, June 2010.

[57] G. Giovannetti, P. A. Khomyakov, G. Brocks, V. M. Karpan, J. van den Brink, and P. J. Kelly. Doping Graphene with Metal Contacts. *Phys. Rev. Lett.*, 101(2):026803, July 2008.

[58] M. Goerbig and G. Montambaux. Dirac Fermions in Condensed Matter and Beyond. In B. Duplantier, V. Rivasseau, and J.-N. Fuchs, editors, *Dirac Matter*, number 71 in Progress in Mathematical Physics, pages 25–53. Springer International Publishing, 2017. DOI: 10.1007/978-3-319-32536-1_2.

[59] M. O. Goerbig. Electronic properties of graphene in a strong magnetic field. *Rev. Mod. Phys.*, 83(4):1193–1243, Nov. 2011.

[60] J. Goldstone, A. Salam, and S. Weinberg. Broken Symmetries. *Phys. Rev.*, 127(3):965–970, Aug. 1962.

[61] K. K. Gomes, W. Mar, W. Ko, F. Guinea, and H. C. Manoharan. Designer Dirac fermions and topological phases in molecular graphene. *Nature*, 483(7389):306–310, Mar. 2012.

[62] S. Gottardi, K. Müller, L. Bignardi, J. C. Moreno-López, T. A. Pham, O. Ivashenko, M. Yablonskikh, A. Barinov, J. Björk, P. Rudolf, and M. Stöhr. Comparing Graphene Growth on Cu(111) versus Oxidized Cu(111). *Nano Lett.*, 15(2):917–922, Feb. 2015.

[63] S. Grandthyll, S. Gsell, M. Weinl, M. Schreck, S. Hüfner, and F. Müller. Epitaxial growth of graphene on transition metal surfaces: chemical vapor deposition versus liquid phase deposition. *J. Phys. Condens. Matter*, 24(31):314204, Aug. 2012.

[64] S. Grimme. Semiempirical GGA-type density functional constructed with a long-range dispersion correction. *J. Comput. Chem.*, 27(15):1787–1799, Nov. 2006.

[65] C. Gutiérrez, C.-J. Kim, L. Brown, T. Schiros, D. Nordlund, E. B. Lochocki, K. M. Shen, J. Park, and A. N. Pasupathy. Imaging chiral symmetry breaking from Kekulé bond order in graphene. *Nature Phys.*, 12(10):950–958, May 2016.

[66] G. Haase and M. Asscher. Adsorption and dissociation of N_2 on Re single crystal surfaces. *Surf. Sci.*, 191:75–92, 1987.

[67] K. Hahn and M. Mavrikakis. Atomic and Molecular Adsorption on Re(0001). *Top. Catal.*, 57(1-4):54–68, Feb. 2014.

[68] S. J. Haigh, A. Gholinia, R. Jalil, S. Romani, L. Britnell, D. C. Elias, K. S. Novoselov, L. A. Ponomarenko, A. K. Geim, and R. Gorbachev. Cross-sectional imaging of individual layers and buried interfaces of graphene-based heterostructures and superlattices. *Nat. Mater.*, 11(9):764–767, July 2012.

[69] B. I. Halperin and D. R. Nelson. Theory of two-dimensional melting. *Phys. Rev. Lett.*, 41(2):121, 1978.

[70] J. Hass, R. Feng, J. E. Millán-Otoya, X. Li, M. Sprinkle, P. N. First, W. A. de Heer, E. H. Conrad, and C. Berger. Structural properties of the multilayer graphene/4H-SiC(000$\bar{1}$) system as determined by surface x-ray diffraction. *Phys. Rev. B*, 75(21):214109, June 2007.

[71] J. Hass, F. Varchon, J. E. Millán-Otoya, M. Sprinkle, N. Sharma, W. A. de Heer, C. Berger, P. N. First, L. Magaud, and E. H. Conrad. Why multilayer graphene on 4H-SiC (000$\bar{1}$) behaves like a single sheet of graphene. *Phys. Rev. Lett.*, 100(12):125504, Mar. 2008.

[72] H. Hattab, A. T. N'Diaye, D. Wall, G. Jnawali, J. Coraux, C. Busse, R. van Gastel, B. Poelsema, T. Michely, F.-J. Meyer zu Heringdorf, and M. Horn-von Hoegen. Growth temperature dependent graphene alignment on Ir(111). *Appl. Phys. Lett.*, 98(14):141903, 2011.

[73] H. Hattab, A. T. N'Diaye, D. Wall, C. Klein, G. Jnawali, J. Coraux, C. Busse, R. van Gastel, B. Poelsema, T. Michely, F.-J. Meyer zu Heringdorf, and M. Horn-von Hoegen. Interplay of wrinkles, strain, and lattice parameter in graphene on iridium. *Nano Lett.*, 12(2):678–682, Feb. 2012.

[74] A. J. Heeger, S. Kivelson, J. R. Schrieffer, and W.-P. Su. Solitons in conducting polymers. *Rev. Mod. Phys.*, 60(3):781, 1988.

[75] K. Hermann. Periodic overlayers and moiré patterns: theoretical studies of geometric properties. *J. Phys. Condens. Matter*, 24(31):314210, Aug. 2012.

[76] S. K. Hämäläinen, M. P. Boneschanscher, P. H. Jacobse, I. Swart, K. Pussi, W. Moritz, J. Lahtinen, P. Liljeroth, and J. Sainio. Structure and local variations of the graphene moiré on Ir(111). *Phys. Rev. B*, 88(20):201406(R), Nov. 2013.

[77] P. C. Hohenberg. Existence of Long-Range Order in One and Two Dimensions. *Phys. Rev.*, 158(2):383–386, June 1967.

[78] C.-Y. Hou, C. Chamon, and C. Mudry. Electron Fractionalization in Two-Dimensional Graphenelike Structures. *Phys. Rev. Lett.*, 98(18):186809, May 2007.

[79] M. Héritier. *Physique de la matière condensée: Des atomes froids aux supraconducteurs à haute température critique.* EDP Sciences, Sept. 2013.

[80] B. Hunt, D. Sanchez-Yamagishi, A. F. Young, M. Yankowitz, B. J. LeRoy, K. Watanabe, T. Taniguchi, P. Moon, M. Koshino, P. Jarillo-Herrero, and E. Ashoori. Massive Dirac fermions and Hofstadter butterfly in a van der Waals heterostructure. *Science*, 340(6139):1427–1430, June 2013.

[81] M. Iannuzzi, I. Kalichava, H. Ma, S. J. Leake, H. Zhou, G. Li, Y. Zhang, O. Bunk, H. Gao, J. Hutter, P. R. Willmott, and T. Greber. Moiré beatings in graphene on Ru(0001). *Phys. Rev. B*, 88(12):125433, Sept. 2013.

[82] E. B. Isaacs and C. A. Marianetti. Ideal strength and phonon instability of strained monolayer materials. *Phys. Rev. B*, 89(18):184111, May 2014.

[83] R. Jackiw and C. Rebbi. Solitons with fermion number $\frac{1}{2}$. *Phys. Rev. D*, 13(12):3398–3409, June 1976.

[84] F. Jean, T. Zhou, N. Blanc, R. Felici, J. Coraux, and G. Renaud. Effect of preparation on the commensurabilities and thermal expansion of graphene on Ir(111) between 10 and 1300 K. *Phys. Rev. B*, 88(16):165406, Oct. 2013.

[85] F. Jean, T. Zhou, N. Blanc, R. Felici, J. Coraux, and G. Renaud. Topography of the graphene/Ir(111) moiré studied by surface x-ray diffraction. *Phys. Rev. B*, 91(24):245424, June 2015.

[86] M. H. Jensen and P. Bak. Pinning and annealing of solitons in modulated systems. *Phys. Rev. B*, 29(11):6280–6284, June 1984.

[87] L. Ju, Z. Shi, N. Nair, Y. Lv, C. Jin, J. Velasco, C. Ojeda-Aristizabal, H. A. Bechtel, M. C. Martin, A. Zettl, J. Analytis, and F. Wang. Topological valley transport at bilayer graphene domain walls. *Nature*, 520(7549):650–655, Apr. 2015.

[88] P. Kaghazchi and T. Jacob. Structure of rhenium surfaces in an oxygen environment. *Phys. Rev. B*, 83(3):035417, Jan. 2011.

[89] B. Kandemir and A. Mogulkoc. Zone-boundary phonon induced mini band gap formation in graphene. *Solid State Commun.*, 177:80–83, Jan. 2014.

[90] M. I. Katsnelson and A. Fasolino. Graphene as a Prototype Crystalline Membrane. *Acc. Chem. Res.*, 46(1):97–105, Jan. 2013.

[91] M. I. Katsnelson, K. S. Novoselov, and A. K. Geim. Chiral tunnelling and the Klein paradox in graphene. *Nature Phys.*, 2(9):620–625, Sept. 2006.

[92] D. G. Kelly, A. J. Gellman, M. Salmeron, G. A. Somorjai, V. Maurice, M. Huber, and J. Oudar. Adsorption and coadsorption of sulfur and carbon monoxide on rhenium single crystal surfaces. *Surf. Sci.*, 204:1–25, 1988.

[93] K. Kern, P. Zeppenfeld, R. David, and G. Comsa. Incommensurate to high-order commensurate phase transition of Kr on Pt(111). *Phys. Rev. Lett.*, 59(1):79–82, July 1987.

[94] P. A. Khomyakov, G. Giovannetti, P. C. Rusu, G. Brocks, J. van den Brink, and P. J. Kelly. First-principles study of the interaction and charge transfer between graphene and metals. *Phys. Rev. B*, 79(19):195425, May 2009.

[95] M. Kindermann and P. N. First. Local sublattice-symmetry breaking in rotationally faulted multilayer graphene. *Phys. Rev. B*, 83(4):045425, Jan. 2011.

[96] M. Kindermann, B. Uchoa, and D. L. Miller. Zero-energy modes and gate-tunable gap in graphene on hexagonal boron nitride. *Phys. Rev. B*, 86(11):115415, Sept. 2012.

[97] H. W. King. *CRC Handbook of Chemistry and Physics.* CRC Press 74th edition, Lide D. R. edition, 1993.

[98] B. Kiraly, E. V. Iski, A. J. Mannix, B. L. Fisher, M. C. Hersam, and N. P. Guisinger. Solid-source growth and atomic-scale characterization of graphene on Ag(111). *Nat. Commun.*, 4:2804, Nov. 2013.

[99] W. Kohn. Image of the Fermi Surface in the Vibration Spectrum of a Metal. *Phys. Rev. Lett.*, 2(9):393, 1959.

[100] W. Kohn and L. J. Sham. Self-Consistent Equations Including Exchange and Correlation Effects. *Phys. Rev.*, 140(4A):A1133–A1138, 1965.

[101] A. Koma. Van der Waals epitaxy—a new epitaxial growth method for a highly lattice-mismatched system. *Thin Solid Films*, 216(1):72–76, Aug. 1992.

[102] J. M. Kosterlitz and D. J. Thouless. Long range order and metastability in two dimensional solids and superfluids. *J. Phys. C: Solid State Phys.*, 5:L124–L126, 1972.

[103] J. M. Kosterlitz and D. J. Thouless. Ordering, metastability and phase transitions in two-dimensional systems. *J. Phys. C: Solid State Phys.*, 6:1181–1203, 1973.

[104] M. Kralj, I. Pletikosić, M. Petrović, P. Pervan, M. Milun, A. T. N'Diaye, C. Busse, T. Michely, J. Fujii, and I. Vobornik. Graphene on Ir(111) characterized by angle-resolved photoemission. *Phys. Rev. B*, 84(7):075427, Aug. 2011.

[105] G. Kresse and J. Hafner. Ab initio molecular dynamics for liquid metals. *Phys. Rev. B*, 47(1):558–561, 1993.

[106] G. Kresse and D. Joubert. From ultrasoft pseudopotentials to the projector augmented-wave method. *Phys. Rev. B*, 59(3):1758, 1999.

[107] P. Lacovig, M. Pozzo, D. Alfè, P. Vilmercati, A. Baraldi, and S. Lizzit. Growth of Dome-Shaped Carbon Nanoislands on Ir(111): The Intermediate between Carbidic Clusters and Quasi-Free-Standing Graphene. *Phys. Rev. Lett.*, 103(16):166101, Oct. 2009.

[108] J. Lahiri, Y. Lin, P. Bozkurt, I. I. Oleynik, and M. Batzill. An extended defect in graphene as a metallic wire. *Nat. Nanotech.*, 5(5):326–329, May 2010.

[109] J. Lahiri, T. Miller, L. Adamska, I. I. Oleynik, and M. Batzill. Graphene Growth on Ni(111) by Transformation of a Surface Carbide. *Nano Lett.*, 11(2):518–522, Feb. 2011.

[110] T. A. Land, T. Michely, R. J. Behm, J. C. Hemminger, and G. Comsa. STM investigation of the adsorption and temperature dependent reactions of ethylene on Pt (111). *Appl. Phys. A*, 53(5):414–417, 1991.

[111] J.-U. Lee, D. Yoon, and H. Cheong. Estimation of Young's modulus of graphene by Raman spectroscopy. *Nano Lett.*, 12(9):4444–4448, Sept. 2012.

[112] S.-H. Lee, H.-J. Chung, J. Heo, H. Yang, J. Shin, U.-I. Chung, and S. Seo. Band Gap Opening by Two-Dimensional Manifestation of Peierls Instability in Graphene. *ACS Nano*, 5(4):2964–2969, Apr. 2011.

[113] O. Lehtinen, S. Kurasch, A. Krasheninnikov, and U. Kaiser. Atomic scale study of the life cycle of a dislocation in graphene from birth to annihilation. *Nat. Commun.*, 4, June 2013.

[114] P. Leicht, L. Zielke, S. Bouvron, R. Moroni, E. Voloshina, L. Hammerschmidt, Y. S. Dedkov, and M. Fonin. *In Situ* Fabrication Of Quasi-Free-Standing Epitaxial Graphene Nanoflakes On Gold. *ACS Nano*, 8(4):3735–3742, Apr. 2014.

[115] J. Li, K. Wang, K. J. McFaul, Z. Zern, Y. Ren, K. Watanabe, T. Taniguchi, Z. Qiao, and J. Zhu. Gate-controlled topological conducting channels in bilayer graphene. *Nat. Nanotech.*, 11(12):1060–1065, Aug. 2016.

[116] X. Li, W. Cai, J. An, S. Kim, J. Nah, D. Yang, R. Piner, A. Velamakanni, I. Jung, E. Tutuc, S. K. Banerjee, L. Colombo, and R. S. Ruoff. Large-Area Synthesis of High-Quality and Uniform Graphene Films on Copper Foils. *Science*, 324(5932):1312–1314, June 2009.

[117] K. S. Liang, K. L. D'Amico, C. H. Lee, and E. Y. Sheu. Domain-wall pinning in uniaxial phases of Pb adlayers on a Cu(110) surface. *Phys. Rev. Lett.*, 65(24):3025–3028, Dec. 1990.

[118] T. L. Linnik. Effective Hamiltonian of strained graphene. *J. Phys. Condens. Matter*, 24(20):205302, May 2012.

[119] E. Loginova, N. C. Bartelt, P. J. Feibelman, and K. F. McCarty. Evidence for graphene growth by C cluster attachment. *New J. Phys.*, 10(9):093026, Sept. 2008.

[120] E. Loginova, S. Nie, K. Thürmer, N. C. Bartelt, and K. F. McCarty. Defects of graphene on Ir(111): rotational domains and ridges. *Phys. Rev. B*, 80(8):085430, Aug. 2009.

[121] J. Lu, P. S. E. Yeo, C. K. Gan, P. Wu, and K. P. Loh. Transforming C_{60} molecules into graphene quantum dots. *Nat. Nanotech.*, 6(4):247–252, Apr. 2011.

[122] A. Luican, G. Li, A. Reina, J. Kong, R. R. Nair, K. S. Novoselov, A. K. Geim, and E. Y. Andrei. Single-layer behavior and its breakdown in twisted graphene layers. *Phys. Rev. Lett.*, 106(12):126802, Mar. 2011.

[123] J. L. Mañes. Symmetry-based approach to electron-phonon interactions in graphene. *Phys. Rev. B*, 76(4), July 2007.

[124] J. E. Mahan, K. M. Geib, G. Y. Robinson, and R. G. Long. A review of the geometrical fundamentals of reflection high-energy electron diffraction with application to silicon surfaces. *J. Vac. Sci. Technol. A*, 8(5):3692–3700, Sept. 1990.

[125] P. Mallet, F. Varchon, C. Naud, L. Magaud, C. Berger, and J.-Y. Veuillen. Electron states of mono- and bilayer graphene on SiC probed by scanning-tunneling microscopy. *Phys. Rev. B*, 76(4):041403(R), July 2007.

[126] K. L. Man and M. S. Altman. Small-angle lattice rotations in graphene on Ru(0001). *Phys. Rev. B*, 84(23):235415, Dec. 2011.

[127] D. Marchenko, A. Varykhalov, M. Scholz, G. Bihlmayer, E. Rashba, A. Rybkin, A. Shikin, and O. Rader. Giant Rashba splitting in graphene due to hybridization with gold. *Nat. Commun.*, 3:1232, Nov. 2012.

[128] D. Marchenko, A. Varykhalov, J. Sánchez-Barriga, T. Seyller, and O. Rader. Rashba splitting of 100 meV in Au-intercalated graphene on SiC. *Appl. Phys. Lett.*, 108(17):172405, Apr. 2016.

[129] S. Marchini, S. Günther, and J. Wintterlin. Scanning tunneling microscopy of graphene on Ru(0001). *Phys. Rev. B*, 76(7):075429, Aug. 2007.

[130] C. A. Marianetti and H. G. Yevick. Failure Mechanisms of Graphene under Tension. *Phys. Rev. Lett.*, 105(24):245502, Dec. 2010.

[131] I. Martin, Y. M. Blanter, and A. F. Morpurgo. Topological Confinement in Bilayer Graphene. *Phys. Rev. Lett.*, 100(3):036804, Jan. 2008.

[132] A. J. Martínez-Galera, I. Brihuega, and J. M. Gómez-Rodríguez. Ethylene Irradiation: A New Route to Grow Graphene on Low Reactivity Metals. *Nano Lett.*, 11(9):3576–3580, Sept. 2011.

[133] A. J. Martínez-Galera and J. M. Gómez-Rodríguez. Surface diffusion of simple organic molecules on graphene on Pt(111). *J. Phys. Chem. C*, 115(46):23036–23042, Nov. 2011.

[134] D. Martoccia, P. R. Willmott, T. Brugger, M. Björck, S. Günther, C. M. Schlepütz, A. Cervellino, S. A. Pauli, B. D. Patterson, S. Marchini, J. Wintterlin, W. Moritz, and T. Greber. Graphene on Ru(0001): a 25 × 25 supercell. *Phys. Rev. Lett.*, 101(12):126102, Sept. 2008.

[135] K. F. McCarty, P. J. Feibelman, E. Loginova, and N. C. Bartelt. Kinetics and thermodynamics of carbon segregation and graphene growth on Ru(0001). *Carbon*, 47(7):1806–1813, June 2009.

[136] L. Meng, R. Wu, L. Zhang, L. Li, S. Du, Y. Wang, and H.-J. Gao. Multi-oriented moiré superstructures of graphene on Ir(111): experimental observations and theoretical models. *J. Phys. Condens. Matter*, 24(31):314214, Aug. 2012.

[137] P. Merino, M. Švec, A. L. Pinardi, G. Otero, and J. A. Martín-Gago. Strain-driven moiré superstructures of epitaxial graphene on transition metal surfaces. *ACS Nano*, 5(7):5627–5634, July 2011.

[138] N. D. Mermin. Crystalline order in two dimensions. *Phys. Rev.*, 176(1):250, 1968.

[139] N. D. Mermin. The topological theory of defects in ordered media. *Rev. Mod. Phys.*, 51(3):591, 1979.

[140] N. D. Mermin and H. Wagner. Absence of ferromagnetism or antiferromagnetism in one-or two-dimensional isotropic Heisenberg models. *Phys. Rev. Lett.*, 17(22):1133, 1966.

[141] J. C. Meyer, A. K. Geim, M. I. Katsnelson, K. S. Novoselov, T. J. Booth, and S. Roth. The structure of suspended graphene sheets. *Nature*, 446(7131):60–63, Mar. 2007.

[142] E. Miniussi, M. Pozzo, A. Baraldi, E. Vesselli, R. R. Zhan, G. Comelli, T. O. Menteş, M. A. Niño, A. Locatelli, S. Lizzit, and D. Alfè. Thermal stability of corrugated epitaxial graphene grown on Re(0001). *Phys. Rev. Lett.*, 106(21):216101, May 2011.

[143] E. Miniussi, M. Pozzo, T. Menteş, M. Niño, A. Locatelli, E. Vesselli, G. Comelli, S. Lizzit, D. Alfè, and A. Baraldi. The competition for graphene formation on Re(0001): A complex interplay between carbon segregation, dissolution and carburisation. *Carbon*, 73:389–402, July 2014.

[144] K. Miyake, K. Akutsu, T. Yamada, K. Hata, R. Morita, M. Yamashita, and H. Shigekawa. Giant superstructures formed on graphite surface treated with NaOH solutions studied by scanning tunneling microscopy. *Ultramicroscopy*, 73(1):185–189, 1998.

[145] M. N. Nair, M. Cranney, F. Vonau, D. Aubel, P. Le Fèvre, A. Tejeda, F. Bertran, A. Taleb-Ibrahimi, and L. Simon. High van Hove singularity extension and Fermi velocity increase in epitaxial graphene functionalized by intercalated gold clusters. *Phys. Rev. B*, 85(24):245421, June 2012.

[146] F. D. Natterer, S. Rusponi, M. Papagno, C. Carbone, and H. Brune. Optimizing long-range order, band gap, and group velocities for graphene on close-packed metal surfaces. *J. Phys. Condens. Matter*, 24(31):314203, Aug. 2012.

[147] A. T. N'Diaye, J. Coraux, T. N. Plasa, C. Busse, and T. Michely. Structure of epitaxial graphene on Ir(111). *New J. Phys.*, 10(4):043033, Apr. 2008.

[148] D. R. Nelson and B. I. Halperin. Dislocation-mediated melting in two dimensions. *Phys. Rev. B*, 19(5):2457–2484, Mar. 1979.

[149] V. H. Nguyen and P. Dollfus. Strain-induced modulation of Dirac cones and van Hove singularities in a twisted graphene bilayer. *2D Mater.*, 2(3):035005, July 2015.

[150] S. Nie, N. C. Bartelt, J. M. Wofford, O. D. Dubon, K. F. McCarty, and K. Thürmer. Scanning tunneling microscopy study of graphene on Au(111):

Growth mechanisms and substrate interactions. *Phys. Rev. B*, 85(20):205406, May 2012.

[151] K. S. Novoselov, A. K. Geim, S. V. Morozov, D. Jiang, M. I. Katsnelson, I. V. Grigorieva, S. V. Dubonos, and A. A. Firsov. Two-dimensional gas of massless Dirac fermions in graphene. *Nature*, 438(7065):197–200, Nov. 2005.

[152] K. S. Novoselov, A. K. Geim, S. V. Morozov, D. Jiang, Y. Zhang, S. V. Dubonos, I. V. Grigorieva, and A. A. Firsov. Electric field effect in atomically thin carbon films. *Science*, 306:666–669, 2004.

[153] B. Nysten, J.-C. Roux, S. Flandrois, C. Daulan, and H. Saadaoui. AFM-STM studies of carbonization and graphitization of polyimide films. *Phys. Rev. B*, 48(17):12527–12551, Nov. 1993.

[154] T. Ohta, J. T. Robinson, P. J. Feibelman, A. Bostwick, E. Rotenberg, and T. E. Beechem. Evidence for interlayer coupling and moiré periodic potentials in twisted bilayer graphene. *Phys. Rev. Lett.*, 109(18):186807, Nov. 2012.

[155] M. Orlita, C. Faugeras, P. Plochocka, P. Neugebauer, G. Martinez, D. K. Maude, A.-L. Barra, M. Sprinkle, C. Berger, W. A. de Heer, and M. Potemski. Approaching the Dirac point in high-mobility multilayer epitaxial graphene. *Phys. Rev. Lett.*, 101(26):267601, Dec. 2008.

[156] J. Osing and I. V. Shvets. Bulk defects in graphite observed with a scanning tunneling microscope. *Surf. Sci.*, 417:145–150, 1998.

[157] Y. Pan, H. Zhang, D. Shi, J. Sun, S. Du, F. Liu, and H.-j. Gao. Highly ordered, millimeter-scale, continuous, single-crystalline graphene monolayer formed on Ru(0001). *Adv. Mater.*, 21(27):2777–2780, July 2009.

[158] M. Papagno, P. Moras, P. M. Sheverdyaeva, J. Doppler, A. Garhofer, F. Mittendorfer, J. Redinger, and C. Carbone. Hybridization of graphene and a Ag monolayer supported on Re(0001). *Phys. Rev. B*, 88(23):235430, Dec. 2013.

[159] C.-H. Park, L. Yang, Y.-W. Son, M. L. Cohen, and S. G. Louie. Anisotropic behaviours of massless Dirac fermions in graphene under periodic potentials. *Nature Phys.*, 4(3):213–217, Mar. 2008.

[160] C.-H. Park, L. Yang, Y.-W. Son, M. L. Cohen, and S. G. Louie. New generation of massless Dirac fermions in graphene under external periodic potentials. *Phys. Rev. Lett.*, 101(12):126804, Sept. 2008.

[161] L. L. Patera, C. Africh, R. S. Weatherup, R. Blume, S. Bhardwaj, C. Castellarin-Cudia, A. Knop-Gericke, R. Schloegl, G. Comelli, S. Hofmann, and C. Cepek. *In Situ* Observations of the Atomistic Mechanisms of Ni Catalyzed Low Temperature Graphene Growth. *ACS Nano*, 7(9):7901–7912, Sept. 2013.

[162] H. Peled and M. Asscher. Dissociative chemisorption of CO_2 on a Re (0001) single crystal surface. *Surf. Sci.*, 183(1-2):201–215, 1987.

[163] J. P. Perdew, J. A. Chevary, S. H. Vosko, K. A. Jackson, M. R. Pederson, D. J. Singh, and C. Fiolhais. Atoms, molecules, solids, and surfaces: Applications of the generalized gradient approximation for exchange and correlation. *Phys. Rev. B*, 46(11):6671–6687, 1992.

[164] J. P. Perdrew, K. Burke, and M. Ernzerhof. General gradient approximation made simple. *Phys. Rev. Lett.*, 77(18):3865–3868, 1996.

[165] S. Piscanec, M. Lazzeri, F. Mauri, A. C. Ferrari, and J. Robertson. Kohn Anomalies and Electron-Phonon Interactions in Graphite. *Phys. Rev. Lett.*, 93(18):185503, Oct. 2004.

[166] I. Pletikosić, M. Kralj, P. Pervan, R. Brako, J. Coraux, A. T. N'Diaye, C. Busse, and T. Michely. Dirac cones and minigaps for graphene on Ir(111). *Phys. Rev. Lett.*, 102(5):056808, Feb. 2009.

[167] A. Politano, F. de Juan, G. Chiarello, and H. A. Fertig. Emergence of an Out-of-Plane Optical Phonon (ZO) Kohn Anomaly in Quasifreestanding Epitaxial Graphene. *Phys. Rev. Lett.*, 115(7), Aug. 2015.

[168] L. A. Ponomarenko, R. V. Gorbachev, G. L. Yu, D. C. Elias, R. Jalil, A. A. Patel, A. Mishchenko, A. S. Mayorov, C. R. Woods, J. R. Wallbank, M. Mucha-Kruczynski, B. A. Piot, M. Potemski, I. V. Grigorieva, K. S. Novoselov, F. Guinea, V. I. Fal'ko, and A. K. Geim. Cloning of Dirac fermions in graphene superlattices. *Nature*, 497(7451):594–597, May 2013.

[169] B. Premlal, M. Cranney, F. Vonau, D. Aubel, D. Casterman, M. M. De Souza, and L. Simon. Surface intercalation of gold underneath a graphene monolayer on SiC(0001) studied by scanning tunneling microscopy and spectroscopy. *Appl. Phys. Lett.*, 94(26):263115, 2009.

[170] Y. Que, W. Xiao, X. Fei, H. Chen, L. Huang, S. X. Du, and H.-J. Gao. Epitaxial growth of large-area bilayer graphene on Ru(0001). *Appl. Phys. Lett.*, 104(9):093110, Mar. 2014.

[171] S. Reich, J. Maultzsch, C. Thomsen, and P. Ordejón. Tight-binding description of graphene. *Phys. Rev. B*, 66(3):035412, July 2002.

[172] J. Repp, G. Meyer, S. M. Stojković, A. Gourdon, and C. Joachim. Molecules on Insulating Films: Scanning-Tunneling Microscopy Imaging of Individual Molecular Orbitals. *Phys. Rev. Lett.*, 94(2):026803, Jan. 2005.

[173] C. Riedl, C. Coletti, and U. Starke. Structural and electronic properties of epitaxial graphene on SiC(0001): a review of growth, characterization, transfer doping and hydrogen intercalation. *J. Phys. D: Appl. Phys.*, 43(37):374009, Sept. 2010.

[174] A. W. Robertson, G.-D. Lee, K. He, Y. Fan, C. S. Allen, S. Lee, H. Kim, E. Yoon, H. Zheng, A. I. Kirkland, and J. H. Warner. Partial Dislocations in Graphene and Their Atomic Level Migration Dynamics. *Nano Letters*, 15(9):5950–5955, Sept. 2015.

[175] R. Roldán, A. Fasolino, K. V. Zakharchenko, and M. I. Katsnelson. Suppression of anharmonicities in crystalline membranes by external strain. *Phys. Rev. B*, 83(17):174104, May 2011.

[176] S. Roth, F. Matsui, T. Greber, and J. Osterwalder. Chemical Vapor Deposition and Characterization of Aligned and Incommensurate Graphene/Hexagonal Boron Nitride Heterostack on Cu(111). *Nano Lett.*, 13(6):2668–2675, June 2013.

[177] G. M. Rutter, J. N. Crain, N. P. Guisinger, T. Li, P. N. First, and J. A. Stroscio. Scattering and Interference in Epitaxial Graphene. *Science*, 317(5835):219–222, July 2007.

[178] G. G. Samsonidze, E. B. Barros, R. Saito, J. Jiang, G. Dresselhaus, and M. S. Dresselhaus. Electron-phonon coupling mechanism in two-dimensional graphite and single-wall carbon nanotubes. *Phys. Rev. B*, 75(15):155420, Apr. 2007.

[179] J. Sławińska, P. Dabrowski, and I. Zasada. Doping of graphene by a Au(111) substrate: Calculation strategy within the local density approximation and a semiempirical van der Waals approach. *Phys. Rev. B*, 83(24):245429, June 2011.

[180] G. W. Semenoff. Condensed-matter simulation of a three-dimensional anomaly. *Phys. Rev. Lett.*, 53(26):2449, 1984.

[181] G. W. Semenoff, V. Semenoff, and F. Zhou. Domain Walls in Gapped Graphene. *Phys. Rev. Lett.*, 101(8):087204, Aug. 2008.

[182] J. P. Sethna. *Statistical Mechanics: Entropy, Order Parameters and Complexity.* OUP Oxford, Oxford ; New York, 2006.

[183] A. M. Shikin, A. G. Rybkin, D. Marchenko, A. A. Rybkina, M. R. Scholz, O. Rader, and A. Varykhalov. Induced spin–orbit splitting in graphene: the role of atomic number of the intercalated metal and π–d hybridization. *New J. Phys.*, 15(1):013016, Jan. 2013.

[184] J. Sánchez-Barriga, A. Varykhalov, D. Marchenko, M. R. Scholz, and O. Rader. Minigap isotropy and broken chirality in graphene with periodic corrugation enhanced by cluster superlattices. *Phys. Rev. B*, 85(20):201413(R), May 2012.

[185] D. Stradi, S. Barja, C. Díaz, M. Garnica, B. Borca, J. J. Hinarejos, D. Sánchez-Portal, M. Alcamí, A. Arnau, A. L. Vázquez de Parga, R. Miranda, and F. Martín. Role of dispersion forces in the structure of graphene monolayers on Ru surfaces. *Phys. Rev. Lett.*, 106(18):186101, May 2011.

[186] K. J. Strandburg. Two-dimensional melting. *Rev. Mod. Phys.*, 60(1):161, 1988.

[187] W. Su, J. R. Schrieffer, and A. J. Heeger. Solitons in polyacetylene. *Phys. Rev. Lett.*, 42(25):1698, 1979.

[188] W. P. Su, J. R. Schrieffer, and A. J. Heeger. Soliton excitations in polyacetylene. *Phys. Rev. B*, 22(4):2099–2111, Aug. 1980.

[189] P. Sutter, M. S. Hybertsen, J. T. Sadowski, and E. Sutter. Electronic structure of few-layer epitaxial graphene on Ru(0001). *Nano Lett.*, 9(7):2654–2660, July 2009.

[190] P. Sutter, J. T. Sadowski, and E. Sutter. Graphene on Pt(111): growth and substrate interaction. *Phys. Rev. B*, 80(24):245411, Dec. 2009.

[191] H. Tetlow, J. Posthuma de Boer, I. Ford, D. Vvedensky, J. Coraux, and L. Kantorovich. Growth of epitaxial graphene: theory and experiment. *Phys. Rep.*, 542(3):195–295, Sept. 2014.

[192] G. Theodorou and T. M. Rice. Statics and dynamics of incommensurate lattices. *Phys. Rev. B*, 18(6):2840–2856, Sept. 1978.

[193] C. Tonnoir, A. Kimouche, J. Coraux, L. Magaud, B. Delsol, B. Gilles, and C. Chapelier. Induced superconductivity in graphene grown on rhenium. *Phys. Rev. Lett.*, 111(24):246805, Dec. 2013.

[194] G. Trambly de Laissardière, D. Mayou, and L. Magaud. Numerical studies of confined states in rotated bilayers of graphene. *Phys. Rev. B*, 86(12):125413, Sept. 2012.

[195] H. Ueta, M. Saida, C. Nakai, Y. Yamada, M. Sasaki, and S. Yamamoto. Highly oriented monolayer graphite formation on Pt(111) by a supersonic methane beam. *Surf. Sci.*, 560(1-3):183–190, July 2004.

[196] M. M. Ugeda, D. Fernández-Torre, I. Brihuega, P. Pou, A. J. Martínez-Galera, R. Pérez, and J. M. Gómez-Rodríguez. Point defects on graphene on metals. *Phys. Rev. Lett.*, 107(11):116803, Sept. 2011.

[197] D. Usachov, V. K. Adamchuk, D. Haberer, A. Grüneis, H. Sachdev, A. B. Preobrajenski, C. Laubschat, and D. V. Vyalikh. Quasifreestanding single-layer hexagonal boron nitride as a substrate for graphene synthesis. *Phys. Rev. B*, 82(7):075415, Aug. 2010.

[198] D. Usachov, A. Fedorov, O. Vilkov, V. K. Adamchuk, L. V. Yashina, L. Bondarenko, A. A. Saranin, A. Grüneis, and D. V. Vyalikh. Experimental and computational insight into the properties of the lattice-mismatched structures: Monolayers of h -BN and graphene on Ir(111). *Phys. Rev. B*, 86(15):155151, Oct. 2012.

[199] A. Vaezi, Y. Liang, D. H. Ngai, L. Yang, and E.-A. Kim. Topological Edge States at a Tilt Boundary in Gated Multilayer Graphene. *Phys. Rev. X*, 3(2):021018, June 2013.

[200] J. H. van der Merwe. Equilibrium Structure of a Thin Epitaxial Film. *J. Appl. Phys.*, 41(11):4725, 1970.

[201] F. Varchon, P. Mallet, L. Magaud, and J.-Y. Veuillen. Rotational disorder in few-layer graphene films on 6H-SiC(000-1) : A scanning tunneling microscopy study. *Phys. Rev. B*, 77(16):165415, Apr. 2008.

[202] A. Varykhalov, M. R. Scholz, T. K. Kim, and O. Rader. Effect of noble-metal contacts on doping and band gap of graphene. *Phys. Rev. B*, 82(12):121101(R), Sept. 2010.

[203] A. Varykhalov, J. Sánchez-Barriga, A. M. Shikin, C. Biswas, E. Vescovo, A. Rybkin, D. Marchenko, and O. Rader. Electronic and Magnetic Properties of Quasifreestanding Graphene on Ni. *Phys. Rev. B*, 101(15):157601, Oct. 2008.

[204] P. Venezuela, M. Lazzeri, and F. Mauri. Theory of double-resonant Raman spectra in graphene: Intensity and line shape of defect-induced and two-phonon bands. *Phys. Rev. B*, 84(3):035433, July 2011.

[205] C. Vo-Van, A. Kimouche, A. Reserbat-Plantey, O. Fruchart, P. Bayle-Guillemaud, N. Bendiab, and J. Coraux. Epitaxial graphene prepared by chemical vapor deposition on single crystal thin iridium films on sapphire. *Appl. Phys. Lett.*, 98(18):181903, 2011.

[206] E. N. Voloshina and Y. S. Dedkov. General approach to understanding the electronic structure of graphene on metals. *Mater. Res. Express*, 1(3):035603, Aug. 2014.

[207] E. N. Voloshina, Y. S. Dedkov, S. Torbrügge, A. Thissen, and M. Fonin. Graphene on Rh(111): Scanning tunneling and atomic force microscopies studies. *Appl. Phys. Lett.*, 100(24):241606, 2012.

[208] E. N. Voloshina, A. Generalov, M. Weser, S. Böttcher, K. Horn, and Y. S. Dedkov. Structural and electronic properties of the graphene/Al/Ni(111) intercalation system. *New J. Phys.*, 13(11):113028, Nov. 2011.

[209] A. L. Vázquez de Parga, F. Calleja, B. Borca, M. C. G. Passeggi, J. J. Hinarejos, F. Guinea, and R. Miranda. Periodically Rippled Graphene: Growth and Spatially Resolved Electronic Structure. *Phys. Rev. Lett.*, 100(5):056807, Feb. 2008.

[210] P. Wallace. The band theory of graphite. *Phys. Rev.*, 71(9):622–634, 1947.

[211] J. R. Wallbank, A. A. Patel, M. Mucha-Kruczyński, A. K. Geim, and V. I. Fal'ko. Generic miniband structure of graphene on a hexagonal substrate. *Phys. Rev. B*, 87(24):245408, June 2013.

[212] A. L. Walter, S. Nie, A. Bostwick, K. S. Kim, L. Moreschini, Y. J. Chang, D. Innocenti, K. Horn, K. F. McCarty, and E. Rotenberg. Electronic structure of graphene on single-crystal copper substrates. *Phys. Rev. B*, 84(19):195433, Nov. 2011.

[213] B. Wang, M.-L. Bocquet, S. Marchini, S. Günther, and J. Wintterlin. Chemical origin of a graphene moiré overlayer on Ru(0001). *Phys. Chem. Chems. Phys.*, 10(24):3530, 2008.

[214] B. Wang, M. Caffio, C. Bromley, H. Früchtl, and R. Schaub. Coupling Epitaxy, Chemical Bonding, and Work Function at the Local Scale in Transition Metal-Supported Graphene. *ACS Nano*, 4(10):5773–5782, Oct. 2010.

[215] B. Wang, X. Ma, M. Caffio, R. Schaub, and W.-X. Li. Size-Selective Carbon Nanoclusters as Precursors to the Growth of Epitaxial Graphene. *Nano Lett.*, 11(2):424–430, Feb. 2011.

[216] E. Wang, X. Lu, S. Ding, W. Yao, M. Yan, G. Wan, K. Deng, S. Wang, G. Chen, L. Ma, J. Jung, A. V. Fedorov, Y. Zhang, G. Zhang, and S. Zhou. Gaps induced by inversion symmetry breaking and second-generation Dirac cones in graphene/hexagonal boron nitride. *Nature Phys.*, 12(12):1111–1115, Dec. 2016.

[217] J. Wintterlin and M.-L. Bocquet. Graphene on metal surfaces. *Surf. Sci.*, 603(10-12):1841–1852, June 2009.

[218] J. M. Wofford, E. Starodub, A. L. Walter, S. Nie, A. Bostwick, N. C. Bartelt, K. Thürmer, E. Rotenberg, K. F. McCarty, and O. D. Dubon. Extraordinary epitaxial alignment of graphene islands on Au(111). *New J. Phys.*, 14(5):053008, May 2012.

[219] A. R. Wright and T. Hyart. Robust one-dimensional wires in lattice mismatched bilayer graphene. *Appl. Phys. Lett.*, 98(25):251902, 2011.

[220] K. Yang, W. D. Xiao, Y. H. Jiang, H. G. Zhang, L. W. Liu, J. H. Mao, H. T. Zhou, S. X. Du, and H.-J. Gao. Molecule–substrate coupling between metal phthalocyanines and epitaxial graphene grown on Ru(0001) and Pt(111). *J. Phys. Chem. C*, 116(26):14052–14056, July 2012.

[221] M. Yankowitz, J. Xue, D. Cormode, J. D. Sanchez-Yamagishi, K. Watanabe, T. Taniguchi, P. Jarillo-Herrero, P. Jacquod, and B. J. LeRoy. Emergence of superlattice Dirac points in graphene on hexagonal boron nitride. *Nature Phys.*, 8(5):382–386, Mar. 2012.

[222] W. Yao, E. Wang, K. Deng, S. Yang, W. Wu, A. V. Fedorov, S.-K. Mo, E. F. Schwier, M. Zheng, Y. Kojima, H. Iwasawa, K. Shimada, K. Jiang, P. Yu, J. Li, and S. Zhou. Monolayer charge-neutral graphene on platinum with extremely weak electron-phonon coupling. *Phys. Rev. B*, 92(11):115421, Sept. 2015.

[223] L.-J. Yin, H. Jiang, J.-B. Qiao, and L. He. Direct imaging of topological edge states at a bilayer graphene domain wall. *Nat. Commun.*, 7:11760, June 2016.

[224] A. F. Young and P. Kim. Quantum interference and Klein tunnelling in graphene heterojunctions. *Nature Phys.*, 5(3):222–226, Mar. 2009.

[225] Q. Yu, J. Lian, S. Siriponglert, H. Li, Y. P. Chen, and S.-S. Pei. Graphene segregated on Ni surfaces and transferred to insulators. *Appl. Phys. Lett.*, 93(11):113103, 2008.

[226] Q. Yuan, J. Gao, H. Shu, J. Zhao, X. Chen, and F. Ding. Magic Carbon Clusters in the Chemical Vapor Deposition Growth of Graphene. *J. Am. Chem. Soc.*, 134(6):2970–2975, Feb. 2012.

[227] P. Zeller, S. Dänhardt, S. Gsell, M. Schreck, and J. Wintterlin. Scalable synthesis of graphene on single crystal Ir(111) films. *Surf. Sci.*, 606(19-20):1475–1480, Oct. 2012.

[228] P. Zeller and S. Günther. What are the possible moiré patterns of graphene on hexagonally packed surfaces? *New J. Phys.*, 16(8):083028, Aug. 2014.

[229] F. Zhang, A. H. MacDonald, and E. J. Mele. Valley Chern numbers and boundary modes in gapped bilayer graphene. *Proc. Natl. Acad. Sci.*, 110(26):10546–10551, June 2013.

[230] H. G. Zhang, J. T. Sun, T. Low, L. Z. Zhang, Y. Pan, Q. Liu, J. H. Mao, H. T. Zhou, H. M. Guo, S. X. Du, F. Guinea, and H.-J. Gao. Assembly of iron phthalocyanine and pentacene molecules on a graphene monolayer grown on Ru(0001). *Phys. Rev. B*, 84(24):245436, Dec. 2011.

[231] S. Y. Zhou, G.-H. Gweon, A. V. Fedorov, P. N. First, W. A. de Heer, D.-H. Lee, F. Guinea, A. H. Castro Neto, and A. Lanzara. Substrate-induced bandgap opening in epitaxial graphene. *Nat. Mater.*, 6(10):770–775, Oct. 2007.

[232] R. S. Zimmer and W. D. Robertson. A carbon structure on the Re (0001) surface. *Surf. Sci.*, 29(1):230–236, 1972.

Quasi-ordre à longue distance et défauts topologiques dans le graphène sur rhénium étudié par microscopie à effet tunnel

La matière telle que nous en faisons l'expérience au quotidien se présente sous différents états : solide, liquide, gazeuse, etc. Parmi ces états, l'état cristallin présente un ordre régulier des atomes à grande échelle. Cependant, lorsque la matière est confinée dans un plan, comme dans le cas du graphène, elle ne peut pas être cristalline. L'ordre des atomes, bien que régulier localement, fluctue à grande échelle, donnant lieu à un quasi-ordre à longue distance.

Dans cette thèse, la structure du graphène sur rhénium est étudiée à l'échelle atomique par microscopie à effet tunnel (STM). Le rhénium peut être considéré comme une influence extérieure qui altère le quasi-ordre en imposant son ordre cristallin.

Il est déduit des images STM que des réactions chimiques entrent en compétition lors de la croissance du graphène. Cela aboutit à une structure présentant un ordre local, mais pas global. Ainsi, au lieu d'imposer un ordre cristallin, le rhénium donne lieu à un état dit chaotique.

Quasi-long-range order and topological defects in graphene on rhenium studied by scanning tunneling microscopy

Matter as we experience it on a daily basis exists in different states: solid, liquid, gaseous, etc. Among these states, the crystalline state displays a regular order of atoms on a large scale. However, when matter is confined to a plane, like for graphene, it cannot be crystalline. Although regular locally, the order of atoms fluctuates on a large scale, giving rise to so-called quasi-long-range order.

In this thesis, graphene's structure on rhenium is studied at the atomic scale using scanning tunneling microscopy (STM). Rhenium can be considered as an outside influence that alters quasi-long-range order by imposing its crystalline order.

Chemical reactions that compete during graphene growth are deduced from the STM images. This ends up forming a structure with local but not global order. Thus, instead of imposing crystalline order, rhenium gives rise to a so-called chaotic state.